University of Tennessee, Knoxville
Trace: Tennessee Research and Creative Exchange

Doctoral Dissertations | Graduate School

8-2009

A Study of Helium Ion Induced Secondary Electron Production

Ranjan Ramachandra
University of Tennessee - Knoxville

Recommended Citation

Ramachandra, Ranjan, "A Study of Helium Ion Induced Secondary Electron Production. " PhD diss., University of Tennessee, 2009.
https://trace.tennessee.edu/utk_graddiss/103

This Dissertation is brought to you for free and open access by the Graduate School at Trace: Tennessee Research and Creative Exchange. It has been accepted for inclusion in Doctoral Dissertations by an authorized administrator of Trace: Tennessee Research and Creative Exchange. For more information, please contact trace@utk.edu.

To the Graduate Council:

I am submitting herewith a dissertation written by Ranjan Ramachandra entitled "A Study of Helium Ion Induced Secondary Electron Production." I have examined the final electronic copy of this dissertation for form and content and recommend that it be accepted in partial fulfillment of the requirements for the degree of Doctor of Philosophy, with a major in Materials Science and Engineering.

David Joy, Major Professor

We have read this dissertation and recommend its acceptance:

Philip D Rack, Michael Simpson, John Biggerstaff, Harry Meyer III

Accepted for the Council:
Dixie L. Thompson

Vice Provost and Dean of the Graduate School

(Original signatures are on file with official student records.)

To the Graduate Council:
I am submitting herewith a dissertation written by Ranjan Ramachandra entitled "A Study of Helium Ion Induced Secondary Electron Production." I have examined the final electronic copy of this dissertation for form and content and recommend that it be accepted in partial fulfillment of the requirements for the degree of Doctor of Philosophy, with a major in Material Science and Engineering.

David Joy, Major Professor

We have read this dissertation
and recommend its acceptance

Philip D Rack

Michael Simpson

John Biggerstaff

Harry Meyer III

Accepted for the Council:

Carolyn R.Hodges
Vice Provost and Dean of the Graduate School

(Original signatures are on file with official student records)

A Study of Helium Ion Induced Secondary Electron Production

A
Dissertation
Presented for the
Philosophy
Degree
The University of Tennessee, Knoxville

Ranjan Ramachandra
August 2009

Acknowledgements

I would like to thank number of people who have contributed and helped me in numerous ways. Firstly I would like to thank my high school physics teacher Mr. Vijay Kumar for instilling in me an interest in physics and mathematics. I would like to thank former MSE department head late Dr. Ray Buchanan for encouraging me to pursue my graduate studies in MSE, one of the better decisions I have made. I am gratefully indebted to MSE department secretary Mrs. Sandy Maples for helping me finding assistantship for my master's studies when I was on the verge of quitting my studies due to financial constraints. I would like to thank my Master of Science advisor Dr. Larry Wadsworth for funding my MS program and also for all his kindness.

I would like to thank my Doctoral advisor Dr. David Joy for all the help over the years. His always optimistic attitude has always been an inspiration to me. His kind words have lighted up many of the arduous days. This dissertation would not have been possible without his faith in my abilities. My sincere thanks to all my committee members Drs. Philip Rack, Michael Simpson, John Biggerstaff and Harry Meyer III for their support and suggestions. I would also like to thank my lab secretary Mrs. Jennifer Trollinger, group mates, classmates and many friends for their encouragement. I would also like to thank our collaborator Dr. Brendan Griffin for his help and guidance in this project. Thanks to SRC and project manager Dr. Dan Herr for funding this project.

A journey of thousand miles starts with a single step, but the first step is probably the most difficult one. This step was less strenuous due by the pioneering work of Drs. Ziegler, Biersack and Littmark (ZBL) of the SRIM group. I would like to express my gratitude to Dr. Scott Wight

of NIST for kindly sharing his conference presentation and Dr. Dale Newbury of NIST for his encouragement. I would also like to thank Drs. John Villurubia and Andras Vladar for their discussions and interest about this project. Special thanks to Drs. Nicholas Economou, John Notte, Larry Scipioni, Bill Thompson, Clarke Fenner, Mohan Ananth, David Voci of Carl Zeiss SMT for their recognition of my work and their consistent support throughout this project.

I would like to thank Dr. Lucille Giannuzzi of FEI for her encouragement and ideas to take the simulation to the next level.

I would like to thank my parents Mr. H.S. Ramachandra and Mrs. Janakey Ramachandra for all their sacrifices and moral support over the years, to my wife Mrs. Anjana Prasad for bringing the stability in my life. There are many more people that I want to thank, the kind ways in which they have helped me are running through my mind while I am writing this paragraph, I am not including their names only due to paucity of space. Finally I want to express my gratitude to God for his support and strength.

Abstract

The scanning electron microscope (SEM) is a popular instrument used for imaging because of its high resolution images it can generate. However the new scanning helium ion scanning microscope (SHIM) can produce higher resolution and better contrast images than the conventional SEM. In both the microscopes secondary electron (SE) signal is the most widely used imaging mode because of their high yield efficiency and their high spatial resolution. In order to be able to properly evaluate the relative strengths and weaknesses of electron induced SE (eSE) and ion induced SE (iSE) imaging a detailed model able to quantify them is required. Unlike in the case of eSE where there have been considerable amount of experimental and theoretical studies, there have been very few for iSE. A detailed Monte Carlo simulation of helium ion beam interaction with solids , IONiSE (Ion Induced SE) was developed. IONiSE is designed to provide data on questions such as the variation of the incident beam range, and the yield δ_{iSE} of iSE, as a function of the He+ ion energy and choice of sample, as well as the behavior of iSE yield with surface topography, spatial resolution of the iSE.

This simulation employs a combination of 'semi empirical' model for secondary electron production, and the SRIM routines that describe ion stopping power, scattering, and transport. This is a parametric model and hence requires that the material dependent parameters be determined by fitting to experimental yield data. This model shows predictable behavior for wide range of elements and it can be applied with equal ease to even complex compounds. The model can also be used for other applications like energy deposition profiles in ion beam lithography, critical dimension metrology using helium ions, ion beam deposition and etching studies and ion beam induced current in semiconductor devices.

Table of Contents

1. Introduction to Ion Microscopy 1
1.1 Why Ion Microscopy? 1
1.2 Stopping Powers 1
1.3 Beam Penetration 4
1.4 Ion beam Lithography 13
1.5 Material Analysis 14
2. The Scanning Helium Ion Microscope 17
2.1 The Instrumentation 17
2.2 Best Conditions for imaging in a SHIM 19
2.21 Low accelerating voltage mode 23
2.22 High Accelerating Voltage Mode 26
2.3 Sample Charging 29
2.4 Detector Sensitivity to Signal 34
2.5 Radiation Damage 36
3. The Physics of Ion Scattering 40
3.1 Introduction 40
3.2 Interatomic potential 40
3.3 Classical Scattering Theory 46
3.4 The Classical Scattering Integral 52
3.5 The Angular differential Scattering cross section 59
3.6 The Reduced Energy Parameter 65
3.7 The Reduced Energy Parameter 65
3.8 Nuclear Stopping Power 66
3.9 Electronic Stopping Power 68
4. Review of Ion Induced Secondary Electron 74
4.1 Introduction 74
4.2 Electron induced SE (eSE) 75
4.3 Ion induced SE (iSE) 77
4.4 Potential Electron Emission (PEE) 79
4.5 Threshold Velocities for PEE and KEE 85
4.6 KEE due to primary and backscattered ions 89
4.7 KEE due to recoil target atom 108
4.8 Some other interesting features iSE 112
4.81 Molecular ions 112
4.82 Isotope effect 113
4.83 Effect of temperature 113
4.84 Topographic contrast 116
4.85 Spatial Resolution 118
4.86 Ion Channeling 118
4.9 Conclusion 121
5. Results and Discussions 122

5.1 Introduction 122
5.2 Principle of IONiSE – Ion interaction and Trajectory plotting 124
5.3 Principle of IONiSE – iSE production 128
5.3 iSE yield curves 133
5.4 Applying IONiSE to imaging 164
5.41 Topograghic Yield 164
5.42 The SE2/SE1 Ratio 167
5.5 Radiation damage and iSE yield 169
5.5 Conclusion 170
6. Future Work 172
6.1 Extending the program for other ions:- 172
6.2 Back Scattered ion signal 172
6.2 Transmission of ions 174
6.3 Energy deposition profiles 174
6.4 Line profiles 177
References 179
Vita 188

List of Tables

Table 2.1 – Showing evaluation of a SEM, SHIM and FIB on different parameters.....21

Table 2.2 – Showing the Range in nm of electrons and helium ions.....25

Table 3.1 – Analytical expression of screening function to the Thomas Fermi equation 45

Table 3.2 – Showing Interatomic Screening Length 46

Table 5.1 – Fitted ε(eV) and λ_d(A) (Angstrom) parameters for helium ion beam irradiation of various target elements and the corresponding predicted iSE γ_{max} and Emax (energy) values.....161

Table 5.2 – Fitted ε(eV) and λ_d(A) (Angstrom) parameters for electron beam irradiation of various target elements and the corresponding predicted eSE δ_{max} and Emax (energy) values. R is the range at which maximum eSE occurs.....164

List of Figures

Figure 1.01 – Electron Stopping power as a function of energy. Courtesy of Suichu Luo PhD thesis at UT 3

Figure 1.02 – Ion Stopping power as a function of energy. Courtesy of SRIM 3

Figure 1.03 – Electron and Helium ion stopping powers plotted as a function of velocity.....5

Figure 1.04 – Electron range as a function of energy 6

Figure 1.05 – Relationship of Probe size to probe current at different energy of electron beam in SEM. Courtesy of Goldstein et.al [1] 6

Figure 1.06 – Electron and helium ion interaction for a 10 KeV beam in Al…….……...8

Figure 1.07 – Electron and helium ion interaction for a 50 KeV beam in Al…….8

Figure 1.08 – Helium ion depth distribution profile in Al …….……9

Figure 1.09 – Shows the He ion image of white blood cells. Courtesy of Zeiss [70]…….11

Figure 1.10 – Shows the He ion SIM image of a CNT, the size of fiber is about 20 nm and image shows excellent background information even at such a high resolution…12

Figure 1.11 – Left image shows a SE image of a solder bump and the right image shows RBI image of the same solder bump. Courtesy of Morgan et.al [39]……...16

Figure 2.01 – Showing the ionization of neutral helium atoms when they pass through the ionization disc. Courtesy of Morgan et al [39] ……..18

Figure 2.02 – Showing the emission pattern of ALIS ion source, the formation of the 'Trimer pattern'. Courtesy of Morgan et al [39] …….18

Figure 2.03 – Showing the Zeiss ORION^{TM} installed in NIST. Courtesy of Wight [69]……..20

Figure 2.04 – Showing the Stopping power of helium ions in Cr at low energies. Courtesy of

SRIM [3]…….25

Figure 2.05 – Showing the BSI yield versus energy of the beam. Data from IONiSE…….26

Figure 2.06 – Showing a milled surface image in the SHIM (Left picture) and SEM (Right picture). Courtesy of Wight [69]……...28

Figure 2.07 – Showing the Energy distribution of BSI versus energy of the beam. Data from IONiSE……30

Figure 2.08 – Shows the comparison of an He ion SE image (Left picture) and SEM SE image (Right picture) of Si. Courtesy of Joy [80]...…….....31

Figure 2.09 – Shows the comparison of an He ion SE image (Left picture) and SEM SE image (Right picture) of Au particles. Courtesy of NIST…….31

Figure 2.10 – Charging effect in electron and ion beams……..33

Figure 2.11 –Shows the effect of charging with increasing energy of the beam. Data from IoniSE…….33

Figure 2.12 – Shows the effect of charging on coated polymer spheres in a SHIM image (Left image) as compared to a SEM image (Right image). Courtesy of Wight[69]……....34

Figure 2.13 – Shows the magnified image on coated polymer spheres in a SHIM image (Right image) as compared to a SEM image Left image). Courtesy of Wight [69]…….……..34

Figure 2.14 – Shows dislocation loops on gold specimen irradiated by He^+ ions. Courtesy of Brown et.al [73]……...……39

Figure 2.15 – Shows formation of voids on gold specimen irradiated by He^+ ions. Courtesy of Brown et.al [73]……..……39

Figure 2.16 – Shows blistering of molybdenum after bombardment He^+ ions of different energies (a) 7 KeV (b) 20 KeV (c) 50 KeV (d) 80 KeV. Courtesy of Erents et.al [74]…….40

Figure 3.01 – An ion beam trajectory showing the successive deflections of the ion as it travels in the sample…….48

Figure 3.02 –Ion-atom collisions in Laboratory co-ordinates. Courtesy of Nastasi et.al[43]...48

Figure 3.03 – Ion-atom collision conversion from Center of Mass to Laboratory Co-ordinates. Courtesy of Nastasi et.al[43]…….50

Figure 3.04 – Showing the central force…….. …….53

Figure 3.05 – Showing the view of the trajectory with the impact parameter b and also the distance of closest approach r_{min} (a) for an attractive potential (b) for a repulsive potential. Courtesy of French[44]…….56

Figure 3.06 – Showing the scattering angles and impact parameter for (a) Laboratory co-ordinates (b) Center of Mass co-ordinates. Courtesy of Nastasi et.al[43]…..58

Figure 3.07 – Showing the scattering of a particle with an impact parameter b. Courtesy of Nastasi et.al[43]……62

Figure 3.08 – Showing the change in scattering of a particle with change in impact parameter b. Courtesy of Nastasi et.al[43]……..…..62

Figure 3.09 – Showing the solid angle $d\Omega$ subtended at the scattering angle θ_c by the Incremental angle $d\theta_c$. Courtesy of Nastasi et.al[43]……..64

Figure 3.10 – Showing the Stopping power of Boron on Silicon. Courtesy of SRIM [4]…..…..70

Figure 3.11 – Showing the Variables schematically……..72

Figure 4.01 – Showing Energy spectra by 1 KeV electrons on Gold. Courtesy of

Satya Prasad [50]……..……..78

Figure 4.02 – Showing Number of SE N(E) from ten elements recorded at 1 KeV. Courtesy of Satya Prasad [50]……78

Figure 4.03 – Showing universal yield curve of eSE's . Courtesy of Yinghong Lin [28]…..…79

Figure 4.04 – Showing the Ion induced Secondary Electron (iSE) Mechanisms……..…….80

Figure 4.05 – Showing the PEE yield fit closely to the yield equation proposed by Hagstrum. The values (▲, △) is from Arifov for Ne^+ and Ar^+ ions respectively and (●, ▽, ▼, ◇, ■) is from Hagstrum for He^+ , Ne^+, Kr^+ and Xe^+ ions respectively. The Plot is courtesy of Baragiola et al [61]……..…83

Figure 4.06 – Showing the PEE versus Energy E for Ar^{++}, He^+ , N^+ , O^+ and H^+ On monocrystalline copper Cu(110). Courtesy of Petrov [48]……..84

Figure 4.07 – Showing the Total SE yield (Figure (a)) and the true PEE Yield (Figure (a)) as a function of potential energy of the ion. Courtesy of Wang et al [62]…….85

Figure 4.08 – Showing the iSE spectra for different ions incident on copper at low energies. Courtesy of Ruano et al [59]…….……..86

Figure 4.09 – Showing the SE yield at very low energies for KBR and Mo. Courtesy of Petrov[48]……..……..88

Figure 4.10 – Showing the Probability of electron emission statistics for He^+ on Au. Courtesy of Toglhofer[49]……..……90

Figure 4.11 – Showing the Relative contribution of KEE (K_n) and PEE (P_1) for He^+ on Au. Courtesy of Toglhofer[49]……..92

Figure 4.12 – Showing the Relative contribution of KEE (K_n) and PEE (P_1) for Ar^+

on Au. Courtesy of Toglhofer[49]……..…..93

Figure 4.13 – Showing the Mechanism of Kinetic Electron Emission (KEE)……94

Figure 4.14 – Showing the iSE yields for proton impacts on targets with different atomic number. Courtesy of Hasselkamp et al [34]……..……100

Figure 4.15 – Showing the iSE yields for helium impacts on targets with different atomic number. Courtesy of Hasselkamp et al [34]……..100

Figure 4.16 – Showing the iSE yields for Argon impacts on targets with different atomic number. Courtesy of Hasselkamp et al [34]…….…….101

Figure 4.17 – Showing the proportionality of SE yields to electronic stopping power. Courtesy of Baragoila et al [57]……..……..103

Figure 4.18 – Showing the SE yields to various projectiles on Al. Courtesy of Alonso et al [47]……...……104

Figure 4.19 – SE yields due to ions, electrons and recoils for various projectiles on different targets. Courtesy of Ohya [55]……..106

Figure 4.20 – Total SE yields Vs impact velocity for impact of singly, doubly and trebly charged ions on clean polycrystalline gold. Courtesy of Winter [58]……..……108

Figure 4.21 – Energy distribution of SE emission spectra for different ions on copper. Courtesy of Ruano [59]…….…….109

Figure 4.22 – showing images of metals under bombardment of different projectiles. (a) SE image of 10 KeV electron bombardment (b) SE image of 30 KeV Ga^+ ion (c) Secondary Ion image of 30 KeV Ga^+ ion (d) SE image of 3 KeV Ar^+ ion Courtesy of Sakai [16]…….…….111

Figure 4.23 – Showing the relative contributions of Nuclear and Electronic Stopping powers

of Helium and Gallium ions in Cu. Courtesy of SRIM [3] ……...112

Figure 4.24 – Showing the relative contributions of the recoil target atoms on the total electron yield of Kr^+ and Xe^+, the dashed line showing the recoil atom contribution. Courtesy of Alonso et al [47]……113

Figure 4.25 – Showing the yields for H^+ (open symbols) and D^+ (closed symbols) : $(\nabla, \circ, \triangle, \square)$ for Li,Al,Cu and Ag respectively. Courtesy of Baragiola et al [47]……..……..116

Figure 4.26 – Showing the SE yields as a function of temperature for H2+ and Hg+ ions incident on monocrystalline W and Cu. Courtesy of Petrov [48]…….….117

Figure 4.27 – Showing the Normalized KEE yields for He^+ and Xe^+ on Cu versus angle of incidence. Courtesy of Ferron et al [33] …….…….119

Figure 4.28 – Showing the Spatial distribution of SE's under electron,He^+ ,Ga^+ ion bombardment on C,Si,Au. Coutesy Inai et al [22]……121

Figure 4.29 – Showing the iSE channeling contrast in monocrystalline Copper. Courtesy of Petrov [48]……..……..123

Figure 5.01 – Showing the inelastic and elastic mean free paths as a function of energy of the electron. Courtesy of Joy [6]…….……131

Figure 5.02 – Showing the iSE yield parameters and data fit for Lithium…….136

Figure 5.03 – Showing the iSE yield parameters and data fit for Beryllium……...137

Figure 5.04 – Showing the iSE yield parameters and data fit for Carbon……...138

Figure 5.05 – Showing the iSE yield parameters and data fit for Magnesium……....139

Figure 5.06 – Showing the iSE yield parameters and data fit for Aluminum……..140

Figure 5.07 – Showing the iSE yield parameters and data fit for Titanium……141

Figure 5.08 – Showing the iSE yield parameters and data fit for Chromium……..142

Figure 5.09 – Showing the iSE yield parameters and data fit for Manganese……..……..143

Figure 5.10 – Showing the iSE yield parameters and data fit for Cobalt……144

Figure 5.11 –Showing the iSE yield parameters and data fit for Nickel……....145

Figure 5.12 – Showing the iSE yield parameters and data fit for Copper…….…..146

Figure 5.13 – Showing the iSE yield parameters and data fit for Zinc……147

Figure 5.14 – Showing the iSE yield parameters and data fit for Germanium……....148

Figure 5.15 – Showing the iSE yield parameters and data fit for Zirconium…….……149

Figure 5.16 – Showing the iSE yield parameters and data fit for Niobium…….150

Figure 5.17 – Showing the iSE yield parameters and data fit for Silver…….151

Figure 5.18 – Showing the iSE yield parameters and data fit for Cadmium……..….152

Figure 5.19 – Showing the iSE yield parameters and data fit for Indium……...153

Figure 5.20 – Showing the iSE yield parameters and data fit for Tin…….154

Figure 5.21 – Showing the iSE yield parameters and data fit for Antimony……...155

Figure 5.22 – Showing the iSE yield parameters and data fit for Tantalum……....156

Figure 5.23 – Showing the iSE yield parameters and data fit for Tungsten……157

Figure 5.24 – Showing the iSE yield parameters and data fit for Platinum……...….158

Figure 5.25 – Showing the iSE yield parameters and data fit for Gold……...……159

Figure 5.26 – Showing the Universal Electron yield curve under electron, proton and Helium ion bombardment. ……....160

Figure 5.27 – Showing the change in the local potential energy due to ion implantation, to elaborate the Matthiessen's rule. Courtesy of Kasap [67]…….165

Figure 5.28 – Showing the Topographic yield of He^{+} on Li. Data from IONiSE……...…168

Figure 5.29 – Showing the Topographic yield of He^+ on Cu. Data from IONiSE……..168

Figure 5.30 – Showing the Topographic yield of He^+ on Cu. Data from IONiSE……..169

Figure 5.31 – Showing the SE1 and SE2 creation mechanism. Courtesy of Goldstein et al[1]……...…170

Figure 5.32 – Showing the SE2/SE1 ratio in Helium ion Microscope. Data from IONiSE……...….171

Figure 5.33 – Comparing the iSE and Vacancy yields for He^+ ions. Data from IONiSE and SRIM [3]…….……173

Figure 6.01 – Comparing the interaction volume of 20 KeV electrons, protons, helium and gallium ions on copper. Pictures from Banyan and IONiSE…….. ….176

Figure 6.02 – The 50% transmission range for helium ions. Data from IONiSE. ……..……178

Figure 6.03 – Comparing the energy deposition profile for helium ion (left picture) and electrons. Pictures from Banyan and IONiSE. …….179

Figure 6.04 – showing trajectories for line edge measurements……...181

List of Abbreviations

BSE	Backscattered Electrons
CD SEM	Critical Dimension Scanning Electron Microscope
CM	Center of mass
CSDA	Continuous Slowing Down Approximation
EBL	Electron Beam Lithography
eSE	Electron induced Secondary Electron
ESEM	Environmental Scanning Electron Microscope
FESEM	Field Emitter Scanning Electron Microscope
FIB	Focused Ion Beam
FIM	Field Ion Microscope
FSE	Fast Secondary Electrons
GFIS	Gas Field Ion Source
iSE	Ion induced Secondary Electron
KEE	Kinetic Electron Emission
LMIS	Liquid Metal Ion Source
PEE	Potential Electron Emission
RBI	Rutherford Backscattered Ion
SE	Secondary Electrons
SEM	Scanning Electron Microscope
SHIM	Scanning Helium Ion Microscope
SRIM	Stopping and Range of Ions in Matter by Ziegler et al[3]

TEM	Transmission Electron Microscope
UHV	Ultra High Vacuum

List of Symbols

λ	Wavelength of the source, and also mean free path of electrons and ions
R	Range of electrons and ions
α	Convergence angle of the beam
χ	Coefficient of sample charging
γ	iSE yield
γ_{PEE}	Potential Electron Emission by ions
γ_{KEE}	Kinetic Electron Emission by ions
η	Backscatter electron or ion yield
$\chi(\frac{r}{a})$	Atomic Screening Function
a_o	Bohr radius of hydrogen atom
θ	Scattering angle of the projectile
ϕ	Scattering angle of the recoiling target atom, also as work function
δ	eSE yield, and also depth of the filled band
l	Angular momentum
σ	Cross Section of Scattering
ε	Reduced energy parameter, and also average energy to create an SE
$S(\varepsilon)$	Stopping cross section in terms of Reduced energy parameter
E_F	Fermi energy
λ_d	Diffusion length of SE
τ	Effective scattering time of electrons

1. Introduction to Ion Microscopy

1.1 Why Ion Microscopy?

The resolution of any microscope is of the order of the wavelength of the illumination used. The wavelength of visible light is 300-600 nm , that of electrons for the energies of about 30 KeV at which SEM is operated is about 0.1 A, while the wavelength of ions for the same energies is lesser than 0.01 A. The minimum spot size in a scanning beam instrument varies as $\lambda^{3/4}$, hence using an ion beam will give us potentially a smaller spot size and theoretically a much better resolution. Also a helium ion being much heavier than an electron interacts more strongly with matter and so provides a higher signal for imaging. The purpose of this dissertation is to analyze if ion microscopy (especially helium ion microscopy) does indeed provide better resolution and image contrast than scanning electron microscopy (SEM) which has been a very popular instrument for the last 50 years.

1.2 Stopping Powers

As soon as charged particle beams (either electron or ions) enter a target they begin to interact with the target atoms either elastically or inelastically. Due to these collisions the beam is continuously deflected from its initial direction of motion and it progressively loses energy. The elastic collisions determine the direction of the beam trajectory in the target while the energy lost is determined by the inelastic collisions. For all practical purposes these two events can be considered independent of each other. The rate at which energy is lost by the beam or the

"Stopping Power" in a particular specimen is the most important parameter because it is this which determines the Secondary Electron (SE) yields, as well as Backscatter yields, damage to specimen and the resolution of a lithographic process.

The stopping power for electrons is given by the Joy-Luo [1] modified Bethe expression, which is

$$\frac{dE}{dS} = -78500 * \frac{Z}{AE} * \log_e\left(\frac{1.166(E+0.85J)}{J}\right)\left(\frac{KeV}{cm}\right) \quad \ldots\ldots\ldots\ldots\ldots\ldots\ldots\ldots (1.201)$$

As can be seen from Figure 1.01 the maximum stopping power for electrons in Chromium has a magnitude of about 6 eV/A and it occurs at about 0.1 KeV. The stopping power in case of ions is given by the SRIM [3]. This shows that the Helium ion stopping power maximum occurs at around 500 KeV and has a magnitude of about 70 eV/A as seen in Figure 1.02, which is 12 times that of electrons. A higher stopping power directly correlates to higher SE generation and increased signal. What is even more interesting is that in the operating range of the Zeiss ORION Helium ion SHIM (30 – 60 KeV) the stopping power of the ion increases with increasing energy. The incident ion will thus be more efficient in generating SE's (these are the high resolution SE1 component) than the backscattered ions (which give the undesirable SE2 contribution) i.e. the ratio of SE2 to SE1 is going to be lower than in case of electron bombardment. This indicates that contrast and resolution will both rise with energy in the scanning helium ion microscope (SHIM), whereas in the SEM the contrast falls as the resolution improves with energy.

Electron and ion stopping powers are different in their behavior because charged particle interactions are not energy dependent but velocity dependent as suggested by Thomson[5]. Helium is 7297 times the mass of an electron and so at the same energies travels a factor of 0.0123 times slower than an electron.

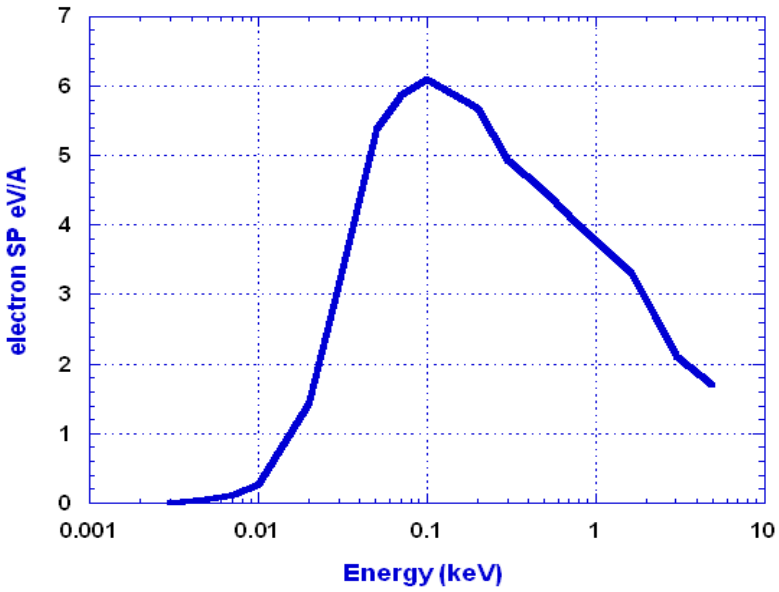

Figure 1.01 Electron Stopping power as a function of energy

(Courtesy of Suichu Luo PhD thesis at UT)

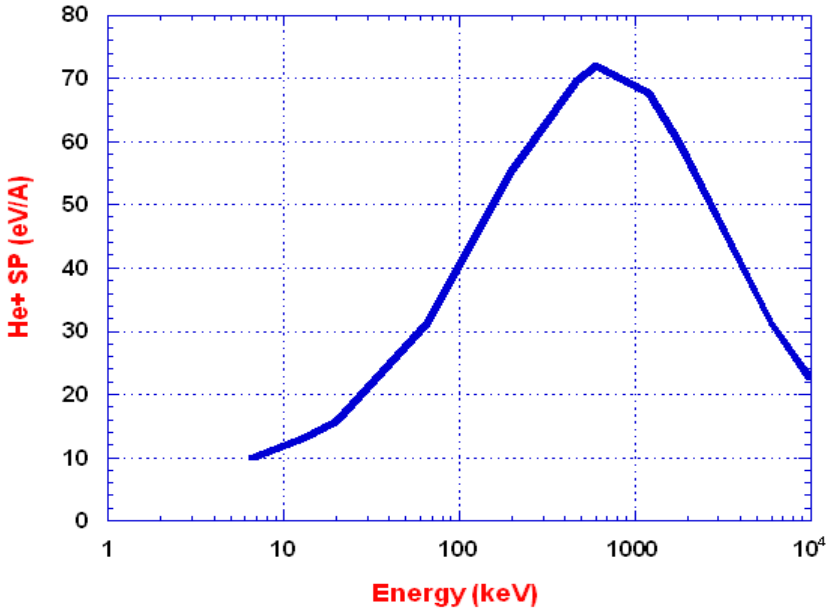

Figure 1.02 Ion Stopping power as a function of energy

(Courtesy of www.SRIM.org)

As seen from Figure 1.03 when the ion and electrons stopping powers are plotted as a function of their velocity rather than their energy then the stopping powers profiles closely resemble each other. However the velocity regimes in which they operate are two extremes of the graph, the SHIM on the left hand side, the electron beam on the right side. Thus a 50 KeV SHIM is equivalent to operating SEM at 10eV, and an SHIM image is going to be much richer in surface detail.

1.3 Beam Penetration

The interaction volume in the sample is caused by beam penetration as the electrons undergoes successive elastic scattering. This volume directly correlates to resolution. A smaller interaction volume means that the signals are generated from a smaller region, hence will result in higher resolution image. For the electrons the Range is given by the Kanaya-Okayama expression

$$R_{electron} = 76.\frac{E^{1.67}}{\rho} \quad (nm) \qquad \text{.....(1.202)}$$

As can be seen from Figure 1.04, as the energy of the beam is increased the beam penetration (and interaction volume) also rapidly rises. Although imaging with a low energy beam may be desirable for high resolution imaging, at low beam energies the probe size in a SEM increases significantly for a fixed probe current as shown in Figure 1.05 and hence degrading the image resolution. The optimum between these factors sets the energy in FESEM at energies between 10 – 30 KeV for high resolution and high contrast imaging. The ion interaction volume is very

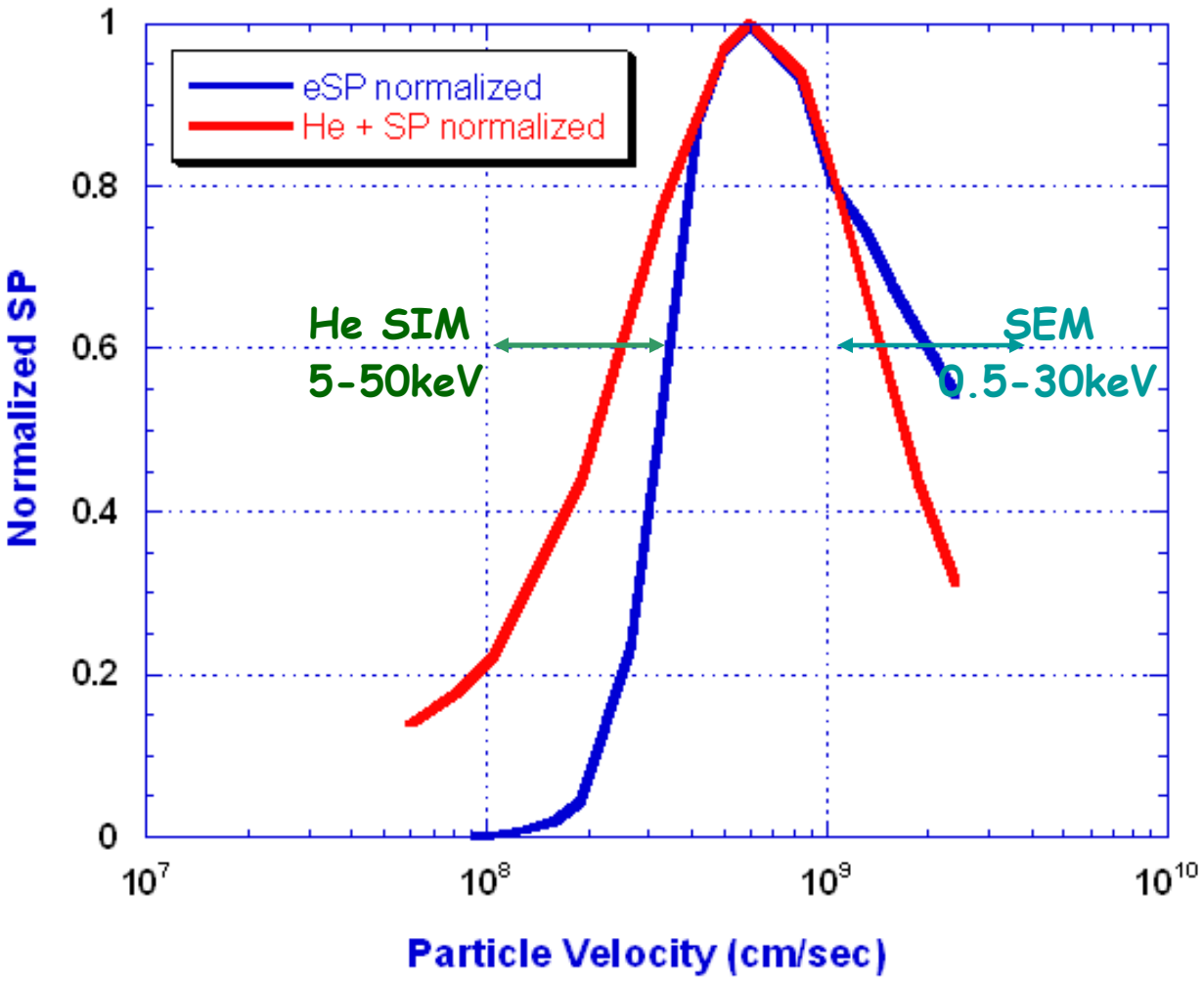

Figure 1.03 Electron and Helium ion stopping powers plotted as a function of velocity.

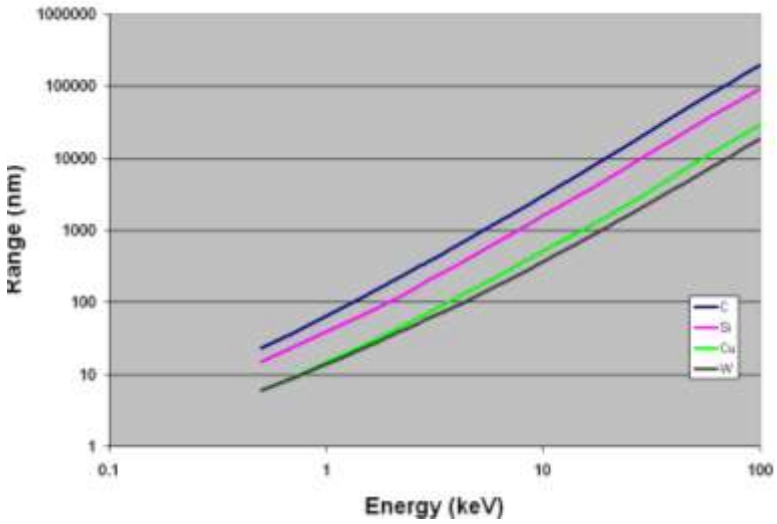

Figure 1.04 Electron range as a function of energy

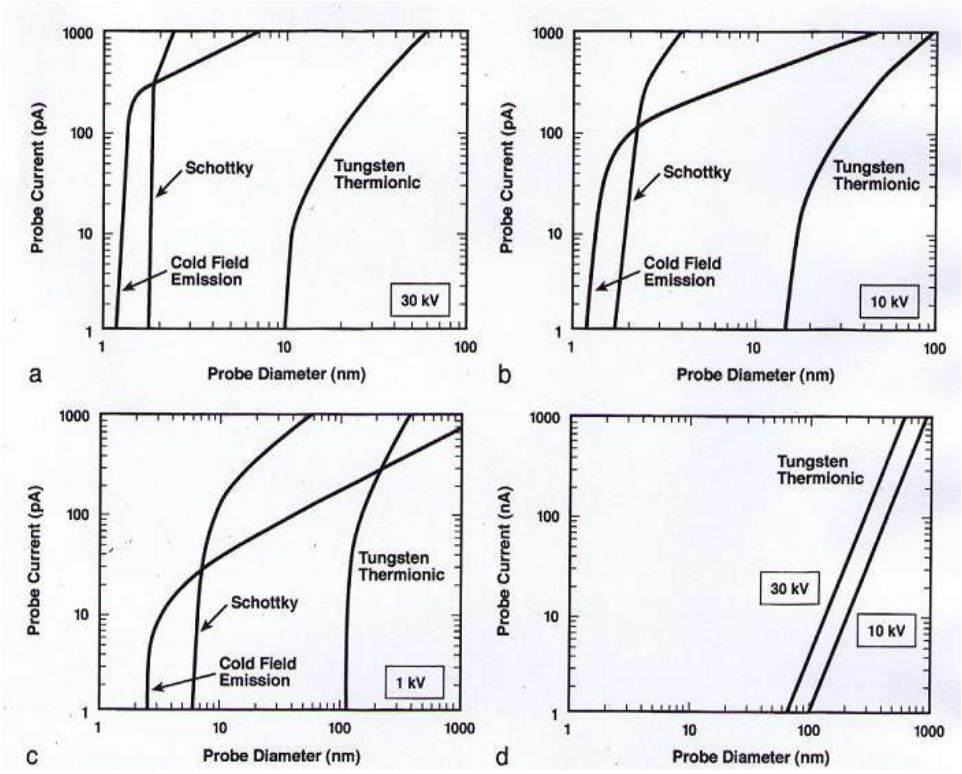

Figure 1.05 Relationship of Probe size to probe current at different energy of electron beam in a SEM. (Courtesy of Goldstein et.al [1])

small compared to that of electron interaction volume. As can be seen from Figure 1.06 and Figure 1.07 with increase in energy the ion interaction shrinks further with respect to the electron interaction volume. The shape of the electron interaction volume depends on the atomic number Z of the specimen, it forms a 'pear' or 'tear-drop' shape for low Z materials and almost a semi hemispherical shape of high Z material. In case of ions, for low Z materials the shape of interaction (not definitely the size) somewhat resembles that of the electron interaction volume but for high Z materials the interaction volume looks a bit erratic. This behavior of ions in high Z materials is due to ion straggle where the ion repeatedly bounces of the target of heavy nuclei. As can be seen from Figure 1.08, the ion depth distribution in any specimen follows a Gaussian profile. Due to the phenomena of straggle it is difficult to give a single Range equation for ions. It is convenient therefore to define a Peak Implant Range (i.e. mean of the Gaussian) which is the most probable place to find an ion, and the 90% Range (Mean + standard deviation of Gaussian) which is the distance within which 90 % of the ions end their trajectories.

The Peak implant $\mathbf{R_{PI}}$ is given by

$$R_{PI} = 80.\frac{E^{0.70}}{\rho}\ (nm).....(1.203)$$

The 90% Range $\mathbf{R_R}$ is given by

$$R_{90\%} = \frac{56.5 * E^{0.84-0.002E}}{\lambda^{0.61}} \qquad (E < 50KeV).....(1.204)$$

although at the highest energies better approximations are

$$R_{90\%} = \frac{56.5 * E^{0.77}}{\lambda^{0.61}} \qquad (\ forE > 50KeV, Z_2 > 20).....(1.205)$$

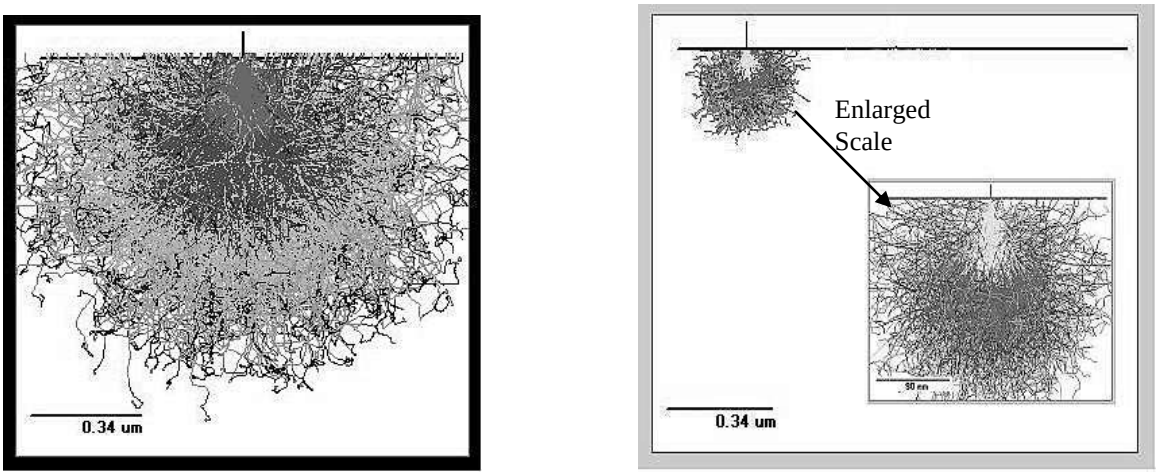

Figure 1.06 Electron and helium ion interaction for a 10 KeV beam in Al

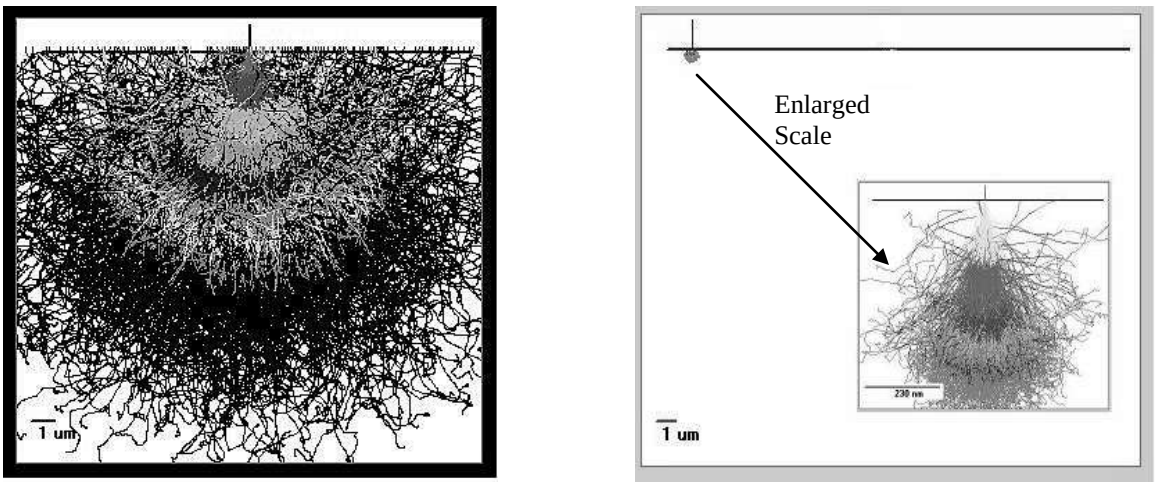

Figure 1.07 Electron and helium ion interaction for a 50 KeV beam in Al

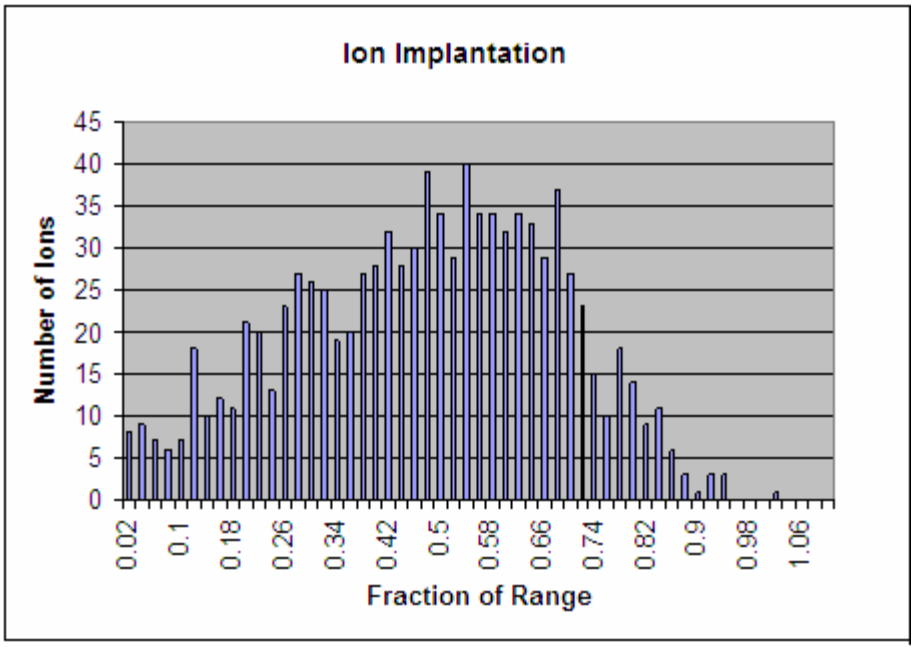

Figure 1.08 Helium ion depth distribution profile in Al

$$R_{90\%} = \frac{56.5 * E^{0.77}}{\lambda^{0.95}} \qquad (forE > 50KeV, Z_2 < 20).....(1.206)$$

The Ion straggle is given by:-

$$\Delta R_P = R_{PI}\ 0.5 + 0.084Z - 0.03E - 0.00168Z * E\ nm .....(1.207)$$

As can be seen from the above equations, the ion straggle increases with Z and reduces with E. These equations now give us a convenient way to find the density of ions implanted at a depth Z and for a particular dose Φi (ions/nm^2)

$$N(z) = \frac{\phi i}{\Delta R_P (2\pi)^{1/2}} \exp\left[-\frac{1}{2}\left(\frac{z - R_{PI}}{\Delta R_P} \right)^2 \right] \left(\frac{ions}{nm^3} \right).....(1.208)$$

The ratio of the Electron Range $\mathbf{R_{electron}}$ (equation 1.2) to the Peak Implant Ion Range $\mathbf{R_{PI}}$ (equation 1.3) is of the order of the energy of the beam used. This is to say that 50 KeV electron beam penetrates at least 50 times more than a 50 KeV ion beam. So an ion image is definitely richer in surface detail, which is clearly evident from Figure 1.09 and Figure 1.10. Since the interaction volume for electrons is in cubic microns and that of ions is in the cubic nanometers, even a single monolayer of gas of few nanometers thick adsorbed on the surface of the specimen is significantly alter the ion image.

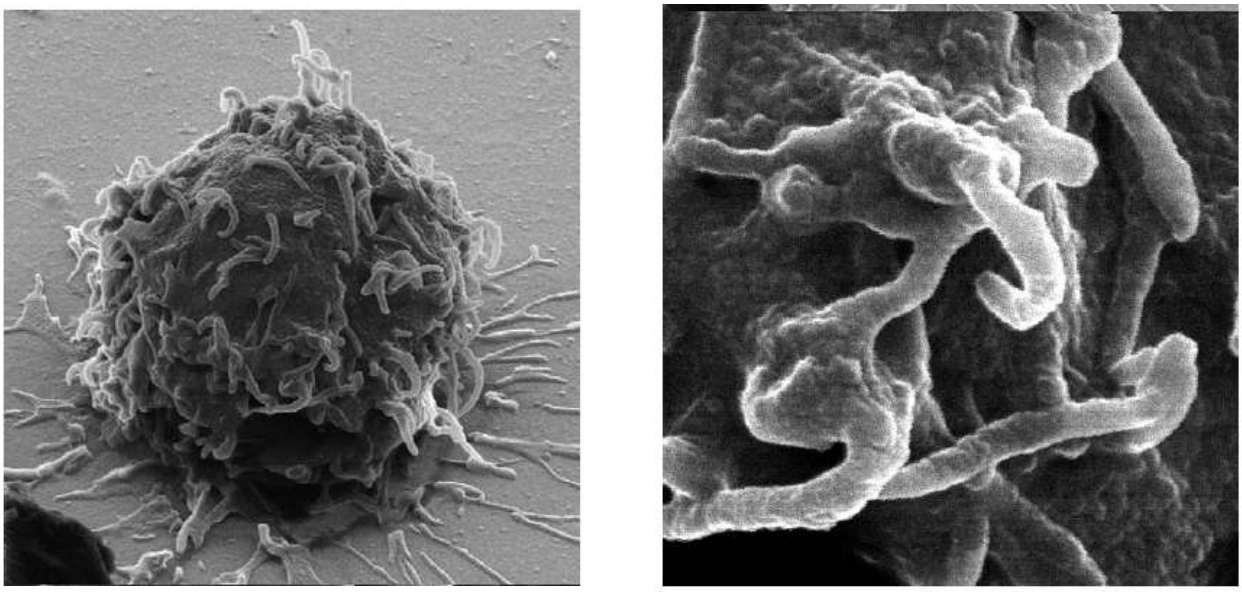

Figure 1.09 Shows the He ion image of white blood cells. Courtesy of Zeiss [70]

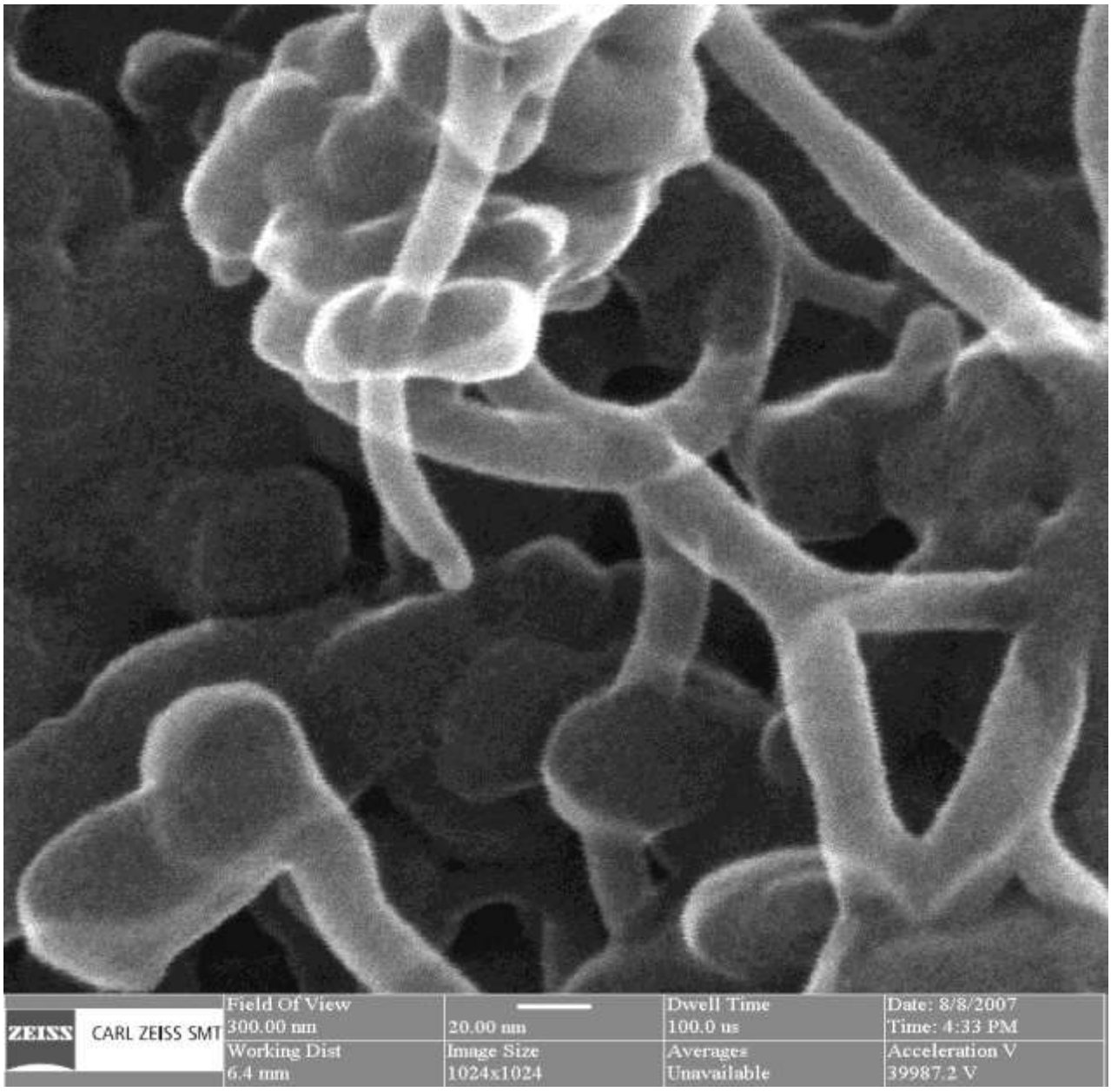

Figure 1.10 Shows the He ion SIM image of a CNT, the size of fiber is about 20 nm and image shows excellent background information even at such a high resolution.

1.4 Ion beam Lithography

The International Technology Roadmap for Semiconductors for 2018 specifies an 18 nm node size which may be the practical limit of e-beam lithography. Helium ion beam seems to hold the promise as a Lithography tool in the future. Theoretically with the use of ion beams much smaller pattern sizes can be written compared to the e-beam lithography due to lesser interaction volume of ions. Also in the case of ions the proximity effect will be lesser than electrons because backscattering is significantly less. Ion straggle is also not significant for soft materials like polymer resists.

However these two are different processes are different, if shooting an e-beam into resist layer is analogous to throwing a ping pong ball in a bucket of water, then an ion beam exposure can be compared to throwing a shot put ball in a bucket of water. So if we assume the solubility limit for the resist is going to be the same (which may not be a very accurate assumption) for both electron and ion dose then the same resist is going to be much more sensitive to ions than to electrons. This will reduce the ion dose significantly which is already much lesser than the electron dose due to the higher stopping power of ions (hence a higher rate of energy loss). It has been suggested in literature that dose for ions are about 2 orders of magnitude lesser in comparison to electron dose. When the required exposure dose becomes lesser than a particular threshold then the edges of pattern features may look like very wavy because the incident ion dose is Poisson distributed, if the dose for exposure is, say 4 ions the delivered dose will fall randomly between $4 \pm 2\sigma$ (i.e. 0 to 8). Hence an ion pattern may have higher line edge roughness for the particular feature width. Since in case of lithography radiation damage may not be too much of concern like in case of imaging, it may be interesting to see the effect of slightly heavier

ions for e.g. argon may have on pattern exposure and development. There has been some suggestion [40] of using heavy ions like Ga^+ and Au^+ for direct write milling. However this causes re-deposition of sputtered particles, also there seems little control on the shape of the trench cut by the ions. What seems to be a clear advantage is for some ion chemistries, resists can be written using dry exposure is possible i.e. after ion beam irradiation, the resist can be directly etched with out development. It has been seen that after the resist has been exposed to Ga^+ and etched with oxygen ions. The exposed regions show a 30 % lower etching rate [6]. This is due to the formation of stable oxide layer Ga_2O_3, which causes the physical hardening of the resist called "Graphitization". This in addition of being faster process because it eliminates the development process step of the conventional E-Beam Lithography process, also removes the undesirable effects of undercutting and swelling of resists that occurs during resist development. The opinions expressed here are from a bird's eye view and only experiments can prove decisively if SHIM can be a lithography tool in future, in which case is going open up a new branch of resist and developer chemistries.

1.5 Material Analysis

The SEM became very popular with material scientists because of its ability to perform chemical microanalysis from characteristic x-rays. This can be done with high spatial resolution of micrometer dimensions and excellent minimum detectable mass ($< 10^{-18}$). The SEM is used in the KeV range to excite the characteristic X-rays of most elements. For helium ion beam to excite characteristic x- rays it needs to be operated at MeV ranges. So SHIM can not possibly be used an effective X-ray microanalysis tool [38]. However the Rutherford Backscattered ion yield

shows a strong dependence on the atomic number of the sample. As seen in the Figure 1.11 SE image although it shows a little bit of Topographic contrast but does not tell anything about material difference. The RBI image of the solder bump shows superior material contrast clearly distinguishing the two materials. The dark regions are of tin and the light regions are of lead. Hence an RBI image can be clearly used for material identification with almost the resolution of few nanometers.

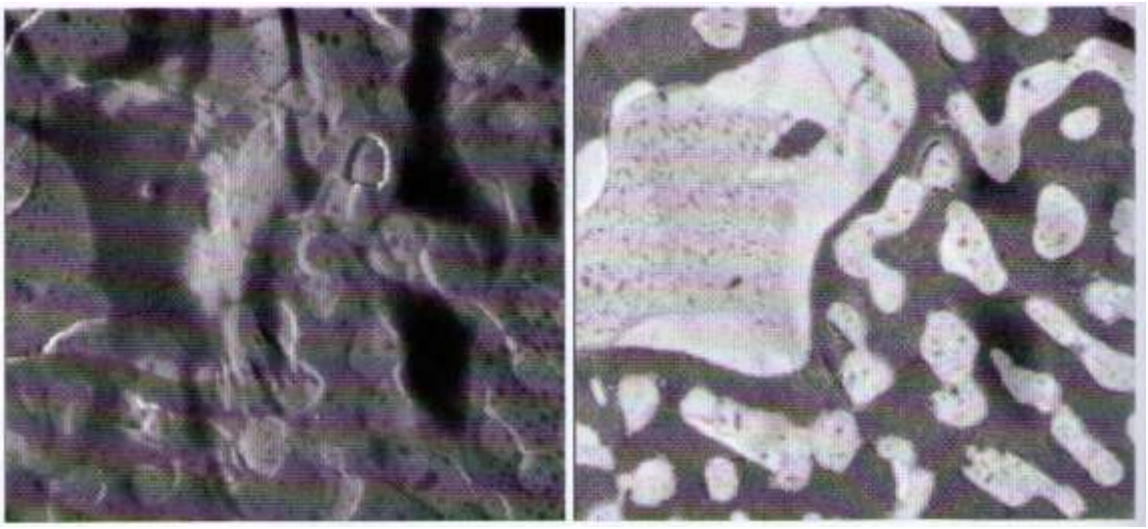

Figure 1.11 Left image shows a SE image of a solder bump and the right image shows RBI image of the same solder bump. Courtesy of Morgan et.al [39]

2. The Scanning Helium Ion Microscope

2.1 The Instrumentation

The Helium ion microscope ORION^{TM} is a patented technology from Carl Zeiss SMT. The ion source developed in this technology is a high brightness monochromatic source which is a development of the Field Ion Microscope (FIM) devised by E.Muller and further improved by Levi-Setti [13,68].

The FIM consists of a cryogenically cooled metal needle, generally tungsten, with a tip radius of the order of 100 nm. When a voltage of several hundred to several thousand volts is applied then the field at the tip becomes of the order of 4 – 6 V/A This is sufficiently high that protruding regions of the tip are field evaporated leaving behind a smooth round profile. Now when the neutral gas atoms are admitted to the vacuum chamber and the voltage reduced, the neutral atoms are attracted to the atomic site on the needle where the field is highest. This acts as a site for ionization of these neutral gas atoms when electrons quantum mechanically tunnel into the needle as shown in Figure 2.01. The ion is then repelled from the tip.

The ALIS helium ion source exploits the FIM technology and enhances it by employing proprietary technique to control the size and shape of the tip at the atomic level. In its most desirable stable configuration the tip has only 3 atoms i.e. a trimer as shown in Figure 2.02, and these three atoms act as sites for the ionization of impinging gas atoms. In operation only one atom of this trimer is selected to produce the ion beam for the Helium ion microscope. The beams from the other two atoms are blocked by an aperture positioned by the operator, .This configuration provides an ion source with a reduced brightness (amps/cm^2/sterad/volt) which is

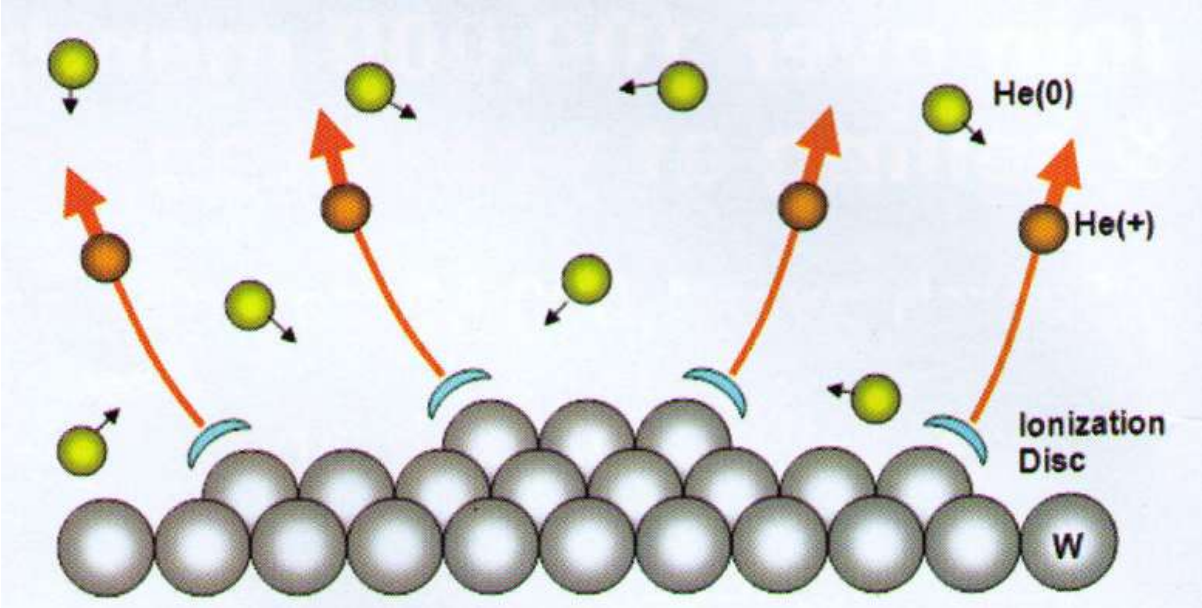

Figure 2.01 Showing the ionization of neutral helium atoms when they pass through the ionization disc. Courtesy of Morgan et al [39]

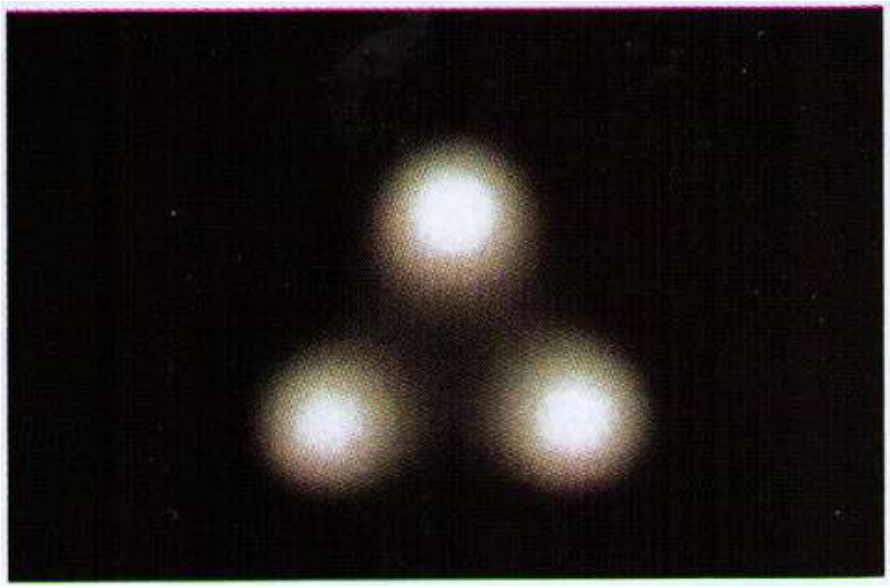

Figure 2.02 Showing the emission pattern of ALIS ion source, the formation of the 'Trimer pattern'. Courtesy of Morgan et al [39]

comparable to that of a cold field emission electron source. The typical emission current is in the range of 1 to 100 pico-amps at an energy of 30keV [2,39]. The first ORION^{TM} instrument, installed at NIST, is shown in Figure 2.03. The SHIM are closely related in design and operation to both the Focussed Ion Beam (FIB) tool and an SEM. All these three instruments are designed to work in the same energy range of about 5 -60 KeV, however their properties differ and a summary of the capabilities is provided in Table 2.1.

2.2 Best Conditions for imaging in a SHIM

Because helium ions are about 7000 times heavier than an electron, in the operating energy range of the microscopes (10-60 KeV) their interactions with solids will be very different to those of electrons. In addition the resolution of any microscope is limited by the minimum spot size it forms, which varies as $\lambda^{3/4}$,for electrons λ is about 0.1 A, but for a helium ion it is about 2 orders of magnitude less than this as already explained in chapter 1. The signals produced in these two instruments are also different. In a SEM, the signals most generally used are secondary electrons (SE), backscattered electrons (BSE) and X-rays. While in the SHIM SE and back scattered ions are the most popular. Both the SEM and SHIM do, however, produce other emissions – such as cathodoluminescence produced as the result of electron-hole pair generation within the sample. A SEM is commonly operated at different energies depending on the desired application. Thus, for electron beam lithography (EBL) the general trend is to use e-beams of energies 50 – 100 KeV, while for metallurgical samples and for BSE imaging energies in the range 10 – 30 KeV and typical, and for polymers and biological specimens energies below 5KeV are widely employed. In this context it is appropriate to consider the best energy range for

Figure 2.03 Showing the Zeiss ORION^{TM} installed in NIST. Courtesy of Wight [69]

Table 2.1 – Showing evaluation of a SEM, SHIM and FIB on different parameters.

	SEM	**SHIM**	**FIB**
Invented by	C.W.Oatley and D.McMullan (1952)	FIM by Muller et al (1955). The SHIM by Ward et al of ALIS group (2006)	Levi-Setti (1970's),Orloff et al (1975) and Krohn (1975)
Beam Wavelengths	Electrons of λ of ~ 0.1 A	Helium ions of λ of ~ 1 pm	Generally Gallium ions λ of ~ 0.3 pm
Source	Thermionic emitters(TE), Field Emitter (FE) among others	Gas Field Ion Source (GFIS)	Liquid Metal Ion Source (LMIS)
Brightness (A/cm2 Sr)	TE ~ 10^5 and FE ~ 10^8	~ $4*10^9$	~ $1*10^7$

Table 2.1 Continued

	SEM	**SHIM**	**FIB**
Energy Spread (eV)	1-3 eV	Less than 1 eV	5-10 eV
Aberration	Moderate. Although chromatic aberration is less, spherical and aperture diffraction compete with each other	Minimal. All the three aberration are small.	Moderate. Although is not diffraction limited, has a high chromatic aberration.
Radiation Damage	Negligible	Minimal	Significant
SE Yield	~0.3 to 1.2	~0.5 to 3	-
Microanalysis	X-ray, BSE image	BSI image	BSI image

the operation of the SHIM.

2.21 Low accelerating voltage mode

In a SEM, the most widely used mode of imaging is the SE rather than the BSE image. This is because BSE's can escape from any where within the entire beam interaction volume – which is of micrometer dimensions, while SE's have escape depth of only about 5-15 nm. Hence SE image gives a superior surface sensitive image while BSE carry information about the sub-surface bulk of the sample, increasingly the beam energy used in an SEM for the observation of soft materials is 5 KeV or less, and the energy of the e-beam used in specialist devices such as the Critical Dimension SEM (CD SEM) is commonly in the range 100eV to 1keV . These low energies are chosen to try and minimize sample damage by reducing the penetration depth to which the sample is exposed and also to try and control or minimize the charging of resists and oxides. . When the energy of the e-beam is low its interaction volume is smaller, i.e. the region from which signals are generated are smaller and so theoretically the resolution of images for is better in all modes of operation. The range of electrons is given by the Kanaya-Okayama [1] range which is:

$$R_{electron} = 76.\frac{0.0276AE^{1.67}}{Z^{0.89}\rho} \text{ nm} \quad \text{.....(2.201)}$$

The corresponding range in the case of helium ions is given by Ramachandra-Joy [66] as:

$$R_{He+} = \frac{56.5 * E^{1.84-0.002E}}{\rho^{0.61}} \text{ nm} \quad \text{.....(2.202)}$$

The range of electrons and helium ions in C, Al and Au at different energies are compared in Table 2.2. As it can be seen from this table, although at very low energies the electron and helium ion range is comparable, the electron range quickly rises to be of the order of micrometers while the He ion range remains limited to the nanometer scale .Because ions are heavier than electrons intuitively it would be imagined that they would cause more damage, so operation at low energies (i.e. around 1 KeV) would seem beneficial. However, using Helium ion at 1 KeV would in fact be the poor choice as far as radiation damage is concerned. As shown in Figure 2.04, the nuclear stopping power which is responsible for radiation damage is highest at 1-5 KeV for He^+ ions, and since the beam is always close to the sample surface the result would be a high level of damage. It thus seems that 5-10 KeV would be a better option in case of CD-SHIM measurements. Also as can be seen from Figure 2.05 which shows the coefficient of backscattered ions (BSI), there is considerable amount of BSI signal at these energies and the depth from which these BSI signals are generated are shallow as seen from Table 2.2. This can give the advantage of using both SE and BSI imaging specially to overcome the problem of bright edge in case of SE images. However at these energies there still would be the problem of charging, which will be discussed in the subsequent sections.

2.22 High Accelerating Voltage Mode

As already discussed for high resolution, the minimum probe size consistent with adequate beam current is desired. In case of an SEM, increasing the energy of beam not only decreases the SE signal but also decreases the probe size, although the decrease in signal is offset by the enhanced brightness of the electron source (which rises linearly with the beam energy). A trade off

Table 2.2 – Showing the Range in nm of electrons and helium ions

Energy in KeV	Silicon		Copper		Gold	
	electron	helium ion	electron	Helium ion	Electron	helium ion
1	3.00E+01	3.40E+01	8.00E+00	1.48E+01	3.00E+00	9.00E+00
5	4.40E+02	1.30E+02	1.13E+02	5.64E+01	5.20E+01	3.50E+01
10	1.39E+03	2.26E+02	3.57E+02	9.80E+01	1.65E+02	6.10E+01
20	4.40E+03	3.76E+02	1.13E+03	1.63E+02	5.23E+02	1.00E+02
30	8.62E+03	4.87E+02	2.21E+03	2.10E+02	1.03E+03	1.31E+02
40	1.39E+04	5.66E+02	3.57E+03	2.45E+02	1.66E+03	1.53E+02
50	2.01E+04	6.20E+02	5.17E+03	2.68E+02	2.40E+03	1.67E+02

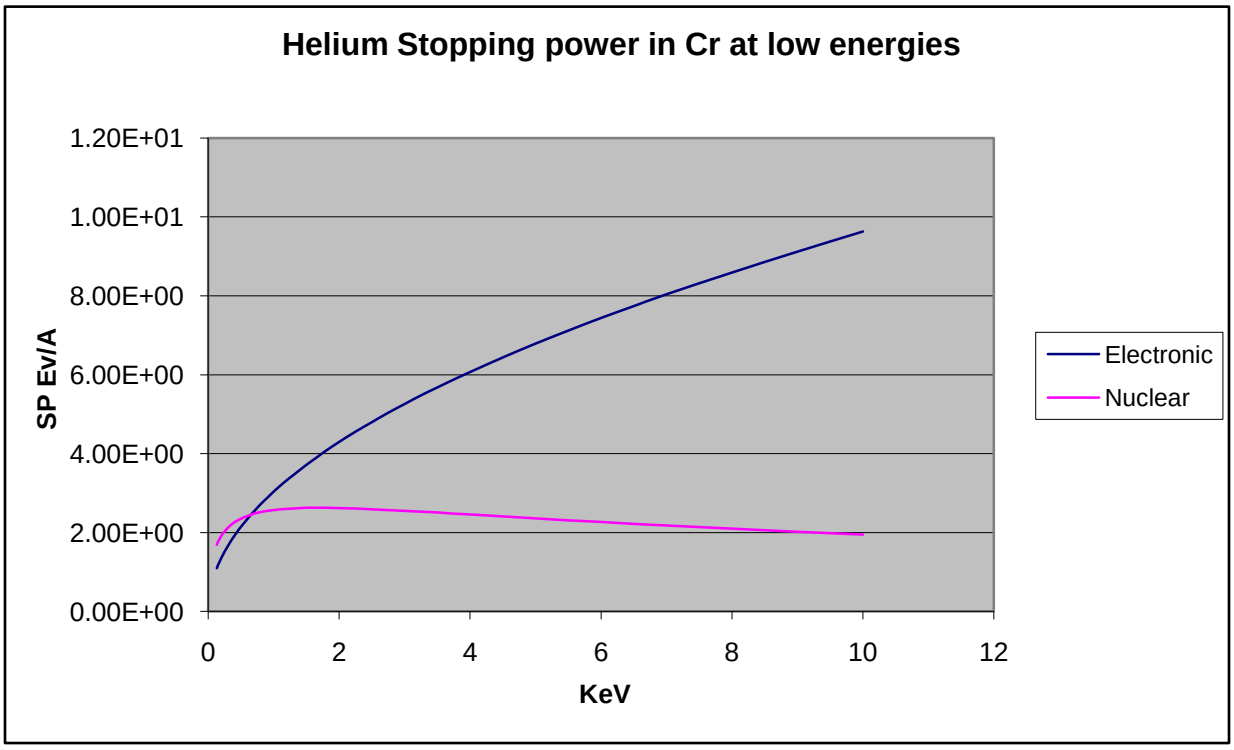

Figure 2.04 Showing the Stopping power of helium ions in Cr at low energies. Courtesy of SRIM [3]

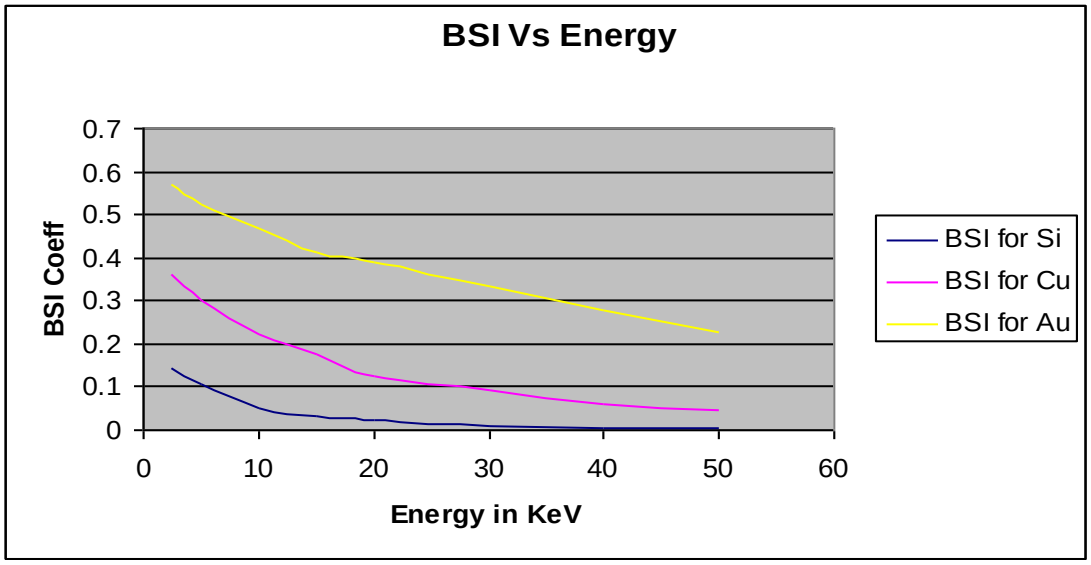

Figure 2.05 Showing the BSI yield versus energy of the beam. Data from IONiSE.

these two factors (and other considerations such as lens aberrations) suggests that the energy for maximum resolution imaging in a conventional SEM is between 10-30 KeV. In case of SHIM going higher in energy seems to be even more favorable because both the SE yield and the source brightness rise along with the increase in the energy of beam and the nuclear stopping power significantly reduces above 50 KeV. Also at higher energies the chromatic aberration, which is given by

$$d_c = C_c \alpha \left(\frac{\Delta E}{E_0} \right) \quad \text{.....(2.203)}$$

where ΔE is the energy spread of the beam, is significantly reduced. The spherical aberration is given by

$$d_S = C_S \alpha^3 \quad \text{.....(2.204)}$$

where α is the convergence angle of the outer ray through the lens, and C_c and C_s are coefficient of chromatic aberration and spherical aberration respectively both of which is proportional to focal length of the lens (or the working distance). By decreasing the focal length, the chromatic and spherical aberrations can be both lowered although this will also decrease the depth of field. In the case of the SHIM this is not an issue because α is so small (<1millirad) that the depth of field is excellent as can be seen from Figure 2.06. SEM image have a poorer depth of field because of the larger angle of beam convergence and so only the top surface in focus ,while in the SHIM image the top surface, the milled depth, and even the 2 micrometer Pt deposit is in focus. The depth of field in the helium microscope can be increased by reducing the convergence angle α, which can be achieved in a SHIM by decreasing the aperture size. Decreasing the aperture size will not cause aberration due to diffraction limiting, which is given by

$$d_d = \frac{0.61\lambda}{\alpha} \quad \text{…….(2.205)}$$

because the wavelength of helium ions is about 2 orders of magnitude lesser than that of electrons. From Figure 2.05 it can be seen that co-efficient of BSI decreases with increase in energy, unlike in a SEM where BSE co-efficient is relatively independent of energy. The SE's that are created can be classified as the high resolution SE1 due to the incident beam, low resolution SE2 created directly by the BSE/BSI and low resolution SE3 due to BSI striking the pole pieces, and inner chamber walls of the SEM. For high resolution imaging SE2 and SE3 component is undesirable.

Therefore in SE imaging in SHIM, an increase in energy not only decreases SE2/SE1 ratio but also decreases the BSI which in return decreases SE3 yield. Figure 2.07 shows the energy profiles of BSI in Si, Cu, and Au for a He ion at 20 KeV. It is evident that the BSI peaks more

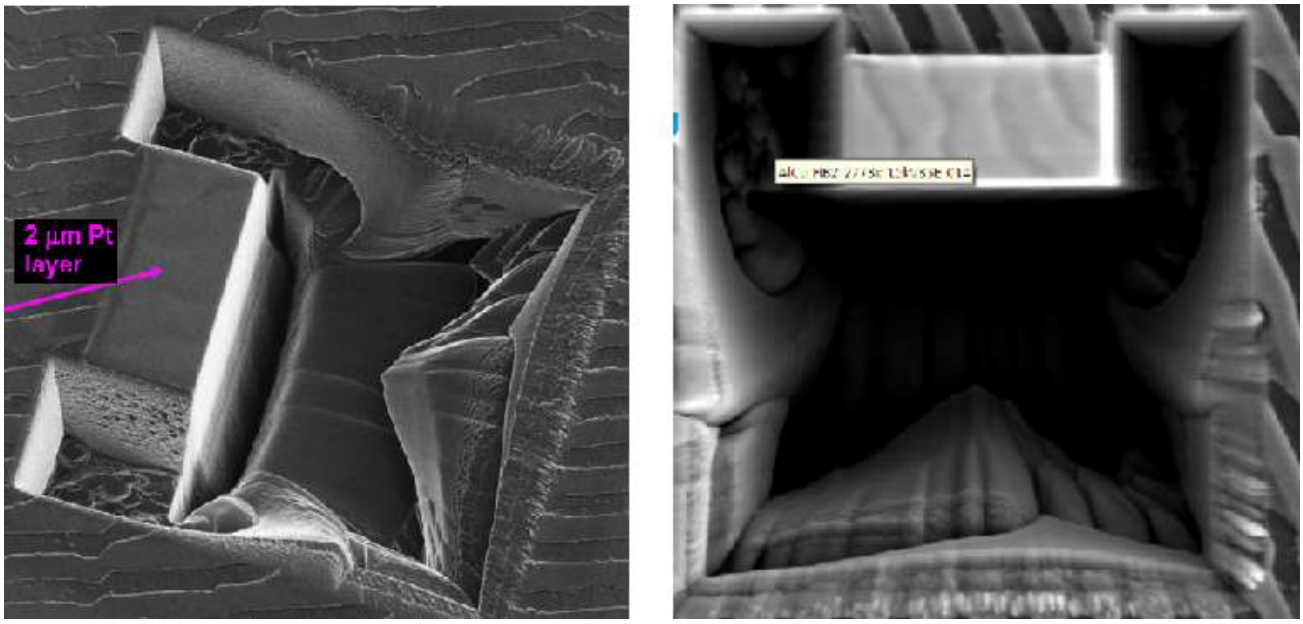

Figure 2.06 Showing a milled surface image in the SHIM (Left picture) and SEM (Right picture). Courtesy of Wight [69]

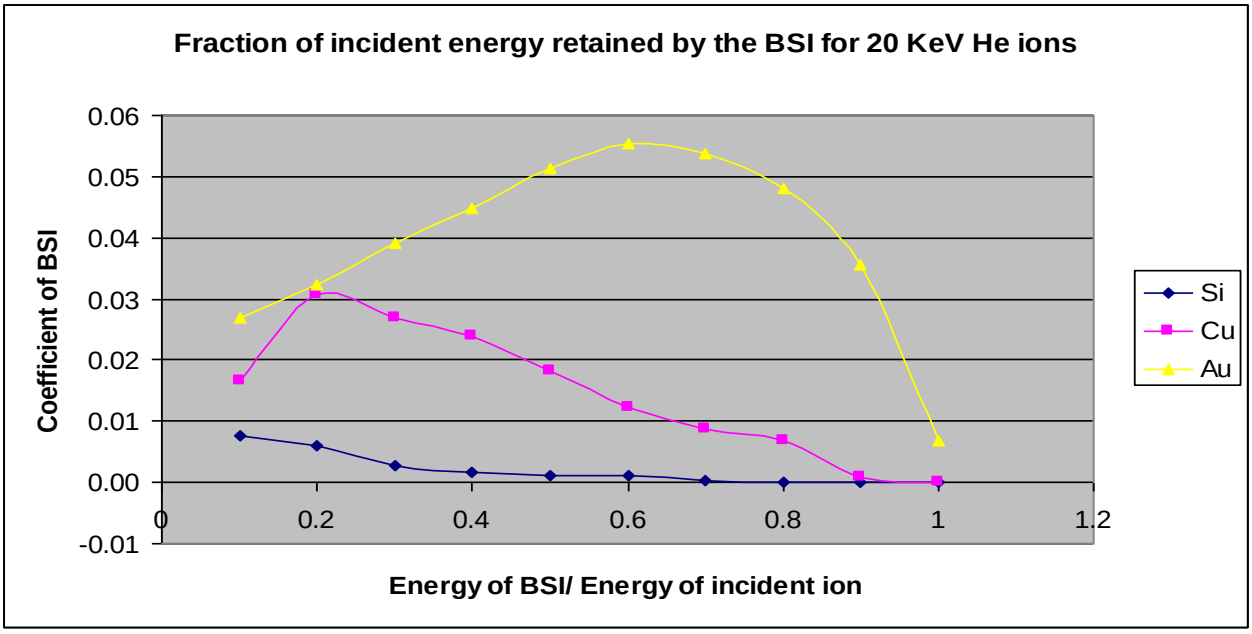

Figure 2.07 Showing the Energy distribution of BSI versus energy of the beam. Data from IONiSE.

towards the incident energy of the beam as the atomic number of the target increases. This could affect the resolution of high Z materials, since a high energy BSI will produce much more SE's than low energy BSI. Hence the resolution of high Z materials such as Au particles in a SHIM, when operated between 5-40 KeV, may not be significantly better than that of SEM. This is readily apparent when comparing Figures 2.08 and Figure 2.09, the SHIM image of Si definitely is better in contrast and resolution than the SEM image, while the SHIM image of Au particles is only comparable to the SEM image of the same. This is because of a high SE2 yield generated by ion struggle and a high SE3 yield due to high yield of high energy BSI in case of Au. Hence this is a poor choice of energy region for imaging. For all the above reasons it seems that the region to operate the SHIM is above 40-50 KeV, this would however increase the effect of sample charging.

2.3 Sample Charging

The specimen charging of insulators and biological samples has been a concern with the SEM, because it affects all forms of imaging. Charging can cause deflection and deceleration of the beam which can cause serious distortions to the image and in extreme cases the image may be lost. Since the interaction volume in the case of electrons is in micrometers, a coating of a thin layer of a few nanometers thick of conducting material like gold will reduce charging significantly. In applications like CD SEM where charging can cause detrimental effect, the SEM can be operated in a "no charge" mode, where for every electron that is entering the target another electron leaves. At a specific energy of the electron beam, the number of electrons entering the sample exactly equals the number of electrons (SE + BSE) leaving the sample. As

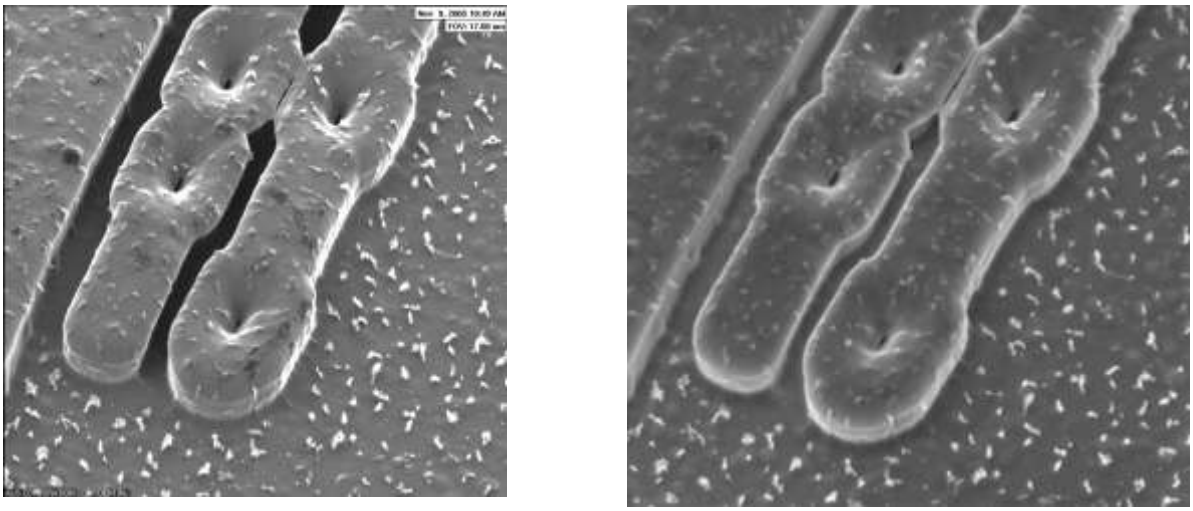

Figure 2.08 Shows the comparison of an He ion SE image (Left picture) and SEM SE image (Right picture) of Si. Courtesy of Joy [80]

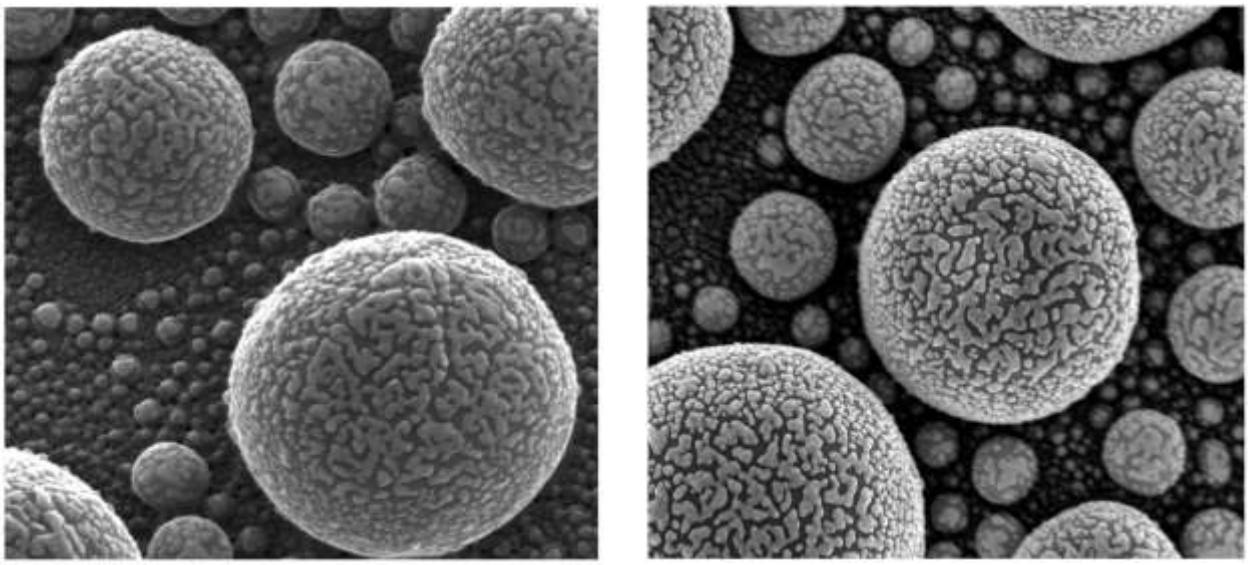

Figure 2.09 Shows the comparison of an He ion SE image (Left picture) and SEM SE image (Right picture) of Au particles. Courtesy of NIST

can be seen from Figure 1.13, the E_1 and E_2 crossovers for e-beams provide a no charging mode of imaging. Although E_1 and E_2 depend on the material, E_1 is generally below 1 KeV and E_2 is about 2 KeV. While below and above those crossovers in the SEM, the specimen becomes negative and positively charged respectively. However for ion beams the specimen will always be positively charged because of the incoming positive ion and the high yield of the outgoing SE. The sample charging increases with energy in the SHIM as shown in Figure 2.10 and Figure 2.11. Sample coating may not be a very good option because the interaction volume of ions itself is nanometer in size. Sample charging χ in case of ions can be found from the equation

$$\chi = 1 + \gamma - \eta \quad \text{.....(2.301)}$$

where γ is the iSE yield and η is the BSI yield, equation 2.301 can be expressed in terms of charging current I_{sc} as

$$I_{sc} = (1 + \gamma - \eta)\, I_0 \quad \text{.....(2.302)}$$

where I_o is the incident ion current.

The effect of charging in a SHIM is clearly evident in Figure 2.12 and Figure 2.13 of polymer coated spheres, in which the resolution is considerably degraded. As can be seen from Figure 2.11 charging can be as high as +2.5 at ion energies of about 60 KeV. One solution to compensate for this is to use a low energy electron flood gun, which is provided in the present version of ORION^{TM} . However this 'solution' has some limitations; firstly the probe size in the ORION is 0.75 nm to 2.5 nm [70], but for near zero energy electrons the probe size is anywhere between 8-200 nm (depending on the electron optical system used) which means that electrons are sprayed around a region that is not possibly charging. Secondly, there needs to be a precise synchronization between the scanning motion of the ion beam and electron flood gun on the

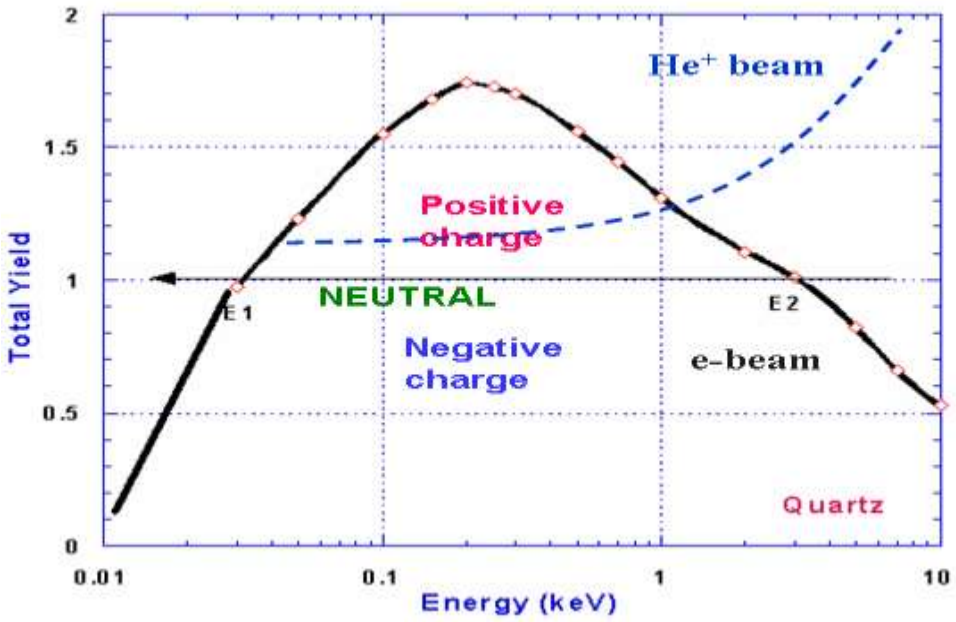

Figure 2.10 Charging effect in electron and ion beams

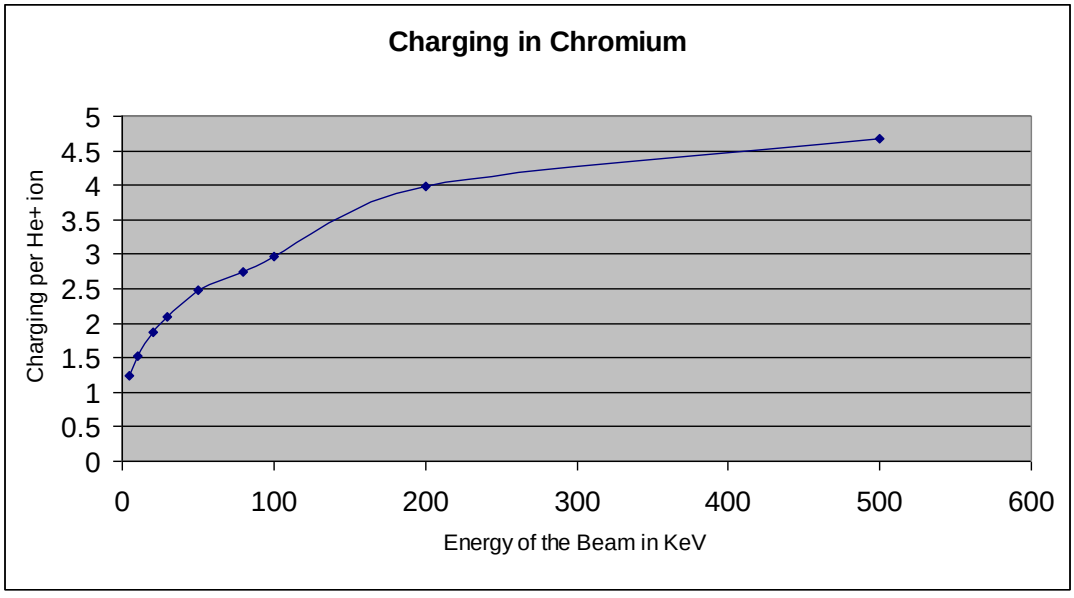

Figure 2.11 Shows the effect of charging with increasing energy of the beam.

Data from IoniSE

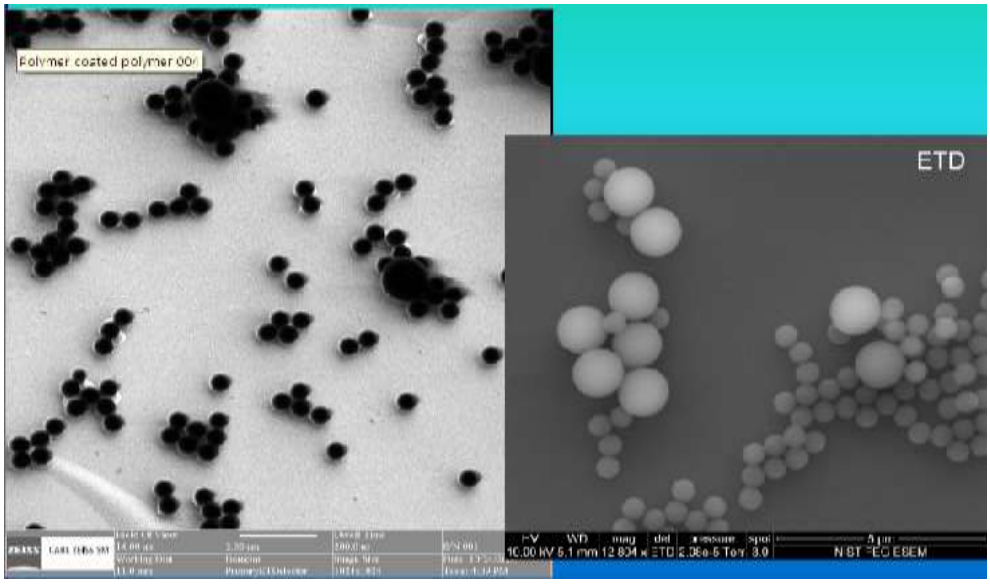

Figure 2.12 Shows the effect of charging on coated polymer spheres in a SHIM image (Left image) as compared to a SEM image (Right image). Courtesy of Wight [69]

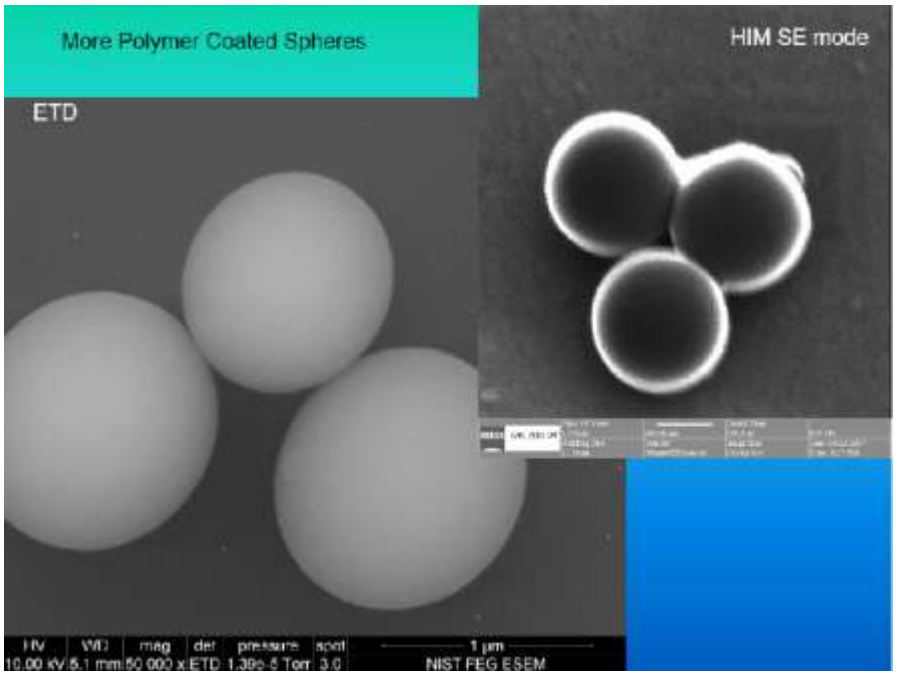

Figure 2.13 Shows the magnified image on coated polymer spheres in a SHIM image (Right image) as compared to a SEM image Left image). Courtesy of Wight [69]

calculated by the instrument. Finally the energy of the electrons in the electron flood gun should be extremely well controlled, for if instead of the zero energy, the electrons have small energy of 1-2 KeV, then they will cause even more electrons to be emitted from the sample (i.e. the region of positive charging in the SEM) which would aggravates the problem. One possible solution to this is the use of gases to overcome charging as is done in the Environmental SEM (ESEM). Since the SE signal generated in the case of SHIM are about 3-7 times that generated in an SEM, and because most of the iSE are low energy SE's which are very efficient in ionizing gas atoms, the gas pressure that may be used in SHIM may far lower than in SEM and also since the ion interaction volume is much lesser, this will lead to further decrease in the required pressure. The typical pressure used in ESEM is 150 Pa, so possibly pressures below << 1Pa would be good for a SHIM to overcome charging. However the incident helium ion travels at speeds of 100 times lesser than a electron at same energies and also the size of helium ion is much higher than the size of electron (which is negligible), this is only going to enhance the probability of the incident ion colliding with gas atoms causing the skirt around the probe diameter hence reducing the image contrast. Although using gases is definitely a viable option, more theory and experiments are required in this area.

2.4 Detector Sensitivity to Signal

The most popular detector in the SEM is the "Everhart-Thornley" detector, which is capable of capturing both SE and BSE signal. But the SE images of the "Everhart-Thornley" detector have a strong BSE component so present day SEM'S have a "Through the Lens" detector for high resolution pure SE images. A Solid State Diode detector is used for high voltage imaging and

Channel Plate Detector for low voltage microscopy. Each of these detectors have response that works best at a particular energy domain, but no single detector seems to have a good response in the entire energy range of SEM.

The detector selection in the case of the helium ion microscope is even more difficult because unlike in the SEM where the signals generated are always caused by negatively charged secondary and backscattered electrons, a helium ion microscope generates negatively charged SE, positively charged and neutral backscattered ions, sputtered atoms and even a small percentage of negative ions. The detector design should be such that it can segregate these signals to the signal of interest. The selection of detector will play a crucial role [38], since the BSI yields shows a linear increase with atomic number of the target when a Si diode BSE detector is used and it shows a shell filling effect when a micro channel plate detector is used. The current version of "ORION Helium ion microscope" uses a "Everhart-Thornley" detector for SE signals and a Micro channel plate detector for BSI signals. E-T detector may be a good choice for measuring SE signal when the incident beam energy is either below 5 KeV or above 60 KeV. In the energy range of 5-60 KeV, as previously discussed there is going to be a large SE3 component and quite a substantial BSI component added to the SE signal. It may also be seen that a 10 KeV BSI helium ion may mask a true SE signal much more than a 10 KeV BSE hitting the detector. An E-T SE detector may therefore not be the optimum choice for this instrument. Rather it seems that a "through the lens" detector, using a magnetic field instead of an electric field to collect the SE signal would be a preferable choice. The magnetic field will strongly deflect negatively charged electrons but it will have no effect on ions or neutral atoms. Also, this detector can be readily used in the "ESHIM" (Environmental SHIM) mode, in which may be difficult to operate using an E-T detector.

2.5 Radiation Damage

The most popular use of ion beams presently is for TEM sample preparation, Lithographic mask repair and micro machining. These process use ions because due to its small wavelength and due to its heavier mass (as compared to electrons) it causes site specific sputtering and removal of material from the sample. Consequently there is a concern of sample damage when helium ions are used as an imaging tool. Calculations using SRIM [3] show that for most materials in the energy range of 10-60 KeV there is no significant sputtering from helium ions for bulk samples. But evidence from several laboratories suggests that on many materials such as nano-spheres and polymers etc damage can be observed. A 10 pA ion beam at 30 KV has a probe size of the order of 1 nm, at this current there are about $6*10^7$ helium ions hitting the sample every second. In the area of highest beam density, one helium ion is implanted for every 1000 Si atoms for a beam dwell time of 1 micro second. What implication this is going to have in real time "fab" line on the semiconductor properties and life is yet to be seen. Hence quantitative data on material property and structural damage using a helium ion microscopy is required. However because the ions generate SE with high efficiency helium ion microscope can be operated with a beam current of few fA (as compared to SEM which is generally operates with a beam current in the nA region) , Specimen damage should therefore be significantly reduced.

There have been evidence in literature of gold specimens irradiated by 25 – 150 KeV He^+ ions showing helium filled voids to a dose of approximately $6*10^{17}$ ions/cm^2 at 100 ^oC [74]. Brown et.al [73] used TEM images to study the damage in gold irradiated with 35 keV He^+ ions to fluences of 10^{14} to 10^{16} ions/cm^2 at room temperatures. From their TEM micrographs it can be seen that damage is visible in the form of dislocation loops, whose average diameter did not

increase with ion dose over three orders of magnitude. An example of their micrograph is shown in Figure 2.14. When irradiated samples were annealed to about 500 ºC the dislocation loops joined to form dislocation tangles and voids started to appear in between these tangles, most of these voids being larger than 200 A. When the sample was further annealed for many hours, significant increases in the diameters of the voids were observed shown in Figure 2.15, from which they concluded that the voids were gas filled, as voids which did not contain gases would have shrunk on annealing. Erents et.al [74] studied the formation of blisters on molybdenum targets irradiated with 7 – 80 KeV helium ion both at near ambient and high temperatures. They observed that blisters occurred after a critical dose of ~ $5*10^{17}$ ions/cm^2,whose average size increased with energy but not with ion dose as shown in Figure 2.16.In their experiments they continuously monitored the release of gas from their instrument, they observed that formation of blisters coincided with gas release from the surface. It is proposed that a large fraction of the incident ions are trapped in the surface and they do not come out due to the low rate of diffusion in metals. However with time the concentration of gas builds up on the surface which leads to blisters.

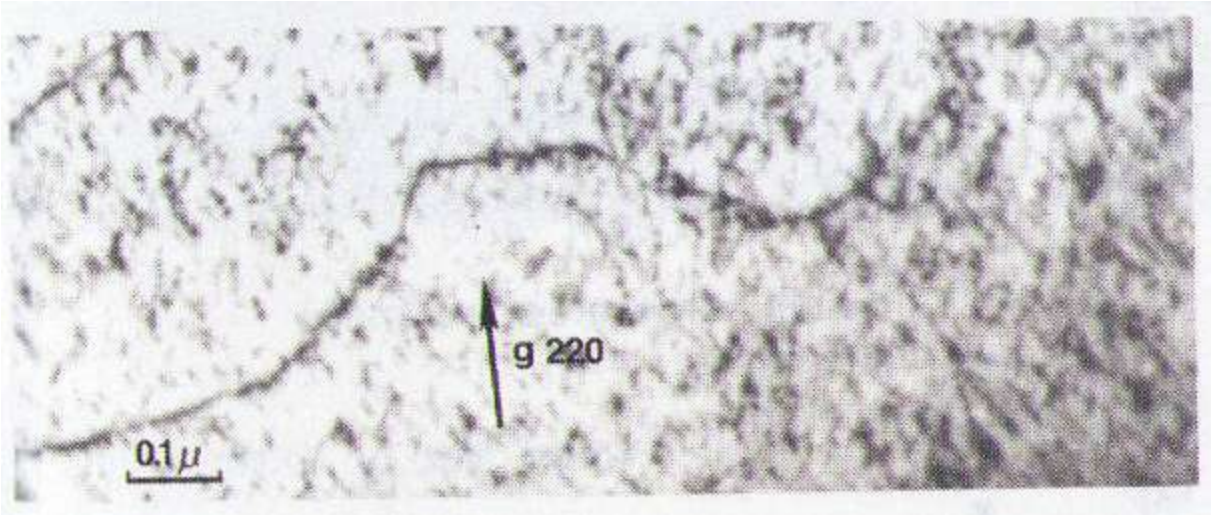

Figure 2.14 Shows dislocation loops on gold specimen irradiated by He^+ ions. Courtesy of Brown et.al [73]

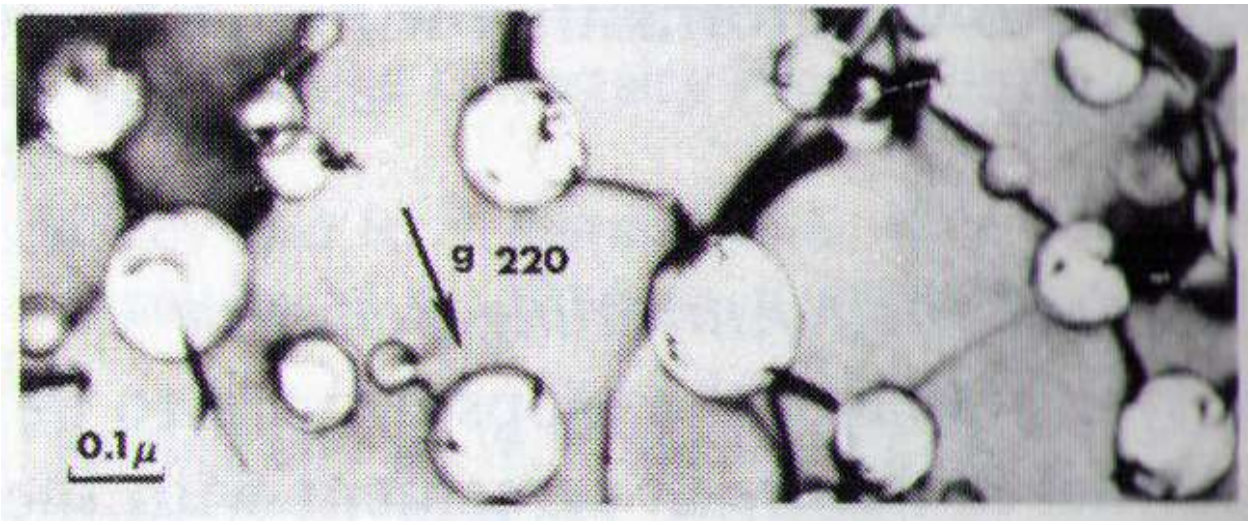

Figure 2.15 Shows formation of voids on gold specimen irradiated by He^+ ions. Courtesy of Brown et.al [73]

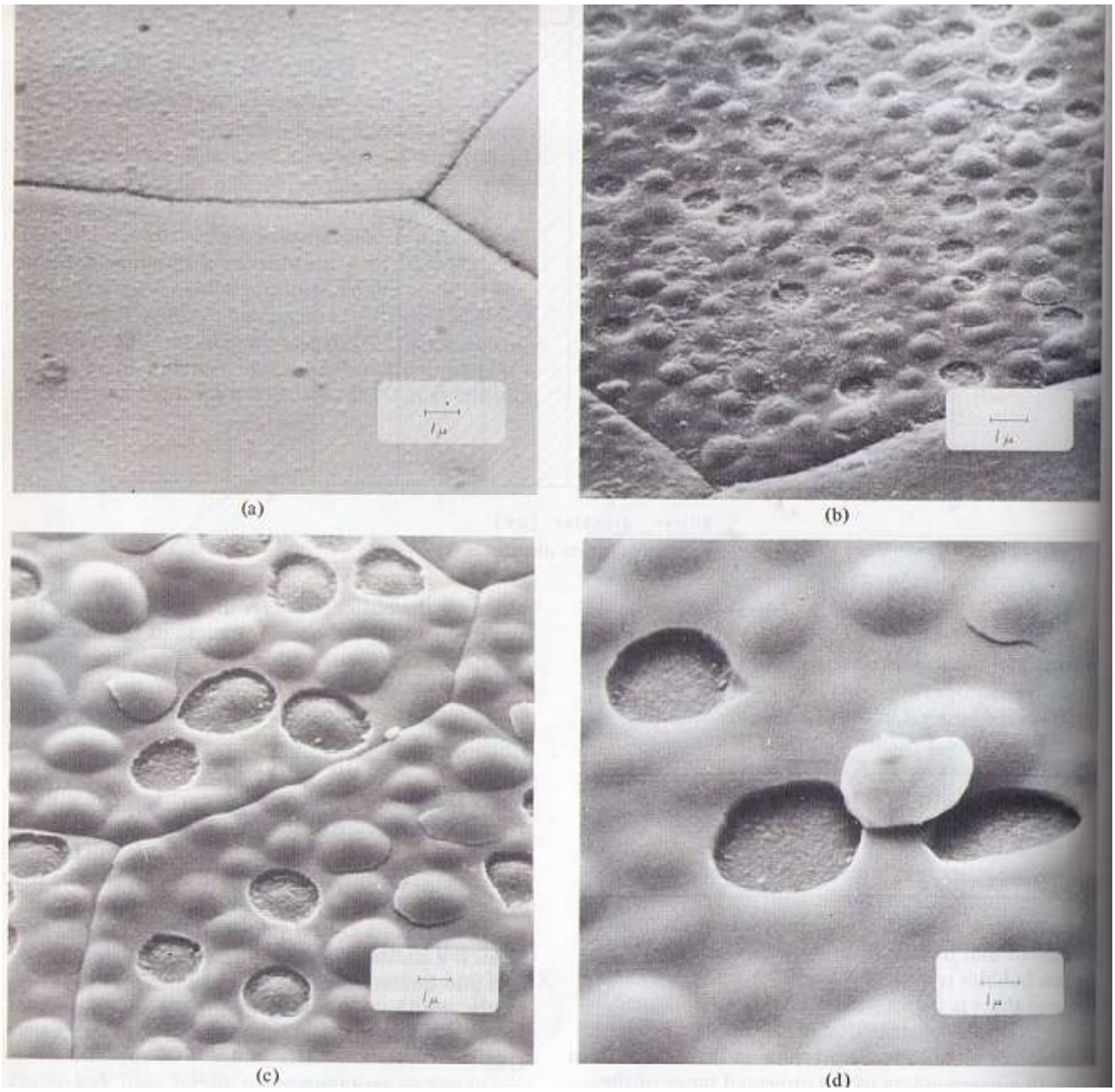

Figure 2.16 Shows blistering of molybdenum after bombardment He^+ ions of different energies (a) 7 KeV (b) 20 KeV (c) 50 KeV (d) 80 KeV. Courtesy of Erents et.al [74]

3. The Physics of Ion Scattering

3.1 Introduction

The interaction of ions with solids is stronger and more complex than is the case for electrons, because ions can interact with negatively charged electrons, with the positive nucleus of the target, and even with the lattice atoms in a 'billiard ball' mode of scattering. The ion - electron interactions are inelastic while the nuclear collisions are elastic events in which the total kinetic energy is conserved but is redistributed between the various bodies involved. Such inelastic collisions result in energy losses for the ion and are classified as the electronic component of the stopping power, which leads to promotion of target electrons to higher energy states and their subsequent release as secondary electrons, Auger electrons, and x-rays. The smaller energy losses suffered by the ion resulting from the elastic collisions comprise the nuclear component of the stopping power, in which the total kinetic energy of the system is conserved. The kinetic energy is transferred from the ion to the target atom as the recoil energy and their subsequent removal from the lattice sites as vacancies and sputtered atoms.

3.2 Interatomic potential

Ion- solid interactions are a binary event, they way in which the potential of the two components varies with the distance separating their two centers and directly determines the scattering probability of the ion. The Coulombic forces between two nuclei considered as point charges separated by a distance r, in the absence of the electron cloud will be,

$$F(r) = \frac{Z_1 Z_2 e^2}{r^2} \quad \text{.....(3.201)}$$

Where Z_1 and Z_2 are the atomic numbers of the two nuclei. The interaction potential due to this point source will be

$$V(r) = \int_r^\infty F(r)dr \quad \text{.....(3.202)}$$

This leads to

$$V(r) = -\left(\frac{Z_1 Z_2 e^2}{r}\right) \text{.....(3.203)}$$

But since the nuclear charge of the proton is screened by the electron cloud around the nucleus, a modified interatomic potential needs to be used which is

$$V(r) = -\left(\frac{Z_1 Z_2 e^2}{r}\right)\chi(r) \text{.....(3.204)}$$

Where $\chi(r)$ is the screening function and is defined as the ratio of the actual interatomic potential at some radius r to the coulomb potential. The value of $\chi(r)$ can be derived from the Thomas-Fermi statistical model. The value of $\chi(r)$ will tend to zero at very large distances and it should tend to unity at very small distances.

The Bohr radius of the hydrogen atom is given by

$$a_o = \frac{\hbar^2}{m_e e^2} = 0.5292 * 10^{-8} cm = 0.05292 nm \text{.....(3.205)}$$

The Bohr velocity of the electron in this orbit is

$$v_o = \frac{\hbar}{m_e a_o} = \frac{e^2}{\hbar} = 2.188 * 10^8 cm/s \text{.....(3.206)}$$

The Thomas-Fermi model assumes that the electron can be treated by the Fermi-Dirac statistics,

in which they behave as an ideal gas of particles of energy E which fill the potential well around the positively charged core. The density of states, n(E) of a free electron gas is

$$n(E) = \frac{L^3}{2\pi^2\hbar^3}(2m_e)^{3/2}E^{1/2} \quad \text{.....(3.207)}$$

Where L is the normalized length of the box.

The number of electrons at point r, N(r) is

$$N(r) = \int_0^{E_F} n(E)dE = \frac{L^3(2m_e)^{3/2}}{3\pi^2\hbar^3}E_F(r)^{3/2} \quad \text{.....(3.208)}$$

The Fermi energy, E_F is the energy of the highest filled state. For a bound electron, the maximum energy the electron will have is when its potential energy equals the Fermi energy. From the equation 3.218, the charge density is

$$\rho = \frac{N(r)}{L^3} = \frac{(2m_e)^{3/2}}{3\pi^2\hbar^3} - V^{3/2} \quad \text{.....(3.209)}$$

From the Poisson's equation

$$-\frac{1}{e}\nabla^2 V = -4\pi ep \quad \text{.....(3.210)}$$

This leads to

$$\nabla^2 V = \frac{-4e^2 + 2m_e V(r)^{3/2}}{3\pi\hbar^3} \quad \text{.....(3.211)}$$

For a single atom, the potential is given by

$$V(r) = \frac{-Ze^2}{r}\chi(r) \quad \text{.....(3.212)}$$

and making the change for the variable r as

$$r = a_{TF}x \quad \text{.....(3.213)}$$

Where a_{TF} is the Thomas-Fermi screening length, given by

$$a_{TF} = \frac{1}{2}\left(\frac{3\pi}{4}\right)^{3/2} \frac{\hbar^2}{m_e e^2 Z^{1/3}} = \frac{0.885 a_o}{Z^{1/3}} \quad \text{……(3.214)}$$

Substituting equation 3.213 and equation 3.212 in the equation 3.211, leads to

$$x^{1/2} = \frac{d^2\chi}{dx^2} = \chi^{3/2} \quad \text{……(3.215)}$$

The above equation is the Thomas-Fermi equation. There have been various analytical expressions for the screening functions proposed by various authors and these are compiled in Torrens [42] and is listed in Table 3.1. When the interatomic potential between two atoms is

$$V(r) = \frac{-Z_1 Z_2 e^2}{r}\chi(r) \quad \text{……..(3.226)}$$

In case of interatomic screening function, the approach is to use simple atomic potentials and then modify the screening length to get the interatomic potential. Estimates of screening length that have been proposed [3] are presented in Table 3.2.

Ziegler, Biersack and Littmark[3] made the study of interatomic potential for 261 pairs of atoms and gave the best fit Screening Length which is often referred to as “Universal Screening Length”. This was then used by them to get the “Universal Screening function” which is given by

$$\chi = 0.1818\exp(-3.2x) + 0.5099\exp(-0.9423x) + 0.2802\exp(-0.4028x) + 0.02817\exp(-0.2016) \quad \text{…….(3.216)}$$

The Universal Screening function seemed to give the results of ion range close to the experimentally observed values.

Table 3.1 Analytical expression of screening function to the Thomas Fermi equation

Author	**Expression**
Sommerfeld	$\left[1+\left(\frac{x}{12^{2/3}}\right)^{0.772}\right]^{-3/0.772}$
Umeda	$\left[1+\left(\frac{x}{12^{2/3}}\right)^{0.8034}\right]^{-3/0.8034}$
Kerner	$[1+1.3501x]^{-1}$
Umeda	$[1+1.3679x]^{-1}$
Moliere	$0.35\exp(-0.3x)+0.55\exp(-1.2x)+0.10\exp(-6.0x)$
Rozental	$0.7345\exp(-0.562x)+0.2655\exp(-3.392x)$
Rozental	$0.255\exp(-0.0246x)+0.581\exp(-0.947x)+0.164\exp(-4.356x)$
Csavinsky	$[0.7111\exp(-0.175x)+0.2889\exp(-1.6625x)]^{-2}$
Roberts	$[1+1.7822x^{1/2}]\exp[-1.7822x^{1/2}]$
Wedepohl	$317x\exp(-6.62x^{1/4})$
Lindhard	$1-\frac{x}{[3+x^2]^{1/2}}$
Lindhard	$1-\frac{1}{2x}$
Lenz-Jensen	$[0.7466\exp(-1.038x)]+[0.2433\exp(-0.3876x)]+[0.01018\exp(-0.206x)]$

Table 3.2 Interatomic Screening Length[3]

Thomas-Fermi	$a = \frac{0.88534 a_o}{\left(Z_1^{1/2} + Z_2^{1/2}\right)^2}$
Bohr	$a = \frac{a_o}{\left(Z_1^{2/3} + Z_2^{2/3}\right)^{1/2}}$
Firsov	$a = \frac{0.8853 a_o}{\left(Z_1^{1/2} + Z_2^{1/2}\right)^{2/3}}$
Lindhard	$a = \frac{0.8853 a_o}{\left(Z_1^{1/2} + Z_2^{1/2}\right)^{2/3}}$
Ziegler, Biesack, Littmark	$a = \frac{0.8854 a_o}{\left(Z_1^{0.23} + Z_2^{0.23}\right)}$

3.3 Classical Scattering Theory

Ion - electron interactions are inelastic while the nuclear collisions are to a good approximation elastic events in which the total kinetic energy is conserved although is redistributed between the various bodies involved. The inelastic collisions however do not change the trajectory of the incoming beam significantly [6], and so it is the elastic collisions with lattice atoms that cause the ion to deflect.

As shown in Figure 3.01 as the ion travels in the specimen they are continuously getting deflected, when the net deflection becomes greater than 90º and ion is close to surface of the sample, then it may emerge as a backscattered ion. During its course the ion transfers energy to the target atoms which are assumed to be initially at rest, and if the energy transferred is greater than some threshold then the target atom begins to recoil. A binary model of collision is assumed, where the ion collides with only a single target atom at any particular instant. This two body collision is valid when the mean free path of the ion (which is the average distance traveled by the ion between successive collisions) is greater than the interatomic spacing of the target atoms. Since the deflection of the ion is an elastic process, the deflection angle can be found out using classical dynamics. The elastic collision kinematics can be solved using the principles of conservation of energy and momentum. If Z_1, M_1 is the atomic number and mass of the ion and Z_2, M_2 is the atomic number and mass of the target atom. Where θ, ϕ are the ion scattering angle and the recoil angle of the target atom respectively in the laboratory co-ordinates as shown in Figure 3.02.

Then from law of conservation of energy

$$E_o = \frac{1}{2} M_1 v_o^{\,2} = \frac{1}{2} M_1 v_1^{\,2} + \frac{1}{2} M_2 v_2^{\,2} \quad \text{.....(3.301)}$$

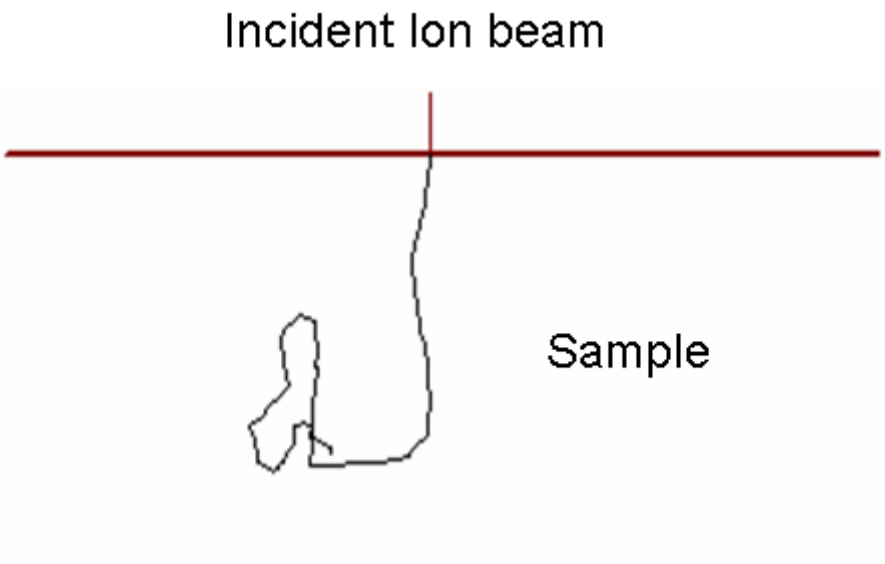

Figure 3.01 An ion beam trajectory showing the successive deflections of the ion as it travels in the sample

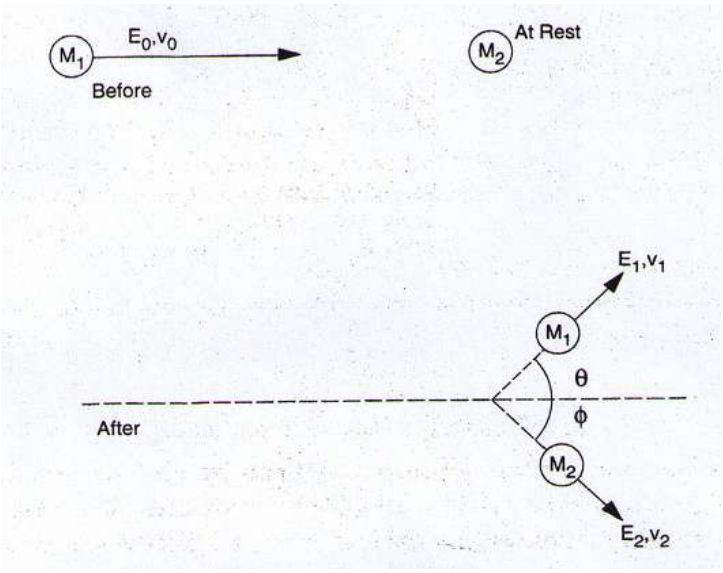

Figure 3.02 Ion-atom collisions in Laboratory co-ordinates. Courtesy of Nastasi et.al[43]

From the law of conservation of longitudinal momentum

$$M_1 v_o = M_1 v_1 \cos\theta + M_2 v_2 \cos\phi \quad \text{……..(3.302)}$$

From the law of conservation of transverse momentum

$$0 = M_1 v_1 \sin\theta - M_2 v_2 \sin\phi \quad \text{…….(3.303)}$$

Where v_o is the initial velocity of the ion, E_o is the incident ion energy and v_1, v_2 are the final velocities of the ion and target atom respectively.

It is very convenient to describe the ion scattering using center-of-mass (CM) co-ordinate system, because no matter how complex the force between the ions and the target atom, if it acts along the line joining them, the relative motion of the two particles can be reduced to that of a single particle moving in an interatomic potential centered at the origin of the center-of-mass coordinates as shown in Figure 3.03. The mutual interaction of the two colliding is described by the interatomic potential V(r) and the motion of both the particles is given by one equation of motion. The total change in linear momentum of a CM system is zero. Therefore

$$F_T = F_1 + F_2 = \frac{dP_T}{dt} = 0 \quad \text{…….(3.304)}$$

Where F_1 and F_2 being the forces acting on the ion and target atom respectively. Since the CM system is reduced to a single particle moving in a force field, there is no net change in the CM system velocity v_c of the particle before and after collision. The CM velocity v_c can be defined as

$$M_1 v_o = (M_1 + M_2)\, \tilde{v}_c \quad \text{……(3.305)}$$

The CM reduced mass M_c is given by

$$\frac{1}{M_c} = \frac{1}{M_1} + \frac{1}{M_2} \quad \text{……..(3.306)}$$

Or equivalently

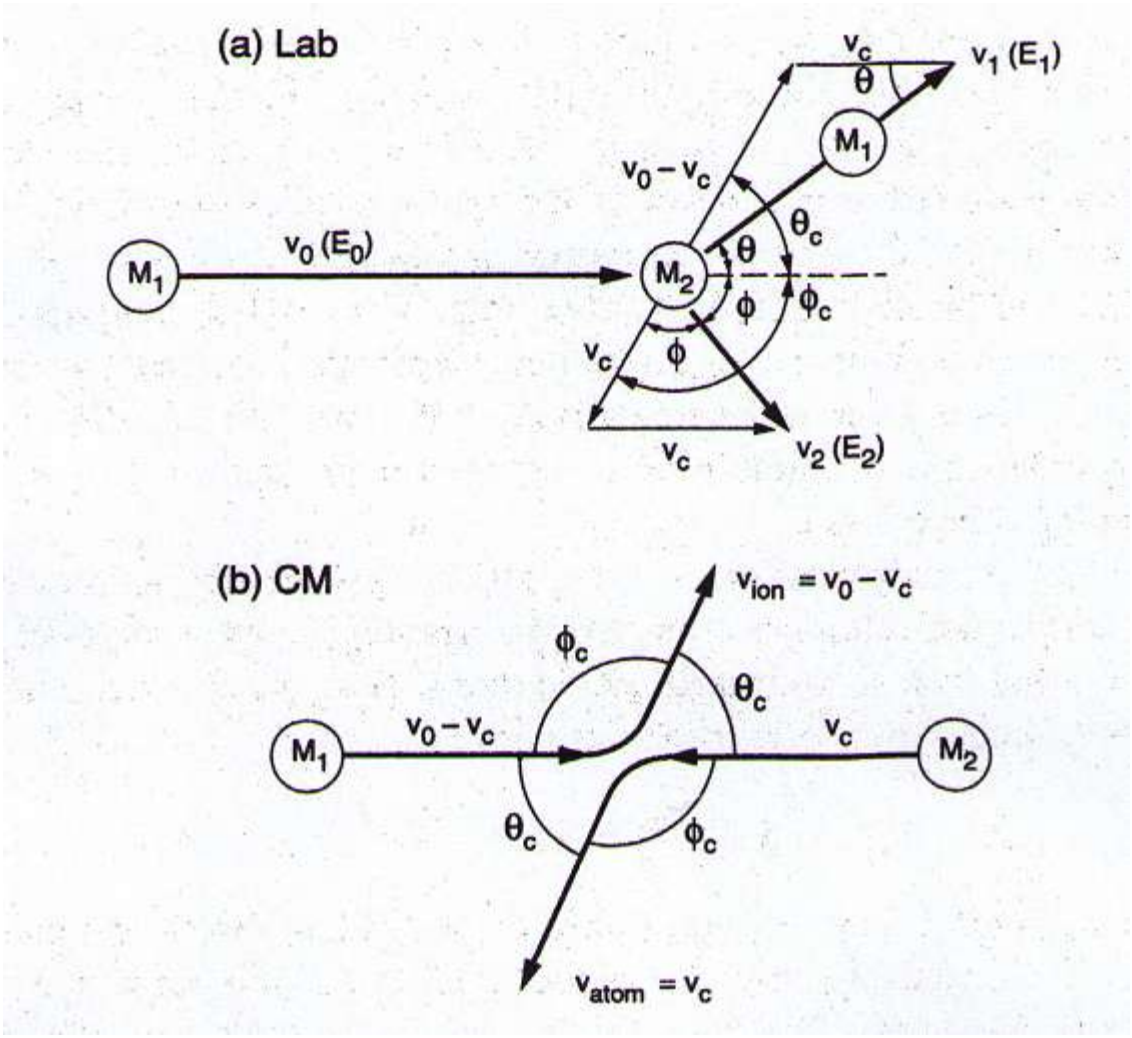

Figure 3.03 Ion-atom collision conversion from Center of Mass to Laboratory Co-ordinates. Courtesy of Nastasi et.al[43]

$$M_c = \frac{M_1 M_2}{M_1 + M_2} \quad \text{……..(3.307)}$$

Substituting equation(3.307) in equation(3.305) we get

$$v_c = v_o \frac{M_c}{M_2} \quad \text{……...(3.308)}$$

The CM ion and atom velocities can be derived from the vector diagrams of Figure 3.03, which are

$$v_{ion} = v_o - v_c = v_o \frac{M_c}{M_1} \quad \text{……..(3.309)}$$

$$v_{atom} = v_c = v_o \frac{M_c}{M_2} \text{ ……(3.310)}$$

The system velocity, ion velocity and atom velocity in the CM co-ordinate system remains constant and is independent of the scattering of ion and the target atom. The CM total energy E_c is the CM initial kinetic energy

$$E_c = \frac{1}{2} M_c v_o^{\,2} = \frac{1}{2} \frac{M_1 M_2}{M_1 + M_2} v_o^{\,2} = \frac{M_2}{M_1 + M_2} E_o \text{ ……(3.311)}$$

If θ_c and Φ_c are the center of mass scattering angle of the ion and the target atom as shown in Figure 3.03. From the Figure 3.03 we get

$$\Phi_c = 2\phi \text{ ……(3.312)}$$

$$\theta_c + \Phi_c = \pi \text{ ……(3.313)}$$

Substituting equation(3.313) into equation(3.312) we get

$$\phi = \frac{\pi - \theta_c}{2} \text{ ……(3.314)}$$

From the vector diagram in Figure 3.03 and the law of cosines, we get

$$v_2^{\,2} = v_c^{\,2} + v_c^{\,2} - 2v_c^{\,2}\cos(\pi - \phi_c) \quad \text{.....(3.315)}$$

Substituting equation (3.314) into equation (3.315), we get

$$v_2 = 2v_o \frac{M_c}{M_2}\cos\phi \quad \text{.....(3.316)}$$

The energy transferred to the target atom (or energy of recoil) is

$$E_2 = T = \frac{1}{2} M_2 v_2^{\,2} \quad \text{.....(3.317)}$$

Substituting equation (3.316) into equation (3.317) we get

$$E_2 = T = \frac{1}{2} M_2 \left(\frac{v_o M_c \cos\phi}{M_2} \right)^2 \quad \text{.....(3.318)}$$

Substituting equation (3.314) into equation (3.318) we get

$$E_2 = T = \frac{4E_c M_c}{M_1}\sin^2\left(\frac{\theta_c}{2}\right) = E_o \frac{4M_1 M_2}{(M_1 + M_2)^2}\sin^2\left(\frac{\theta_c}{2}\right) \quad \text{.....(3.319)}$$

The maximum energy transferred to the target atom is when there is a head on collision between the ion and the atom i.e. θ_c=180º, in which case the equation (3.319) reduces to

$$T_M = E_o \frac{4M_1 M_2}{(M_1 + M_2)^2} \quad \text{.....(3.320)}$$

From equation(3.320) we see that, the energy transferred for a head on collision is 0.75 E_o, 0.22 E_o and 0.078 E_o for Carbon, Silicon and Gold respectively. As the mass of the target atom increases the energy lost to it in a single collision decreases significantly, however the probability of ion undergoing an elastic collision also increases drastically.

3.4 The Classical Scattering Integral

The reason for using the center of mass system is because of its convenience for describing interactions using a central potential V(r) which is acts along the line of separation r of the atom and the ion.

For a force F acting at the origin of a particle at a distance r away from the point as shown in Figure 3.04, then the torque is given by

$$\tau = r \quad X \quad F = r \quad X \quad \frac{dv}{dt} \quad \text{……..(3.401)}$$

The angular momentum $\boldsymbol{l}$ of the particle is given by

$$l = r \quad X \quad Mv = r \quad X \quad p \quad \text{…….(3.402)}$$

The rate of change of angular momentum is given by

$$\frac{dl}{dt} = \frac{dr}{dt} \quad X \quad Mv \quad + r \quad X \quad M \frac{dv}{dt} \quad \text{……..(3.403)}$$

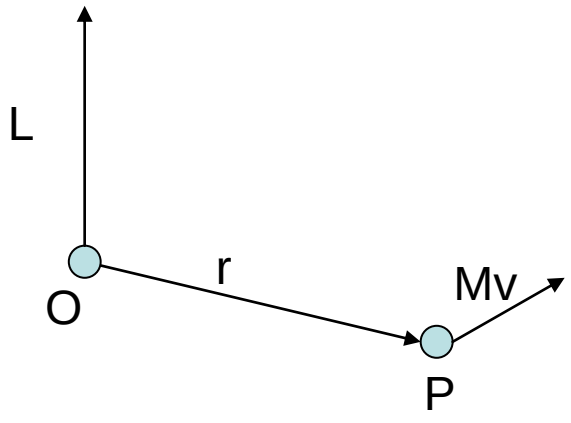

Figure 3.04 Showing the central force

For an Central Force F(r) acting radially along the distance of separation r

$$v = \frac{dr}{dt} \qquad \text{.....(3.404)}$$

Substituting equation(3.404) into equation(3.403) we get

$$\frac{dl}{dt} = v \quad X \quad Mv \quad + r \quad X \quad M \frac{dv}{dt} \text{ .....(3.405)}$$

The first term in equation(3.405) is zero, hence it reduces to

$$\frac{dl}{dt} = r \quad X \quad M \frac{dv}{dt} \text{ .....(3.406)}$$

Which is

$$\frac{dl}{dt} = r \quad X \quad F = \tau \text{ .....(3.407)}$$

Since the force (from the central potential V(r)) is directed radially outward or inward along r, the torque τ is zero. Hence equation(3.407) further reduces to

$$\frac{dl}{dt} = 0 \text{ .....(3.408)}$$

Therefore equation(3.408) says that the angular momentum $\boldsymbol{l}$ is always conserved i.e.

$$l = r \quad X \quad p = \text{constant} \quad \text{.....(3.409)}$$

From equation(3.402) and equation(3.409) we have

$$l = rMv_{\perp} = Mr^2 \frac{d\theta}{dt} = \text{ Constant.....(3.410)}$$

Where $v_{\perp}$ is the component of velocity perpendicular to radial vector **r**.

The total energy of the particle can be written as

$$E = \frac{M}{2} v^2 + V(r) \quad \text{……(3.411)}$$

The equation(3.411) can be written as

$$E = \frac{M}{2} (v_\perp^2 + v_r^2) + V(r) \quad \text{……(3.412)}$$

Where v_r is velocity component along the radial vector **r**.

Substituting equation(3.410) into equation(3.412) we get

$$E = \frac{Mv_r^2}{2} + \frac{l^2}{2Mr^2} + V(r) \quad \text{……..(3.413)}$$

In the equation(3.413) the first term is the kinetic energy term, the second term is the centrifugal term and the third term is the interatomic potential energy term. The interatomic potential V(r) tends to zero as r approaches infinity. As the distance between the two particles decreases the interatomic potential becomes negative, and at some particular distance of separation the kinetic energy of the particle becomes zero. This distance r_{min} is called the distance of closest approach as shown in Figure 3.05. The energy of the particle at r_{min} is given by

$$E(r_{min}) = V(r_{min}) + \frac{l^2}{2Mr_{min}^2} \quad \text{……(3.414)}$$

The particle's direction of motion is offset from a parallel line through the center of the target atom by a distance b, which is also called impact parameter.

The angular momentum can be defined as

$$l = Mr_{min} v_\perp \quad \text{……(3.415)}$$

As r approaches infinity

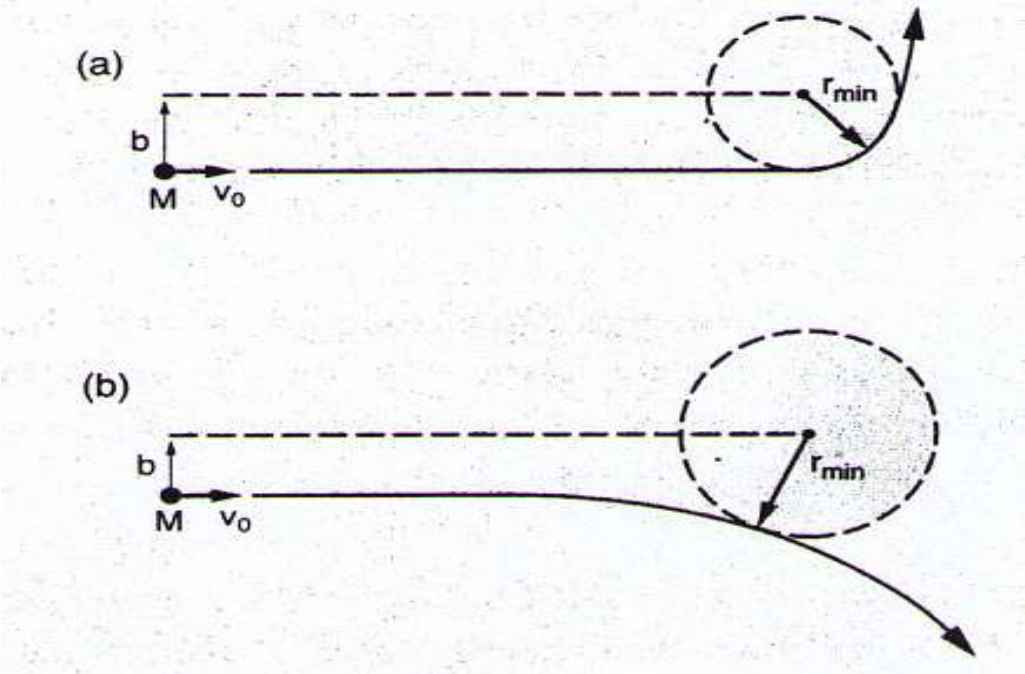

Figure 3.05 Showing the view of the trajectory with the impact parameter b and also the distance of closest approach r_{min} (a) for an attractive potential (b) for a repulsive potential. Courtesy of French[44]

$$l = Mv_o b \quad \text{……(3.416)}$$

Substituting equation(3.416) into equation(3.414) we get

$$0 = 1 - \frac{V(r_{min})}{E} - \frac{b^2}{r_{min}^2} \quad \text{……..(3.417)}$$

The classical scattering angle can be derived with respect to the interatomic potential and impact parameter, by making conversions from the laboratory co-ordinates and the CM co-ordinate system as shown in Figure 3.06. Also for the equations derived above the mass M and energy E have to be replaced by the CM mass M_c and CM energy E_c.

The equation(3.413) in the CM system is

$$E_c = \frac{M_c v_r^2}{2} + \frac{l^2}{2M_c r^2} + V(r) \quad \text{……(3.418)}$$

From Figure 3.06 and equation(3.410) , the equation(3.418) can be reduced to

$$E_c = \frac{M_c}{2}\left(\left(\frac{dr}{dt}\right)^2 + r^2\left(\frac{d\Theta}{dt}\right)^2\right) + V(r) \quad \text{……..(3.419)}$$

Where r is the distance between the scattering centers and from Figure 3.06, it can be defined as

$$r = r_1 + r_2 \quad \text{……..(3.420)}$$

The angle Θ is the angle between the line $r_1 + r_2$ and the perpendicular to the line $r_{min.}$ From the law of conservation of angular momentum we have

$$l = M_c r^2 \frac{d\Theta_c}{dt} \quad \text{……(3.421)}$$

From equation(3.416) and equation(3.421) we get

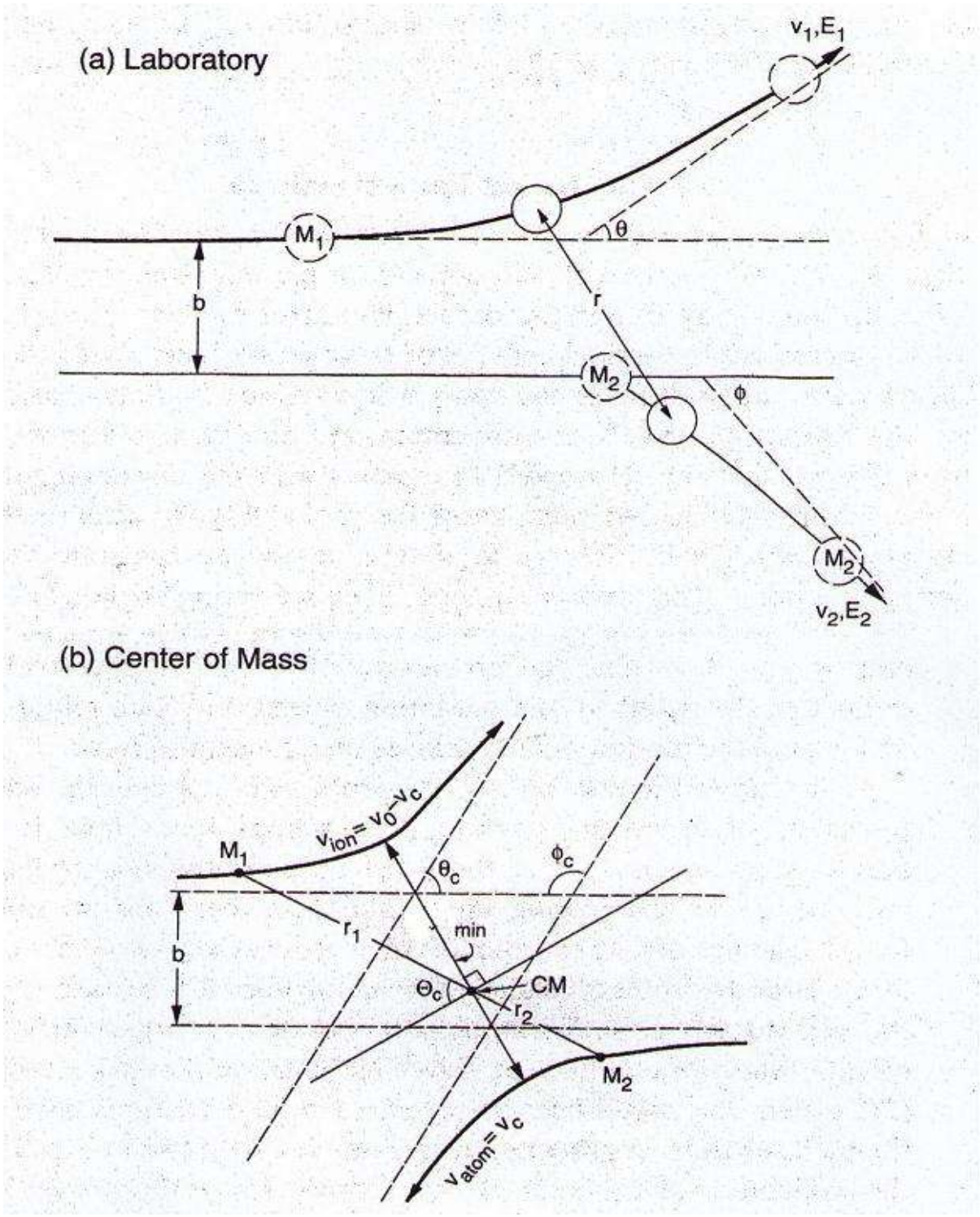

Figure 3.06 Showing the scattering angles and impact parameter for (a) Laboratory co-ordinates (b) Center of Mass co-ordinates. Courtesy of Nastasi et.al[43]

$$l = M_c r^2 \frac{d\Theta_c}{dt} = M_c v_o b \quad \text{……(3.422)}$$

From equation(3.422) we get

$$\frac{d\Theta_c}{dt} = \frac{v_o b}{r^2} \quad \text{……(3.423)}$$

Substituting equation(3.423) into equation(3.419) we get

$$\frac{dr}{dt} = v_o \left(1 - \frac{V(r)}{E_c} - \left(\frac{b}{r}\right)^2\right)^{1/2} \quad \text{……..(3.424)}$$

From equation(3.424) we get

$$\frac{d\Theta_c}{dt} \cdot \frac{dt}{dr} = \frac{d\Theta_c}{dr} = \frac{b}{r^2\left[1 - \frac{V(r)}{E_c} - \left(\frac{b}{r}\right)^2\right]^{1/2}} \quad \text{……..(3.425)}$$

The CM scattering angle θ_c can be found by integrating the equation (3.424) between the integration limits $\theta_c/2$ to $\pi/2$ which corresponds to integration limits on the right hand side from r_{min} to infinity. The integration limits corresponds to half orbit of rotation. Integrating the equation(3.425) we get

$$\int_{\theta_c}^{\pi/2} d\Theta_c = \int_{r_{min}}^{\infty} \frac{b\,dr}{r^2\left[1 - \frac{V(r)}{E_c} - \left(\frac{b}{r}\right)^2\right]^{1/2}} \quad \text{……(3.426)}$$

This leads to

$$\frac{1}{2}\left(\pi-\theta_c\right)=\int_{r_{\min}}^{\infty}\frac{bdr}{r^2\left[1-\frac{V(r)}{E_c}-\left(\frac{b}{r}\right)^2\right]^{1/2}} \quad \text{.....(3.427)}$$

Which further reduces to

$$\theta_c=\pi-2b\int_{r_{\min}}^{\infty}\frac{dr}{r^2\left[1-\frac{V(r)}{E_c}-\left(\frac{b}{r}\right)^2\right]^{1/2}} \quad \text{.....(3.428)}$$

This equation (3.428) is known as the **Classical Scattering integral**.

3.5 The Angular differential Scattering cross section

The angle of deflection of the ion or the classical scattering angle can be found if the interatomic potential, the energy of the ion, and the impact parameter are known. However the impact parameter is a probabilistic event and hence determines probability of scattering the ion into some angle between θ_c and $d\theta_c+\theta_c$. This probability is called the differential cross section, and can be expressed as either the probability of transferring energy T in the range between T and T + dT or as explained previously scattering the ion through a particular angle.

If the ions are incident perpendicularly on the sample and the detector is moved across the specimen chamber at different angles with respect to the sample and the ions are collected and counted by the detector. Then the number of ions collected by the detector for every ion incident for a particular angle of the detector gives the angular differential cross section. However this angular differential cross section is like an average since it is a cumulative effect of multiple scattering process depending on the thickness of the sample. This angular deflection cross

section needs to be found out for individual scattering event. The concept of a cross section is described by the analogy given by Rudolf Peierls as " If I throw a ball at a glass window one square foot in area, there may be one chance in ten that the window will break and nine chances in ten that the ball will just bounce. In the physicist's language this particular window, for a ball thrown in this particular way, has a disintegration (inelastic!) cross section of 0.1 square feet and an elastic cross section of 0.9 square feet." The total cross section has units of area and can be expressed as cm^2 or barns (one barn is 10^{-24} cm^2).

The scattering center in a binary collision is the target nucleus and cross section is the effective area around each nucleus which can effectively scatter the particle. It can be seen from Figure 3.07 how the impact parameter affects the scattering angle, if the impact parameter is less than b then the particle will be deflected. However if the impact parameter is greater than b then the particle will go undeflected. Hence the scattering cross section is the area of the radius whose radius is b. Hence the total cross section $\sigma(\theta_c)$ is given by

$$\sigma(\theta_c) = \pi b^2 \quad \text{.....(3.501)}$$

It can be also seen that when the impact parameter is lesser (i.e. the particle is closer to the nucleus of the target) the particle will be deflected through a greater angle as can be seen in Figure 3.08. From differentiating the equation 3.501 we get

$$\frac{d\sigma(\theta_c)}{db} = 2\pi b \text{ .....(3.502)}$$

In order to get the differential cross section in terms of the scattering angle, the equation 3.502 can be conveniently expressed as

$$d\sigma(\theta_c) = 2\pi b(\theta_c)\left|\frac{db(\theta_c)}{d\theta_c}\right| d\theta_c \text{ .....(3.503)}$$

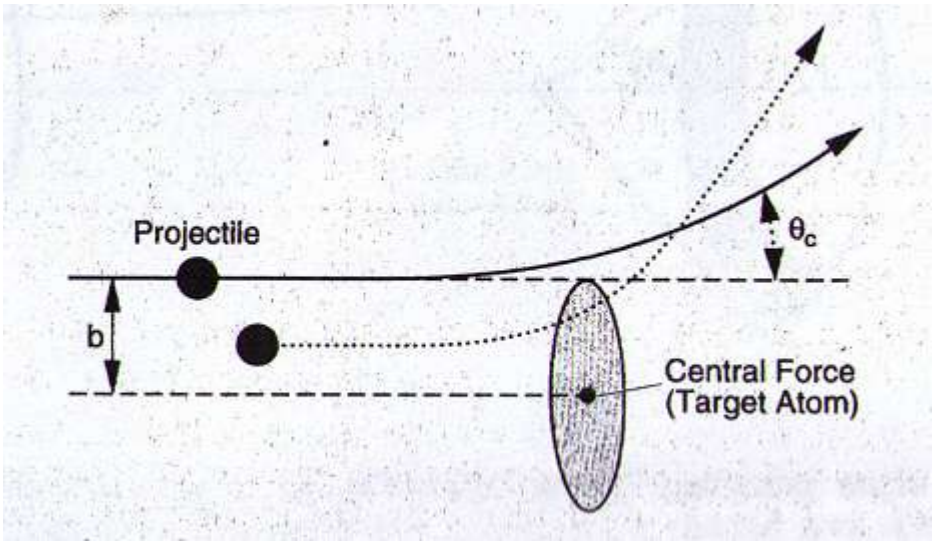

Figure 3.07 Showing the scattering of a particle with an impact parameter b. Courtesy of Nastasi et.al[43]

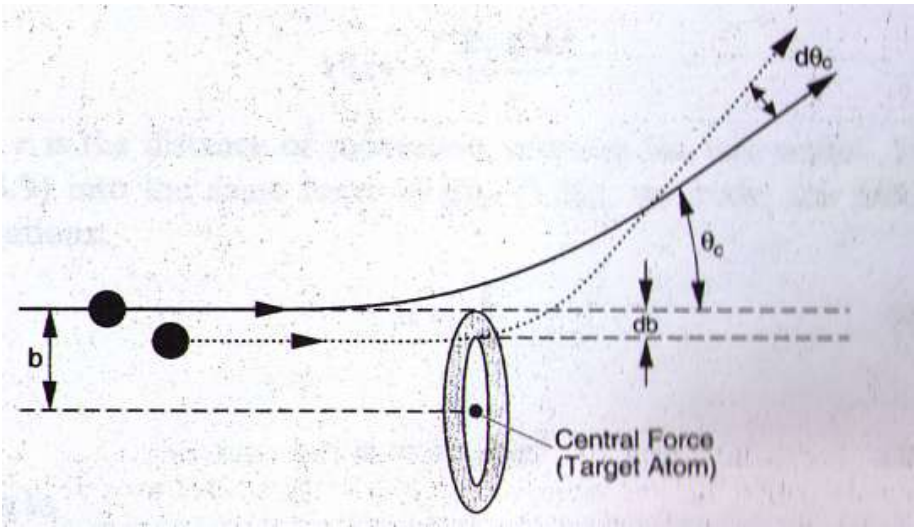

Figure 3.08 Showing the change in scattering of a particle with change in impact parameter b. Courtesy of Nastasi et.al[43]

From the Figure 3.09 it can be seen that for a small change in the scattering angle $d\theta_c$ the area along which it can be detected is the shaded region. The area of the shaded region is given by

$$dA = 2\pi R \sin\theta_c R d\theta_c \quad \text{.....(3.504)}$$

The change in solid angle is given by

$$d\Omega = \frac{dA}{R^2} \quad \text{.....(3.505)}$$

From equation 3.504 and equation 3.505 we get

$$d\Omega = 2\pi \sin\theta_c d\theta_c \quad \text{.....(3.506)}$$

Substituting the equation 3.506 into equation 3.503 we get

$$\frac{d\sigma(\theta_c)}{d\Omega} = \frac{b}{\sin\theta_c}\left|\frac{db}{d\theta_c}\right| \quad \text{.....(3.507)}$$

Using the coulomb interaction potential $V(r) = \frac{Z_1 Z_2 e^2}{r}$ in the Classical Scattering integral in equation 3.428. And integrating it we get

$$\theta_c = \pi - 2\left[\sin^{-1}\left(\frac{-\left(\frac{b}{r}+\frac{\alpha}{2E_c b}\right)}{\left(1+\frac{\alpha^2}{4E_c^2 b^2}\right)^{1/2}}\right)\right]_0^{1/r\min} \quad \text{.....(3.508)}$$

The above equation can be solved for b and this yields

$$b = \frac{\alpha}{2E_c}\cot\left(\frac{\theta_c}{2}\right) = \frac{\alpha}{2E_c}\frac{\cos(\theta_c/2}{\sin\theta_c/2} \quad \text{.....(3.509)}$$

Differentiating the above equation we get

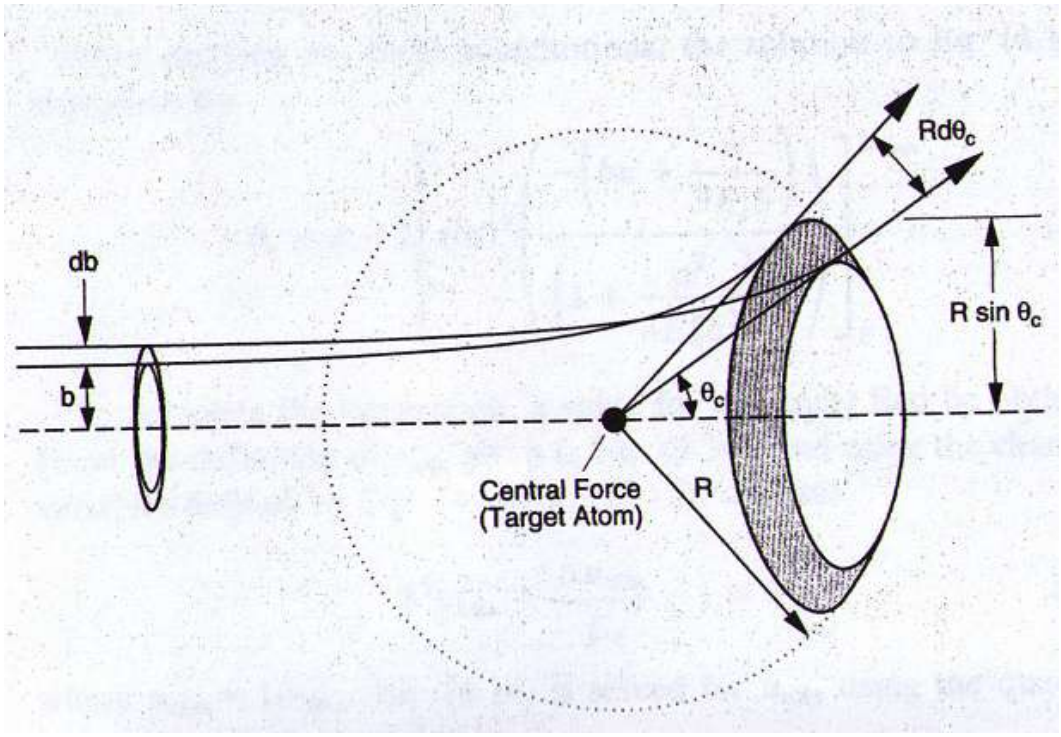

Figure 3.09 Showing the solid angle dΩ subtended at the scattering angle θ_c by the incremental angle $d\theta_c$. Courtesy of Nastasi et.al[43]

$$\frac{db}{d\theta_c} = \frac{\alpha}{2E_c}\frac{d\left(\cot\theta_c/2\right)}{d\theta_c} = \frac{\alpha}{2E_c}\frac{d}{d\theta_c}\left(\frac{\sin\theta_c/2}{1-\cos\theta_c/2}\right) = \frac{\alpha}{4E_c\sin^2\theta_c/2} \quad \text{.....(3.510)}$$

Substituting the equation 3.510 into equation 3.503 we get

$$\frac{d\sigma(\theta_c)}{d\Omega} = \frac{b}{\sin\theta_c}\left|\frac{db}{d\theta_c}\right| = \frac{1}{2}\left(\frac{\alpha}{2E_c}\right)^2 \frac{\cot\theta_c/2}{\sin\theta_c\sin\theta_c/2} \quad \text{.....(3.511)}$$

Simplifying the above equation we get

$$\frac{d\sigma(\theta_c)}{d\Omega} = \left(\frac{\alpha}{4E_c}\right)^2 \frac{1}{\sin^4(\theta_c/2)} \quad \text{.....(3.512)}$$

Using equation 3.506 and equation 3.512 we get

$$\frac{d\sigma(\theta_c)}{d\theta_c} = \frac{d\sigma(\theta_c)}{d\Omega}\frac{d\Omega}{d\theta_c} = 2\pi\left(\frac{\alpha}{2E_c}\right)^2 \frac{\cos\theta_c/2}{\sin^3\theta_c/2} \quad \text{.....(3.513)}$$

This is the angular differential cross section and since coulomb potential was used in the derivation it is also called Coulomb angular differential cross section or Rutherford differential cross sections.

The equation 3.513 gives the probability of the particle deflecting through an angle θ_c, it may also be required to find the probability of the particle while undergoing a scattering event to transfer a amount of energy T. The equation 3.319 gives the energy transferred to the target atom, this can be differentiated to give

$$\frac{d\sigma(\theta_c)}{dT} = \frac{d\sigma(\theta_c)}{d\theta_c}\frac{d\theta_c}{dT} = 2\pi\left(\frac{\alpha}{2E_c}\right)^2 \frac{1}{\sin^4\theta_c/2} \quad \text{.....(3.514)}$$

3.6 The Reduced Energy Parameter

From equation 3.417 we get the equation of closest approach to the target atom as

$$\frac{V(r_{\min})}{1-b^2/r_{\min}^2} = E_c = \frac{M_2}{M_1+M_2}E_o \quad \text{.....(3.601)}$$

For a head-on collision b=0, therefore from equation 3.601 we get

$$d_c = r_{\min}(b=0) = \frac{M_1+M_2}{M_2 E_o} Z_1 Z_2 e^2 \quad \text{.....(3.602)}$$

The parameter d_c is called the collision diameter.

It was proposed by Lindhard et.al [8] that a dimensionless parameter of energy ε was more convenient to manipulate in equations. The parameter ε is defined as

$$\varepsilon = \frac{a_{TF}}{d_c} = \frac{a_{TF}E_c}{Z_1 Z_2 e^2} = \frac{E}{Z_1 Z_2 e^2}\frac{a_{TF}M_2}{M_1+M_2} \quad \text{.....(3.603)}$$

The Reduced energy parameter ε gives an indication of how violent the projectile target collisions are. For example the Thomas-Fermi radius a_{TF} for He on Si is about $1.5*10^{-2}$ nm. For a 100 KeV He ion incident on Si, the collision diameter is about $4.6*10^{-4}$ nm. Hence the collision diameter is much lesser than the Thomas-Fermi radius and ε is found to be $3.4*10^{2}$.

3.7 The Reduced Energy Parameter

To simplify the differential scattering cross section Lindhard, Nielsen and Scharff [8] proposed a differential cross section equation based on the reduced energy parameter

$$d\sigma = \frac{-\pi a_{TF}^a}{2}\frac{f(t^{1/2})}{t^{3/2}}dt \quad \text{.....(3.701)}$$

Where t is defined as

$$t \equiv \varepsilon^2 \frac{T}{T_M} = \varepsilon^2 \sin^2\left(\frac{\theta_c}{2}\right) \quad \text{.....(3.702)}$$

The fitting function $f(t^{1/2})$ was expressed analytically by Winterbon et.al[9] as

$$f(t^{1/2}) = \lambda' t^{1/6}\left(1 + (\lambda' t^{2/3})^2\right)^{-3/2} \quad \text{.....(3.703)}$$

With $\lambda' = 1.309$

The fitting function $f(t^{1/2})$ is given by the power law approximation as

$$f(t^{1/2}) = \lambda_m t^{1/2-m} \quad \text{.....(3.704)}$$

3.8 Nuclear Stopping Power

The stopping power is the rate of energy loss, which is expressed in units of eV/nm or KeV/um. It is also useful to express the energy loss rate in terms of stopping cross-section S, which is energy loss per scattering center which has units of eV cm^2/atom. The stopping cross-section is defined as

$$S = \frac{dE/dx}{N} \quad \text{.....(3.801)}$$

Where N is the atomic density of the target.

The nuclear stopping power can be now derived from equation 3.701 as

$$\left.\frac{dE}{dx}\right|_n = -N\pi a_{TF}^2 \int_0^{T_M} T \frac{f(t^{1/2})}{2t^{3/2}} dt \quad \text{.....(3.802)}$$

Substituting equation 3.702 into equation 3.801 we get

$$\left.\frac{dE}{dx}\right|_n = \frac{-N\pi a_{TF}^2 T_M}{\varepsilon^2}\int_0^{T_M} f(t^{1/2})\,dt^{1/2} \quad \ldots\ldots\ldots\ldots\ldots\ldots\ldots\ldots(3.803)$$

It is more convenient to write the Stopping power in the form of reduced stopping cross section S(ε) which is expressed in terms of reduced length ρ_L

$$S(\varepsilon) = \frac{d\varepsilon}{d\rho_L} \quad \ldots\ldots\ldots\ldots\ldots\ldots\ldots\ldots\ldots\ldots\ldots\ldots\ldots\ldots(3.804)$$

Where ρ_L is given by

$$\rho_L = LNM_2 4\pi a_{TF}^2 \frac{M_1}{(M_1 + M_2)^2} \ldots\ldots\ldots\ldots\ldots\ldots\ldots\ldots\ldots\ldots\ldots(3.805)$$

The equation (3.802) can be converted to the from of equation (3.804)

$$\frac{dE}{dx} = NS(E) = \frac{d\varepsilon}{d\rho_L}\left(\frac{dE}{d\varepsilon}\frac{d\rho_L}{dL}\right) \quad \ldots\ldots\ldots\ldots\ldots\ldots\ldots\ldots(3.806)$$

By differentiating equation (3.603) and equation (3.805) we get

$$S_n(\varepsilon) = \frac{M_1 + M_2}{M_1}\frac{1}{4\pi a_{TF}^2 Z_1 Z_2 e^2} S_n(E) \quad \ldots\ldots\ldots\ldots\ldots\ldots\ldots(3.807)$$

Substituting the equation (3.803) into equation (3.807) we get

$$\left.\frac{d\varepsilon}{d\rho_L}\right|_n \equiv S_n(\varepsilon) = \frac{1}{\varepsilon}\int_0^{\varepsilon} f(t^{1/2})dt^{1/2} \quad \ldots\ldots\ldots\ldots\ldots\ldots\ldots\ldots(3.808)$$

Substituting equation (3.704) into equation (3.808) we get

$$S_n(\varepsilon) = \frac{\lambda_m}{2(1-m)}\varepsilon^{1-2m} \quad \ldots\ldots\ldots\ldots\ldots\ldots\ldots\ldots\ldots\ldots\ldots\ldots(3.809)$$

The equation 3.809 is the equation of reduced nuclear cross section.

The above stopping cross section was calculated using the Thomas-Fermi screening function. A more accurate stopping cross section was however provided by Ziegler et.al [4] which is

$$S_n(\varepsilon) = \frac{0.5\ln(1+1.1383\varepsilon)}{\varepsilon + 0.01321\varepsilon^{0.21226} + 0.19593\varepsilon^{0.5}} \quad \text{.....(3.810)}$$

3.9 Electronic Stopping Power

The dominant mechanism of energy loss for helium ions at energies of 5-30 KeV (depending on the ion) is the electronic energy loss rather than the nuclear energy loss. This can also be termed as the inelastic energy loss because energy is transferred from the ion to the target electrons. The Figure 3.10 which shows the nuclear and electronic stopping power plotted as a function of beam energy demonstrates this point. The electronic stopping power is what determines the depth of penetration of the ions in the target while the nuclear stopping power determines the lateral distribution of ions in the target. The inelastic energy loss results in electron emission from solids. When the velocity of the ion is low (generally below 2 X 10^7 cm/sec) then the electron emission occurs due to the energy released during the neutralization of the ion, this is called Potential Electron Emission (PEE). At higher energies however the electrons are emitted from the solid directly due to the kinetic energy of the ion, this is called the Kinetic Electron Emission (KEE). At very high velocities corresponding to energies in the MeV range, the inelastic energy loss of ions can also generate X rays.

When velocity range of the ion is between $0.1\vartheta_0$ to $Z^{2/3}\vartheta_o$ the electronic energy loss is proportional to the ion velocity or $E^{1/2}$. However at ion velocities greater than $Z^{2/3}\vartheta_o$ the ion gets stripped of all its electrons and just acts as a positive nucleus. At these velocities the interactions can be described by a pure coulomb interaction potential. For an impulse approximation of interaction, the change in momentum is given by

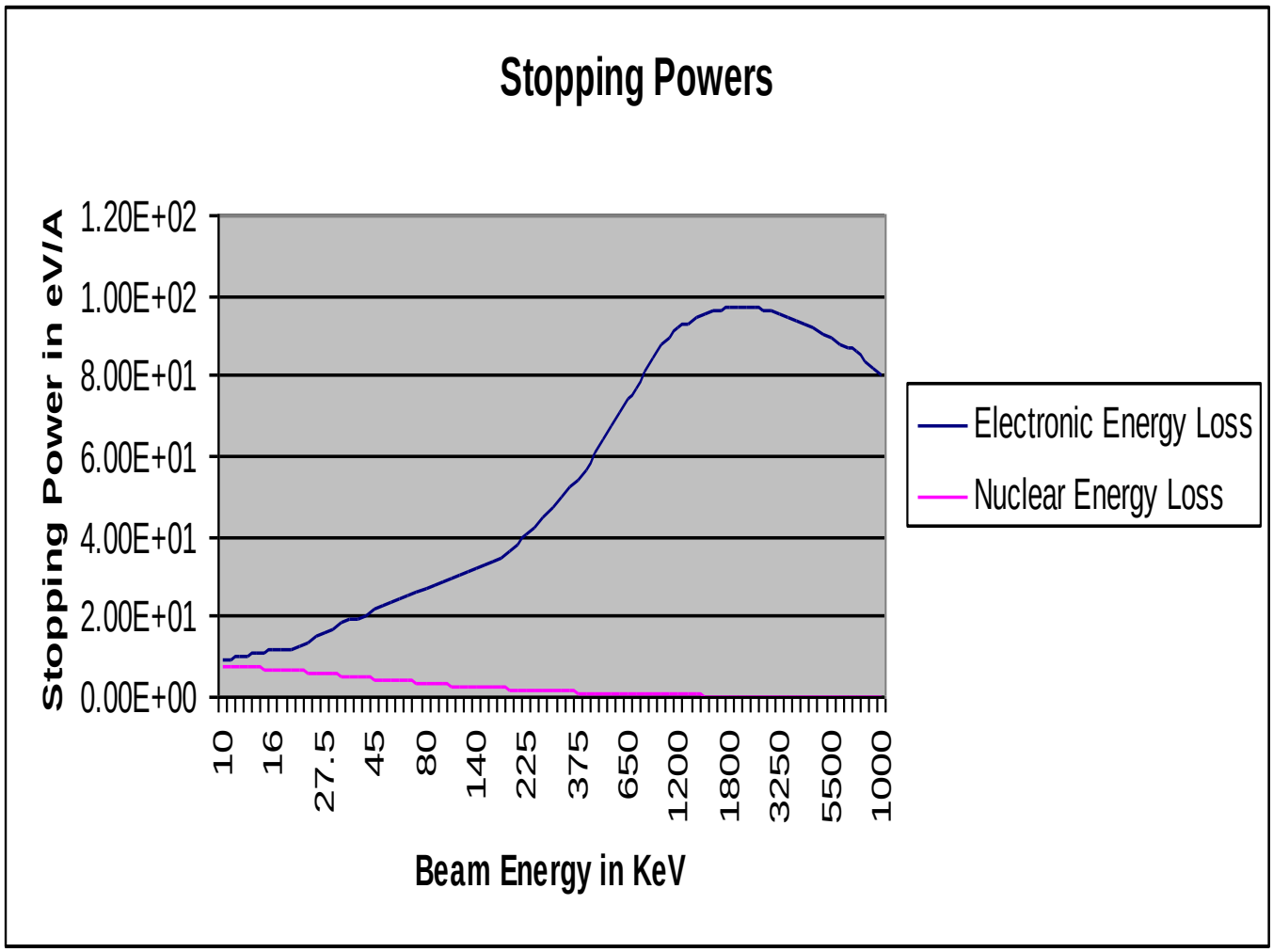

Figure 3.10 Showing the Stopping power of Boron on Silicon. Courtesy of SRIM [4]

$$\Delta p = \int_{-\infty}^{\infty} F_0 dt \quad \text{……(3.901)}$$

This can be expressed as

$$\Delta p = \frac{1}{v}\int_{-\infty}^{\infty} F_0 dx \quad \text{……(3.902)}$$

Where the force can be written as

$$F_0 = -\frac{dV(r)}{dy} \quad \text{……..(3.903)}$$

From Figure 3.11, the equation 3.903 can be further reduced to

$$F_0 = -\frac{dV(r)}{dy} = -\frac{dV\left(x^2 + b^2\right)^{1/2}}{db} \quad \text{……(3.904)}$$

For a purely Columbic potential

$$V(r) = \frac{Z_1 Z_2 e^2}{r} \quad \text{……(3.905)}$$

Or

$$V\left(x^2 + b^2\right)^{1/2} = \frac{Z_1 Z_2 e^2}{\left(x^2 + b^2\right)^{1/2}} \quad \text{…….(3.906)}$$

Differentiating the above equation gives us

$$-\frac{d}{db}\left(\frac{Z_1 Z_2 e^2}{\left(x^2 + b^2\right)^{1/2}}\right) = b\frac{Z_1 Z_2 e^2}{\left(x^2 + b^2\right)^{3/2}} \quad \text{…….(3.907)}$$

Inserting equation (3.907) into equation (3.902) we get

$$\Delta p = \frac{Z_1 Z_2 e^2}{\upsilon b}\int_{-\infty}^{\infty} \frac{b^2 dx}{\left(x^2 + b^2\right)^{3/2}} = \frac{2Z_1 Z_2 e^2}{\upsilon b} \quad \text{……(3.908)}$$

In case of energy transfer to a electron Z_2 will be 1, the electron kinetic energy transferred in the collision will be

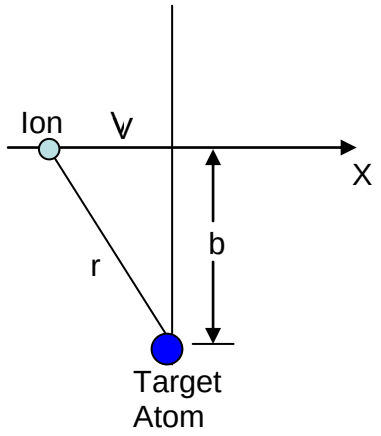

Figure 3.11 Showing the Variables schematically

$$T = \frac{\Delta p^2}{2m} = \frac{2Z_1^2 e^4}{b^2 m_e \upsilon} \quad \text{……(3.909)}$$

Where m_e is the electron mass.

The electronic energy loss per unit length is then given by

$$-\left.\frac{dE}{dx}\right|_e = n_e \int_{T_{\min}}^{T_M} T \frac{d\sigma(E)}{dT} dT \quad \text{……..(3.910)}$$

The equation 3.910 can be re-written as

$$-\left.\frac{dE}{dx}\right|_e = n_e \int_{b_{\min}}^{b_{\max}} T 2\pi b db \quad \text{……..(3.911)}$$

Substituting equation (3.909) into equation (3.911) we get

$$-\left.\frac{dE}{dx}\right|_e = \frac{4\pi Z_1^2 e^4 n_e}{m_e \upsilon^2} 1n \frac{b_{\max}}{b_{\min}} \quad \text{……(3.912)}$$

The value of $b_{\min}$ occurs when the ion collides head on with the electron. The velocity of the

electron is given by equation 3.316

$$v_2 = 2v_o \frac{M_c}{M_2} \cos\phi \quad \text{……(3.913)}$$

For head on collision ϕ is zero, hence

$$v_2 = 2v_o \frac{M_1 M_2}{M_2 (M_1 + M_2)} = 2v_o \frac{M_1}{(M_1 + M_2)} \quad \text{……(3.914)}$$

In the equation 3.914 since the M_2 is the mass of the electron and M_1 is the mass of the ion, M_2 can be neglected in the denominator. Hence equation 3.914 then becomes

$$v_2 = 2v_o \quad \text{……(3.915)}$$

In which case the energy transferred to the electron becomes

$$T_{\max} = \frac{m_e (2v_o)^2}{2} = 2m_e v_o^2 \quad \text{……..(3.916)}$$

Substituting this in equation 3.909 we get

$$b_{\min} = \frac{Z_1 e^2}{m_e v^2} \quad \text{……..(3.917)}$$

Similarly the value of $b_{\max}$ can be obtained by equating $T_{\min}$ to the average excitation of an electron I. Hence $b_{\max}$ is

$$b_{\max} = \frac{2Z_1 e^2}{(m_e v^2 I)^{1/2}} \quad \text{……(3.918)}$$

Substituting equation (3.917) and equation (3.918) into equation (3.912) we get

$$-\left.\frac{dE}{dx}\right|_e = \frac{2\pi Z_1 Z_2 e^4 n_e}{m_e v^2} \ln \frac{2m_e v^2}{I} \quad \text{…….(3.919)}$$

The equation (3.917) is due to the direct collision with the electrons and when the energy transfer

due to distant resonant energy transfer is considered then the equation (3.919) doubles itself and hence the electronic energy loss becomes

$$-\left.\frac{dE}{dx}\right|_e = \frac{4\pi Z_1 Z_2 e^4 n_e}{m_e \upsilon^2} 1n \frac{2m_e \upsilon^2}{I} \quad \text{……..(3.920)}$$

When the projectile ion velocity is lesser than the Bohr velocity the above stopping power is not accurate, at such low velocities it is convenient to use Lindhard-Scharff stopping cross-section, which is

$$S_e(E) = 3.83 \frac{Z_1^{7/6} Z_2}{\left(Z_1^{2/3} + Z_2^{2/3}\right)^{3/2}} \left(\frac{E}{M_1}\right)^{1/2} = K_L E^{1/2} \quad \text{……(3.921)}$$

This stopping cross section clearly demonstrates that the inelastic collisions are directly proportional to the ion velocity. The equation (3.921) can be expressed in the reduced notation as

$$S_e(\varepsilon) = \left(\frac{d\varepsilon}{d\rho}\right)_e = k\varepsilon^{1/2} \quad \text{…….(3.922)}$$

Where $$k = \frac{Z_1^{2/3} Z_2^{1/2} \left(1 + \frac{M_2}{M_1}\right)^{3/2}}{12.6 \left(Z_1^{2/3} + Z_2^{2/3}\right)^{3/4} M_2^{1/2}} \quad \text{…….(3.923)}$$

To conclude that in the case of ion interaction with solids both the elastic energy loss (or quasi-elastic energy loss) and the inelastic energy loss should be accounted separately. While in the case of electron interaction the Bethe energy loss equation accounts for all the energy losses that occur due to which it is also called Continuous Slowing Down Approximation (CSDA). For ions the Nuclear energy loss equation given by Ziegler et.al [4] is accurate, and for electronic energy loss at very high energies the equation given by Bethe theory is used while for low velocities it is more accurate to use the electronic stopping power given by Lindhard-Scharff [8].

4. Review of Ion Induced Secondary Electron

4.1 Introduction

When a target surface is bombarded by energetic particles (electrons, ions, neutrals) an inevitable result is the production of secondary electrons (SE). Ion induced secondary electron (iSE) emission was first observed by Villard [46] and pre-dated the discovery of electron induced secondary electron (eSE) by Austin and Stark [45]. The first applications of eSE was in electron multipliers where a single electron incident on metals produced many electrons, the electrons that are emitted can then further create more SE's producing a signal gain of as high as 10^8. Although the secondary electrons are emitted from the entire volume of the particle interaction (which can be in micrometers depending on the energy of the beam), only the SE that are created with 5 – 10 nm from the target surface can escape out from the specimen into vacuum. This feature of SE (or eSE) that is it is very surface sensitive is made use of in the SEM, and the study of eSE has been of great importance in the SEM.

The study of iSE began with the growth of atomic collision physics because the ejection of iSE's are of great importance in regard with the Plasma-wall interactions in the thermonuclear fusion reactors. The renewed interest in iSE began with the development of the Focused Ion Microscope (FIM) and Focused Ion Beam (FIB) which were used to image and manipulate materials in the nanometer scale.

4.2 Electron induced SE (eSE)

When the energy distribution of electrons emitted from a sample in a SEM is measured over the range from the incident beam energy down to 0 KeV, a profile of the type shown in Figure 4.01 is obtained. Most of the energy distribution is dominated by the high and medium energy electrons shown as regions III and II. These are the backscattered electrons (BSE), which is the net cumulative effects of elastic scattering of the incident electron (also called Primary Electron) becomes greater than 90º that it exits out of the surface. When the region II in the graph is extrapolated to zero energy the energy falls smoothly to zero as expected , however at very low energies of the order of a few tens of eV the number of electrons emitted increases sharply [1] which is represented by the region I in the Figure 4.01. These are called the secondary electrons (SE or eSE) are differentiated from BSE's based on their kinetic energy. Conventionally electrons emitted with energy less than 50 eV are considered as SE's and all the rest as BSE. Although this is most accepted definition of an eSE, it may be different depending on the context. For example in describing the electron-solid interaction, electrons excited from the sample as a result of inelastic scattering are called secondary electrons, some of these electrons can have energies in the KeV region.

The eSE's emitted from the specimen is narrow and peaked at 2-5 eV , with 90% of eSE's having energies below 10 eV[1]. For most materials the maximum eSE yield is between 1 – 1.7, comprehensive list is collected by Joy [51]. Also the eSE curve for all materials follow the universal yield curve as shown in Figure 4.02 and Figure 4.03 where the yield rises from zero and reaches a maximum δ^m at some energy E_{PE}^{m} which is generally about 1 KeV, and then it falls monotonically as $1/E_{PE}$.

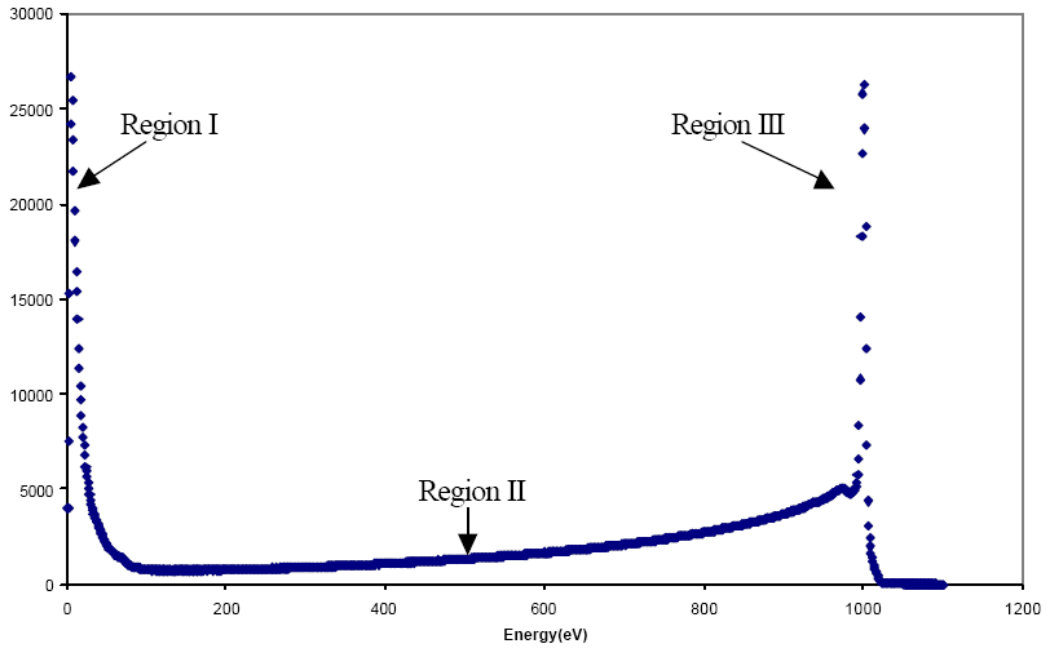

Figure 4.01 Showing Energy spectra by 1 KeV electrons on Gold. Courtesy of Satya Prasad [50]

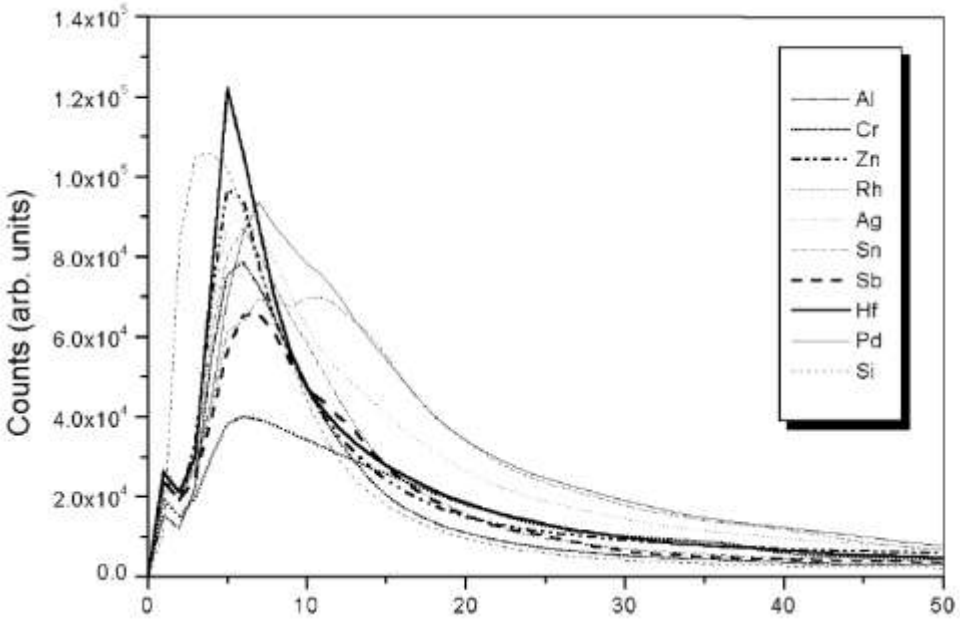

Figure 4.02 Showing Number of SE N(E) from ten elements recorded at 1 KeV. Courtesy of Satya Prasad [50]

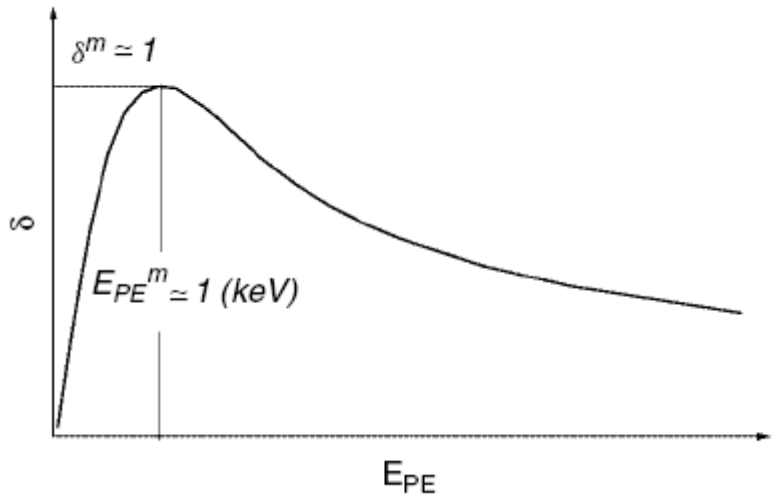

Figure 4.03 Showing universal yield curve of eSE's .

Courtesy of Yinghong Lin [28]

4.3 Ion induced SE (iSE)

Even though in case of eSE, the projectile is always an electron, an examination of eSE yield data published over the last 100 years, shows that the level of agreement between different data sets is rarely better than 25% and often shows divergences of greater than 100% [28]. In the case of iSE's it becomes even more complicated because the projectile can be any ion of any element from the periodic table, and each ion itself can have multiple charge states. An ion impinging on a target surface has a potential energy which is the energy of ionization of the ion and kinetic energy due to its velocity. Both the Potential energy of the ion and the Kinetic energy of the ion are capable of ejecting electron, these two processes are known as Potential Electron Emission (PEE) and Kinetic Electron Emission (KEE) which are schematically shown in Figure 4.04.
In all studies of iSE by various authors Kishinevskii et al [52,53], Baragoila et al [16,31,33,47], Toglhofer et al [48] , Ohya[54,55,22] it has always been considered that these two processes PEE

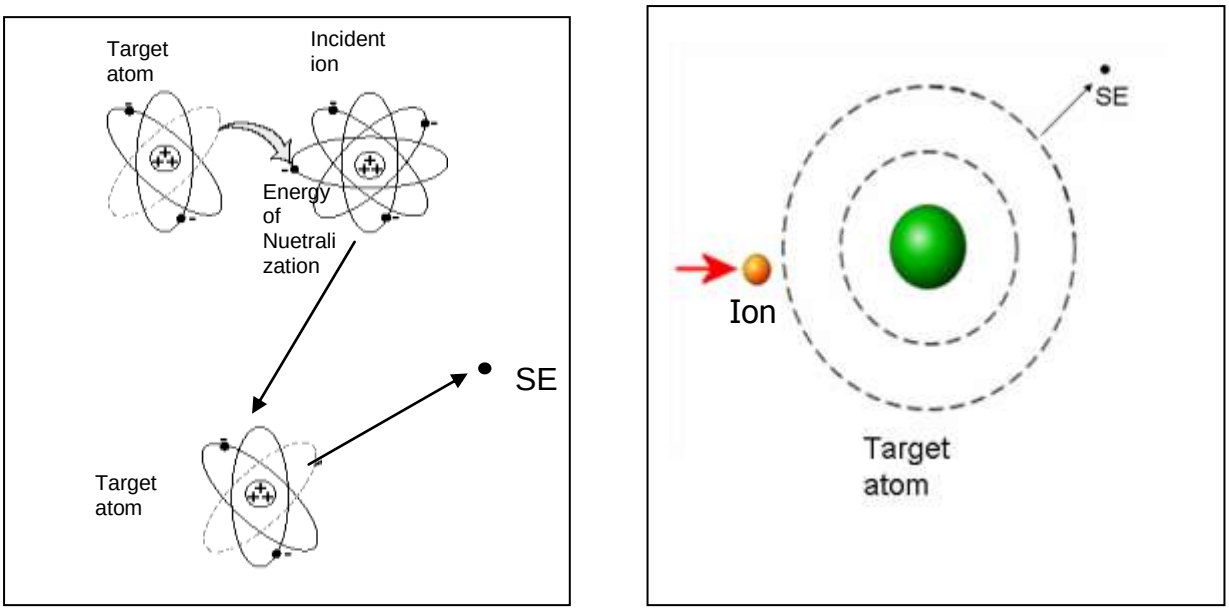

Potential Electron Emission (PEE)

Kinetic Electron Emission (KEE)

Figure 4.04 Showing the Ion induced Secondary Electron (iSE) Mechanisms

and KEE are independent of each other. It has also been agreed that PEE dominates the electron emission at low particle velocities while the KEE dominates at higher particle velocities.

4.4 Potential Electron Emission (PEE)

When the ionization energy of the incident particle exceeds twice the work function, then neutralization of the ion can result in the formation and subsequent release of free electrons in a Auger like mechanism, which is termed as Potential Energy Electrons (PEE) emission. Kishinevskii et al [52,53] used the semi-phenomenological approach of Hagstrum to derive a yield equation for PEE. In this model the PEE yield is given by:

$$\gamma = \int_0^{\infty} N_o(E_K)\,dE_K = \int_{\varepsilon_0}^{\infty} N_i(\varepsilon_K)\,P_e(\varepsilon_K)\,d\varepsilon_K \quad \text{.....(4.401)}$$

where $N_o(E_K)$ and $N_i(\varepsilon_K)$ is the energy distributions of Auger electrons outside and with in the metal respectively, and $P_e(\varepsilon_K)$ is the probability function. Then using many assumptions and simplifications they obtained the PEE yield equations as

$$\gamma_P = \frac{0.2}{\varepsilon_F}(0.8E_i - 2\varphi) \quad \text{.....(4.402)}$$

where ε_F is the Fermi Energy, E_i is the energy of neutralization and φ the work function of the target. This yield equation fits data well when $3\varphi < E_i < 2(\varepsilon_F + \varphi)$.

Equation 4.402 is similar to one proposed by Hagstrum [61]

$$\gamma_P = 0.032(0.78E_i - 2\varphi) \quad \text{.....(4.403)}$$

Baragoila et al [61] plotted the experimental PEE yield values as a function of $0.78E_i - 2\varphi$ for many ions and the yield resembles equation 4.403 very closely as shown in Figure 4.05. Petrov [48] calculated PEE yields for many types of ions incident on Cu using a technique that is discussed in more detail in section 4.8, his yield data is presented in Figure 4.06. Wang et al [62] performed very interesting experiments to find out the true PEE yield. They measured the total electron yield at a given energy for the same projectile but of different charge states q. They then plotted the total SE yield as a function of the potential energy (or energy of ionization) of the ion, and they obtained straight line fits as shown in Figure 4.07 (a). Expressing this yield as a straight line equation they obtained

$$\gamma_T = \gamma_{KE} + kW_q \quad \text{.....(4.404)}$$

where γ_{KE} is the intercept of the line. And γ_{PE} can be obtained as

$$\gamma_{PE} = kW_q \quad \text{.....(4.405)}$$

The proportionality constant k depends on the ion velocity. The graphs they obtain for pure PEE yields is shown in 4.07 (b). They also found out that with increase in ion energy PEE decreased, the decrease in PEE was more pronounced for the ions having higher charge states. Nishimura et al [63] showed experimentally that PEE from Ar^+ impact is lesser than for He^+ ion because the ionization energy of Ar^+ is lesser. Ruano et al [59] elaborates the point made by Nishimura, in his experimental data shown in Figure 4.08 he points out that the width of emission spectra in case of He^+ ions incident on Cu in the low energy region 1 -2 KeV is more than that of Li^+, Ne^+, Ar^+ because of higher Auger emission.

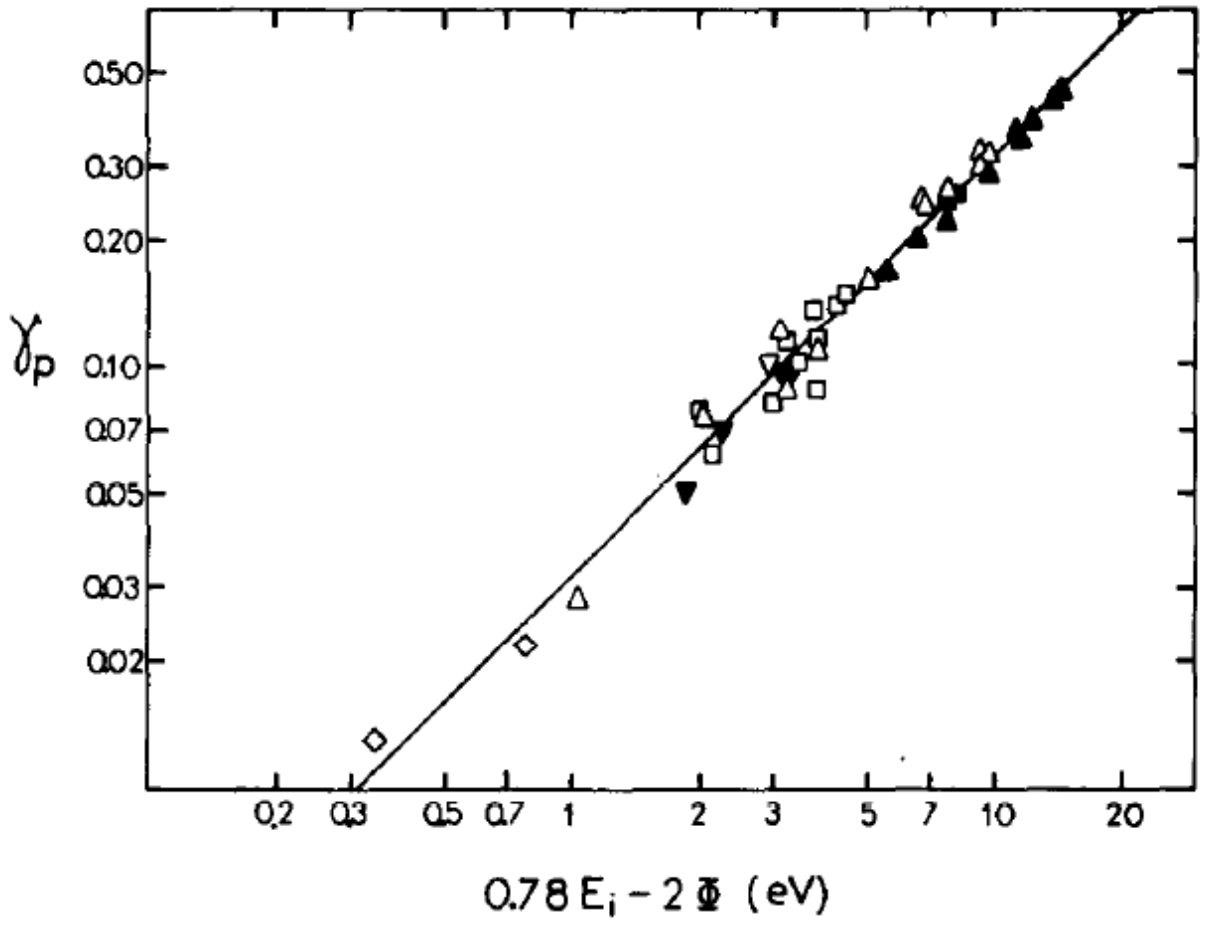

Figure 4.05 Showing the PEE yield fit closely to the yield equation proposed by Hagstrum. The values (▲, △) is from Arifov for Ne^+ and Ar^+ ions respectively and (●, ▽, ▼, ◇, ■) is from Hagstrum for He^+ , Ne^+, Kr^+ and Xe^+ ions respectively. The Plot is courtesy of Baragiola et al [61]

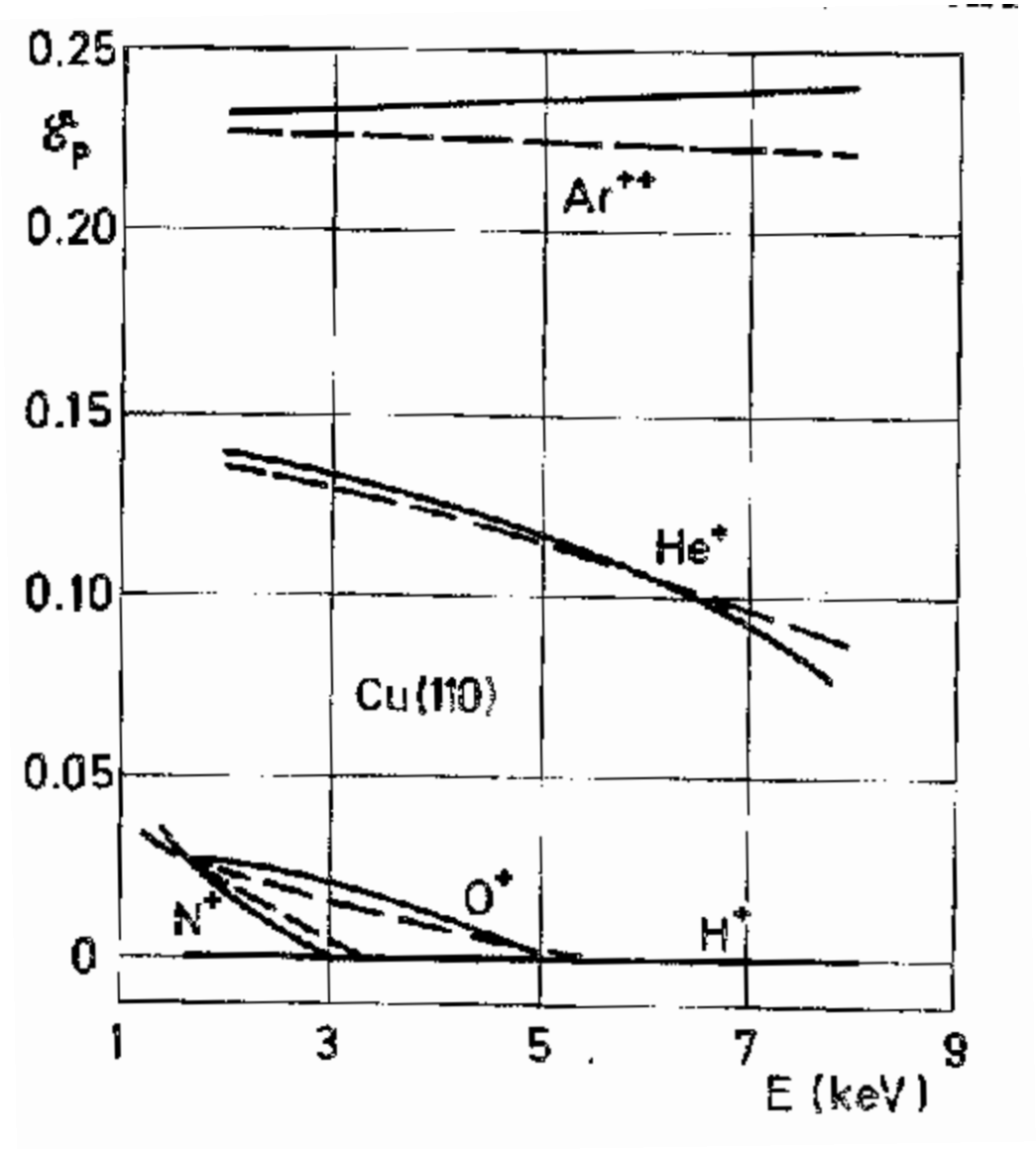

Figure 4.06 Showing the PEE versus Energy E for Ar^{++}, He^+, N^+, O^+ and H^+ On monocrystalline copper Cu(110). Courtesy of Petrov [48]

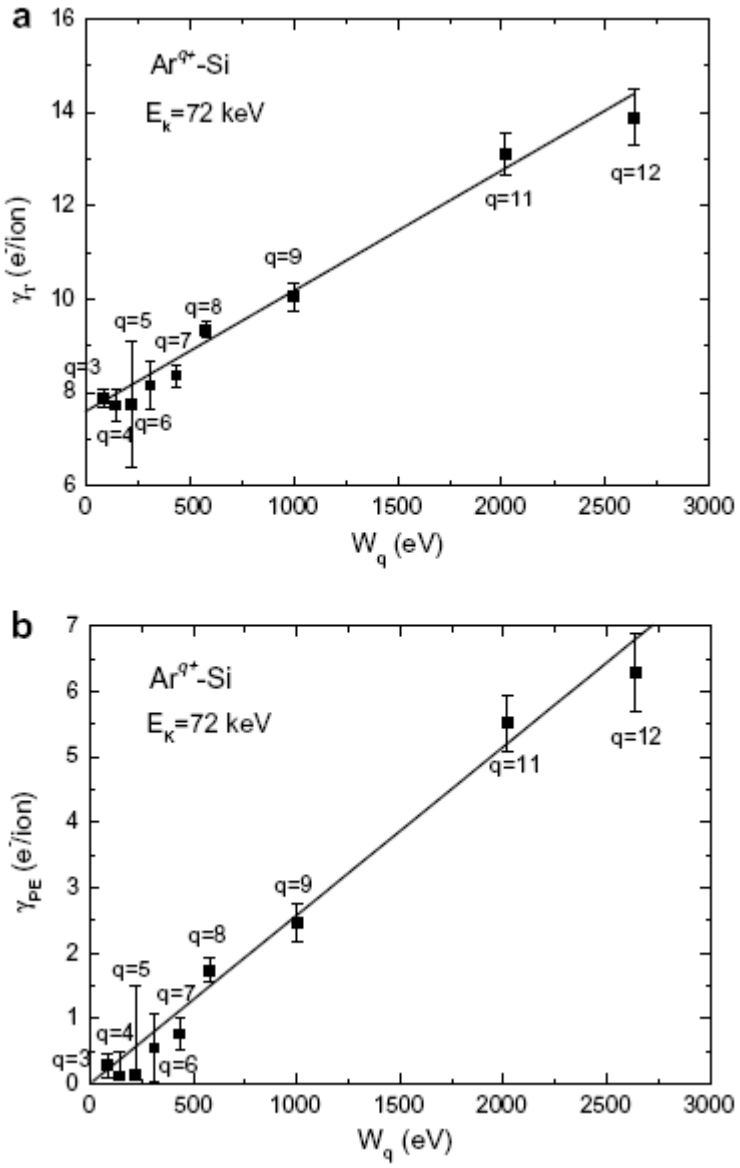

Figure 4.07 Showing the Total SE yield (Figure (a)) and the true PEE Yield (Figure (a)) as a function of potential energy of the ion.

Courtesy of Wang et al [62]

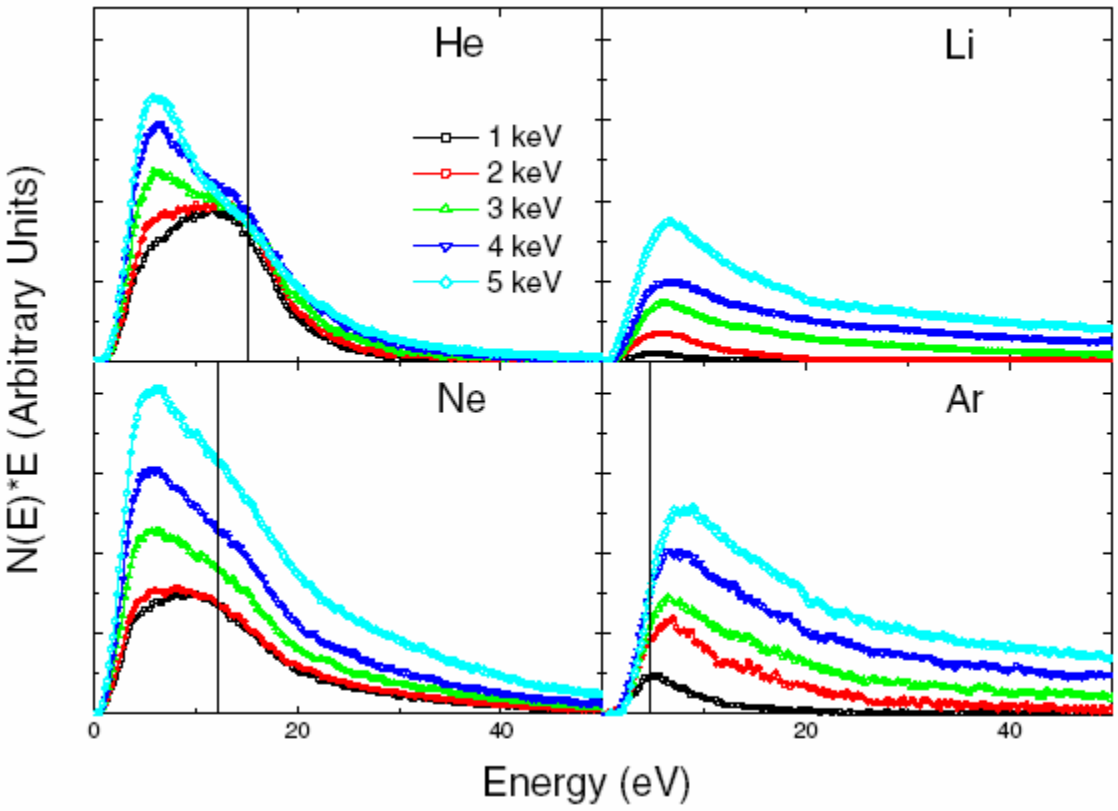

Figure 4.08 Showing the iSE spectra for different ions incident on copper at low energies. Courtesy of Ruano et al [59]

4.5 Threshold Velocities for PEE and KEE

There has been considerable interest in knowing the energy range in which the two mechanisms of iSE production dominate. As the name suggests KEE should dominate when the kinetic energy of the ion is high i.e. at higher velocities of the beam. Because particular ion with a specific charge always comes with constant potential energy (the energy of ionization of the ion), it may be assumed that PEE may be a constant. Although this is not true, with increasing energy the KEE yield rises rapidly but there is a marginal decrease in PEE, so the KEE yield completely overshadows the effect of PEE. The reason for the decrease in PEE yields with energy is that at higher velocities the ion gets less time to neutralize (which has to occur just before the ion enters the target or in the top surface layers of the target). Kishinevskii et al [52,53] suggested that PEE starts to lose dominance in iSE yield at velocities of 6-7 X 10^7 cm/sec, but most experimental work suggests much lower threshold energies. Baragoila et al [16,31,33,47] calculated the threshold for KEE by assuming that at very low energies where the KEE threshold starts, the KEE electrons that will be emitted from the target are the free electrons. They considered the maximum energy that could be transferred to an electron gas is

$$T_m = 2m_e v(v + v_F) \quad \text{.....(4.501)}$$

Where m_e is the mass of the electron and v, v_F are the projectile ion velocity and Fermi velocity of the target electrons. The threshold velocity v_u can be calculated from re-arranging equation 4.501 as

$$v_u = \frac{1}{2} v_F \left(1 + 2\phi / m v_F^2\right)^{1/2} - 1 \quad \text{.....(4.502)}$$

From equation 4.502 they calculate the threshold velocity for KEE from Aluminum target to be 1.75 x 10^7 cm/sec (~ 0.64 KeV for He ions). The authors also say that since the valence electrons are not really free, their exchange of momentum with the lattice during excitation will cause T_m to be larger than equation 4.501 and the v_u to be slightly smaller than equation 4.502. However their equation seems to be in good agreement with experimental results.

Petrov [48] agrees that the threshold for KEE for He^+ is about 0.4 KeV but for all other noble gas ions it is greater than 1 KeV. He further explains that although there is a clear demarcation in case of metals as to where the KEE begins, the same does not hold true for semiconductors and insulators. Figure 4.09 shows insulator KBR (001) being bombarded by both K^+ and Ar^+, noting that K^+ are incapable of ejecting PEE. This Figure 4.09 also shows Ar^+ incident on polycrystalline Mo, where the emission is only due to PEE.

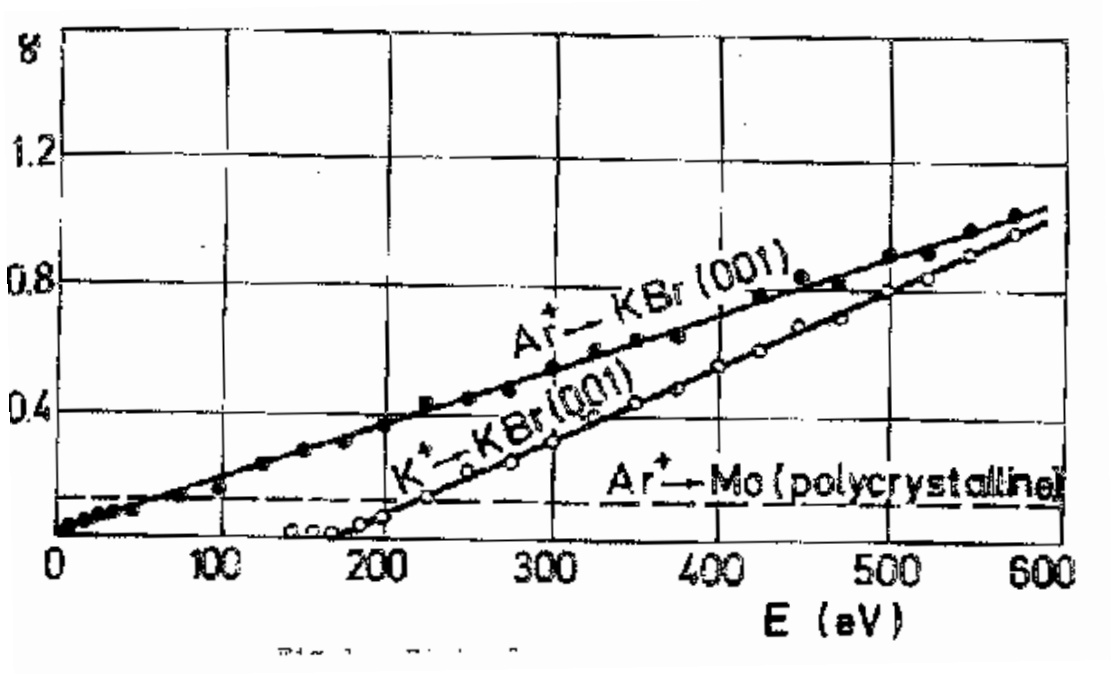

Figure 4.09 Showing the SE yield at very low energies for KBR and Mo. Courtesy of Petrov[48]

As can be seen for this case of Ar^+ bombarding Mo the SE yield $\gamma = \gamma_{PEE} = constant$ for the energies shown. This is region of constant γ_{PEE} is absent in case of Ar^+ bombarding KBR. The author assumes that this behavior in the case of insulators is due to the peculiarity of their electronic band structure which causes a low probability of electronic exchange between the target and incident ions. Hence the ions are not neutralized prior to impact on the insulators as is the general case with metals.

Toglhofer et al [49] used emission statistics experiments to investigate the threshold energy for KEE onset. In his interesting experimental set up he used ion fluxes below 10^3 ions/sec so as to avoid pile up effects of the emission. The author cites that PEE processes last not longer than 10^{-13} sec and that of KEE lasts for about 10^{-12}- 10^{-11} sec. Since all the emitted electrons will reach the detector with in 10^{-9} sec, the total energy of a group of n electrons ejected due to impact of a single particle will cause one single detector pulse. The author then runs the experiment any times for a particular ions with a specific energy and finds out the probability W of the ions able to eject 0,1,2…electrons at that energy. The total electron yield can be found out as the sum of probabilities as shown

$$\gamma = \sum_{n=1}^{\infty} n W_n \quad \text{.....(4.503)}$$

Where

$$\sum_{n=0}^{\infty} W_n = 1 \quad \text{.....(4.504)}$$

This is shown in Figure 4.10 which shows the probabilities W_n of electron emission due to bombardment of He^+ on Au. The author argues that PEE involves well defined

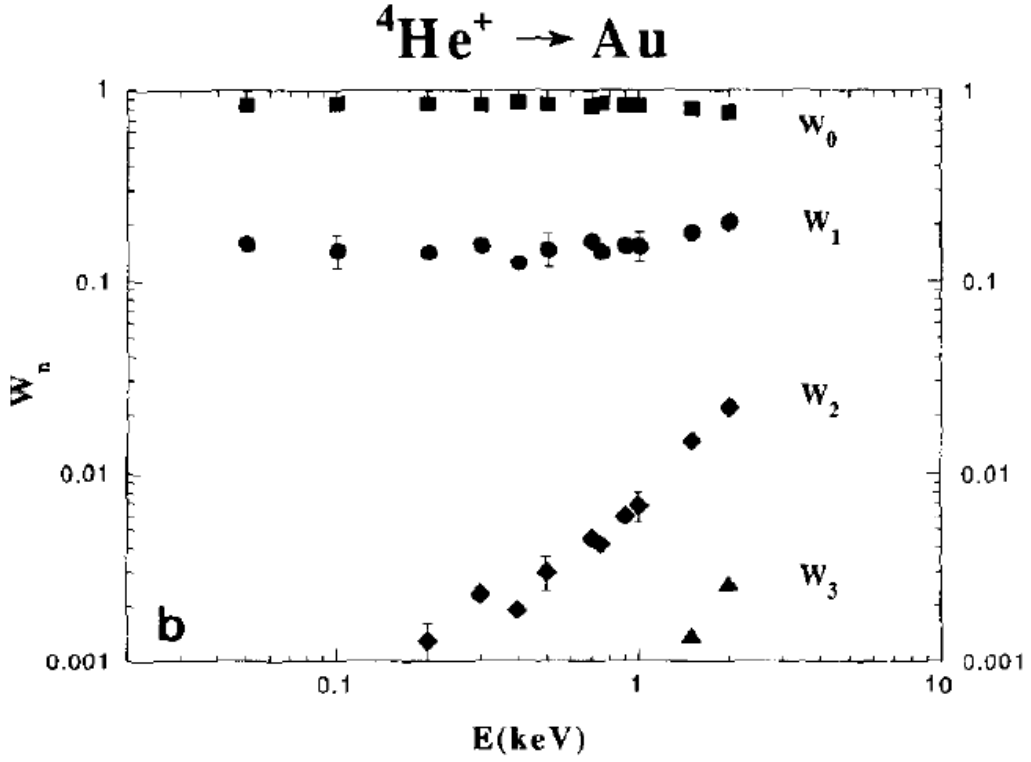

Figure 4.10 Showing the Probability of electron emission statistics for He^+ on Au. Courtesy of Toglhofer[49]

transitions between the projectile and the target surface and hence can emit a well defined number of electrons only. In comparison KEE involves energy transfer between the projectile and large number of the target electrons, which have a chance of being ejected out. The potential energy carried by a singly charged ion is transferred by Auger type electronic transitions to one single electron only, the exception however being He^+ which carries sufficient potential energy to release more than one Auger electron. The author then uses the experimentally calculated probability of emission to filter out the PEE and KEE components from the total electron yield by the following equation

$$W_n = \sum_{i=0}^{n} P_i K_{n-1} \quad \ldots\ldots\ldots\ldots\ldots\ldots\ldots\ldots (4.505)$$

When P_n and K_n are individual probabilities for emisiion of n electrons by PEE and KEE respectively. With the further assumption that $P_n = 0$ for $n \geq 2$ and $K_n = 0$ for $W_{n+1} = 0$. With these the author splits the observed yields into PEE and KEE as shown in Figure 4.11 and 4.12 for He^+ and Ar^+ on Au. As can be seen for He^+ on Au, KEE yields starts to dominate the PEE yield at about 1 KeV, it can be assumed in this case that PEE yield is negligible at energies greater than 5 KeV.

4.6 KEE due to primary and backscattered ions

As previously discussed KEE arises due to the kinetic energy transfer to electrons of the target surface by the impinging ions. The ion may directly impart energy to the target electron or it may impart energy to the target atom which may recoil and subsequently emit electrons in due course as shown in Figure 4.13. The electronic stopping power is responsible for the former type of

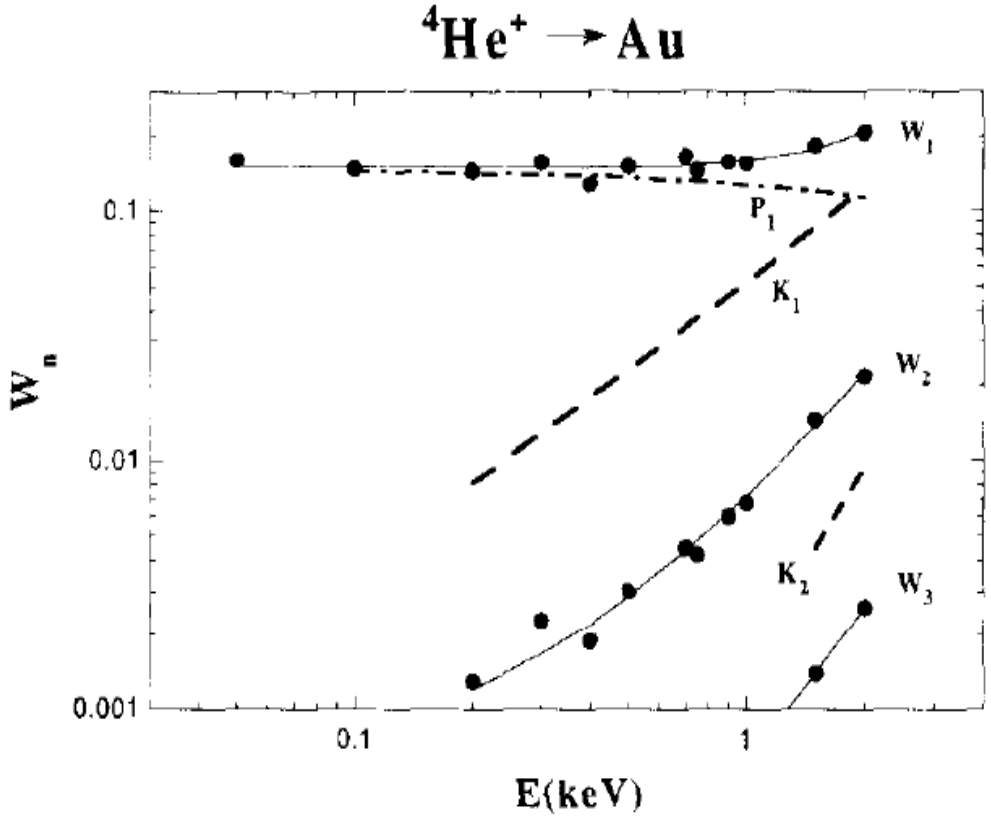

Figure 4.11 Showing the Relative contribution of KEE (K_n) and PEE (P_1) for He^+ on Au. Courtesy of Toglhofer[49]

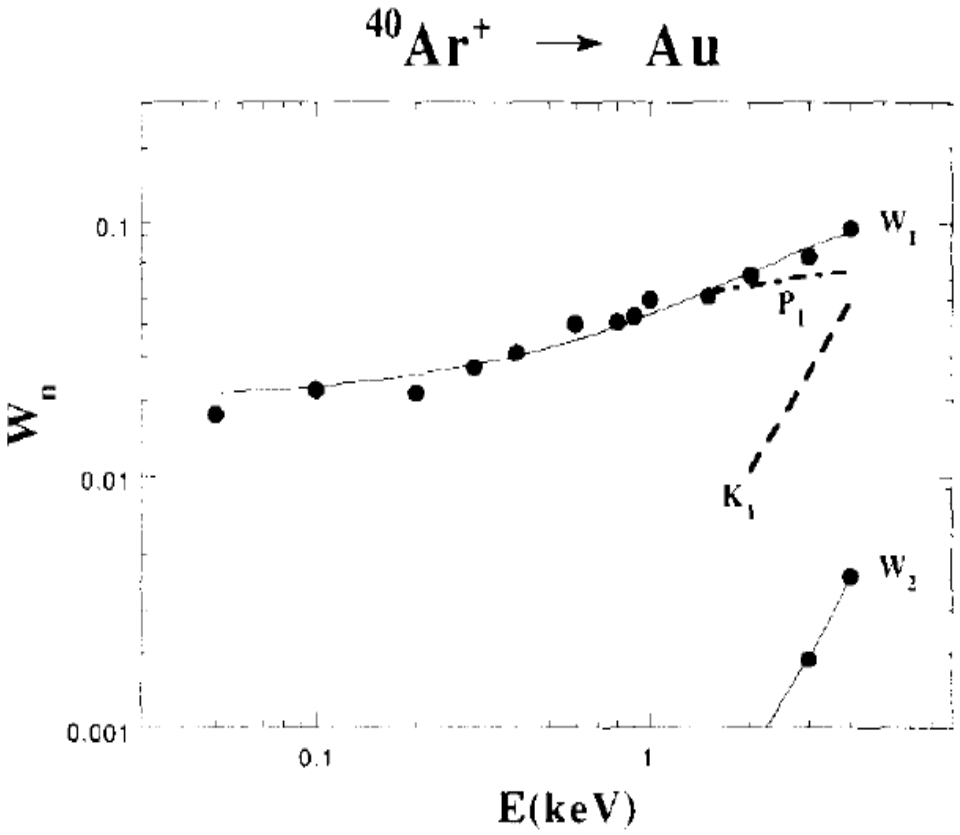

Figure 4.12 Showing the Relative contribution of KEE (K_n) and PEE (P_1) for Ar^+ on Au. Courtesy of Toglhofer[49]

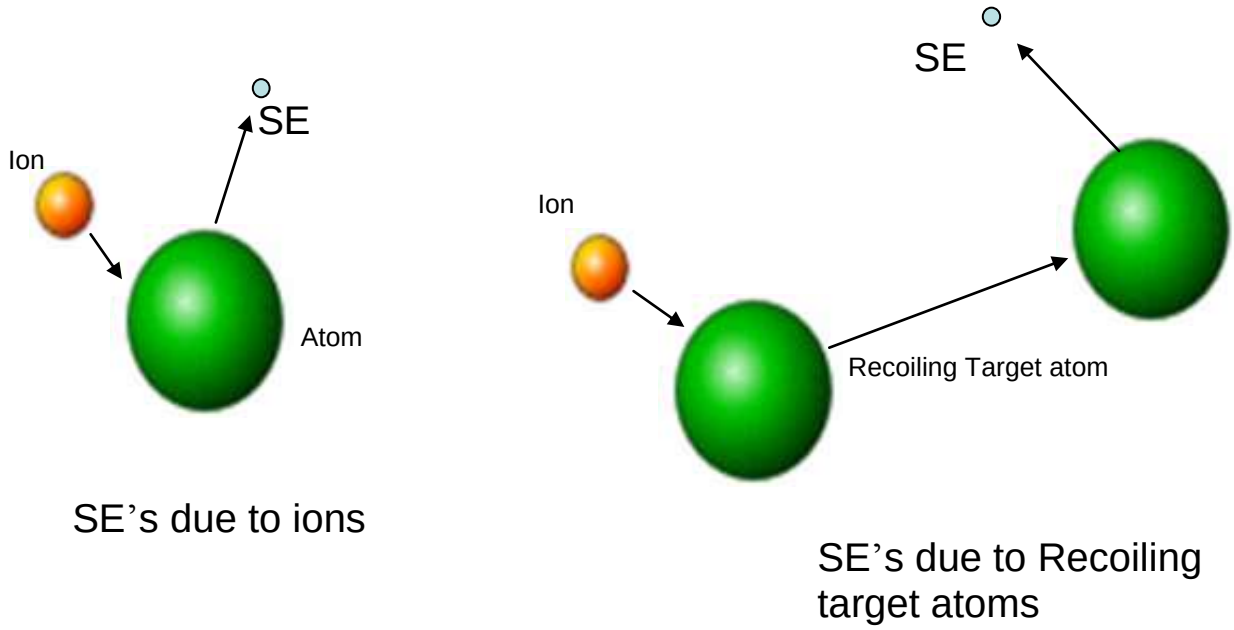

Figure 4.13 Showing the Mechanism of Kinetic Electron Emission (KEE)

electron emission and nuclear stopping power for latter type of electron emission. In this section direct inelastic collisions of ions with electrons will be discussed, the contribution of recoiling target atoms will be discussed in subsequent sections. Kishinevskii et al [52,53] proposed that emission of electrons can happen only due to the promotion of core bound electrons to conduction band, and subsequent release of a electron in a Auger type emission.

The cross section for ejection of electrons into conduction band is then

$$\sigma(u_o) = \frac{1.39 a_o \hbar}{J}\left(\frac{Z_1 + Z_2}{\sqrt{Z_1} + \sqrt{Z_2}}\right)^2 S(u_o) \qquad \text{.....(4.601)}$$

Where u_o is the relative velocity of the colliding atoms, and $S(u_o)$ is given by

$$S(u_o) = 5.25 u_o \arctan 0.6 * 10^{-7}(u_o - u_{\min}) \qquad \text{.....(4.602)}$$

where $u_{\min}$ is the threshold for KEE which is 0.6 -0.7 x 10^7 cm/sec. The electron yield they calculated as

$$\gamma = \int_0^{x_n} \sigma(\bar{W}(\delta)\bar{N}) e^{\frac{-x}{\lambda}} dx \qquad \text{.....(4.603)}$$

where x_n is the depth up to which the ion retains its ability to ionize, and $W(\delta)$ is the probability function given by

$$W(\delta) = 0.016(\delta - 2\phi) \qquad \text{.....(4.604)}$$

Where ϕ is the work function and δ the depth of the filled band. The limitation in this theory is that the authors assume that the entire electronic stopping power is used in the excitation of core electrons, and completely neglects the influence of valence electrons on the stopping power. Their theory may hold true to a reasonable extent but only for heavier ions in heavy targets

because a slow ion moving through a solid creates a strong perturbation around it, which causes the collision to resemble those occurring between free atoms in the gas phase. As shown by various other authors, for targets of light elements there is no proportionality between inner shell excitation cross-sections and electron emission yields. It was shown by Alonso et al [40] that for elements like Al a simple binary model involving free valence electrons was more consistent with experiment.

Ghosh and Khare [56] suggested that internal secondaries are produced by ionization of metal atoms just like in gas phase collisions. They then calculated the escape of internal secondaries from the metal based on transport theory. They calculated secondary electron emission coefficient γ as

$$\gamma_e = 0.5N\sum_{nl} Q_{nl}\left[1/\alpha - e^{-\alpha l}/\alpha\right] \quad \text{.....(4.605)}$$

Where N is the atomic density of the target, Q_{nl} is the Bethe ionization cross section of the nl shell, α is the absorption coefficient and l the range of the ion inside the metal. This theory does not include excitation of inner shell electrons and ignores the cascading of electrons. Also they have compared their theory with experimental values available only for hydrogen ion and atoms and only for Al and brass targets.

The theory provided by Sternglass [18] is widely accepted especially for SE production by high speed light ions. He proposed that the energy by an ion is lost in two ways. Firstly, when the ion produces small perturbations in the target material, this causes a distant collision between the ion and atomic electrons causing release of slow electrons which he called secondaries. The second type of event was a close collision in like a nearly free type of collision releasing high energy

electrons which he called δ rays, which is referred in literature as fast secondary electrons (FSE) [71]. He also mentions that for high speed light ions δ rays will be less and will generally be created below the region of SE escape depth. Using the inelastic scattering cross sections of electrons and diffusion theory to calculate the probability of escape of electrons, which is

$$P(x) = \tau A \exp\left(-x/L_s\right) \quad \ldots\ldots\ldots\ldots\ldots\ldots\ldots\ldots\ldots\ldots(4.606)$$

Where τ is the surface transmission coefficient and A is a constant determined by velocity distribution of the SE's, it is usually about 0.6.The variable L_s is dependent on mean free path for inelastic collisions but also on the mean free path for absorption, and from diffusion theory can be written as

$$L_s = \left(\frac{1}{3}\lambda_{sa}\lambda_{SC}\right)^{1/3} \quad \ldots\ldots\ldots\ldots\ldots\ldots\ldots\ldots\ldots\ldots\ldots\ldots(4.607)$$

where λ_{sa} is the mean free path for absorption, which can be set as $n_c\lambda_{SC}$, and n_c is the number of collisions required before the SE loses it's ability to escape, typically about 2 - 5.

The number SE yield per unit length is then

$$n_{se}(\phi_i, x) = n_{se}(\phi_i, x) + n_{se}(\phi_i, x) \quad \ldots\ldots\ldots\ldots\ldots\ldots\ldots\ldots\ldots\ldots(4.608)$$

where $n_{se}(\phi_i, x)$ is the slow secondaries given by

$$n_{se}(\phi_i, x) = \frac{1}{E_o}\left\langle \frac{dE_i}{dx} \right\rangle_{Av}^{1} \quad \ldots\ldots\ldots\ldots\ldots\ldots\ldots\ldots\ldots\ldots\ldots\ldots(4.609)$$

where $\left\langle \frac{dE_i}{dx} \right\rangle_{Av}^{1}$ is the mean energy spent in production of slow secondaries. And E_o is mean energy loss per secondary formed and $n_{se}(\phi_i, x)$ is the production of δ rays

$$n_{se}(\phi_i, x) = f(\phi_i, x)\frac{1}{E_o}\left\langle \frac{dE_i}{dx} \right\rangle_{Av}^{2} \quad \ldots\ldots\ldots\ldots\ldots\ldots\ldots\ldots\ldots(4.610)$$

The total secondary yield is then given by

$$n = \int_0^{x_n} n_{se}(\phi_i, x)\, P(x)\, dx \quad \ldots\ldots\ldots\ldots\ldots\ldots\ldots\ldots\ldots\ldots..(4.611)$$

Substituting various parameters into equation 4.611 and simplifying it for high energy regions leads to

$$n = 440\left(\frac{\tau A}{E_0 \alpha'}\right) z_i^{\,2} E_{eq}^{-\frac{1}{2}} \quad \ldots\ldots\ldots\ldots\ldots\ldots\ldots\ldots(4.612)$$

Where E_{eq} is (m/M)E ,m being the electron mass, M the ion mass. Sternglass concludes that the parameters τ , A , E_0 , α' in the yield equation 4.612 are not influenced by the atomic number of the target, work function, Fermi energy, crystal structure or density of free electrons. Hence the yield for a given ion charge and velocity should be essentially same in all metals. However experimental results show that SE yield is a strong function of atomic number and also of crystal structure because ions have a tendency to channeling in preferred crystallographic orientation.

Schou [14] considered secondary electron emission from solids under both electron and proton bombardments. All electron emission involved three steps, first the primary ionization by the bombarding particle as well as secondary ionization by energetic secondary electrons. Secondly migration of some of the liberated electrons to the surface and lastly escape of these electrons through the potential barrier at the surface. He assumed that since these steps were common to both electron and ion bombardment, they both can be expressed by a single semi empirical formula. The semi empirical formula deduced by him is

$$\delta = \frac{c_1}{4}\frac{\lambda}{W}\left|\frac{dE}{dx}\right|_e \quad \text{.....(4.613)}$$

where c_1 is a constant that depends on the parameters like Fermi energy, work function etc of the target, W is the average energy required to create an electron-ion pair, and λ is the escape length of SE given by

$$\lambda_i(E_0) = A_i \Big/ \left(E_0 - E_F\right)^2 + B_i\sqrt{E_0 - E_F} \quad \text{.....(4.614)}$$

where A_i and B_i are constants. Schou just compares this theory with experimental data for electrons and protons, for which his theory may have worked because the SE yield for both electrons and protons are comparable usually between 0.6 – 1.6 although the maximum SE yield occurs at different energies in case of electron bombardment about 1 KeV and in case of proton it is about 100 KeV. It remains to be demonstrated if his theory works for those heavier ions which can produce SE yields greater than 3.

Hasselkamp et al [34] performed very careful experiments to measure the SE yields for a variety of projectiles like hydrogen, deuterium, tritium , helium and Argon ions , their results are shown in Figures 4.14,4.15 and 4.16.They used a Van de Graaf generator to deliver the ions, and the target was kept in UHV, at a pressure of 1 - 2 X 10^{-8} Pa. They used an ion current of 50 – 500 nA and a beam diameter of 1.5mm, and took extreme care to avoid contamination and residual gases in the chamber. Hasselkemp was one of the first to show that iSE yield did not increase monotonically with atomic number of the target but showed oscillatory behavior. He also pointed out that the oscillatory effects varied slightly with the projectile used. In the particular period the maximum iSE yield occurred for Au in case of H^+ and He^+ ions , where as the maximum occurred for Pt in case of Ar^+ ions. Their data also shows the generally accepted behavior of

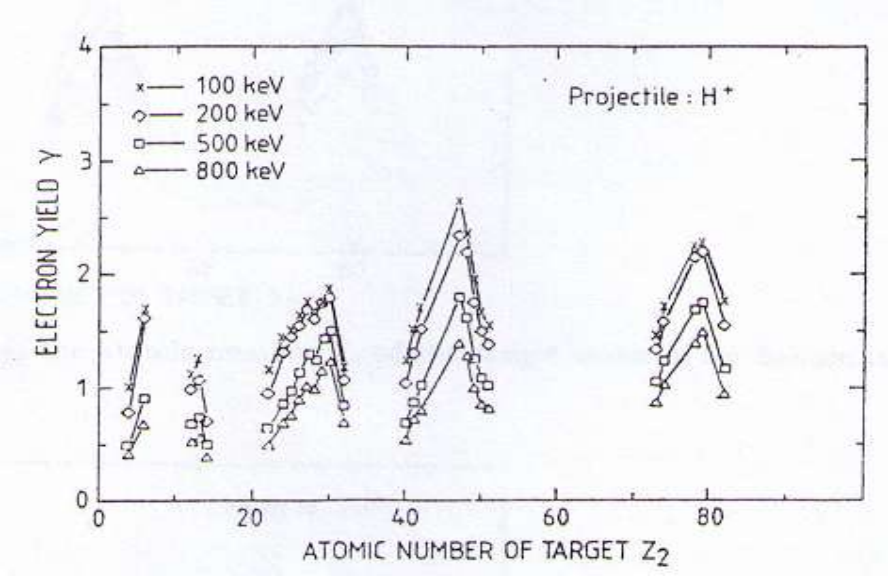

Figure 4.14 showing the iSE yields for proton impacts on targets with Different atomic number. Courtesy of Hasselkamp et al [34]

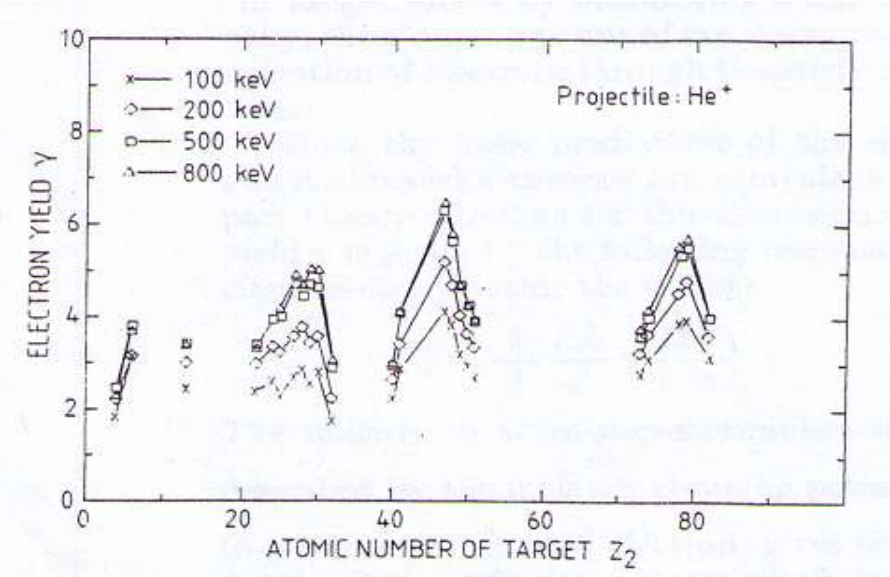

Figure 4.15 Showing the iSE yields for helium impacts on targets with Different atomic number. Courtesy of Hasselkamp et al [34]

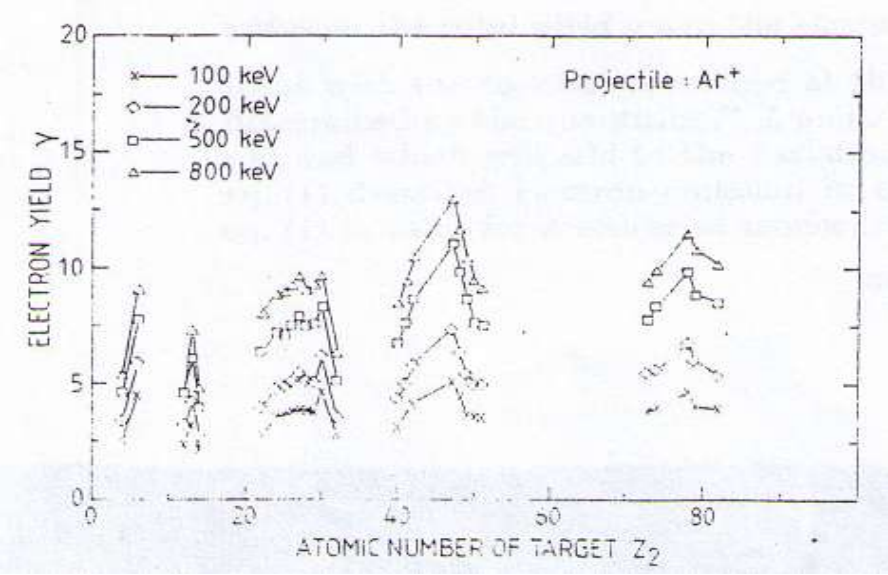

Figure 4.16 Showing the iSE yields for Argon impacts on targets with Different atomic number. Courtesy of Hasselkamp et al [34]

$(iSE)_{H+} < (iSE)_{He+} < (iSE)_{Ar+}$ and that the maximum SE yield in case of H^+ ions occur that about100 KeV whereas for He^+ and Ar^+ it occurs above 800 KeV. Although the their data is highly cited and accepted in literature, they correlate their data with a semi-empirical yield equation derived from transport theory.

Baragoila et al[16,31,33,47] published a number of papers on iSE yield in the low energy region 0-50 KeV, which is the region of interest for ion microscopy. They were instrumental in finding the threshold values for KEE emission which has been discussed in the previous section, and they correlated their data with both Monte Carlo simulations and Transport theory. They assumed that the mean energy required to create an electron-hole pair is independent of the ion velocity and the number of excited electrons generated by the incident ion in a layer of thickness dx at a depth x below the surface is

$$n(\varepsilon, E)dx = \frac{1}{J} S_e(\varepsilon, E)\,dx \quad \ldots\ldots\ldots\ldots\ldots\ldots\ldots\ldots\ldots\ldots (4.615)$$

Where $S_e(\varepsilon, E)$ is the electronic stopping power. They then calculate the total SE yield as

$$\gamma = \frac{P}{2J}\int_0^{\infty} S_e(\varepsilon, E)\, e^{-x/L}\, dx \quad \ldots\ldots\ldots\ldots\ldots\ldots\ldots\ldots\ldots\ldots (4.616)$$

Where P is the average escape probability of the electron and L is the mean attenuation length of electrons in the specimen. They then made a simplification that the ions lost only a very small amount of their initial energy over the mean escape depth of SE's and hence the electronic stopping power term in equation 4.616 can be taken out of the integral and the equation reduces to

$$\gamma = \frac{PLS_e(\varepsilon, E)}{2J} \quad \ldots\ldots\ldots\ldots\ldots\ldots\ldots\ldots\ldots\ldots\ldots\ldots (4.617)$$

The authors have obtained straight lines when the ratio of SE yield divided by electronic stopping power is plotted Vs energy of beam for protons as shown in Figures 4.17.

The authors also make a critical point that proportionality of yields to electronic stopping power is valid only for light ions and when the mass of the projectile is larger than that of the target atom, then the recoiling target atoms also effect the SE yield and the electronic stopping power in equation 4.616 should be replaced by the total inelastic stopping power. They also give a very interesting plot of SE yield for many ions incident on Al as a function of velocity as shown in Figure 4.18. If inelastic collisions are velocity dependent as discussed in chapter 1, then iSE yields due to different ions should not vary significantly in the same velocity region, but as can be seen from Figure 4.18 in practice this is not the case and the iSE yield increases with atomic number of projectile, although the yield increases linearly with velocity for all projectiles. The

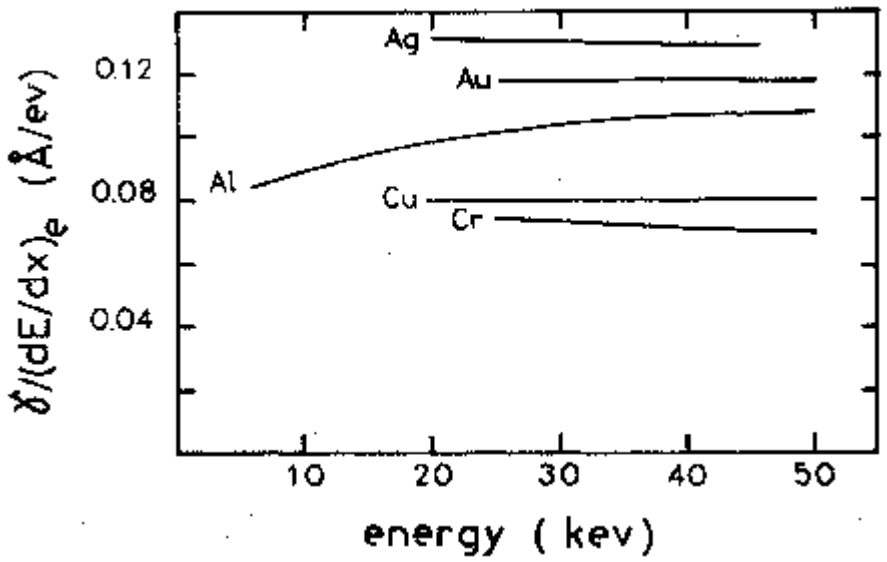

Figure 4.17 Showing the proportionality of SE yields to electronic stopping power. Courtesy of Baragoila et al [57]

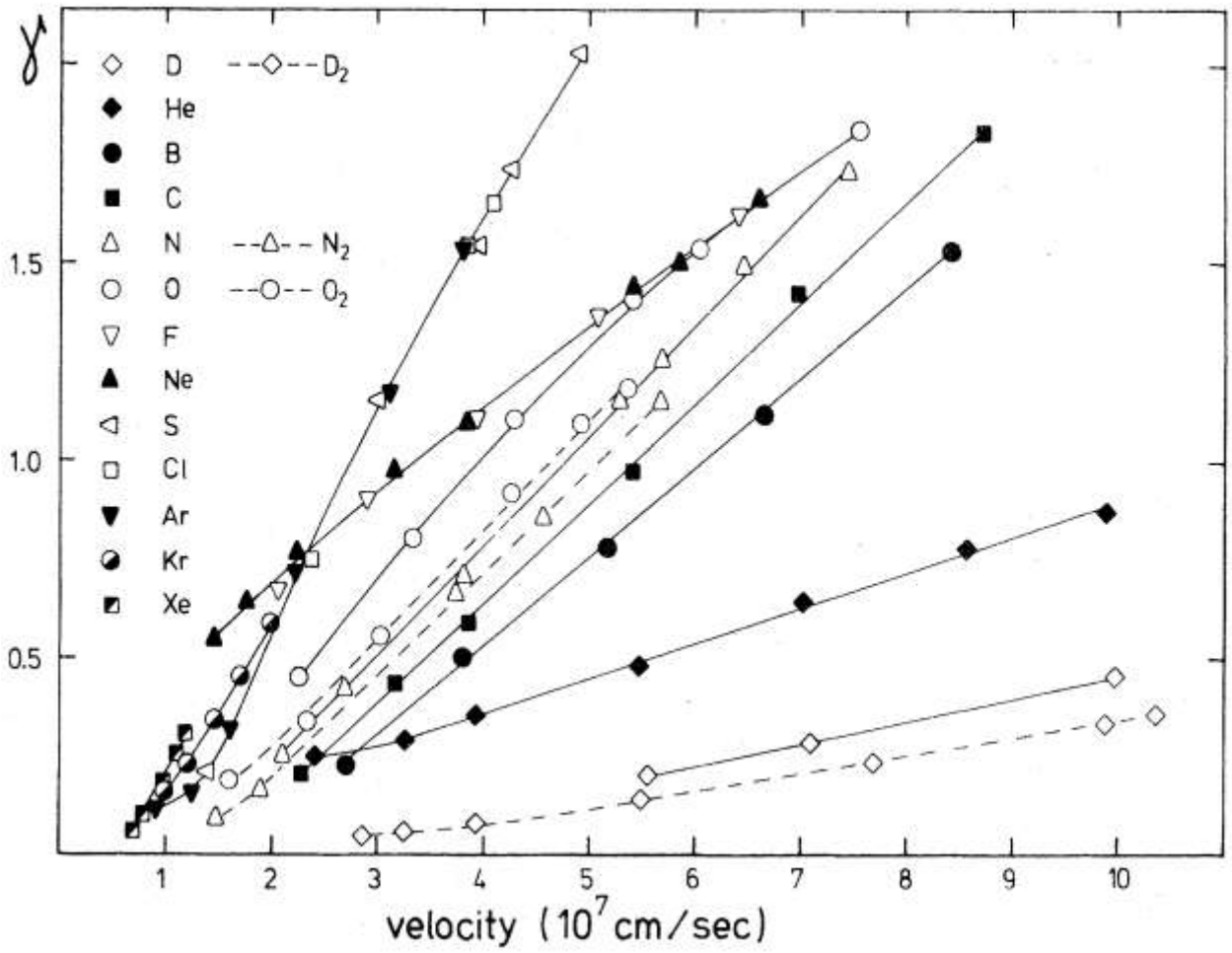

Figure 4.18 Showing the SE yields to various projectiles on Al. Courtesy of Alonso et al [47]

reason for this can be attributed to the fact that higher Z projectiles there is a significant contribution to the SE yield from recoil target atoms and also as the Z of the projectile increases its mean free path decreases and hence it spends more energy within the SE escape depth. It seems that their equation predicts that SE yield only due to the incoming incident ion and may have neglected the effect on SE yield due to backscattered ions.

Ohya et al[54,55,22] proposed that iSE can be created by 3 independent mechanisms that is SE due to the ion (i.e. SE's that are very close to the surface that they can directly escape out), SE due to electron cascade, and finally SE due to recoiling target atoms. They use Monte Carlo models from first principles to calculate the iSE yields. For the electron cascade a random number is pitched to decide if the electron will undergo an elastic collision or if it will undergo inelastic collision, with equal probability of both of these events. This produces an interesting plot of relative contributions of these mechanisms for different ions as shown in Figure 4.19. For light ions the dominant mechanisms of iSE production are the electron cascade and projectile ions while for heavier ions it is due to projectile ions and recoiling target atoms. They also say that iSE yield shows oscillatory effects with atomic number for He^+ ions but decrease monotonically for Ga^+, although the reason for this is not mentioned. They track ion and target atom until their energy becomes lesser than the cohesive energy which is a few eV, this is challenging because for most of the Monte Carlo simulations the termination energy is generally order of a few 100 eV because below this energy the scattering cross section become so large that it makes the simulation less reliable. The limitation in their theory is that they have taken the surface barrier energy for the electron to escape to be $E_F + \phi$, but they found that with this value gave very small yields for heavier ions as compared to experiment, and so they modified

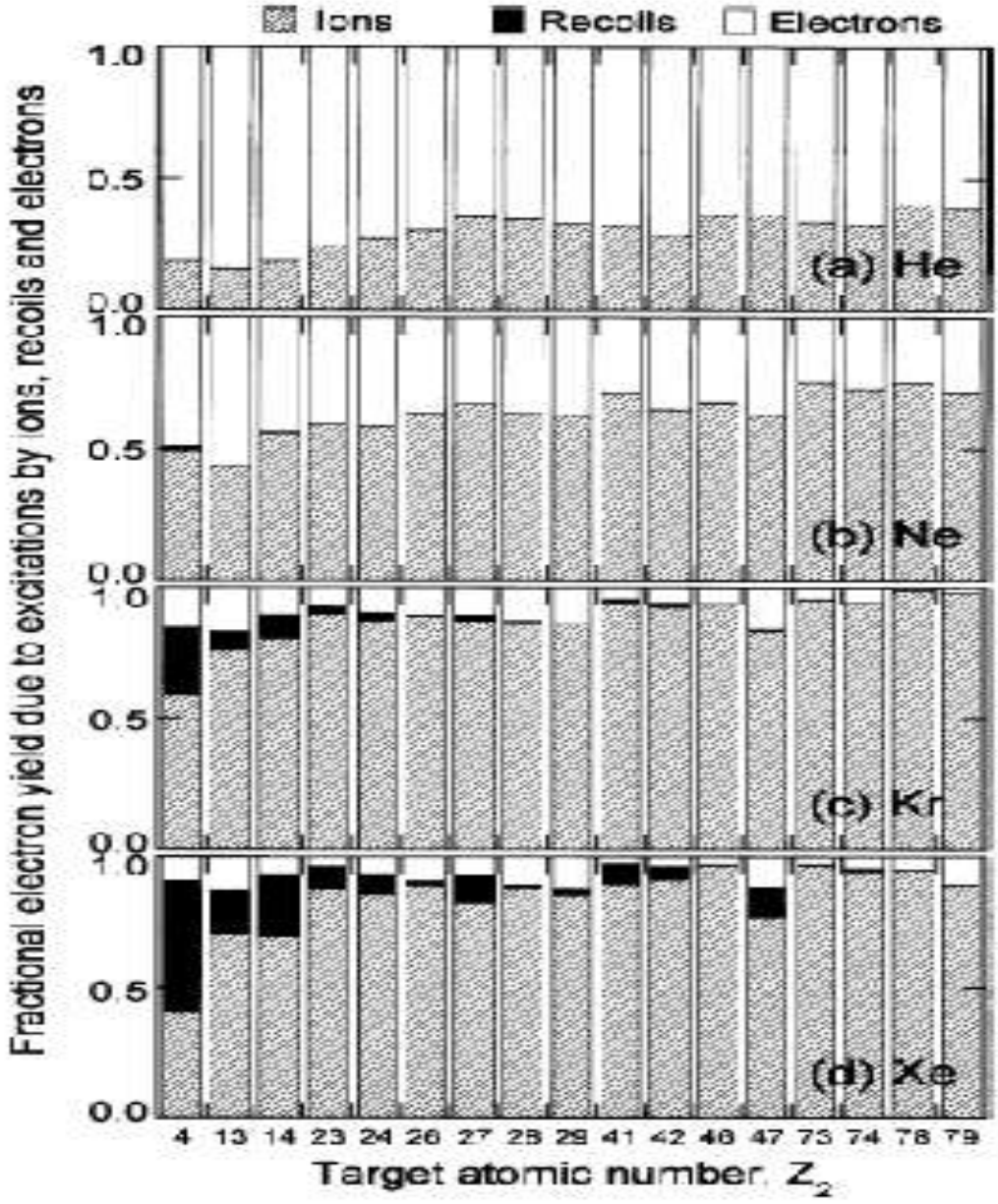

Figure 4.19 SE yields due to ions, electrons and recoils for various projectiles on different targets. Courtesy of Ohya [55]

the surface barrier energy to different values depending on the projectile species. The surface barrier can thus now be anywhere between $E_F + \phi$ and $0.2E_F + \phi$. They have done first principle modeling, but atleast for high Z ions there is some kind of fitting involved. Their simulation however gives very critical information about contribution of various mechanisms to iSE yield.

Winter [58] studied the effect of the charge of the ion on KEE yields and concluded that KEE yields decrease very slightly with increase in charge q of the ion from 1 to 3. for q > 3 there is not much difference. From their data in Figure 4.20, it can be seen that the slope of the SE yields is greater when q is1 than when q is 2 and slope is least when q is 3. In the graph the overall SE yield is higher when q=3 than when q = 2 or q = 1, this is because of increased PEE emission when q=3.

En et al [36] have calculated the SE yield under Argon plasma bombardment. They calculated the SE yield by measuring the total current which composed of ion currents, plasma electron currents and SE currents and obtained linear fit for SE yields with respect to ion velocity. The problem with this approach is that Plasma invariable modifies the surface roughness of the specimen, and SE emission is highly sensitive to surface roughness.

Ruano et al [59] found that iSE's had energies as high as 150 eV as shown in Figure 4.21. They proposed that emission of such high energy iSE's can not be explained by existing theories and that a Fermi Shuttle (FS) mechanism (or pingpong mechanism) is responsible for iSE emission. In the FS mechanism the electron undergoes many elastic collision with the incoming ion and target atoms increasing their velocity each time by 2V, V being the ion velocity.

Sakai [16] et al have compared the iSE and eSE yields with specific reference to Scanning Microscopy. They do this by taking SE images of common metals using electrons, Ar^+ and Ga^+

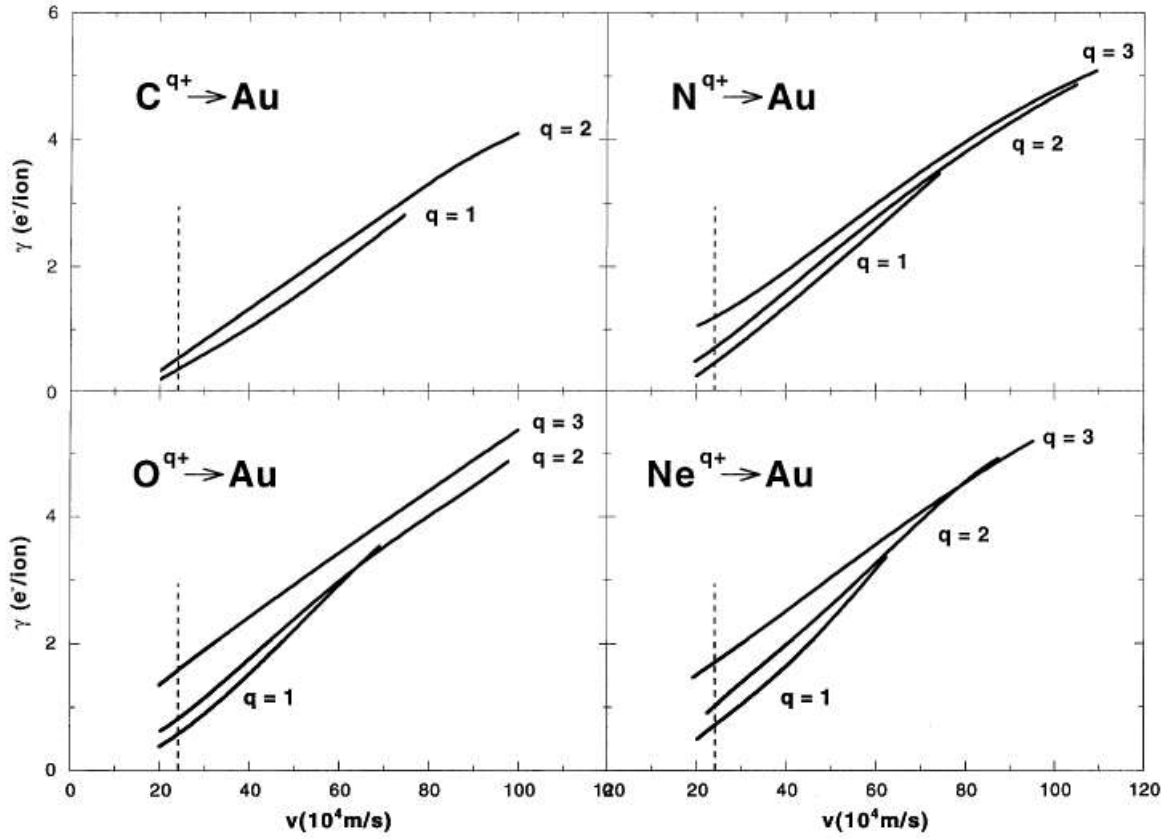

Figure 4.20 Total SE yields Vs impact velocity for impact of singly, doubly and trebly charged ions on clean polycrystalline gold. Courtesy of Winter [58]

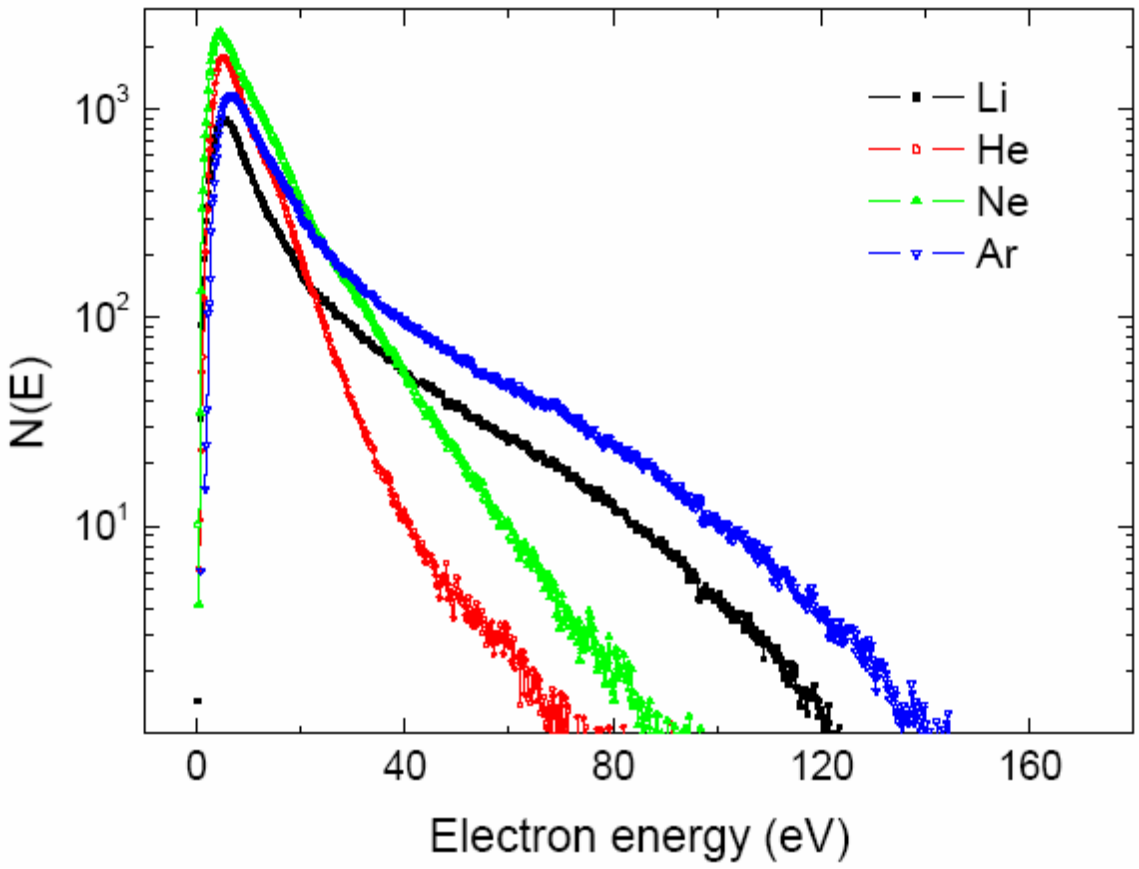

Figure 4.21 Energy distribution of SE emission spectra for different ions on copper.

Courtesy of Ruano [59]

ions of 10 KeV, 3 KeV and 30 KeV as shown in Figure 4.22. Since they have taken images of only 5 metals, they conclude from the images that iSE yield decreases with atomic number of the target. The iSE yield however shows a oscillatory behavior when the elements of the entire periodic table is considered. It is difficult to make comparison of their images since they have used three different energies of the projectiles to compare the images.

4.7 KEE due to recoil target atom

The recoiling target atom not only leads to sputtering and vacancy creation but is also capable of generating the emission of SE because the nuclear stopping power of the ion imparts recoil energy to target atoms. As shown is Figure 4.23 the nuclear stopping power is negligible in the case of helium ions but it dominates the stopping power in case of gallium ions. For the application of ion microscopy it is always desirable to have low nuclear stopping power because it not only reduces the radiation damage but also reduces the production of low resolution recoil SE's.

Beuhler et al [64] compared experimental yields with electronic and nuclear stopping powers, they concluded that nuclear stopping power contributed to the total SE yield only when the ion velocity is $< 2 \times 10^7$ cm/sec (equivalent to 0.8 KeV for He^+ ions and 14.5 KeV for Ga^+ ions).

Alonso et al[47] performed the double Monte Carlo simulation of tracking both the ion and recoiling target atoms trajectories. They say that contribution of recoiling target atoms is negligible for light ions, but for the heavy ion it may be considerable. They present the data of recoil iSE for Kr^+ and Xe^+ on Al as shown in Figure 4.24. Their data is useful but is only for energies upto about 15 KeV.

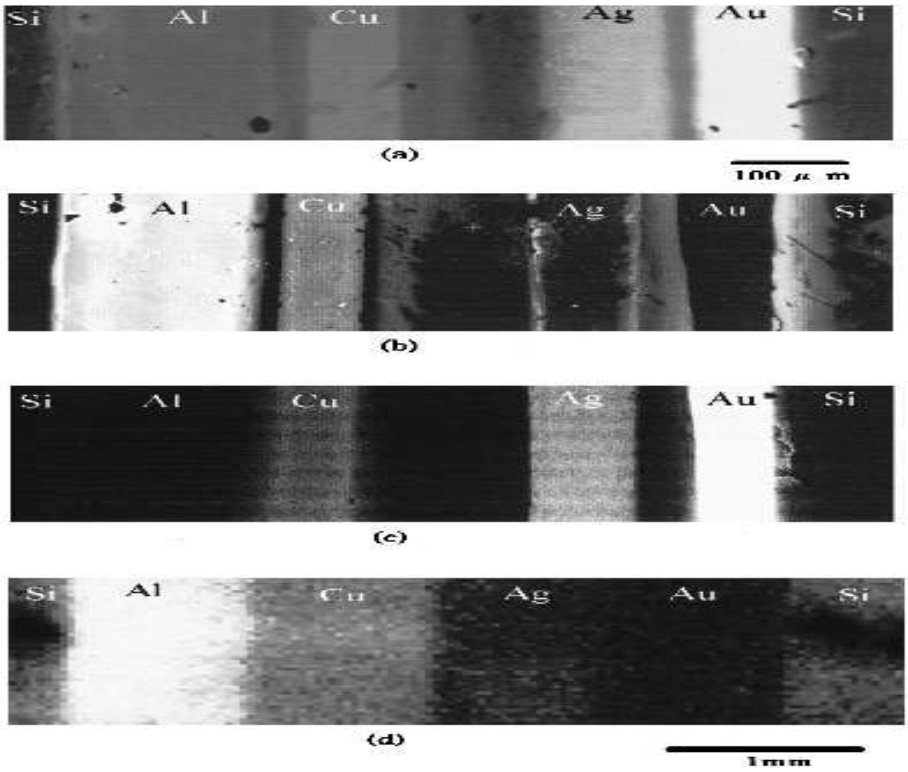

Figure 4.22 showing images of metals under bombardment of different projectiles.

(a) SE image of 10 KeV electron bombardment (b) SE image of 30 KeV Ga^+ ion

(c) Secondary Ion image of 30 KeV Ga^+ ion (d) SE image of 3 KeV Ar^+ ion

Courtesy of Sakai [16]

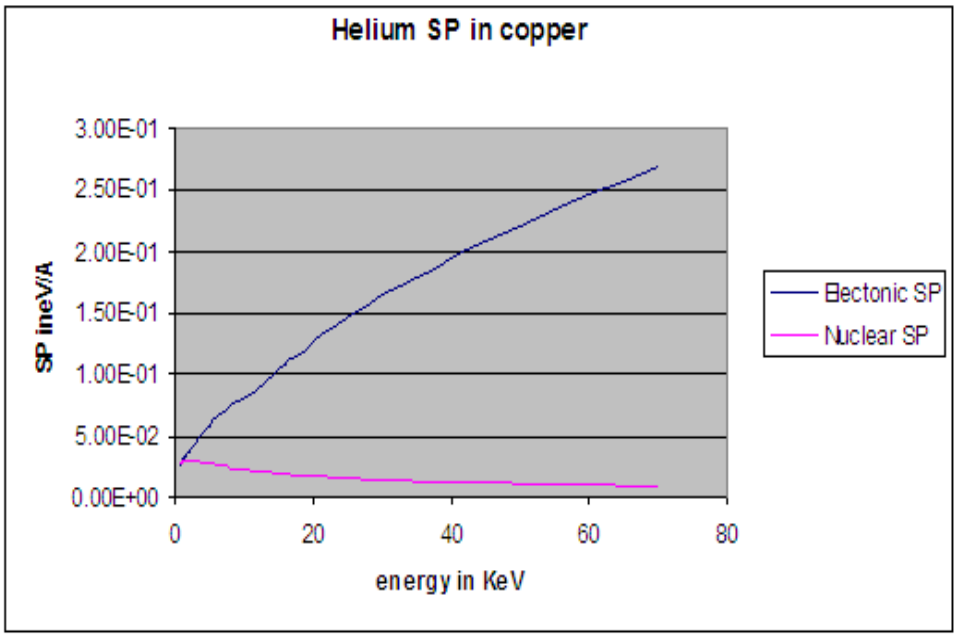

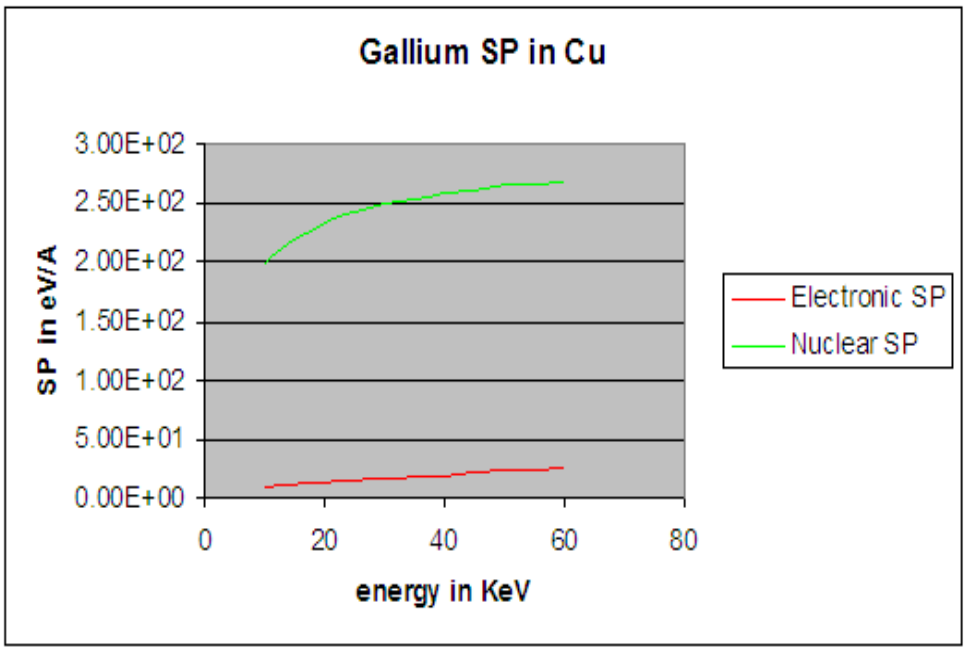

Figure 4.23 Showing the relative contributions of Nuclear and Electronic Stopping powers of Helium and Gallium ions in Cu. Courtesy of SRIM [3]

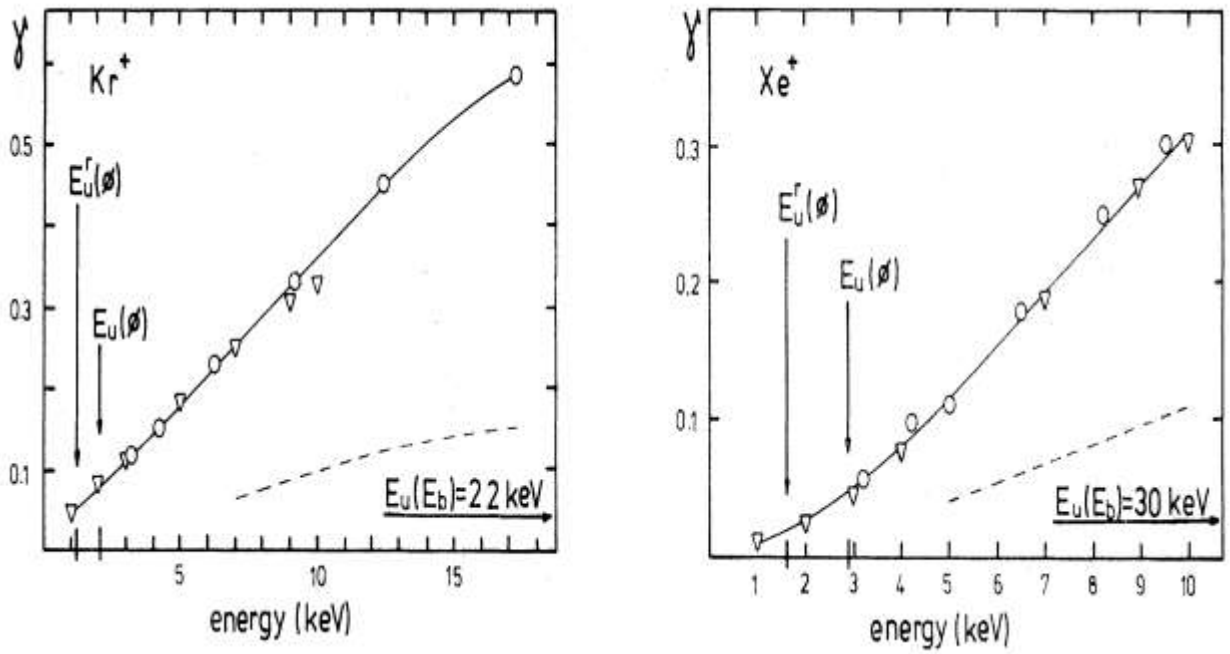

Figure 4.24 Showing the relative contributions of the recoil target atoms on the total electron yield of Kr^+ and Xe^+, the dashed line showing the recoil atom contribution. Courtesy of Alonso et al [47]

4.8 Some other interesting features iSE

4.81 Molecular ions

Ghosh et al [56] proposed that when H_2^+ is incident on metal, it dissociates into H and H^+ and the probability of it dissociating is given by

$$\sigma_d = K\sqrt{T} \quad \text{.....(4.801)}$$

Where σ_d is expressed in units of 10^{-17} cm^2 and T in MeV. K is a constant which is generally about 1.2. They also say that each of the dissociated H and H^+ has half of the energy, although they do not discuss the effect this might have on the trajectories of the ions.

Petrov [48] accepted that KEE from molecular ions is a sum of KEE yields from individual atomic ions of the molecule at the same velocity. He also proposed that PEE yields from molecular ion is negligible as compared to PEE yields of individual ions, he used this to calculate the PEE yields of ions as

$$\gamma_{PEE\ ions} = \gamma_{\exp\ molecules} - \sum \gamma_{KEE\ ions} \quad \text{.....(4.802)}$$

The data he found is plotted in Figure 4.06.

Baragiola et al[60] performed careful experiments on light ions and molecules at energies for which he thought PEE production was negligible. He found that yield for a molecular ion at the same velocity is slightly lesser than individual yields of the atomic species and observed that $2\gamma_{H^+} / \gamma_{H_2^+}$ is slightly greater than 1, the maximum that they found is in the case of H^+ and H_2^+ of about 1.2.

4.82 Isotope effect

Baragiola et al [16,31,33,47] performed experiments on a few isotopes including Hydrogen and Deuterium ions and also with Hydrogen and Deuterium molecular ions. The data they have collected based on their own experiments and also collected from three different authors for H^+ and D^+ ions is shown in Figure 4.25. They conclude that in the velocity range of their data there was no change in SE yields due to different isotopes, however isotope effects my be expected at very low velocities where backscattering, energy degradation and angular straggling of isotopes can vary significantly with in the region of the effective electron escape depth.

4.83 Effect of temperature

Petrov [48] gave experimental yields for H2+ and Hg+ ions as a function of temperature as shown in Figure 4.26.It is however very difficult to compare the data in Figure 4.26 because the velocity of Hg+ which is a heavy ion is too low and is probably completely dominated by the nuclear stopping power. Petrov concludes that the data can not be explained by any specific theory.

Baragiola et al [47] measured their iSE yield data by carefully keeping their targets clean by in situ sputtering by Ar+ ions. When they compared their data of H+ ions with that of Large and Whitlock [72], who that kept their targets clean by heating the target, Baragoila's data was generally higher. They attributed the lower iSE yield in case of Large and Whitlock to the fact that heating may have caused growth of grains with preferred orientation and thus causing channeling of H+ ions. However it is not clear about the temperatures to which the target was heated or the targets that were compared.

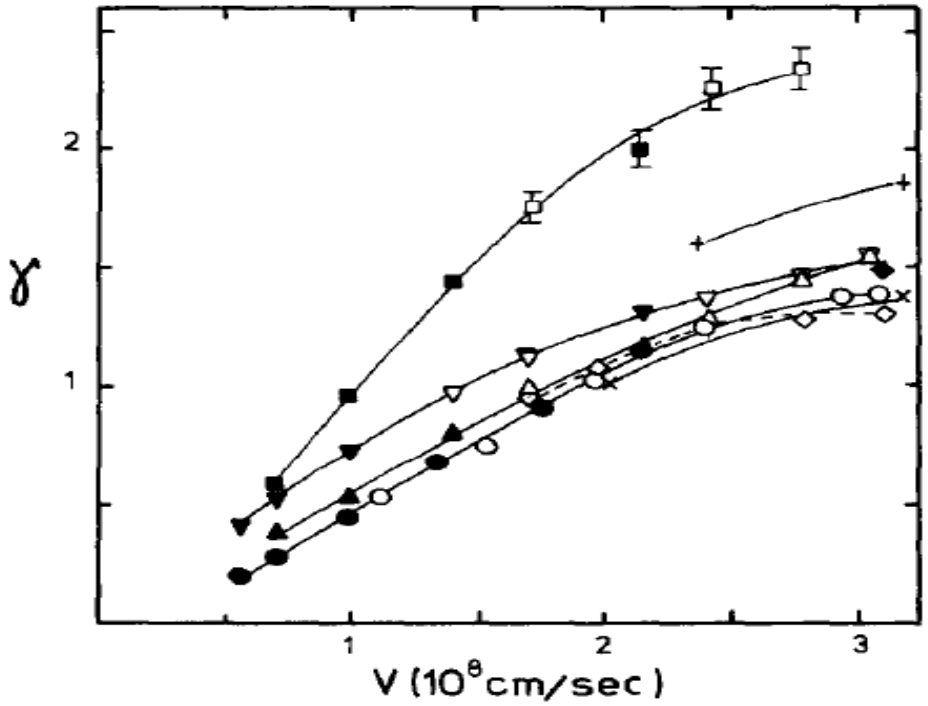

Figure 4.25 Showing the yields for H^+ (open symbols) and D^+ (closed symbols) :

$(\nabla, \circ, \triangle, \square)$ for Li,Al,Cu and Ag respectively. Courtesy of Baragiola et al [47]

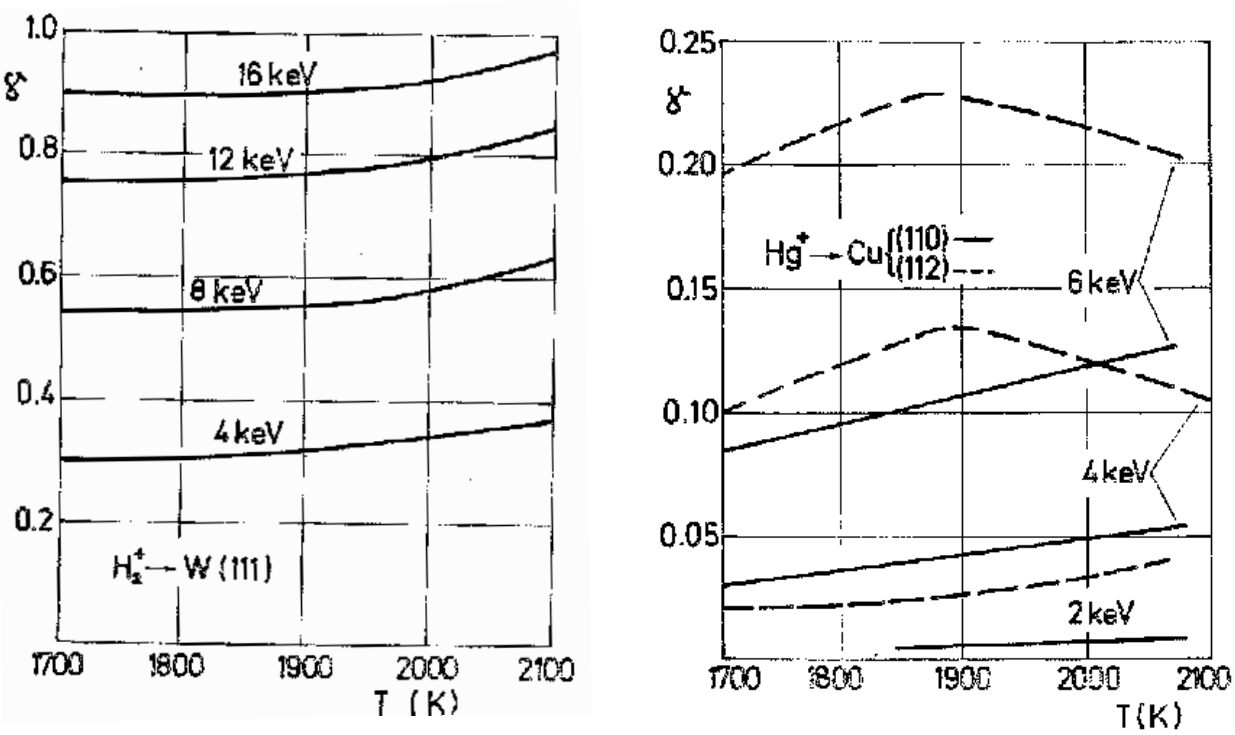

Figure 4.26 Showing the SE yields as a function of temperature for H2+ and Hg+ ions incident on monocrystalline W and Cu. Courtesy of Petrov [48] .

4.84 Topographic contrast

Topographic contrast which can be defined as the variation in SE yield with tilt of the beam, is a important parameter for normal imaging and specially in the case of CD-Metrology. In case of electron induced SE (eSE) the topographic contrast varies approximately as sec (θ) irrespective of the energy of the beam and the target material. Ferron at al [33] did a study of dependence of ion induced SE (iSE) yield on the angle of incidence of the projectile. They collected the topographic iSE yield data for a He+, Ar+ and Xe+ ions of 5- 50 KeV on a number of different targets. They found that iSE yield did not vary as sec (θ) but some function of sec (θ) i.e.

$$\gamma \propto \sec^{f}(\theta) \quad \text{.....(4.803)}$$

They also observed that the topographic contrast was higher at higher energies than it was at lower energies. Also the topographic contrast of light ions was generally above or close to the sec (θ) curve while that for heavier ions it was generally lower than the sec (θ) curve. Their data for He+ and Xe+ is presented in Figure 4.27. They note that the contribution of recoil target atoms to topographic contrast is minimal because the angle at which the maximum iSE yields occurs does not coincide with the angle at which the maximum sputtering occurs, and conclude that although the excited electrons are produced anisotropically in the target material, the mean free path for the electron is so small that a kind of isotropization of the electron emission, nevertheless there is some residual anisotropy which survives this process and causes the SE emission preferentially in the direction of the projectile.

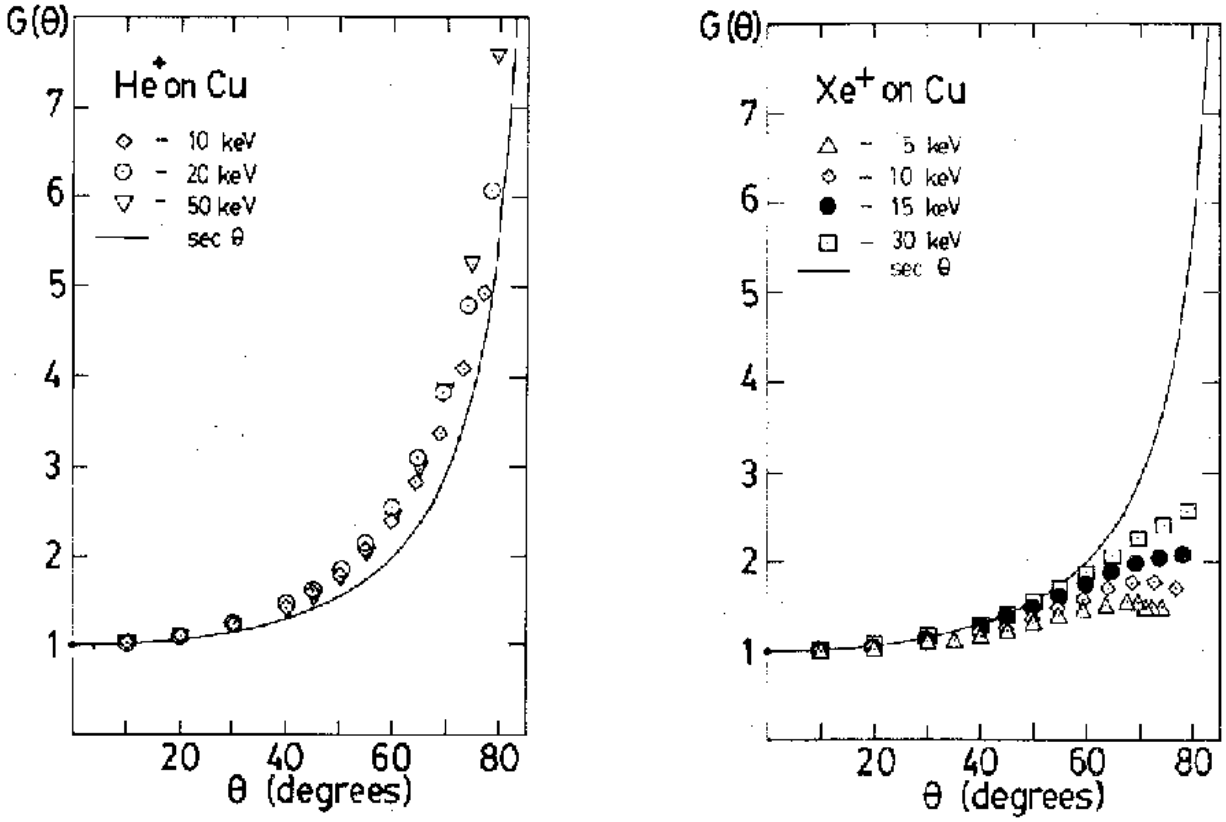

Figure 4.27 Showing the Normalized KEE yields for He^+ and Xe^+ on Cu versus angle of incidence. Courtesy of Ferron et al [33]

4.85 Spatial Resolution

The lateral distribution of the SE emission from the surface is an important parameter that needs to be considered specially while doing high resolution imaging. Inai et al [22] compare the spatial resolution of SE's due to electron bombardment, helium and gallium ion bombardment, their data is presented in Figure 4.28. They define a characteristic SE escape distance X0.5 with in which there is a cumulative probability that 50% of the SE's will be emitted. From their model they predict that this characteristic distance X0.5 for 1 KeV electron bombardment is about 0.9, 2.3 and 0.6 nm for C,Si and Au respectively, while it is 0.4,0.2 and 0.1 for these same elements under 30 KeV Ga+ bombardment.

For a He+ ion at energies of 10-50 KeV whose wavelength is about 1 pm the spatial resolution should be < 0.1 nm. They note however, that for very low energy He+ ion beams and high Z materials the increased contribution of backscattered ions to SE yield may limit the resolution of SHIM. They caution that their data was considered using a zero dimension beam i.e. only one beam incident on the target at any instant of time, and presented the data only from the standpoint of ion-solid interaction. However in real imaging the beam will have a definite probe size and hence effects of Coulombic interactions like Boersch effects also needs to be considered, also beam focusing and aberrations will have a definite effect on the spatial resolution.

4.86 Ion Channeling

It is quite well known that ions strongly channel more in preferred directions of crystal lattice [65]. Petrov [48] did experiments on iSE yields for H_2^+ on the (110), (100) and (111) faces of moncrystalline Copper and his data is shown in Figure 4.29. His data contradicted the earlier

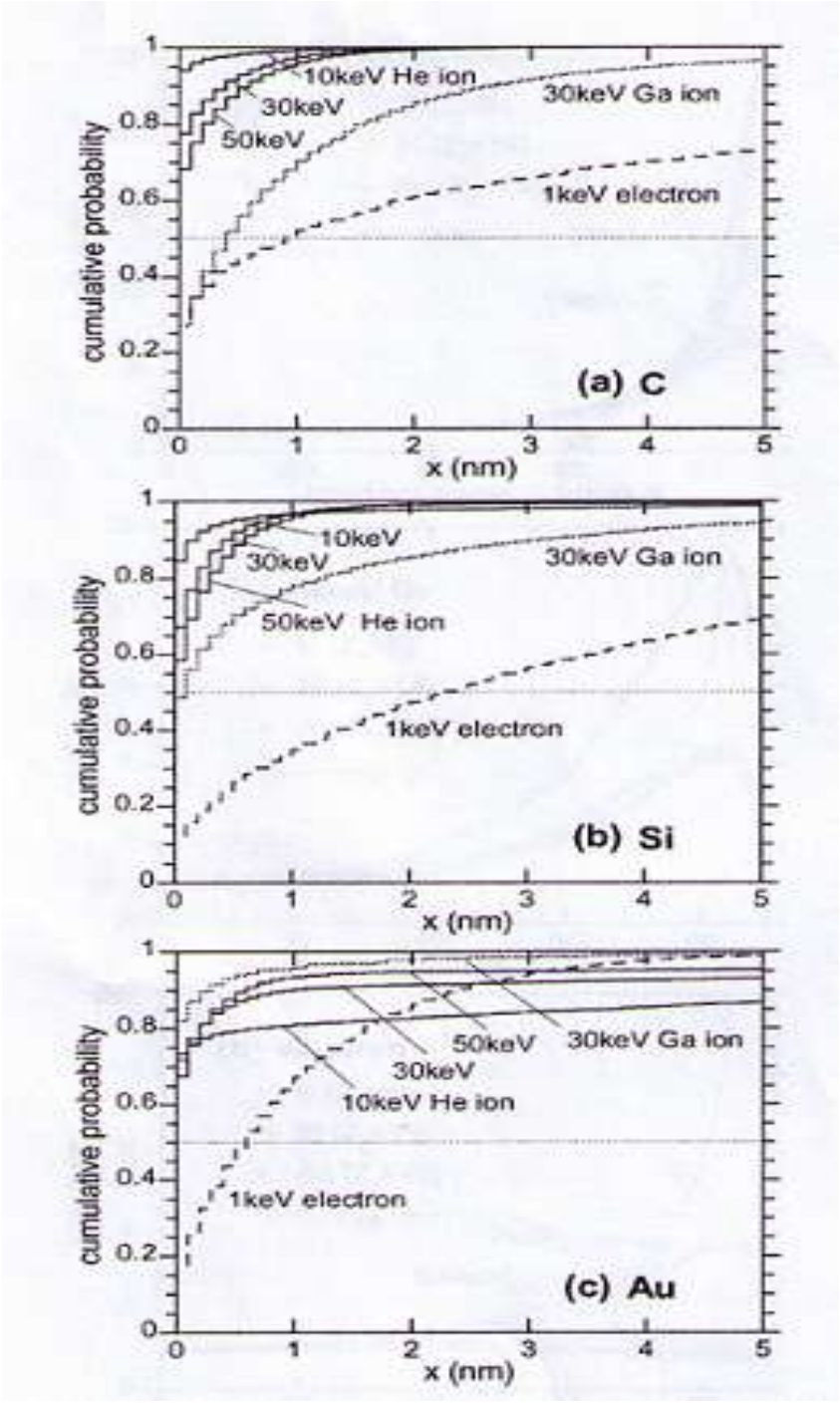

Figure 4.28 Showing the Spatial distribution of SE's under electron, He^+ ,Ga^+ ion bombardment on C,Si,Au. Coutesy Inai et al [22]

theories that ratio of iSE yields on two faces of crystal is only dependant on the ion and the crystal lattice and was independent of the energy of the beam. He found that $\gamma_{100}/\gamma_{110}$ changed from 1.48 to 1.26 and that of $\gamma_{110}/\gamma_{111}$ changes from 1.62 to 1.43 when the energy of the beam is changed from 2 KeV to 16 KeV. Hence it can be inferred that channeling is more significant at lower energies than at higher energies i.e. at lower energies backscattering is more, so the contribution of backscattered ions is more (emission of SE2) than the primary ions in channeling iSE yields.

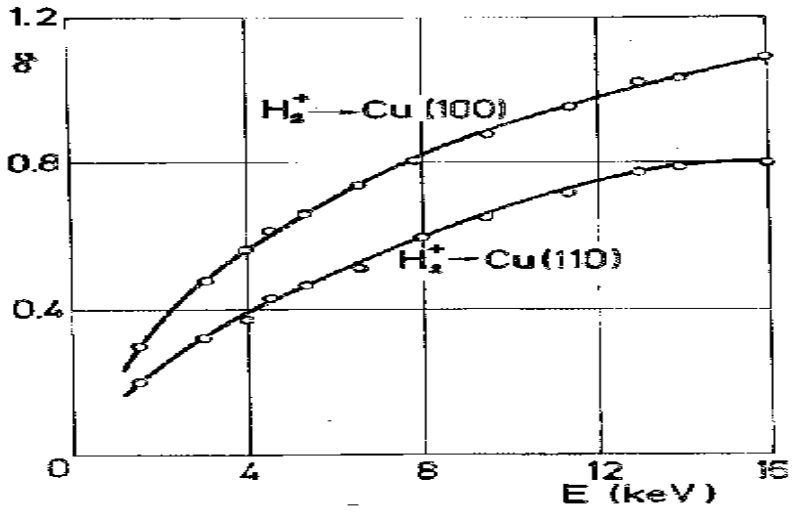

Figure 4.29 Showing the iSE channeling contrast in Monocrystalline Copper. Courtesy of Petrov [48]

4.9 Conclusion

The data presented by various authors clearly shows that the iSE yield when plotted against the velocity of the ion shows a linear fit irrespective of the ion species or the target species, which is very similar to that of eSE behavior. This proves that inelastic collisions are directly proportional to the velocity of the impinging particle. The PEE is dominant only at very low energies below a few KeV. For singly charged ions operating above ~ 5 KeV the contribution of PEE to the total iSE yield can be neglected and only KEE yields need to be considered at these energies. Also the iSE yield is directly proportional to the electronic stopping power of the ions. For light ions like H^+, He^+ the contribution of nuclear stopping power to iSE yield is insignificant.

5. Results and Discussions

5.1 Introduction

Secondary Electrons (SE) are the basis of the most widely used imaging mode of the scanning electron microscope (SEM) because of their high yield efficiency, their high spatial resolution, and the many types of contrast information that they carry [1]. However, SE can also be generated efficiently by ions and with the recent advent [2] of a high performance Helium ion scanning microscope there is now a promising complementary imaging technology to that of the conventional SEM. In order to be able to properly evaluate the relative strengths and weaknesses of electron induced SE (eSE) and ion induced SE (iSE) imaging a detailed model of the beam interaction able to quantify the details of iSE imaging is required. This chapter describes a Monte Carlo simulation, IONiSE (Ion Induced SE), designed to provide data on questions such as the variation of the incident beam range, and the yield γ_{iSE} of iSE, as a function of the He+ ion energy and choice of sample, as well as the behavior of iSE yield with surface topograph [66]. As explained in chapter 1 a comparison between the electron and helium ion stopping powers as a function of energy may suggest that electrons and helium ions interact with the target in completely different ways but this conclusion is incorrect because comparisons on the basis of their energy is not appropriate. As originally shown by Thompson [5] the interaction of swift particles with a solid depends on their velocity not on their energy. A helium ion is 7297x heavier than an electron so at non-relativistic energies (i.e. helium at energies below about 1MeV) the relationship between the velocity of He ions (v_{He+}) and electrons ($v_{electron}$) of the

same energy is

$$v_{He+} = v_{electron} \times 0.0123 \ldots\ldots\ldots\ldots\ldots \quad (5.201)$$

and the velocity of a helium ion of energy E(keV) is

$$v_{He+} = 2.196 \times 10^{7}. (E)^{1/2} \text{ cm/sec} \quad (5.202)$$

If, as shown in Figure (1.03), the stopping power profiles are replotted against velocity and normalized to the same maximum value for convenience then both particles are seen to show similar behavior and both reach their peak value at close to the same velocity (~6 X 10^8 cm/sec). This similarity in the behavior of electrons and ions when they travel at the same velocities is a useful result because it can provide an indication of how electron and ion beams might compare. For example, scanning electron microscopes operate in the energy range 0.5 – 30keV while He ion scanning microscopes operate in the energy range from 5 to 45 keV. For the He ions such energies corresponds to velocities of from 1 to 3 x 10^8cm/sec (i.e. on the left hand side of the stopping power maximum), while for electrons these same energies represent velocities of from 1 to 3 x 10^9 cm/sec and so fall on the right hand side of the stopping power peak. The characteristics of a 30keV helium ion microscope can therefore be viewed as being somewhat comparable with those of an SEM operating at about 3 to 10eV. If the helium beam were to be replaced by a beam of protons of the same energy then the protons, being lighter by a factor of 4x, would be traveling faster and so would correspond to a higher electron energy while replacing helium by the much heavier gallium ions would produce results more consistent with the use of incident electrons with energies below 1eV.

5.2 Principle of IONiSE – Ion interaction and Trajectory plotting

As noted in Chapter 2 the interaction of ions with solid are stronger and more complex than is the case for electrons. Modeling the transport and signal production of an energetic particle within a specimen while properly taking into account all of the possible interactions is not possible with an analytical approach but is conveniently achieved by the well established 'Monte Carlo' random sampling technique pioneered in this context by Fermi and von Neuman (for a brief history see Joy [6]. IONiSE is such a model with a structure similar to that of a 'single scattering' Monte Carlo for electron-solid interactions [6].

The basic sequence of calculations for each step of the ion trajectory consists of :-

(a) determining the starting coordinates (x_n,y_n,z_n) of the ion, and its energy E

(b) computing the scattering angle θ and azimuthal deflection ϕ of the ion from its previous direction of motion

(c) calculating the step length traveled by the ion between successive its last and its next scattering events

(d) determining the energy loss suffered by the ion as it travels along this step of the simulation and hence its residual energy

(e) computing the end point (x_{n+1},y_{n+1},z_{n+1}) of this step of the trajectory

(f) checking to see if the ion is outside the surfaces of the sample, or if its energy is below a selected minimum value (here chosen to be 250eV). If this is the case then this trajectory is terminated and a new trajectory is started from the initial entry coordinates and incident energy.

(g) otherwise this loop is repeated from (a)

The layout of the program closely follows those presented in [6] but, because of the differences between electron and ion interactions noted above, the computation steps must be reformulated and, in the present version, are specific to helium ions He+ with energies above 5keV. The description of the ion interactions, specifically the nuclear scattering cross-section and the stopping power, uses the principles and procedures developed by Ziegler et al. [3]. These routines, incorporated into the widely used TRIM and SRIM [3] programs, have been extensively tested against experimental data and been shown to be reliable across a wide spectrum of energy and ion types.

The scattering angle θ in the center of mass coordinate system is given by the formula [7]

$$Cos\left(\frac{\theta}{2}\right) = \frac{B + R_C + \Delta}{R_o + R_C} \quad \text{..... (5.201)}$$

where B is a random variate, Rc and R_0 are found from the interatomic potential and Δ is a fitting parameter. At high energies (i.e. above 100keV for He) θ is calculated using the unscreened Coulomb interatomic potential, or Rutherford scattering, as suggested by Biersack et al. [7]. The azimuthal scattering angle ϕ is 2π.RND where RND is a random number between 0 and 1.

The mean free path λ is calculated from the Lindhard, Nielson, Scharff (LNS) differential cross section [8] given as:-

$$d\sigma(E,T) = \frac{1}{2}\pi a^2 \frac{E}{\gamma E_L^2} t^{-3/2} f(t^{1/2}) dT \quad \text{..... (5.202)}$$

where, if T is the energy transferred to the target atom

$$t = \frac{E^2}{E_L^2}\frac{T}{\gamma E} \qquad \text{…….. (5.203)}$$

E_L is the Lindhard unit of Energy

$$E_L = Z_1 Z_2 \frac{e^2}{a}\frac{M_1 + M_2}{M_2} \qquad \text{…….. (5.204)}$$

and Z_1, M_1 and Z_2, M_2 are the Atomic number and the Atomic mass of the incident ion and of the target respectively, and 'a' is the universal screening radius given [3] as

$$a = \frac{0.8853 a_B}{Z_1^{0.23} + Z_2^{0.23}} \qquad \text{……. (5.205)}$$

where a_B is the Bohr radius ($0.529 * 10^{-8}$ cm).

Winterbon et al. [9] have fitted the LNS $f(t^{1/2})$ cross-section to the following function

$$f(t^{1/2}) = \Lambda\ t^{1/6}[\,1 + (\,2\,\Lambda\ t^{2/3}\,)^{2/3}]^{-3/2} \text{…... ……..} \quad (5.206)$$

where Λ = 1.309, The total cross-section corresponding to the above LNS differential form has been calculated by Mueller [10]. This total cross-section σ_T can then be used to find the mean free path λ as:

$$\lambda = \frac{M_2}{N_a \rho \sigma_T} \qquad \text{……(5.207)}$$

ρ is the density of the target and Na is the Avogadro's number. The individual step lengths can then be randomized [6] by the equation

$$S = -\lambda \log_e(RND) \text{ ……} \quad (5.208)$$

where RND is a random number falling between 0 and 1. IONiSE uses the random number generator in Visual Basic, reseeding the routine every 100 trajectories to optimize performance [6].

After finding the scattering angle and step length, the energy lost by the ion traversing that particular step needs to be calculated. The nuclear energy loss is calculated as :-

$$(\Delta E)_{\text{nuclear}} = \frac{4M_1M_2}{(M_1+M_2)^2} Sin^2\left(\frac{\theta}{2}\right)E \quad \ldots\ldots\ldots\ldots\ldots\ldots (5.209)$$

and the electronic energy loss is:-

$$(\Delta E)_{\text{electronic}} = S * \left(\frac{dE}{dS}\right)_{Helium\ Electronic} \quad \ldots\ldots\ldots\ldots\ldots\ldots (5.210)$$

The electronic stopping power $\left(\frac{dE}{dS}\right)_{Helium\ Electronic}$ for helium is calculated by scaling the electronic stopping power of the proton

$$\left(\frac{dE}{dS}\right)_{Helium\ Electronic} = 4 * \gamma_{He}^2 * \left(\frac{dE}{dS}\right)_{Proton\ Electronic} \quad \ldots\ldots\ldots\ldots (5.211)$$

where γ_{He} is the fractional effective charge of the Helium ion. The required fractional effective charge and the proton stopping power values are tabulated in the SRIM [3] data base. In IONiSE it is assumed that the density of the target remains constant, hence ignoring effects of sputtering, vacancy generation, and the diffusion of atoms. The effects of sample crystallinity and of the channeling of ions are also ignored. The current version of IONiSE is programmed in Microsoft^{tm} Visual Basic 6.0, runs on any current XP or VISTA Windows system.

5.3 Principle of IONiSE – iSE production

The SE's that are created as the result of knock on collisions with the incident ion cascade through the solid multiplying and losing their energy as they travel, until they either reach the surface and emerge as a SE or they sink back in to the sea of conduction electrons.

The inelastic mean free path for electrons is of the order of 1 – 4 nm and falls with the energy of the electron, so typically an electron travels only a few nm before it transfers some part of its energy. However, when the energy of the electron falls below 20 – 30 eV, its inelastic mean free path increases drastically because at these energies there are no large cross section for inelastic scattering events [6]. The elastic mean free paths also falls with energy but below about 30 eV they become almost constant as shown in Figure 5.01. It is accepted that electrons created below the SE escape depth of 5 to 15 nm can not reach the surface and escape as SE.

A first principles simulation, where trajectories of both the incident ion and the excited electrons are tracked, can provide detailed information of the SE parameters like the energy of emission and the angle of emission. But the excitation cross sections for valence and core shell electrons need to be known for this kind of a calculation, and such cross sections are not known accurately except in a few special cases . Therefore we have used a parametric (or 'semi empirical') model of SE generation which provides adjustable parameters which can be chosen to give the best fit to experimental yield data . A combination of the 'semi empirical' model for secondary electron production, and the TRIM routines which describe ion stopping power, scattering, and transport, has been used to construct a Monte Carlo simulation (IONiSE) which can quantitatively interpret the generation of secondary electrons (SE) from

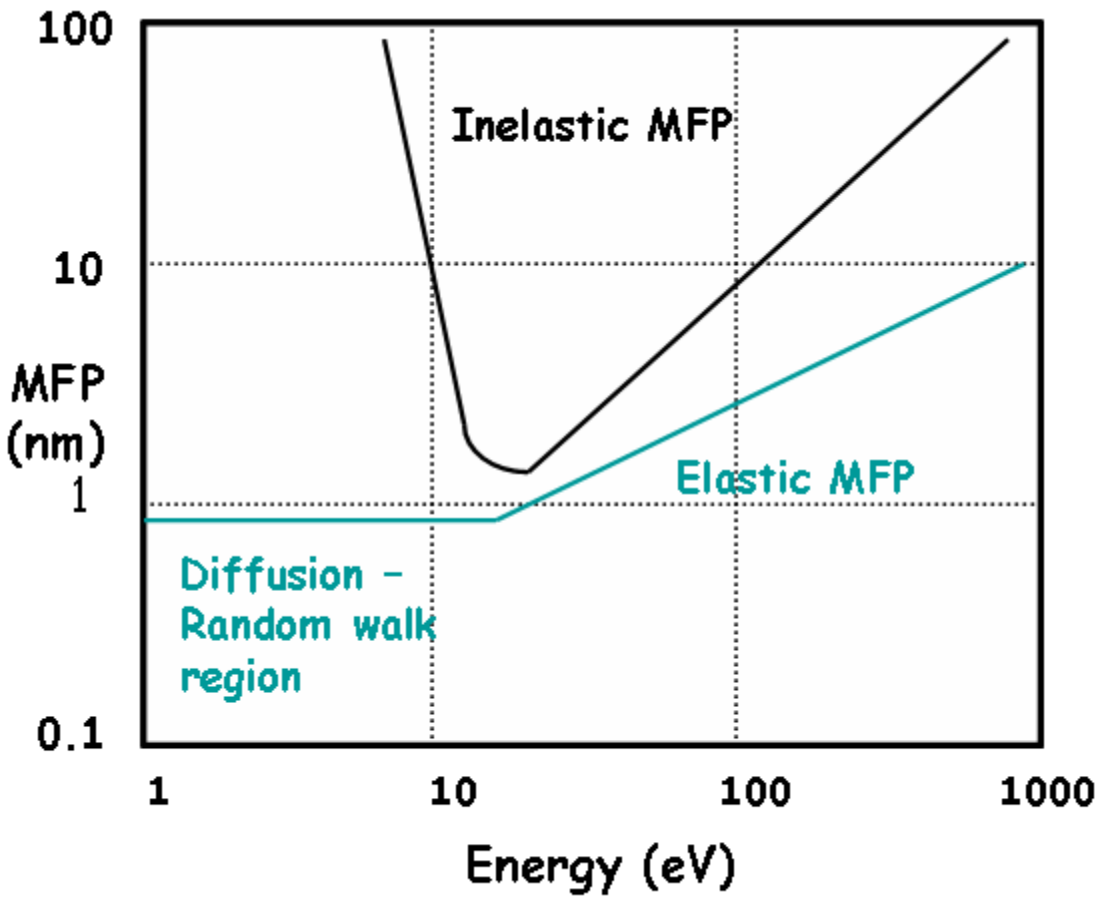

Figure 5.01 Showing the inelastic and elastic mean free paths as a function of energy of the electron. Courtesy of Joy [6]

materials by fast helium ions. This approach lacks the rigour of a first principles calculation but has the merit that, unlike more fundamental models, it can be applied with equal ease to both pure elements and complex compounds.

As discussed in Chapter 3 for helium ion energies of a 5 keV and higher the PEE yield is only a very small fraction of the KEE Yield. PE emission was therefore not considered in determining iSE yields and it is only the kinetic emission mode that is of interest for He ion beam secondary electron imaging.

The physical approach of IONiSE is based on two widely accepted principles that date back to the 1940s [see e.g. 23, 24,25].The first is Bethe's proposition that secondary electrons are generated at a rate that is proportional to the instantaneous stopping power of the incident particle in the solid [26].

Thus

$$\gamma = \frac{1}{\varepsilon}\left(\frac{dE}{ds}\right) \quad \text{……..(5.301)}$$

where γ is the SE yield (electrons/incident particle), $\frac{dE}{ds}$ is the stopping power (ev/A) along the trajectory of the particle, and ε is a scaling constant. Bethe's hypothesis has been experimentally tested [27] and has been shown to be applicable and accurate for both electron and ion impact. As noted in chapter 3 that the nuclear contribution to the iSE is not significant at ion velocities greater than 2 X 10^7 cm/sec, which for the helium ion is about 0.8 KeV and so $\frac{dE}{ds}$ will be taken to be equal to the electronic component of the stopping power.

Secondly, as originally suggested by Salow [23], it is assumed that secondary electrons can be treated as escaping from a solid by a process of diffusion. Thus the probability p(z) of an electron escaping to an infinite flat surface from depth z is

$$p(z) = A * \exp\left(-z/\lambda_d\right) \quad \text{.....(5.302)}$$

where λ_d is the effective diffusion length for the secondary electrons, and A is a scaling constant of magnitude about 0.5 assuming no refraction or reflection of the SE at the surface. The total secondary yield γ can then be written as

$$\gamma = \frac{1}{\varepsilon}\int_0^R \frac{dE}{dz} 0.5 \exp\left(-z/\lambda_d\right) dz \quad \text{.....(5.303)}$$

where R is the total path length (i.e. the range) of the incident particle.

For electron induced secondary emission equation (5.303) can be further simplified by assuming that the stopping power is constant and equal to the incident energy divided by the beam range. The resultant analytical relationship describes experimental eSE yield profiles surprisingly well [24, 25, 28] especially when re-cast in a normalized format to give a 'universal curve' for eSE production [25,28].

In the work presented here the physical mechanism of equation (5.303) is incorporated into the IONiSE Monte Carlo simulation of ion transport. At every step in the program the position, direction of travel, and energy of the incident ion is known. The electronic stopping power given in equation 5.211 from the SRIM code can therefore used to give the instantaneous iSE yield rate if the "ε" constant in equation 5.301 is known. The fraction of these iSE which diffuse to the surface can then be calculated using equation 5.302 given a value for λ_d . This computation is repeated for every step of each trajectory, and the resultant yield data is then summed over a

large number of trajectories and averaged to give γ_{iSE} for the chosen target and incident ion energy. These steps are closely similar to those used to simulate eSE generation in a SEM [30]. The required values of ε and λ_d for each material of interest must be obtained by fitting to appropriate experimental yield data. It is evident from equation 5.301 that ε is simply a scaling constant which changes the absolute magnitude of all computed yields for a given set of conditions by the same amount. The value of λ_d, on the other hand, greatly affects the variation of the iSE yield curve with energy as discussed by Lin [28]. The procedure used here to determine appropriate values for ε,λ_d was therefore as follows. Four sets of iSE yield data for helium beam excitation in the energy range 5keV to 800keV of twenty nine different elements were taken from the literature [31-34]. For four elements - Al, Cu, Ag and Au - a combination of these data sets provided yield values spanning the energy range 5keV to 800keV. The data available for the other elements covered either the 5keV to 45 keV, or 100keV to 800keV range. Some other compilations of low energy He iSE data are available [e.g. 37] but were not included in the analysis here because the iSE yield was produced by plasma irradiation. The electric fields and surface roughening occurring during plasma formation lead to iSE yield results which are not reproducible.

For each element in turn IONiSE was then used to compute iSE yield as a function of incident ion energy using, as trial starting values, published sets [28], of ε,λ values derived by fitting to a comprehensive database of eSE yield profiles. The 'λ_d' parameter was adjusted to give the best match to the shape of the iSE yield curve and once this had been optimized then 'ε' was adjusted to match the absolute yield values. Typically only a few thousand trajectories were required to be

computed to get a stable prediction of the yield for the chosen parameters. Table 5.1 tabulates the values of ε,λ derived in this way for the elements analyzed.

5.3 iSE yield curves

Figure 5.02 to Figure 5.26 display the quality of fit obtained between the original experimental He+ iSE yield data sets and the values obtained from IONiSE using the appropriate parameters . Table 5.1 shows (in columns 3 and 4) the ε and λ values determined by the procedure described above as best fitting the available iSE yield data for the elements tabulated in column 1.Because the experimental data used for this analysis was from 20 to nearly 40 years old it was impossible to determine its accuracy and precision. However, the fact that the four data sets merge quite well with each other is an indication that they are at least self consistent . Arbitrary 10% error bars have been assigned to the measured yields as some indication of the possible precision achieved. The agreement between the experimental and the fitted data, for a given element and choice of the ε and λ_d values, is usually well within the proposed 10% window across the whole range of energies.

For each of elements in Table 5.1 IONiSE has also been applied to calculate the iSE yield profile over the complete energy range from 5keV to 10MeV. These profiles are all generically similar and show a behavior in which the He+ induced iSE yield increases linearly with incident ion velocity [18, 36] reaches a maximum γ_{max} at some energy E_{max} and then decays away as about 1/E. Columns 5 and 6 of Table 5.1 tabulate the predicted γ_{max} and E_{max} values for each of the elements fitted showing that the typical maximum yield ranges from 3 to about 7 (as compared to 1-2 for electrons) and occurs at an energy between 500keV and 1MeV. For He+ this yield

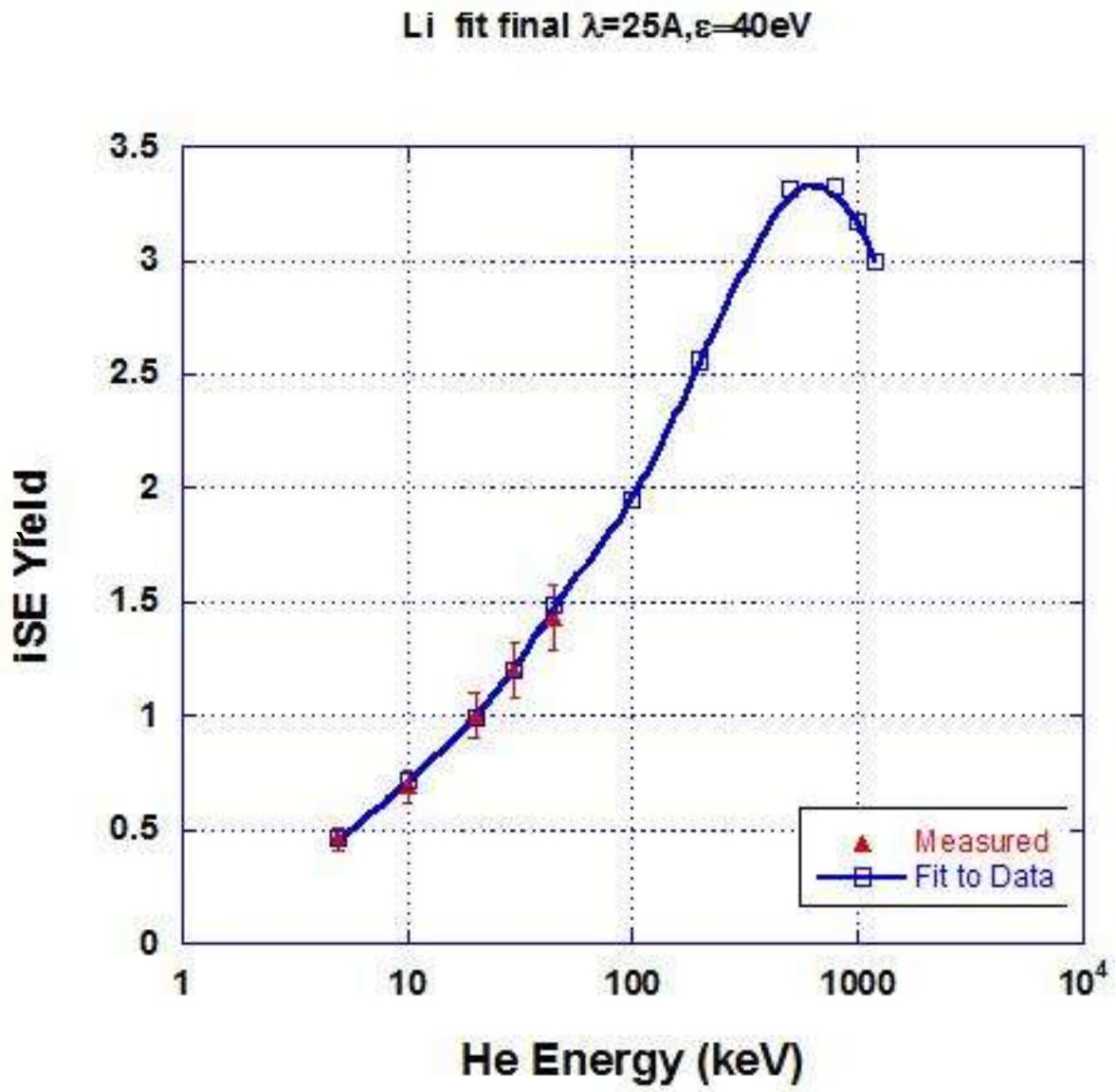

Figure 5.02 Showing the iSE yield parameters and data fit for Lithium

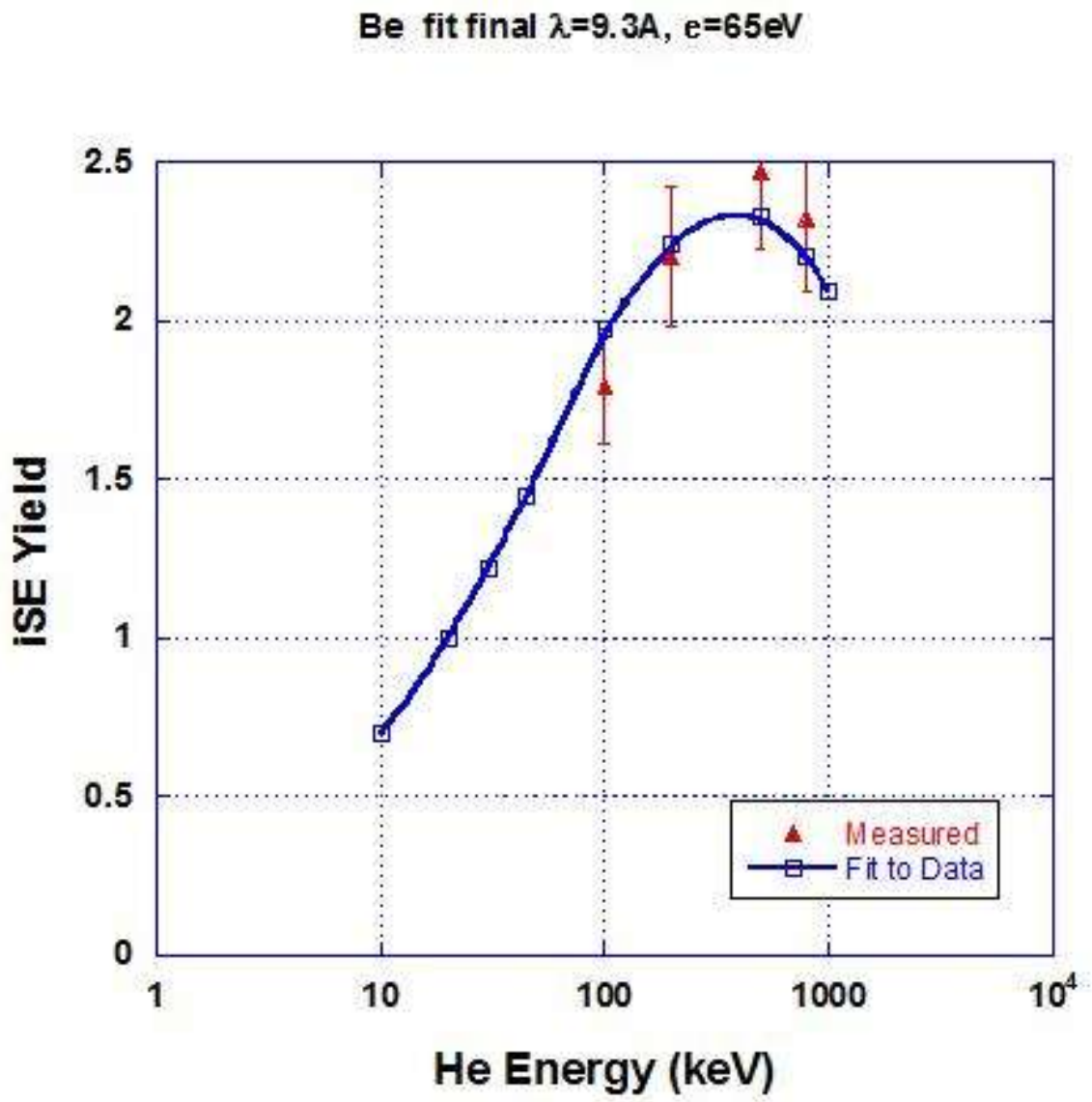

Figure 5.03 Showing the iSE yield parameters and data fit for Beryllium

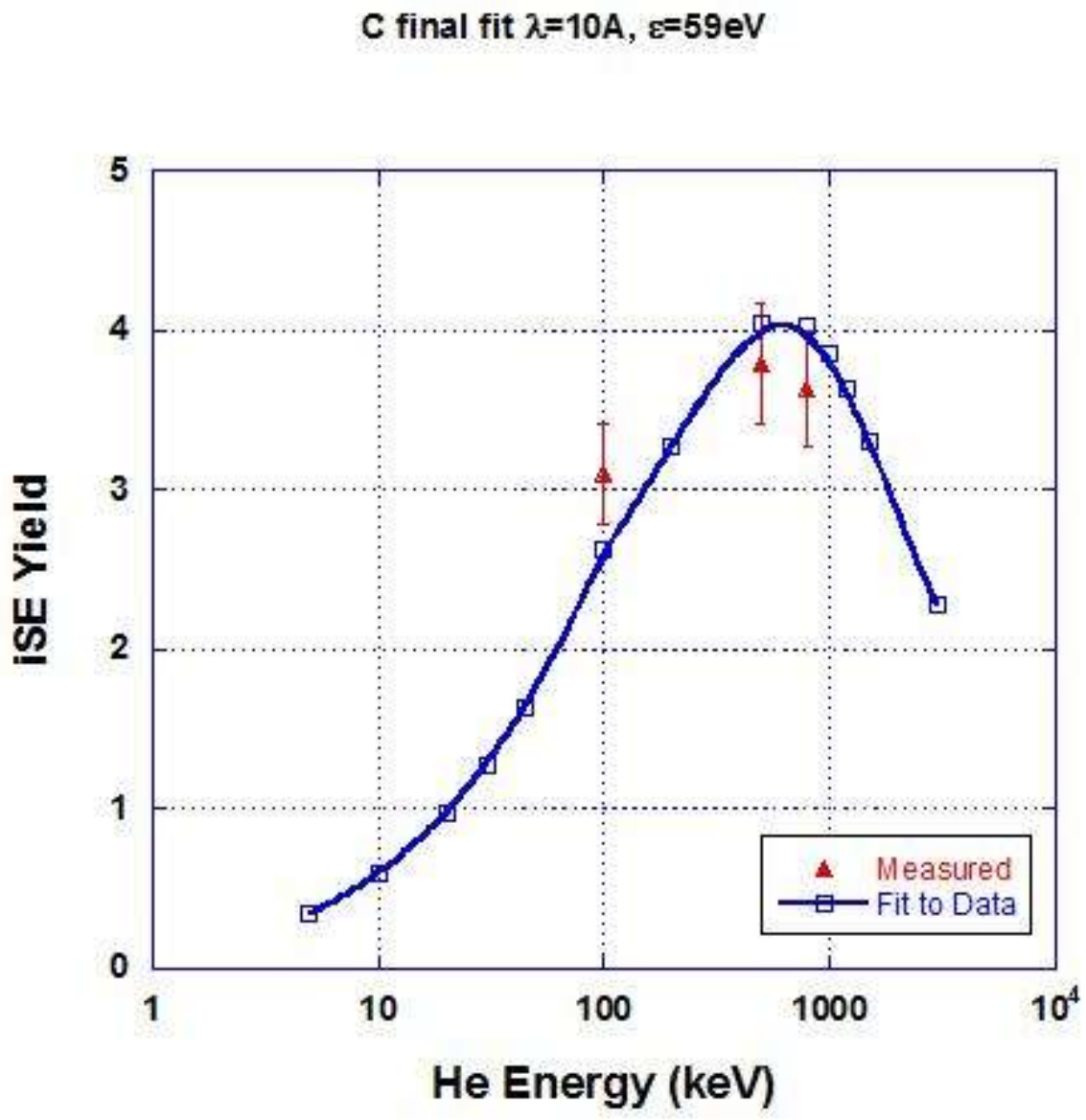

Figure 5.04 Showing the iSE yield parameters and data fit for Carbon

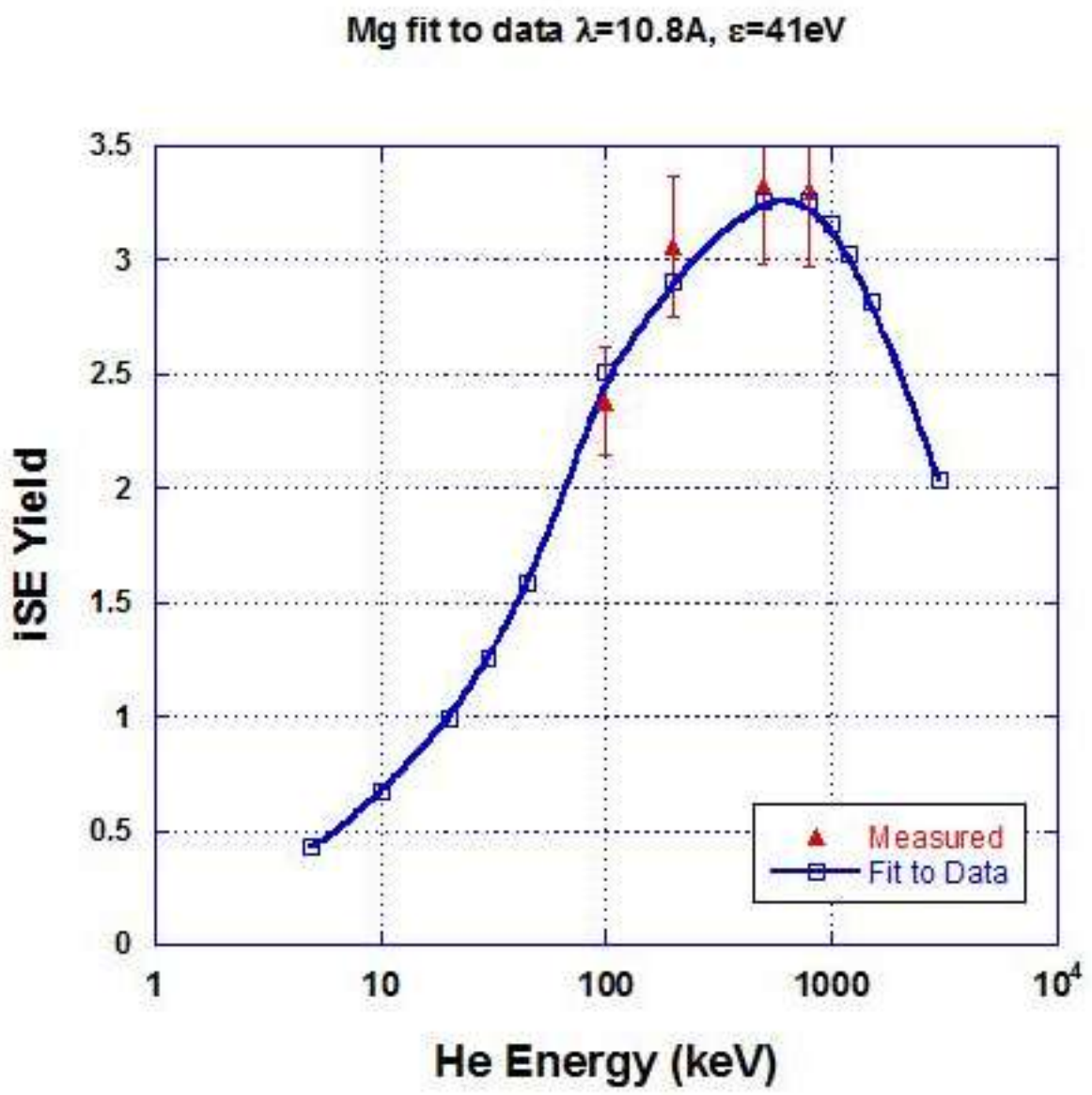

Figure 5.05 Showing the iSE yield parameters and data fit for Magnesium

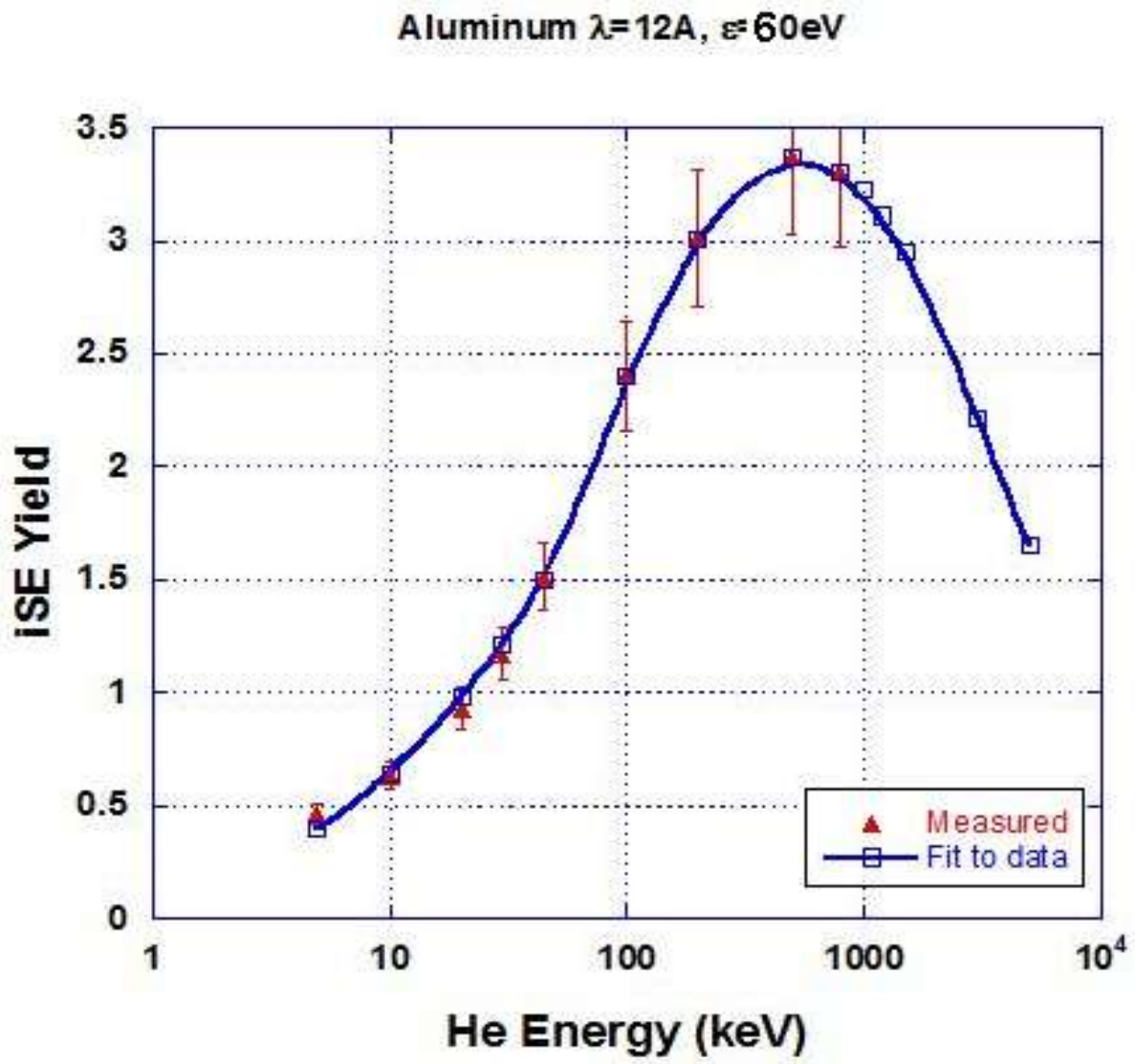

Figure 5.06 Showing the iSE yield parameters and data fit for Aluminum

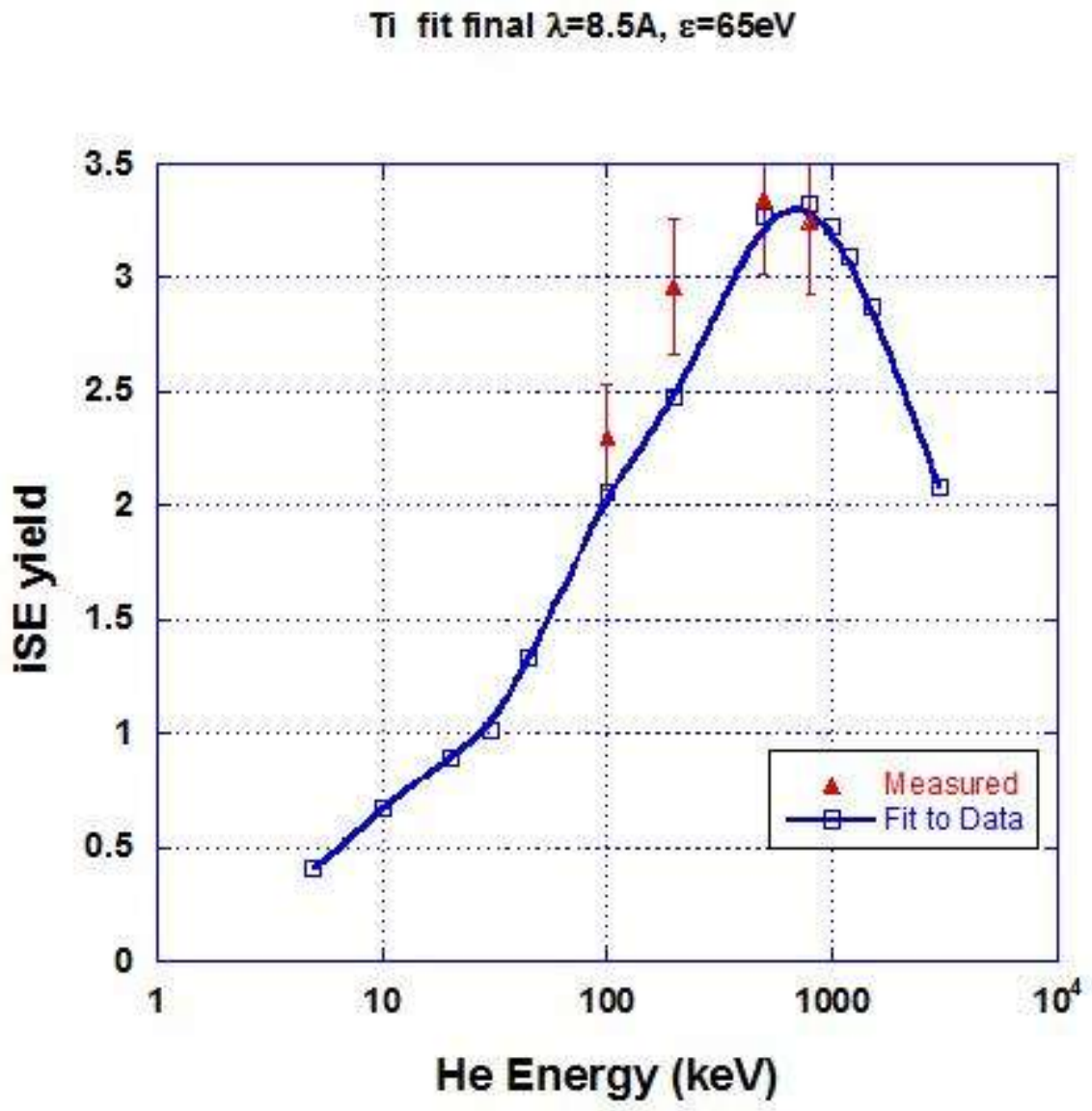

Figure 5.07 Showing the iSE yield parameters and data fit for Titanium

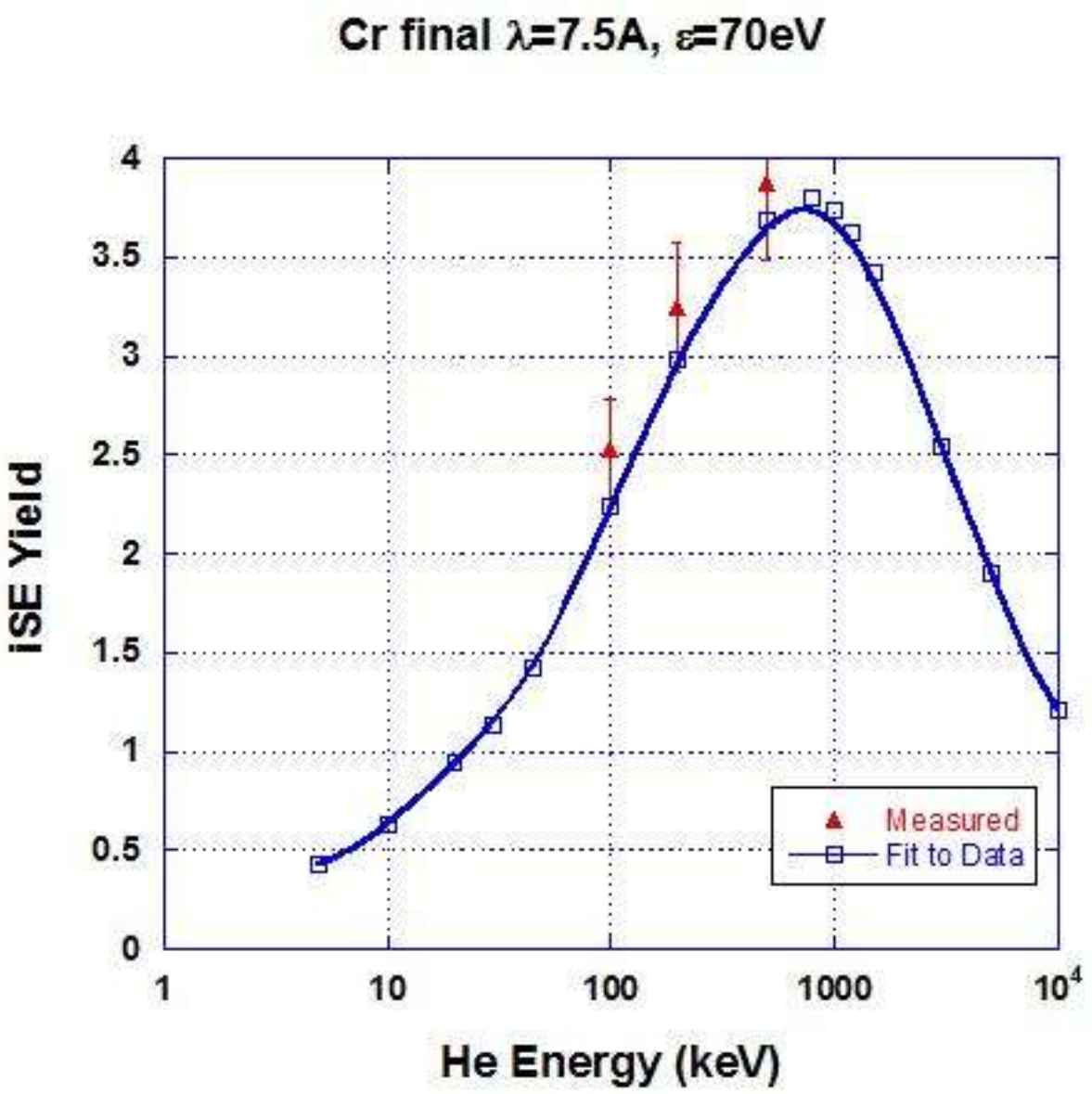

Figure 5.08 Showing the iSE yield parameters and data fit for Chromium

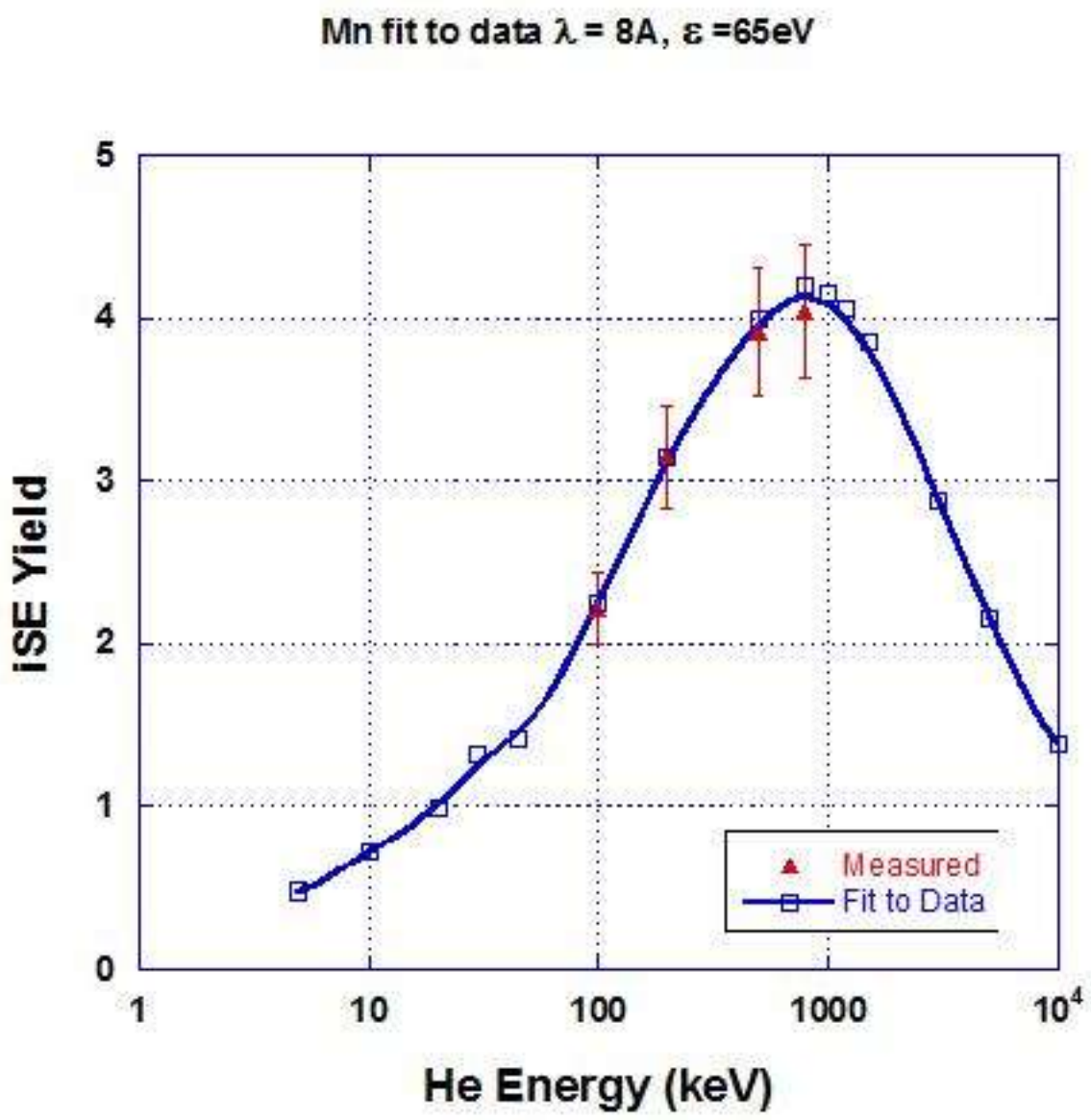

Figure 5.09 Showing the iSE yield parameters and data fit for Manganese

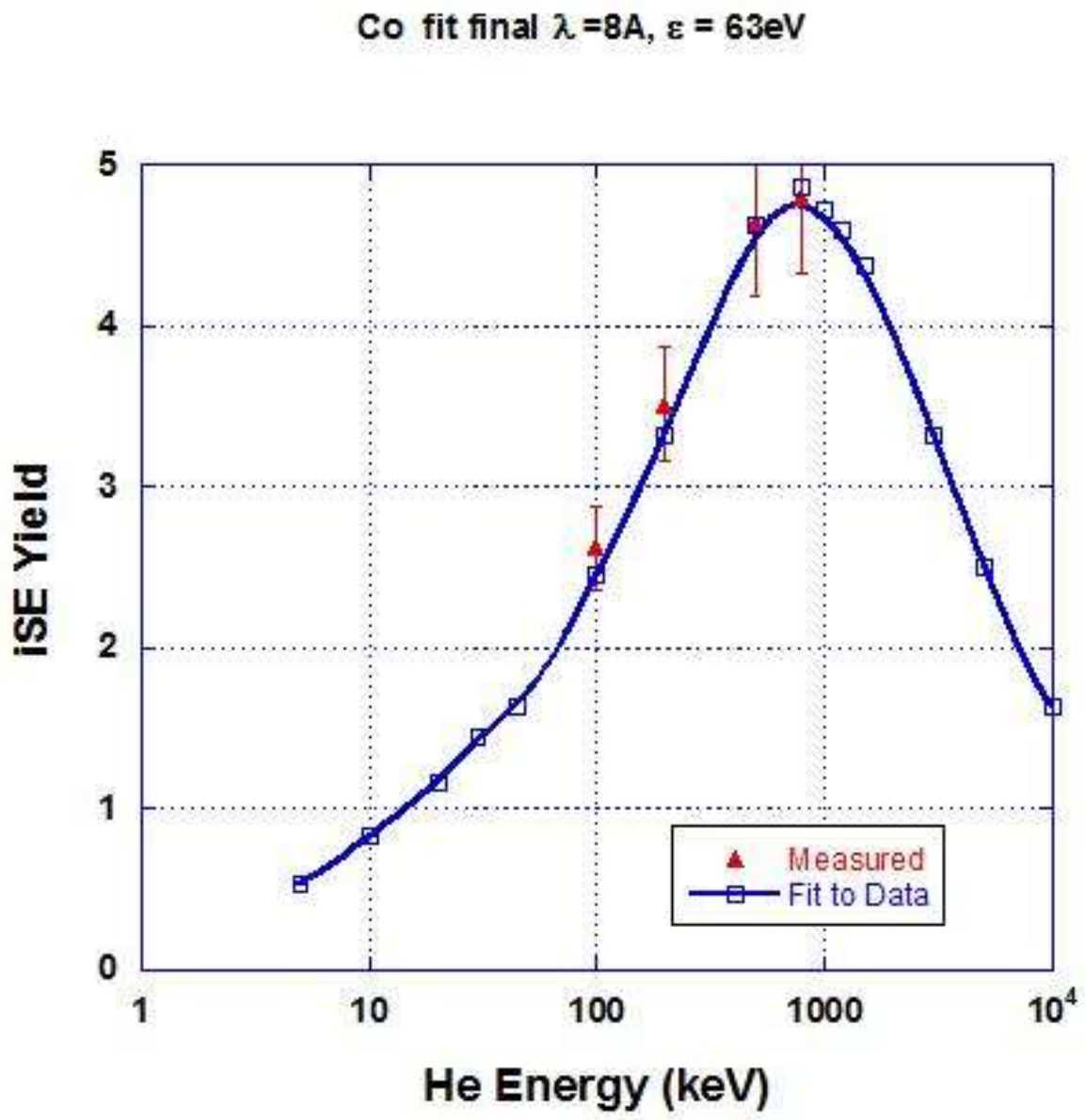

Figure 5.10 Showing the iSE yield parameters and data fit for Cobalt

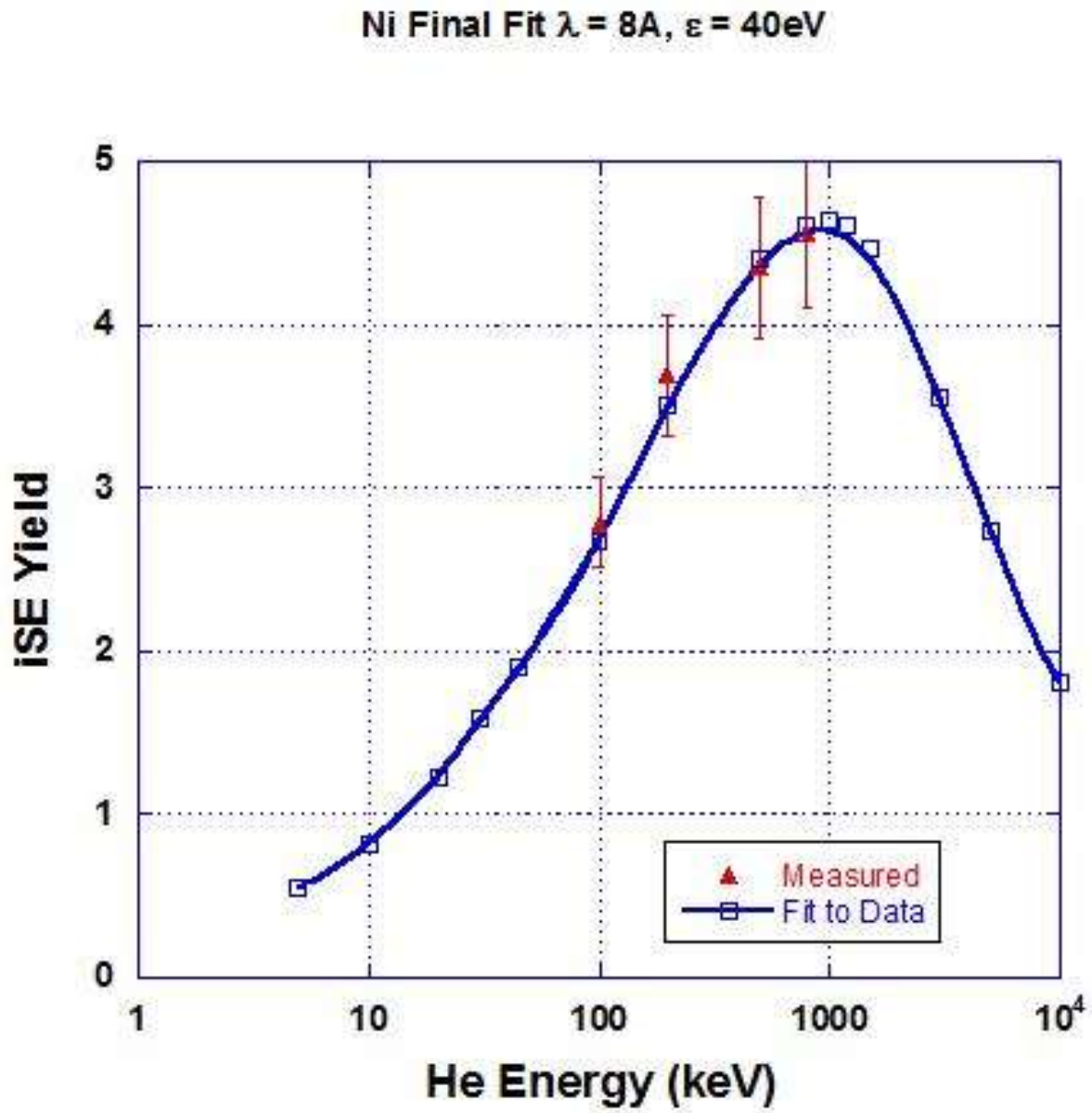

Figure 5.11 Showing the iSE yield parameters and data fit for Nickel

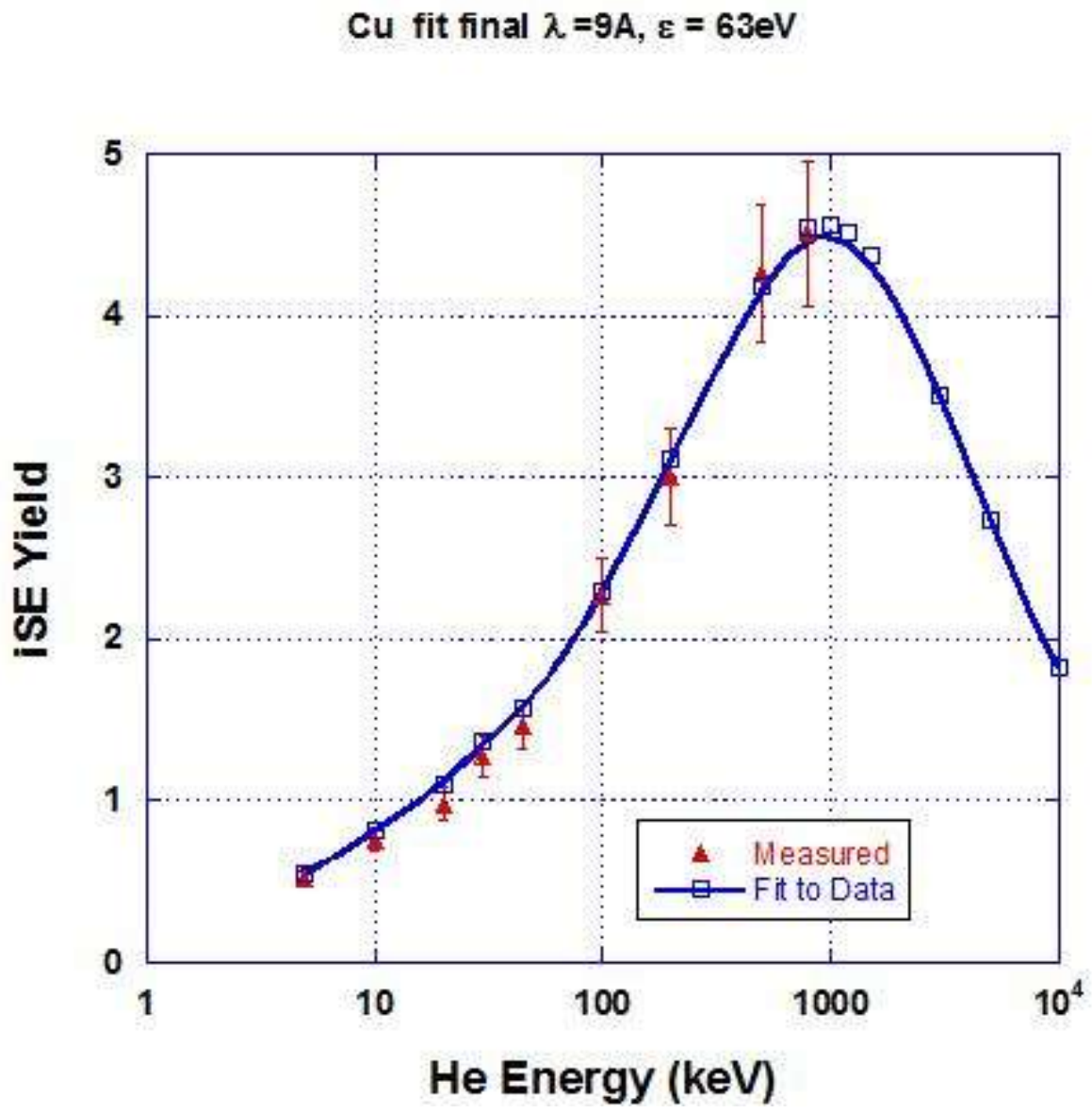

Figure 5.12 Showing the iSE yield parameters and data fit for Copper

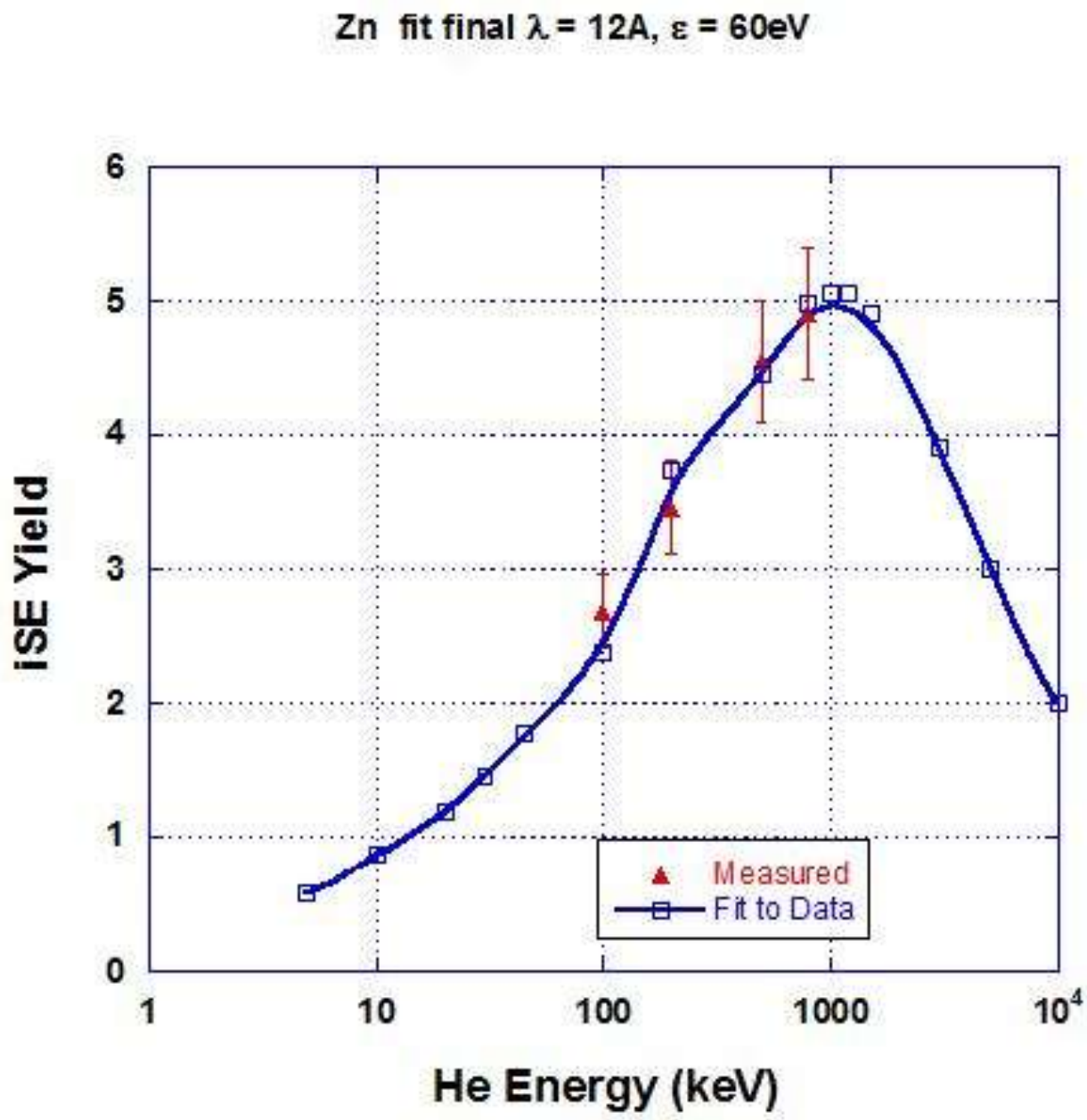

Figure 5.13 Showing the iSE yield parameters and data fit for Zinc

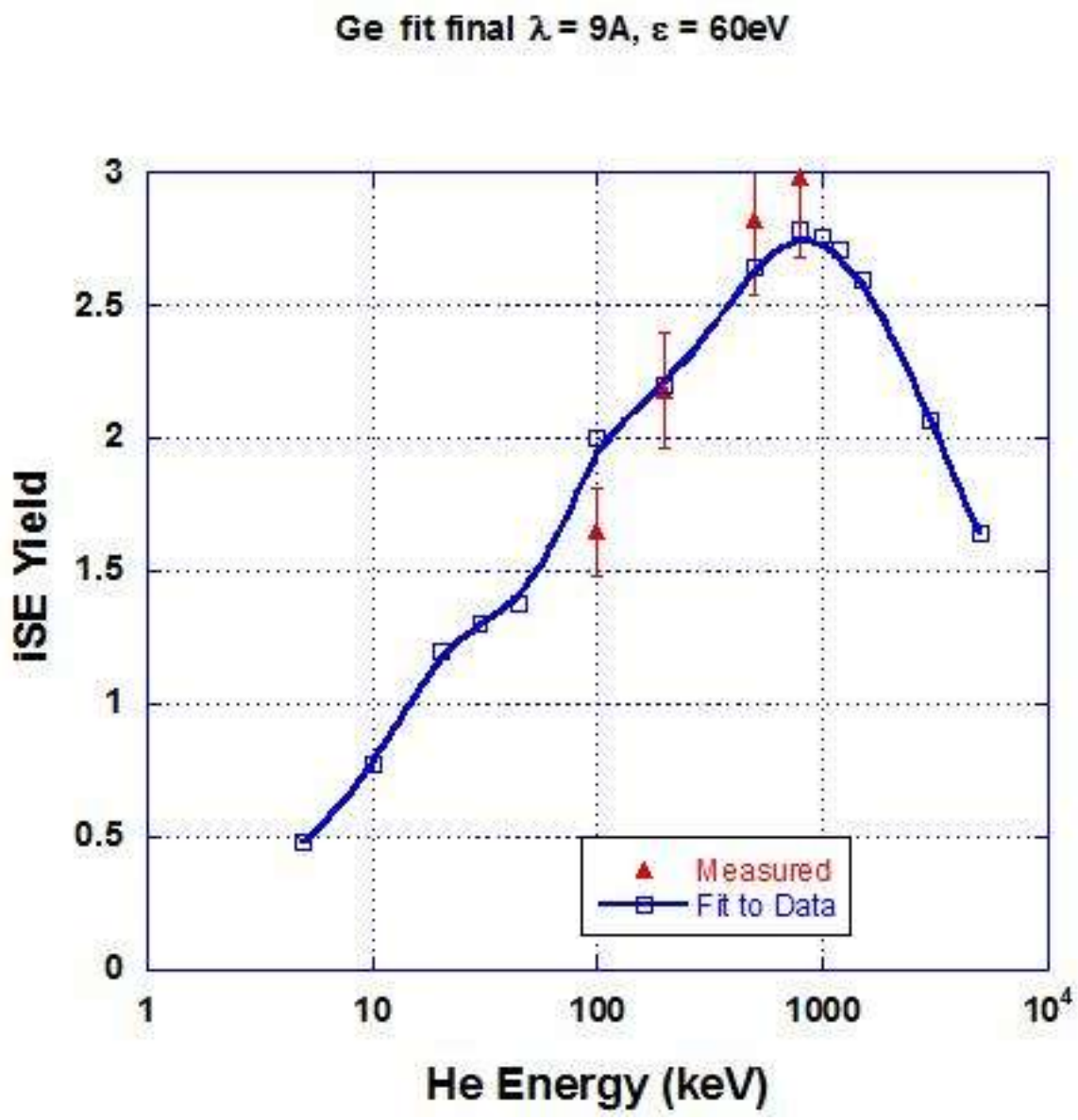

Figure 5.14 Showing the iSE yield parameters and data fit for Germanium

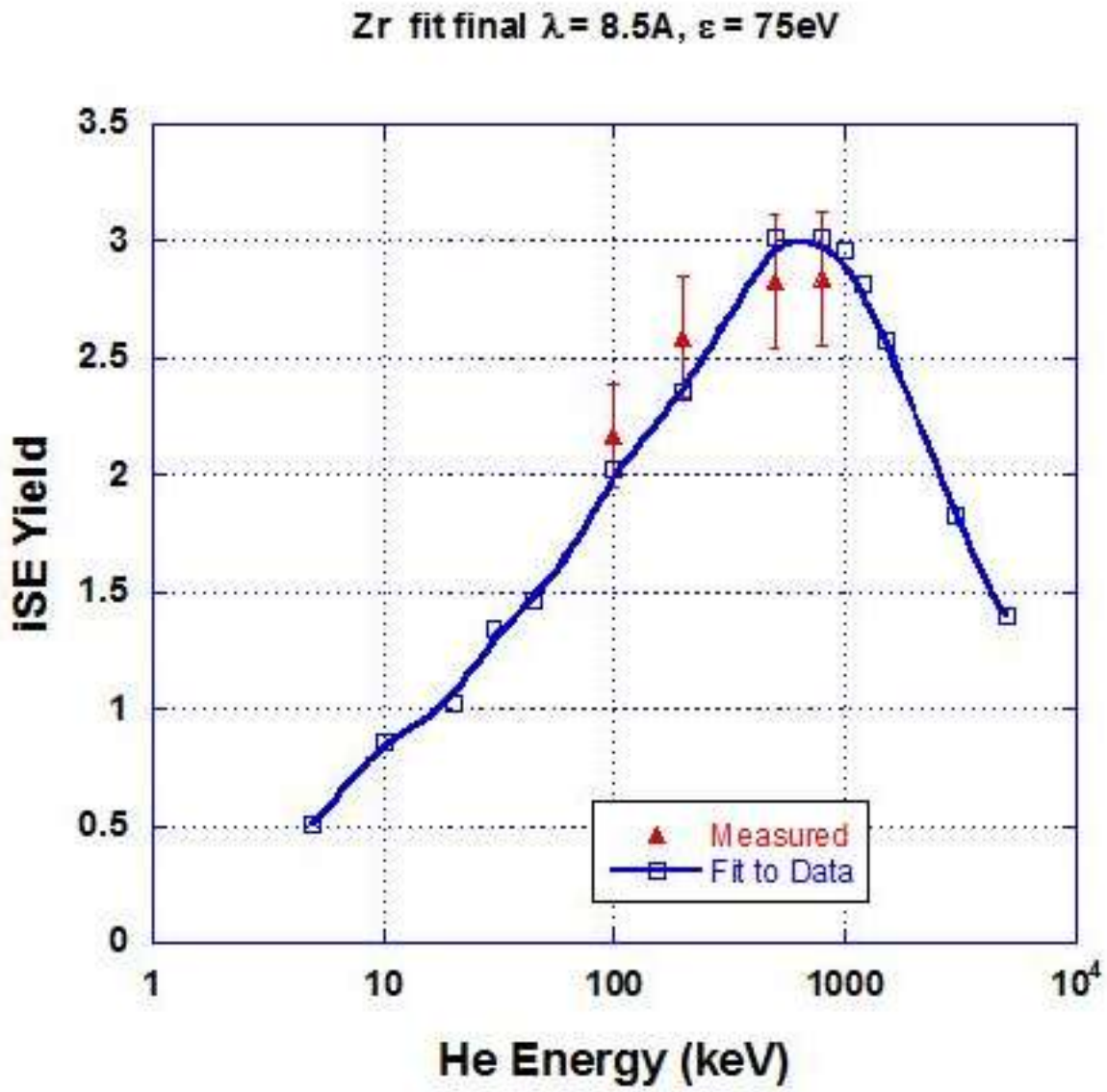

Figure 5.15 Showing the iSE yield parameters and data fit for Zirconium

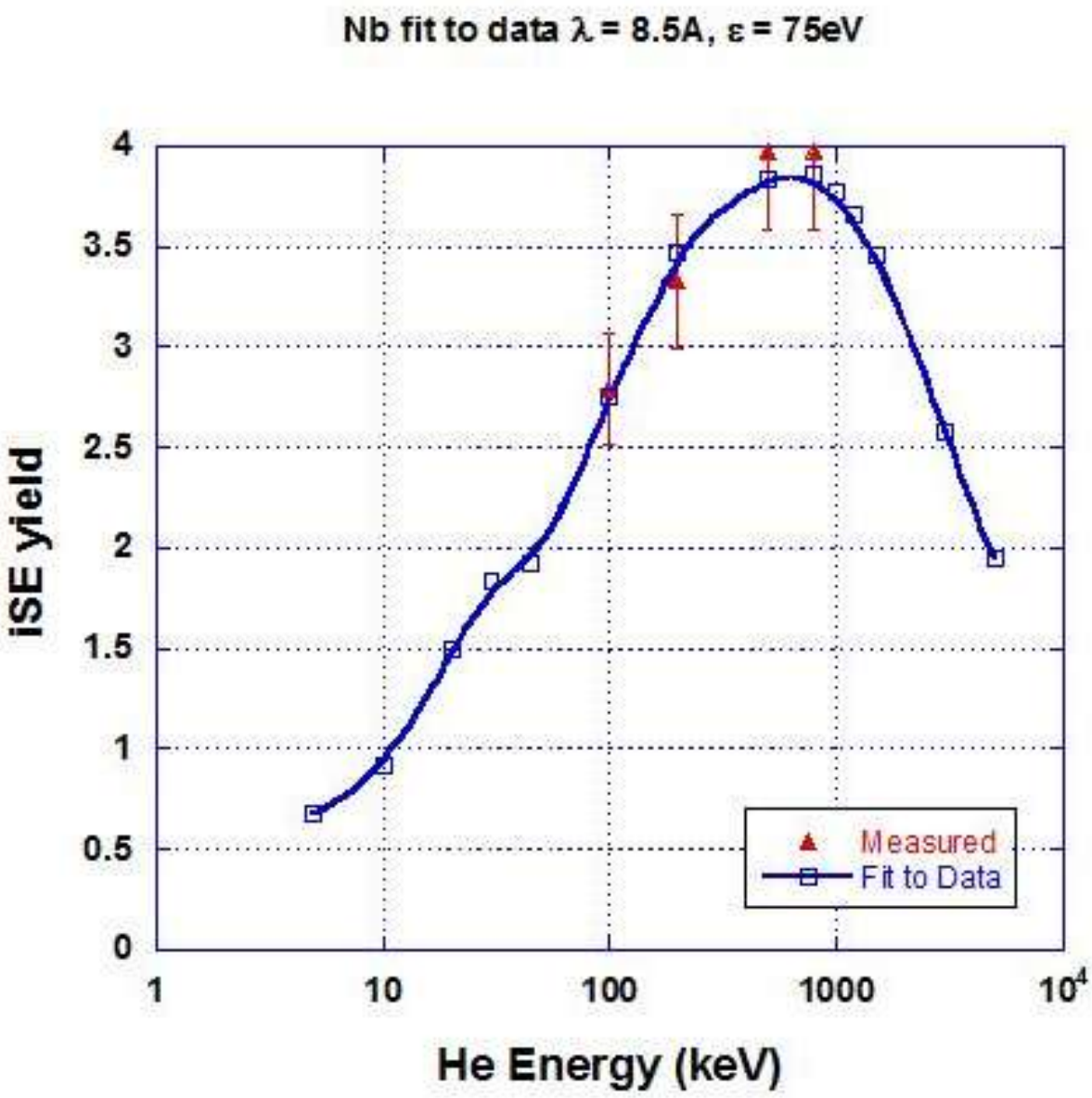

Figure 5.16 Showing the iSE yield parameters and data fit for Niobium

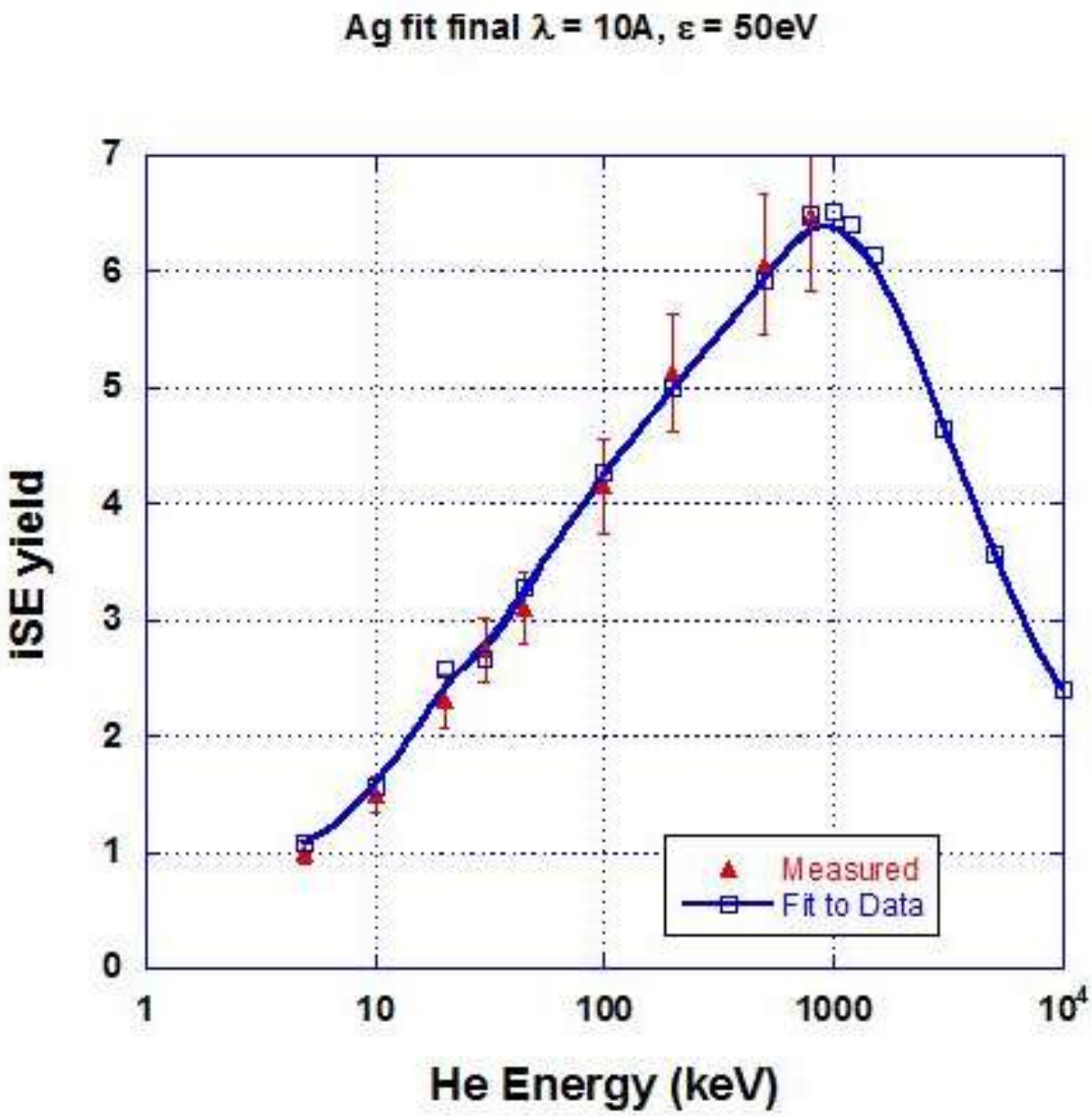

Figure 5.17 Showing the iSE yield parameters and data fit for Silver

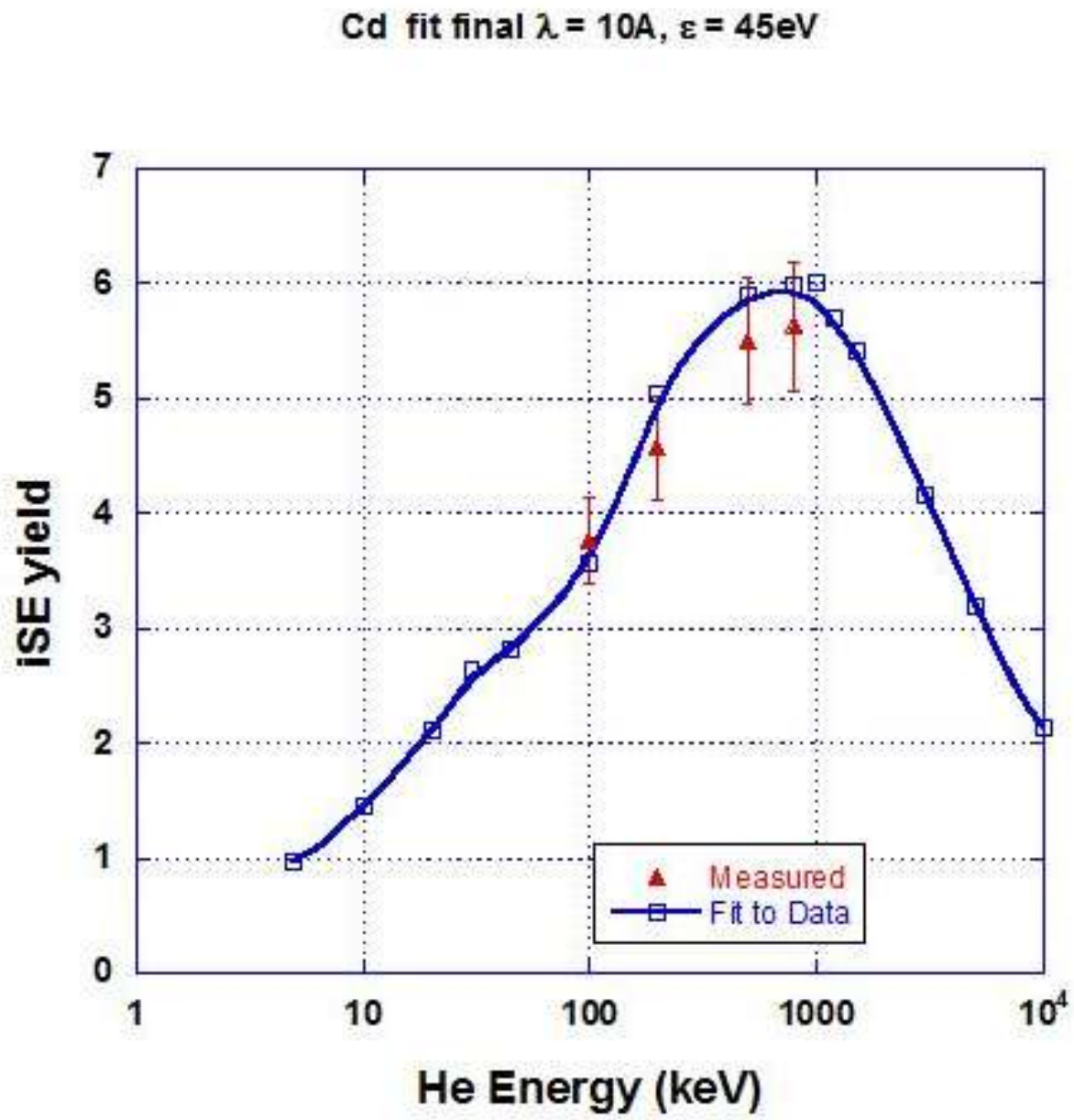

Figure 5.18 Showing the iSE yield parameters and data fit for Cadmium

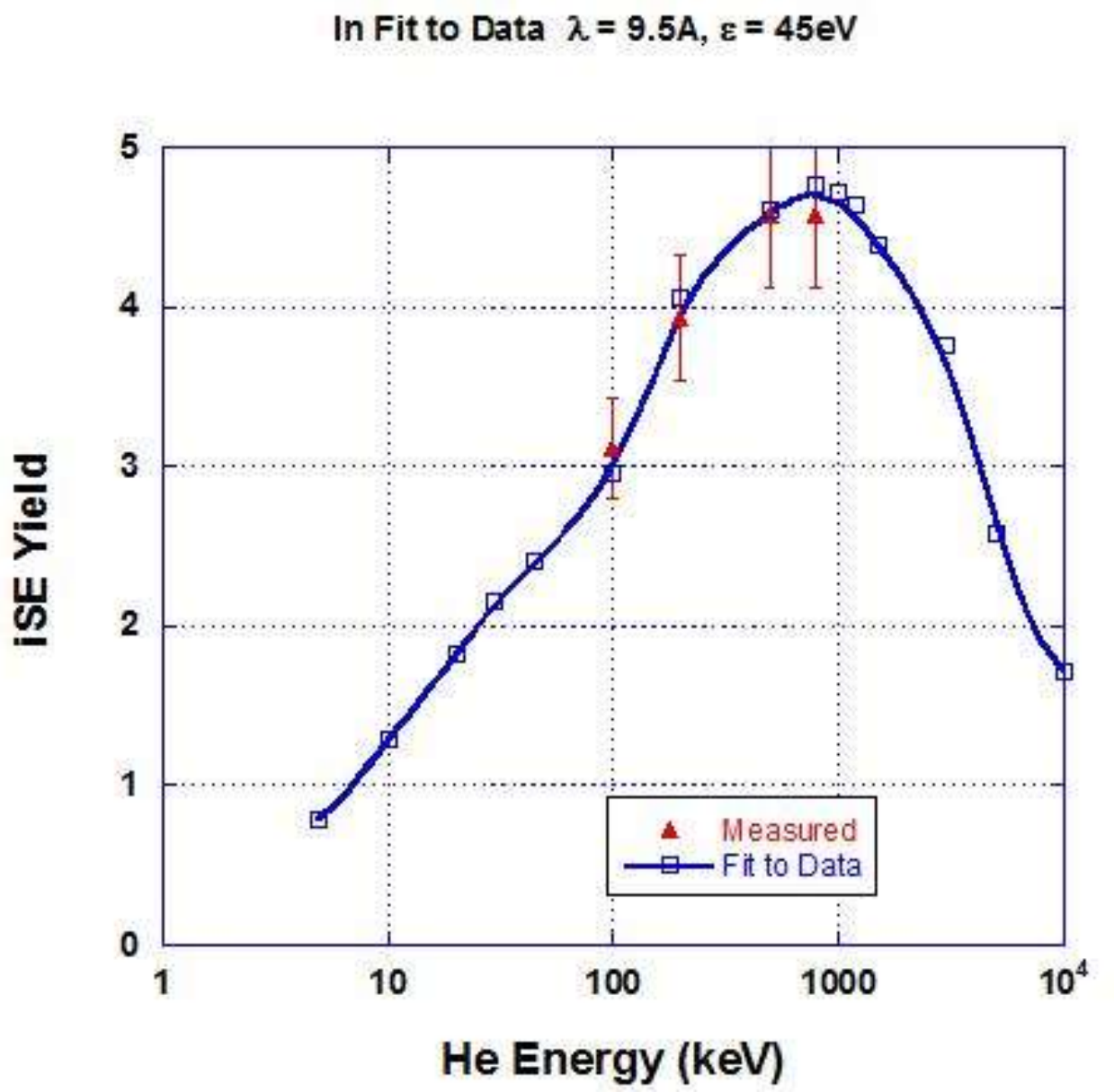

Figure 5.19 Showing the iSE yield parameters and data fit for Indium

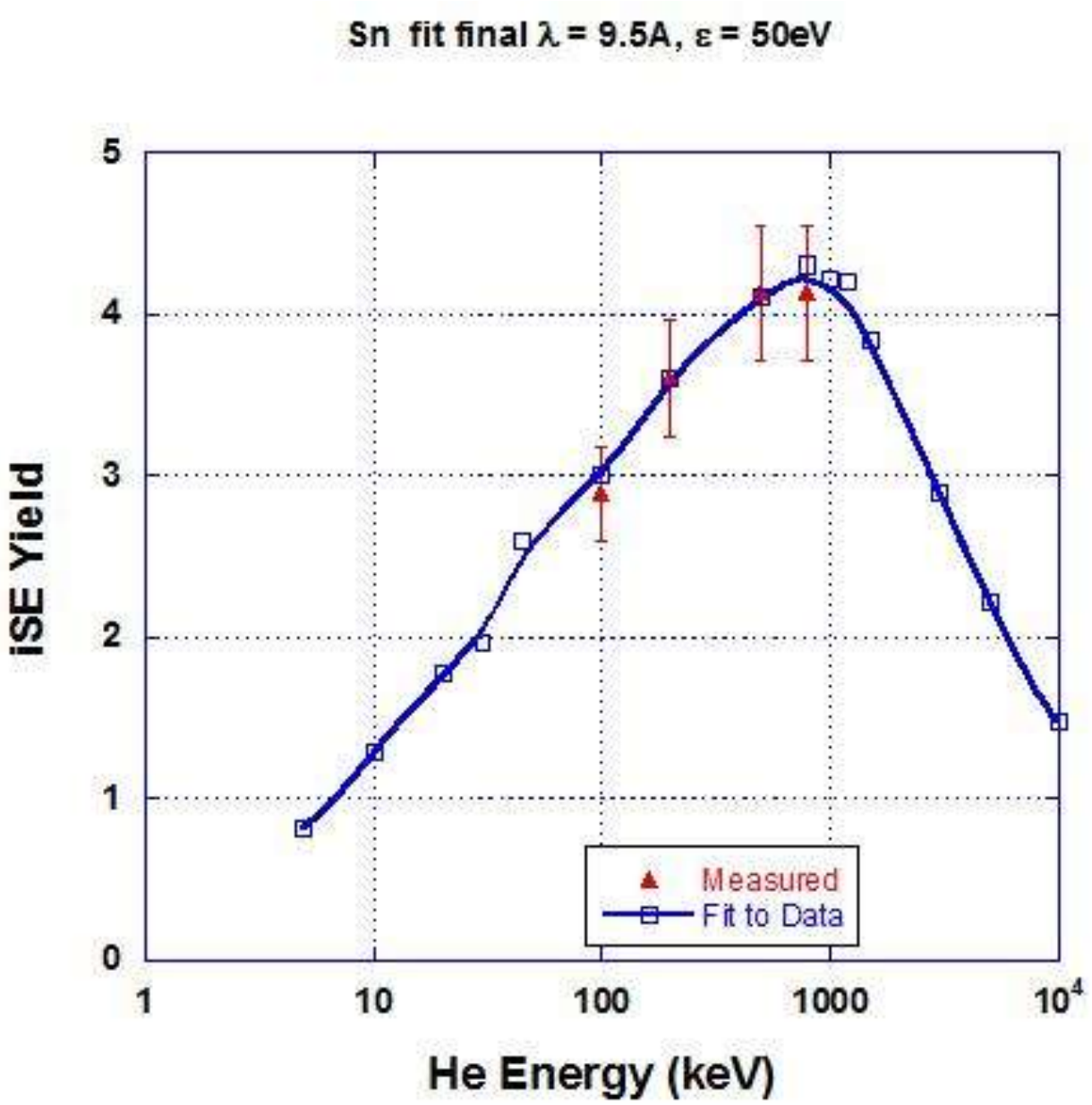

Figure 5.20 Showing the iSE yield parameters and data fit for Tin

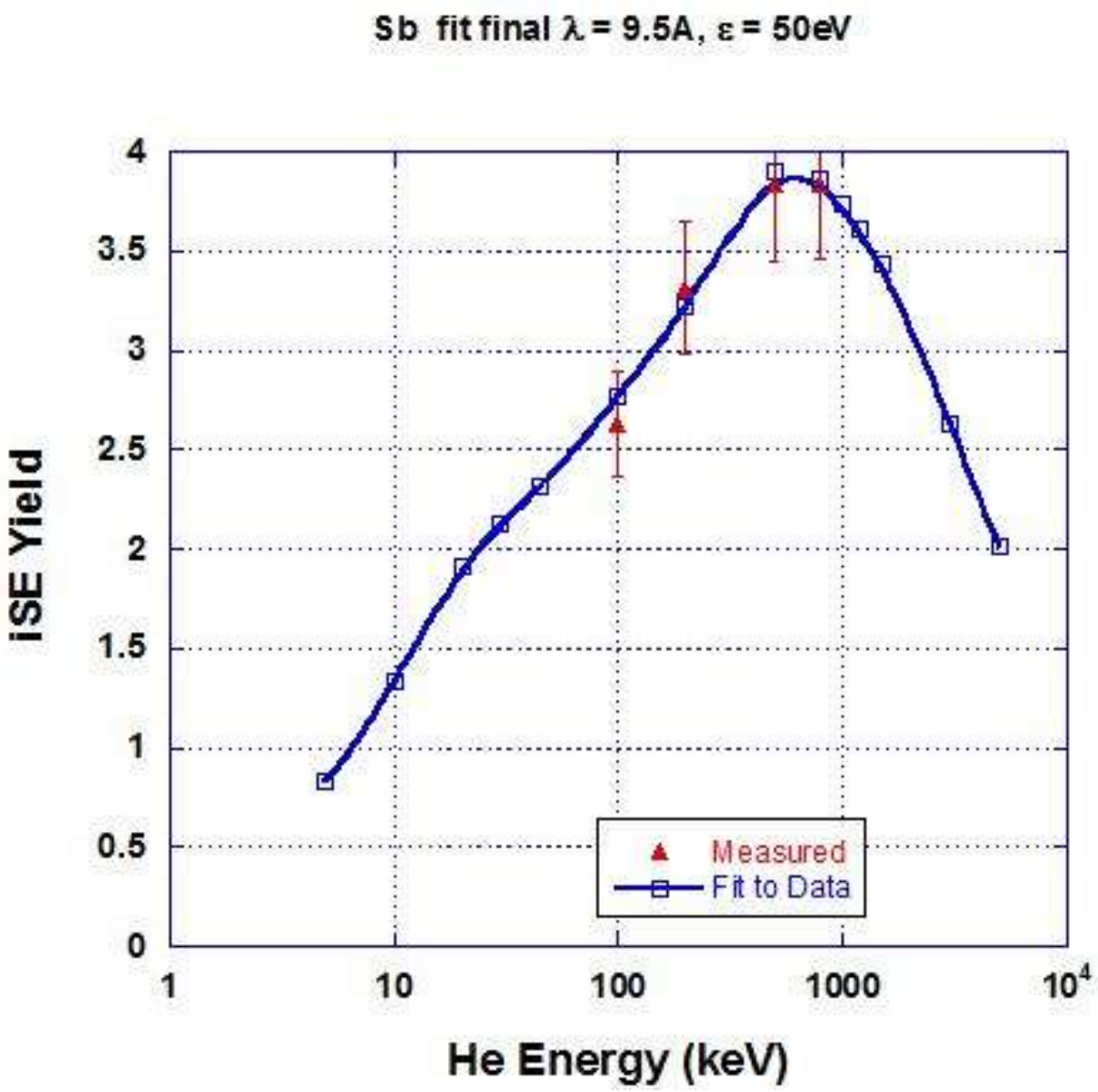

Figure 5.21 Showing the iSE yield parameters and data fit for Antimony

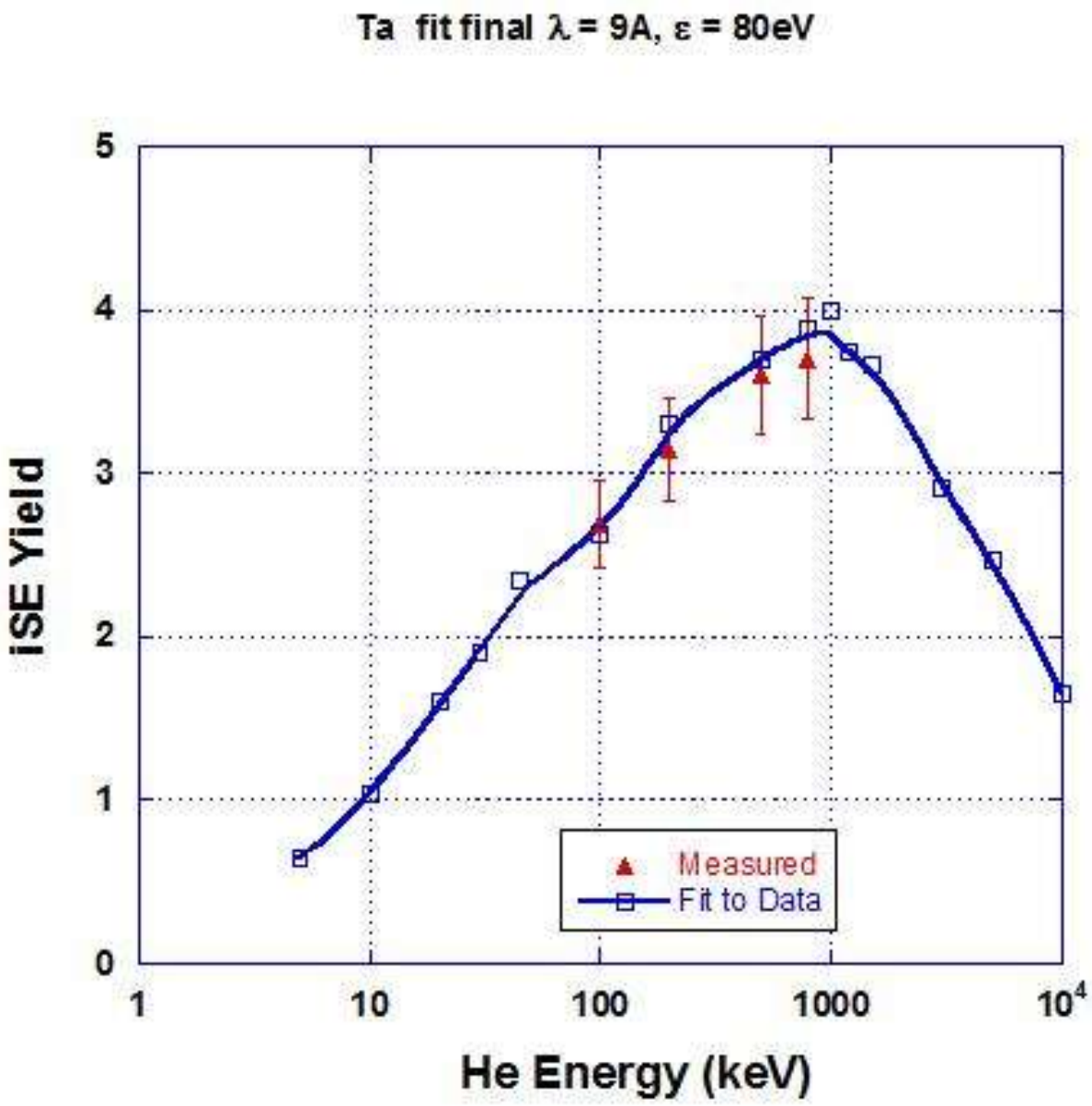

Figure 5.22 Showing the iSE yield parameters and data fit for Tantalum

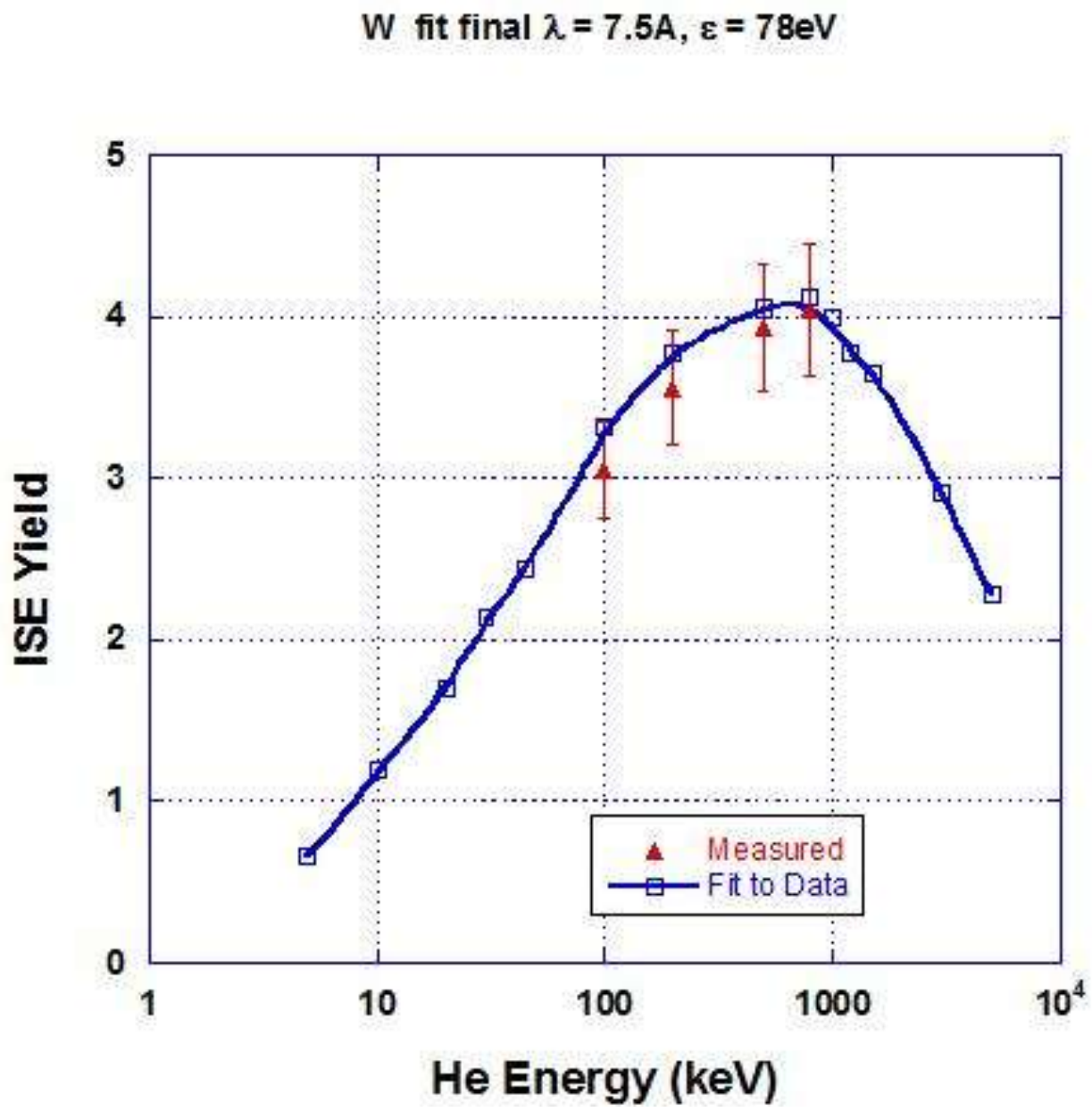

Figure 5.23 Showing the iSE yield parameters and data fit for Tungsten

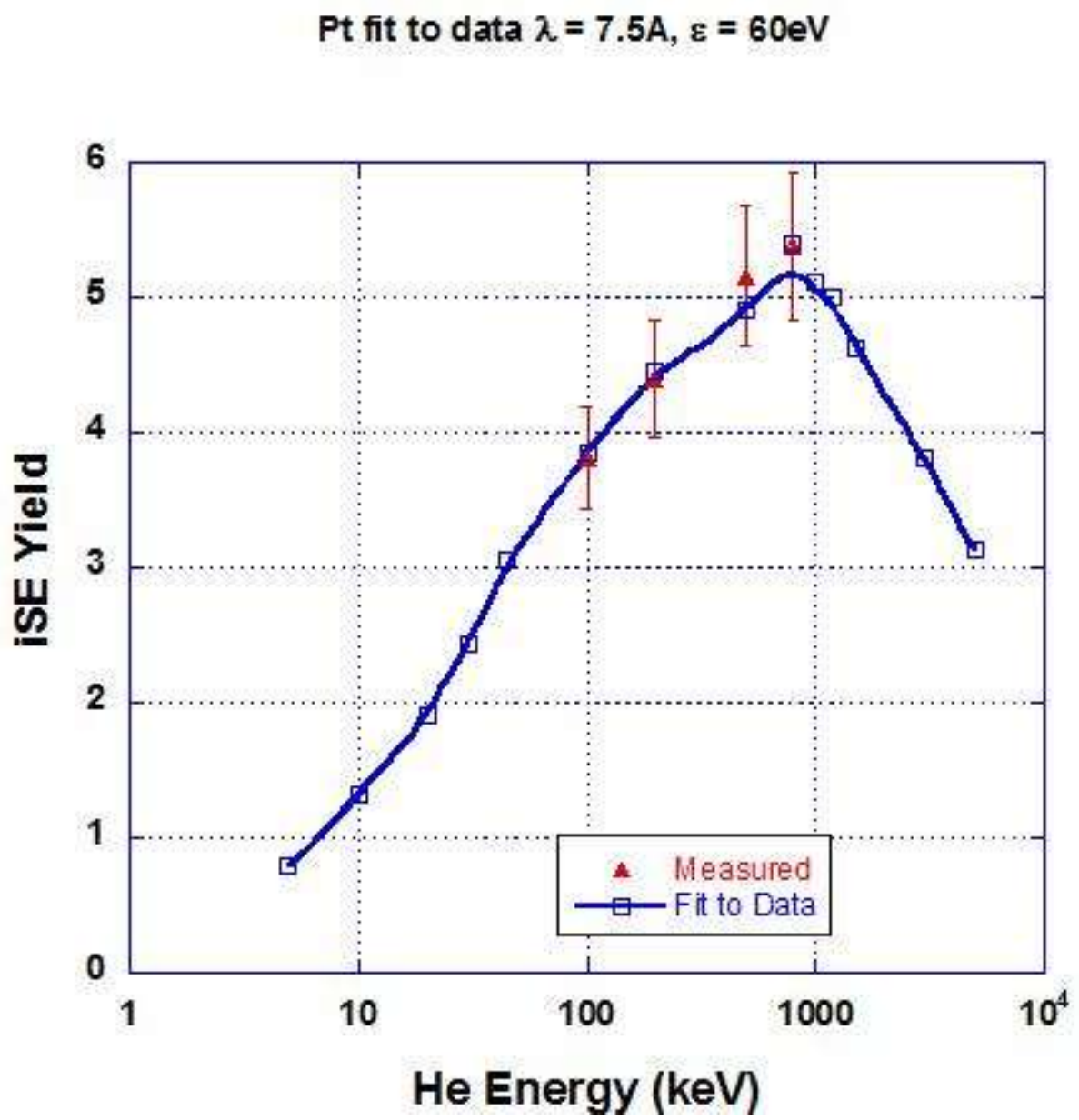

Figure 5.24 Showing the iSE yield parameters and data fit for Platinum

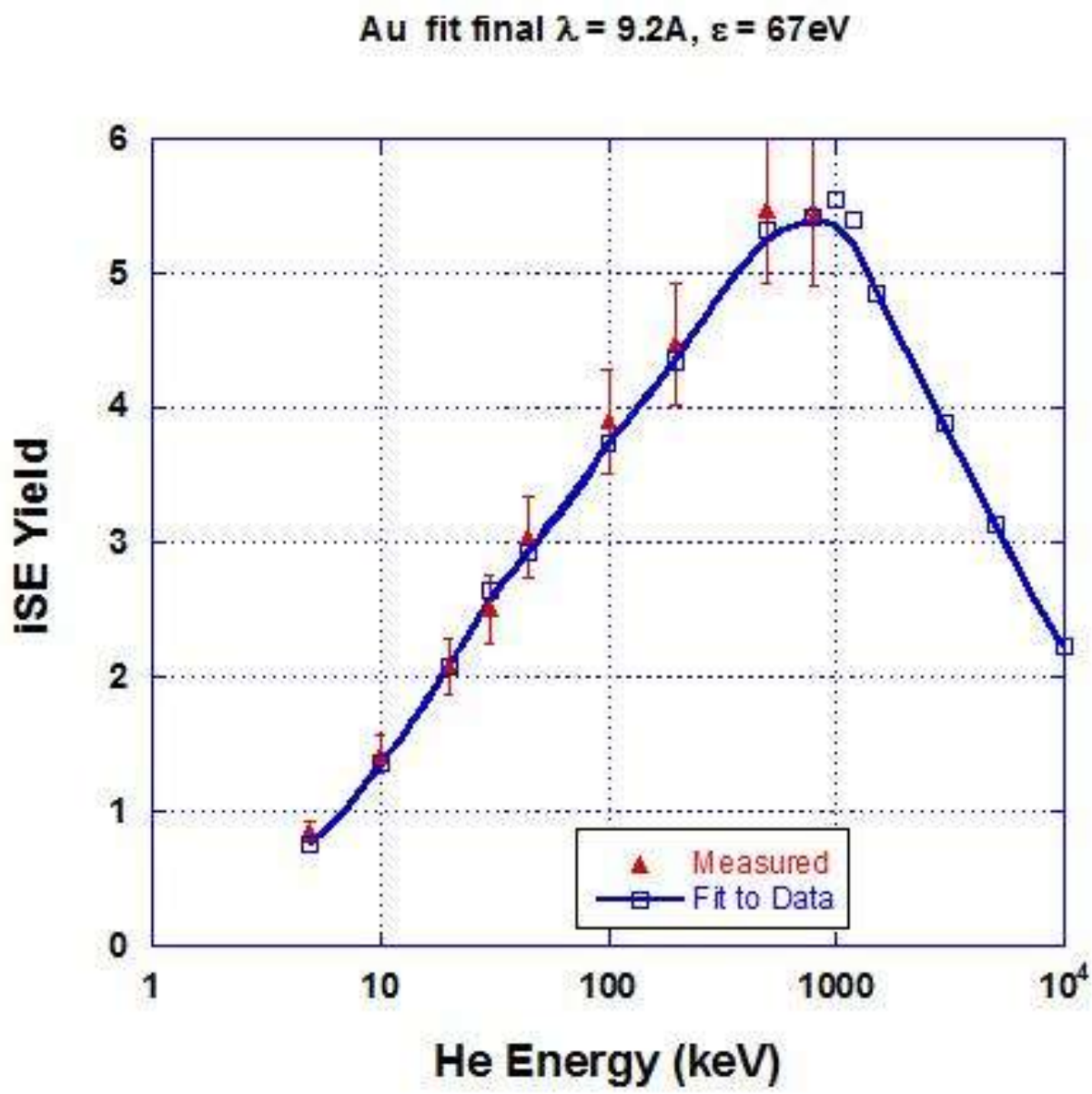

Figure 5.25 Showing the iSE yield parameters and data fit for Gold

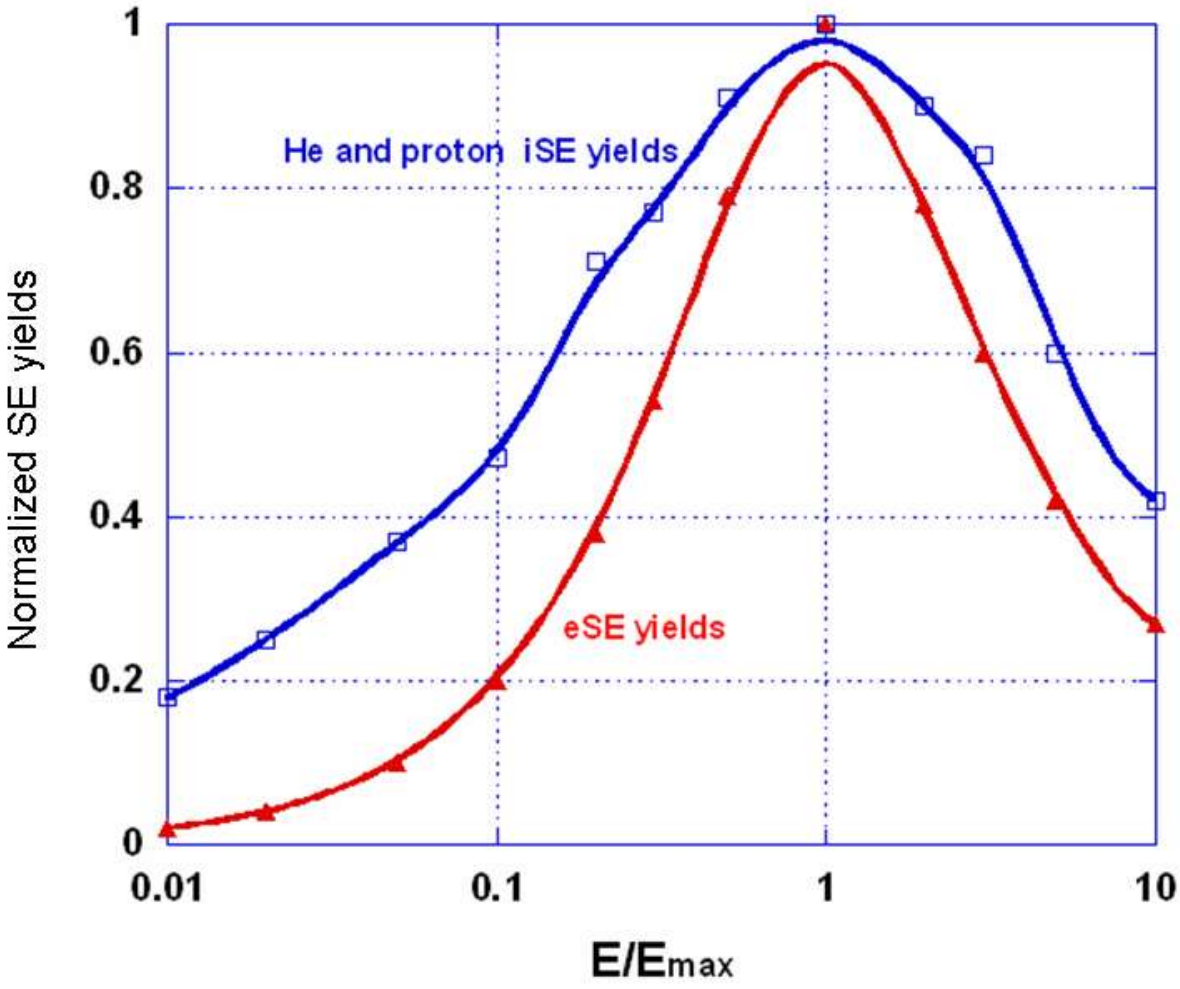

Figure 5.26 Showing the Universal Electron yield curve under electron, proton and Helium ion bombardment.

Table 5.1 – Fitted ε(eV) and λ_d(A) (Angstrom) parameters for helium ion beam irradiation of various target elements and the corresponding predicted iSE γ_{max} and Emax (energy) values.

Z	Element	λ_d(A)	ε(eV)	γ_{max}	E_{max} (keV)
3	Li	25	40	3.3	800
4	Be	9.3	65	2.3	500
6	C	10.8	59	4.1	600
12	Mg	10.8	41	3.3	650
13	Al	12	60	3.4	500
22	Ti	8.5	65	3.3	800
24	Cr	7.5	70	3.8	800
25	Mn	8	65	4.2	800
27	Co	8	63	4.9	800
28	Ni	8	60	4.6	1000
29	Cu	9	63	4.6	950
30	Zn	12	60	5.1	1000
32	Ge	9	60	2.8	800
40	Zr	8.5	75	3	650
41	Nb	8.5	75	3.9	650
47	Ag	10	50	6.5	1000
48	Cd	10	45	6.1	900
49	In	9.5	45	4.8	800
50	Sn	9.5	50	4.3	800
51	Sb	9.5	50	3.9	650
73	Ta	9	80	4	1000
74	W	7.5	78	4.1	800
78	Pt	7.5	60	5.4	800
79	Au	9.2	72	5.6	1000

maximum occurs at a velocity of about 6 to $8*10^8$ cm/sec, a value which corresponds closely to the velocity of electrons in energy range (~ 100eV to 300eV) at which is eSE yield is a maximum (30). For both He ions and electrons these energies or velocities also correspond to the maximum of the relevant stopping power profiles (see Figure 2) so although the iSE yield is both higher than the eSE yield from the same material, and occurs at a much different energy, both the electrons and the helium ions are operating in comparable velocity regimes. There are, however, also important differences between the two cases. For electrons it has been shown [24,25,28,35] that the incident electron range R_{e-} at the $\delta_{max\ eSE}$ condition is approximately

$$R_{e-} \sim 3.\ \lambda_d \quad \text{……..(5.301)}$$

so that eSE yield reaches its maximum because the generation rate (proportional to the stopping power) is high, and because all of the beam interactions occurs close enough to the surface for the SE to escape. In addition there is a significant eSE component from the backscattered electrons. At the $\gamma_{max\ iSE}$ energy, by contrast the helium ions have a range R_{He} of the order

$$R_{He} \sim 1000.\ \lambda_d \qquad (4.302)$$

showing that the maximum in the iSE yield results only from the peak in the stopping power because in this case there is no contribution to the iSE yield from backscattered ions.

Further confirmation of the many similarities between the various types of secondary electron emission is given by the existence of 'universal curves' as shown in Figure 3.03. If eSE yield profiles are plotted in the form $(\delta/\delta_{max\ eSE})$ against $(E/E_{max\ eSE})$, then they all fall, to a good approximation, on a 'universal yield curve' [24,25, 35], a result which is a valuable guide when assessing the accuracy and validity of eSE yield data [28]. As demonstrated in Figure 5.26 IONiSE simulated helium, and experimental proton [12],induced iSE yield profiles when

similarly plotted as ($\gamma/\gamma_{max\ iSE}$) against ($E/E_{max\ iSE}$) also fall on what appears to constitute a 'universal curve' although this is not identical in shape to the electron case. The data so far acquired and analyzed is insufficient to make a convincing case for validity of the 'universal' label, but if such a result can be shown to exist then it will be a valuable step towards gaining a clearer understanding of the behavior of ion generated secondary electrons.

The ε and λ_d from Table 5.2 for iSE can be compared with the ε and λ_d values of Table 5.1 for eSE [28, 30] for the elements in the table. Because the energy spectrum of electron and ion induced secondary electrons differ quite significantly [16] it would not be expected that the 'λ_d' parameter describing the diffusion of the secondary electrons would be identical in the two cases. It is seen, however, that the values are generally similar although the ion values are usually smaller than those for electrons, a result which has implications for high resolution imaging with iSE because the minimum resolvable feature in a scanning microscope image, ignoring beam-optical limitations, has a size of the order of λ_d.

The reason for diffusion length 'λ_d' being lesser in the case of iSE than in the case of eSE can be explained by the 'Matthiessen's Rule' of electrical conductivity in metals and alloys. A helium microscope, invariably implants helium ions into the target (at a rate of a few tens of millions per sec). The implanted He^+ differs in size of that of target atom, its presence creates a local distortion in the crystal lattice as shown in Figure 5.27. Such distortions cause a change in the potential energy PE of the electron as it approaches the impurity, the force experience by the electron due to this being $F = -dPE/dx$. Since these distortions can actually extend several atomic distances they will hinder the motion of the electrons and thereby increase the resistance. Therefore there are now two types of mean times between collisions, one τ_T which is the mean

Table 5.2 – Fitted ε(eV) and λ_d(A) (Angstrom) parameters for electron beam irradiation of various target elements and the corresponding predicted eSE δ_{max} and Emax (energy) values. R is the range at which maximum eSE occurs. Courtesy of Lin and Joy [28]

Z	ε (eV)	λ (nm)	$\frac{\varepsilon}{\lambda}$	R (nm)	$\frac{R}{\lambda}$	δ^m	E_{PE}^m (keV)
3	45	2.0	2.25	8	4.00	0.59	0.15
4	70	1.0	7.0	3	3.00	0.55	0.20
5	40	1.0	4.0	3	3.00	1.05	0.24
6	80	2.5	3.2	7	2.80	1.06	0.40
12	50	1.3	3.85	6	4.62	0.80	0.24
13	32	1.7	1.88	10	4.71	2.00	0.40
14	90	2.7	3.33	12	4.44	0.89	0.45
19	100	2.0	5.0	16	8.00	0.27	0.22
20	40	0.5	8.0	5	10.0	0.33	0.15
21	30	0.5	6.0	4	8.00	0.76	0.20
22	25	0.5	5.0	4	8.00	1.21	0.25
24	47	1.2	3.92	6	6.67	1.80	0.60
26	45	0.6	7.5	4	6.67	1.15	0.35
28	65	1.0	6.5	5	5.00	1.19	0.50
29	35	0.6	5.83	4	6.67	1.53	0.40
30	120	2.5	4.80	11	4.40	1.03	0.70
31	90	1.5	6.00	8	5.33	0.78	0.45
32	50	1.0	5.00	8	8.00	1.00	0.40
34	28	0.5	5.60	5	10.0	0.86	0.25
38	50	1.0	5.00	11	11.0	0.49	0.25
39	60	1.0	6.00	11	11.0	0.65	0.40
40	35	0.5	7.00	5	10.0	0.83	0.30
41	20	0.3	6.67	3	10.0	1.16	0.25
42	60	1.0	6.00	7	7.00	1.14	0.50
46	55	1.0	5.50	7	7.00	1.41	0.55
47	50	1.0	5.00	9	9.00	1.43	0.60
48	70	1.5	4.67	13	8.67	1.16	0.65
49	40	1.0	4.00	11	11.0	1.29	0.50
50	43	1.0	4.30	10	11.0	1.12	0.50
51	80	2.5	3.20	16	7.60	1.16	0.70
52	50	1.0	5.00	9	9.00	0.84	0.35
55	60	3.5	1.71	38	10.9	0.72	0.40
56	53	2.0	2.65	24	12.0	0.83	0.45
57	54	1.0	5.40	15	15.0	0.72	0.50
72	45	1.0	4.50	11	11.0	1.39	0.60
73	60	0.7	8.57	9	12.9	0.93	0.65
74	20	0.2	10.0	3	15.0	1.06	0.25
75	50	0.6	8.33	7	11.7	1.20	0.60
78	30	0.5	6.00	6	12.0	1.69	0.55
79	35	0.5	7.00	7	12.0	1.28	0.50
80	48	1.0	4.80	14	14.0	1.23	0.70
81	40	0.8	5.00	11	13.8	1.09	0.50
82	40	0.8	5.00	12	15.0	1.06	0.50
83	80	2.0	4.00	20	10.0	0.98	0.70

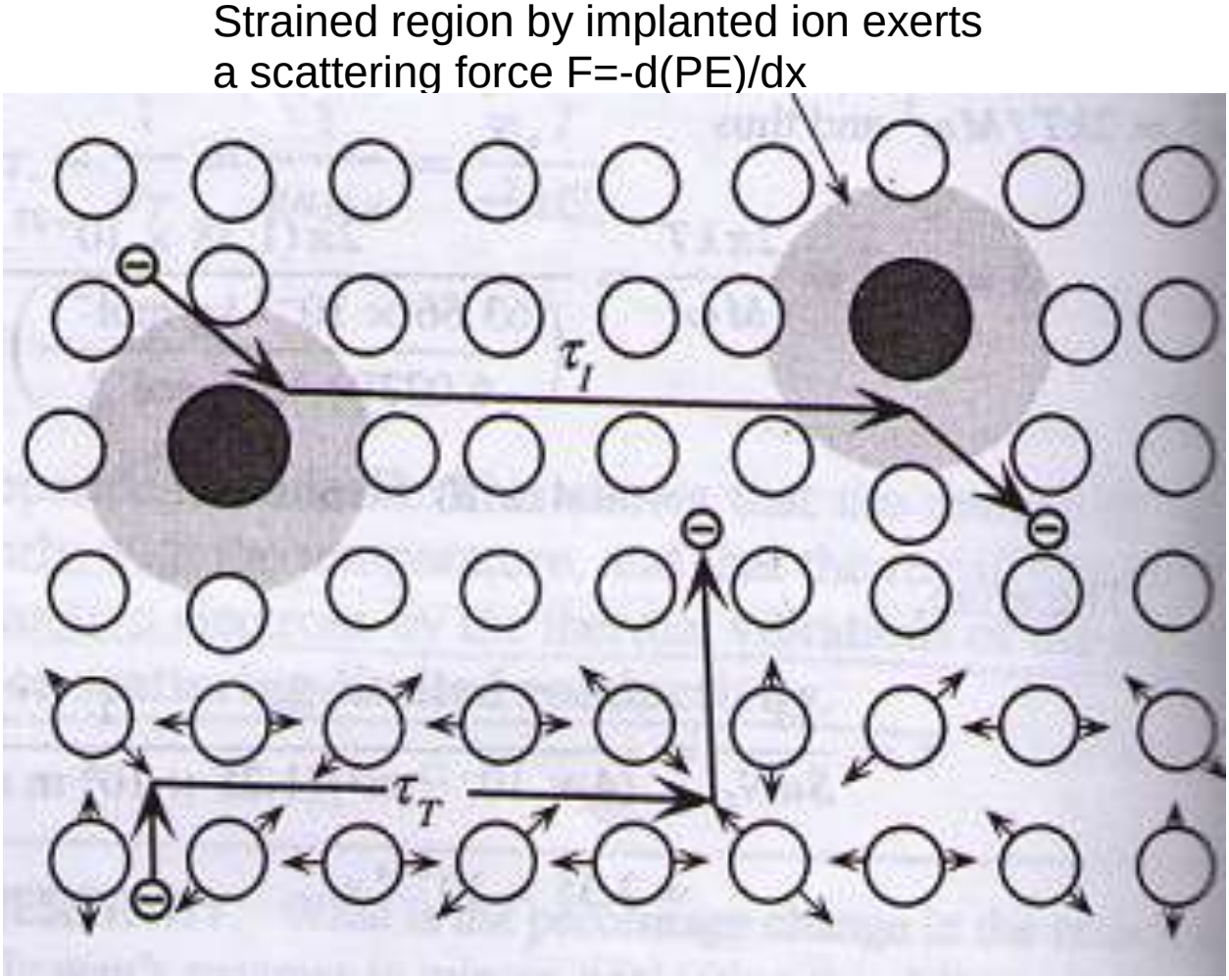

Figure 5.27 Showing the change in the local potential energy due to ion implantation, to elaborate the Matthiessen's rule. Courtesy of Kasap [67].

time between scattering from thermal vibrations of host atoms only and τ_I which is the mean free time between scattering from implanted ions only. The effective mean scattering time τ can then be given as

$$\frac{1}{\tau} = \frac{1}{\tau_T} + \frac{1}{\tau_I} \quad \text{.....(5.303)}$$

Hence the effective mean scattering time τ is lesser than both τ_T and τ_I. The diffusion length 'λ_d' is directly proportional to the mean time between scattering. In case of eSE's the mean scattering time is larger since it is only due to the thermal vibrations of the host atoms, while in the case of iSE's it is smaller because of scattering by both the host atom and the implanted atom. Hence lower mean time between scattering for iSE's corresponds to a lower 'λ_d'.

However from Table 5.1 and Table 5.2 it can be seen that for high atomic number targets like Au, the diffusion length 'λ_d' shows a contradictory behavior being higher in the case of iSE than in the case of eSE. The reason for this is ion straggling from high Z targets

5.4 Applying IONiSE to imaging

With the assistance of IONiSE it is now possible to predict some of the important details of helium iSE imaging and to compare such results with those for the equivalent eSE image, as shown in the following examples.

5.41 Topograghic Yield

The single most important application of secondary electron imaging is to reveal surface topography, a task made possible because of the variation of SE yield with the angle of incidence of the incoming beam to the surface [1]. As already explained in the previous chapter, for

electron irradiation the SE yield $\delta(\theta)$ at some angle of incidence θ is related to the yield $\delta(0)$ at normal incidence by the relation [1, 24,25]

$$\delta(\theta) = \delta(0).\ \sec(\theta) \quad \text{…….(5.401)}$$

This simple expression agrees well with measured data for all incident electron energies above a few keV and applies about equally well to both low and high atomic number targets.

Figures 5.28, 5.29 and 5.30 shows the topographic yield behavior predicted by IONiSE for iSE generated by He ion irradiation for three materials Li, Cu, and Au at 5 and at 30keV. For comparison the sec(θ) variation of the eSE signal is shown as a solid line. At the lower energy the topographic variation from both lithium and copper lies close to and slightly above the 'sec(θ)' profile although the response of the gold falls below the eSE profile at all energies. At the higher energy however iSE topographic yield profiles for that of Li and Cu are above the 'sec(θ)' line, while that of the Au lies below the 'sec(θ)' line . It can be also generalized from these Figures that the topographic contrast is higher at higher energies for all materials. The behavior of the topographic yield profile and the magnitude of the iSE yield with tilt angle predicted by IONiSE are good agreement with those calculated by Inai et al. [22], and with the experimental data by Ferron et al. from clean surfaces in ultra-high vacuum [33]. These results confirm that iSE images will show topographic contrast that is generally similar in form to that from eSE. However, unlike the eSE situation where the topographic yield profile is to a good approximation independent of beam energy and sample composition, the magnitude of the iSE topographic variation depends on both the target material and the incident ion energy. As a consequence in situations where quantitative determinations of topography are required, as for example in semiconductor device metrology, the use of ion beams will require the development

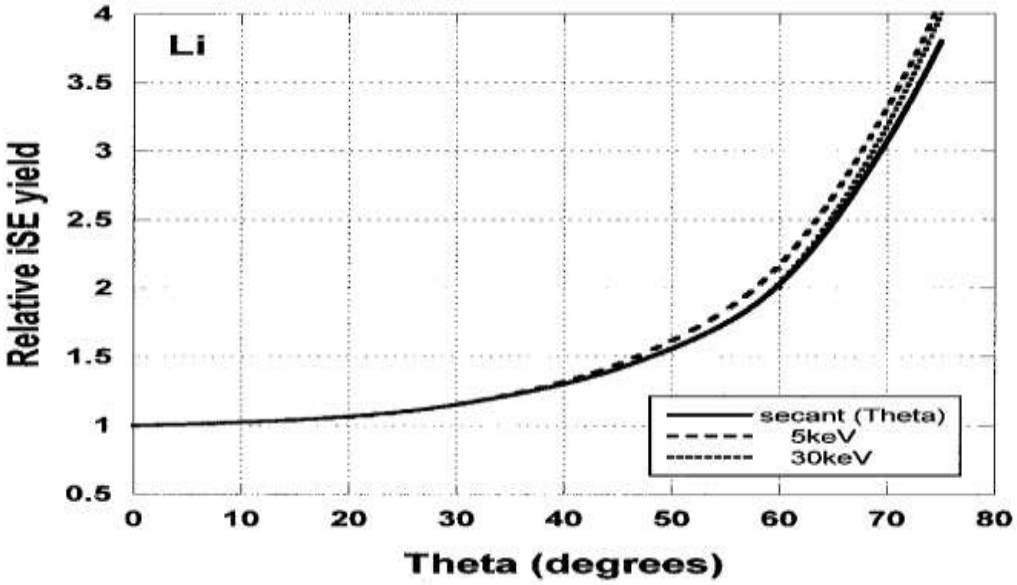

Figure 5.28 Showing the Topographic yield of He^+ on Li. Data from IONiSE

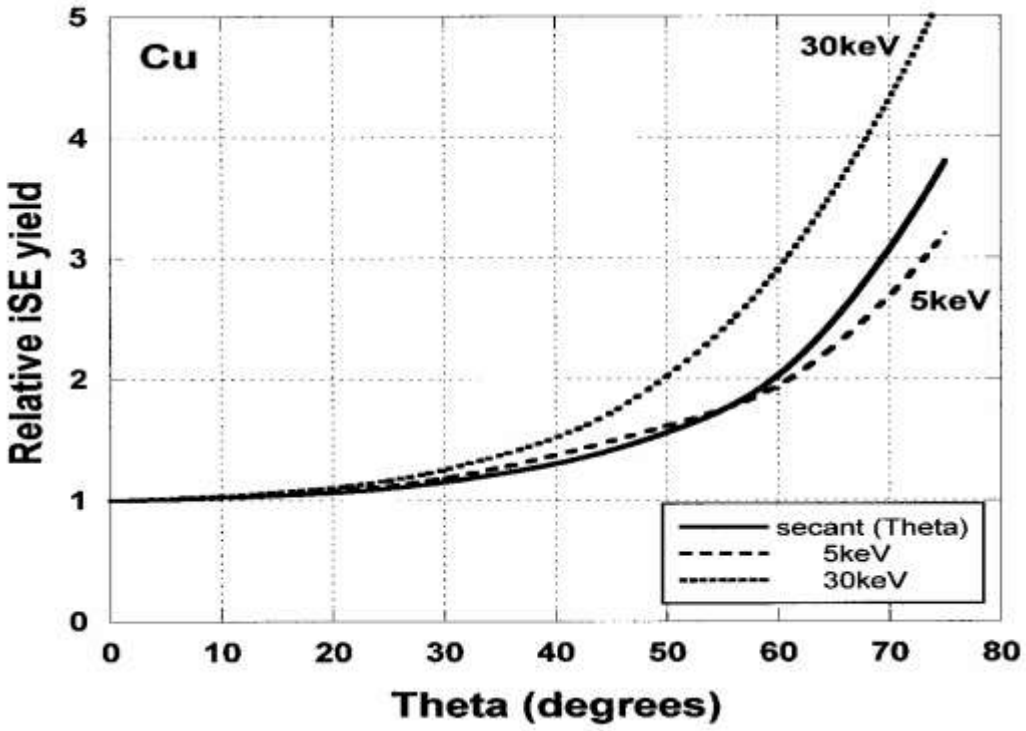

Figure 5.29 Showing the Topographic yield of He^+ on Cu. Data from IONiSE

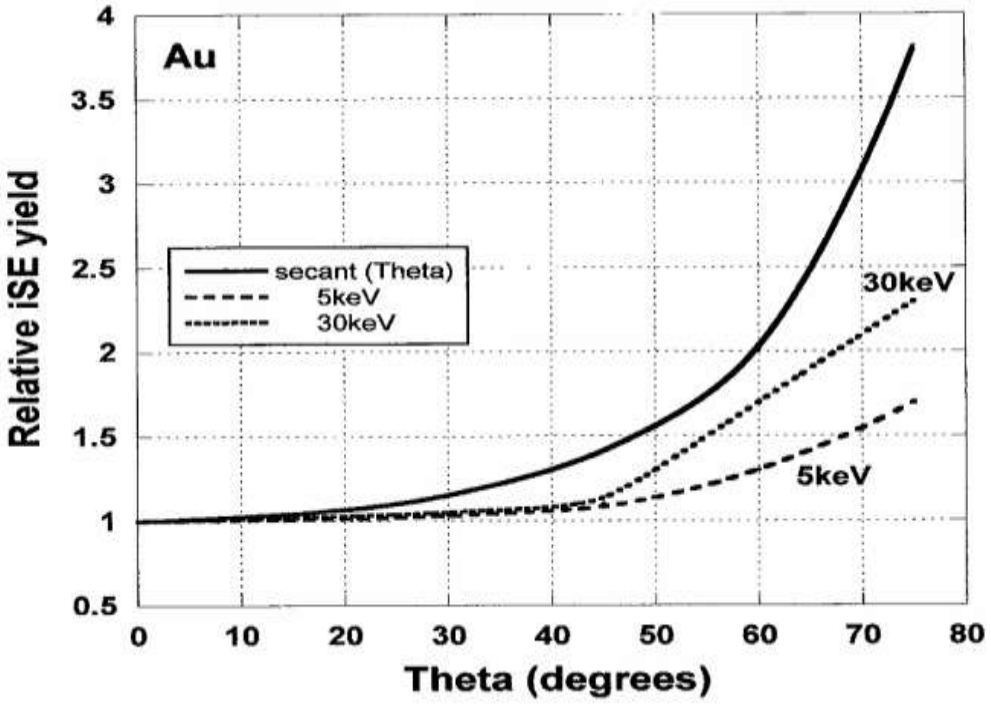

Figure 5.30 Showing the Topographic yield of He^+ on Cu. Data from IONiSE.

of new algorithms which can correct for these effects.

5.42 The SE2/SE1 Ratio

Secondary electrons can only escape from a sample when they are generated close to the surface by either an incident electron or a backscattered electron. Those SE generated by incident particles are classified as being of type SE1, while those generated by exiting backscattered particles are classified as SE2 [24,25] as shown in Figure 5.31. For electron generated SE production at a typical imaging energy of 25keV the ratio eSE2/eSE1 is of the order of 1:1 or higher [25, 31] and consequently the contrast from small features is degraded because, while the eSE1 component is produced at the point of impact of the finely focused electron beam, the eSE2

eSE1 component is produced at the point of impact of the finely focused electron beam, the eSE2 signal emerges from a region the fully width of the interaction volume.

Figure 5.32 shows the iSE2/iSE1 ratio for helium ion irradiation on Al, Cu, Ag, and Au computed by IONiSE. The ratio is seen to vary with both the target material and the beam energy, rising from a low initial value, reaching a peak between 10 and 50keV whose magnitude and position depends on the material, and then falling away steadily at higher energies. This behavior is a consequence of the ion beam energy falling on the left hand side of the stopping power profile (Figures 1.03). Backscattered ions have lower energy than the incident ions and so experience a smaller stopping power and generate fewer SE. As the energy is raised each backscattered ion can produce more SE because the stopping power rises with rising energy. However, the number of backscattered ions falls quickly with energy and the iSE they produce are generated too deep beneath the surface for them to escape, so the iSE2/iSE1 ratio reaches a

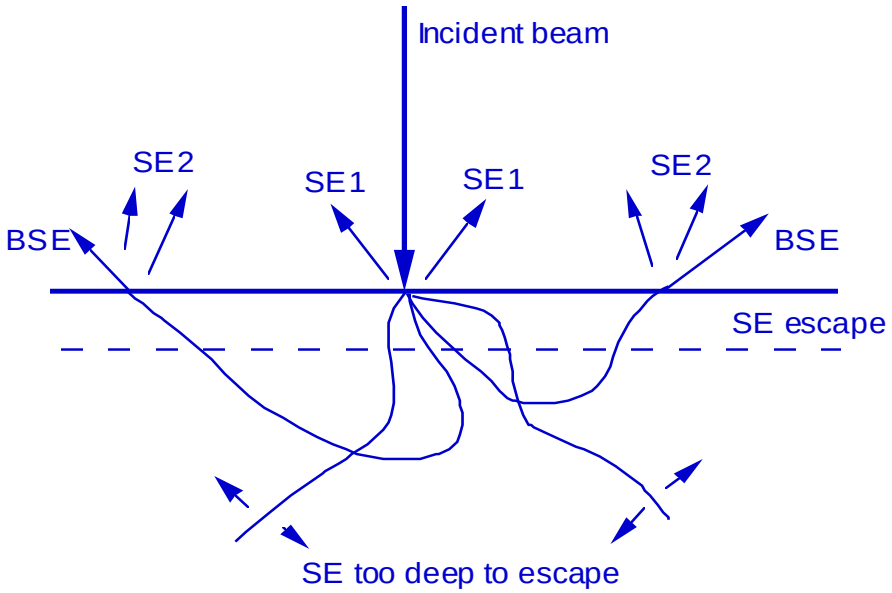

Figure 5.31 Showing the SE1 and SE2 creation mechanism. Courtesy of Goldstein et al[1]

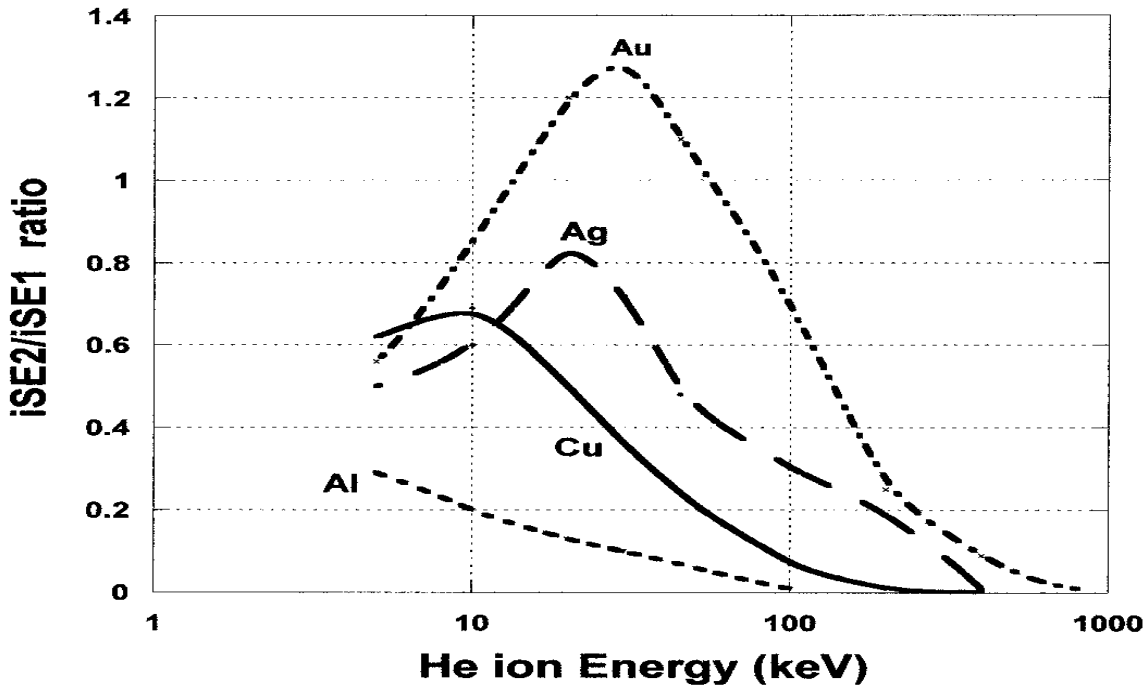

Figure 5.32 Showing the SE2/SE1 ratio in Helium ion Microscope. Data from IONiSE

ratio would probably also be expected for electrons in the energy range below the stopping power maximum i.e. below 200eV, although this variation would be less evident because the change in electron backscattering yield with energy is smaller than that for ion irradiation. For higher He^+ energies (E>50keV) the iSE2/iSE1 ratio is always predicted to be significantly lower than that for electrons which will result in high resolution iSE images whose contrast and detail will be much enhanced compared to those from electron beams.

5.5 Radiation damage and iSE yield

As discussed in chapter 2, Erents et.al [74] clearly showed that size of blisters clearly increased with the energy of the He ions but showed no variation with ion dose, which may indicate that

this mechanism is dependent on the stopping power of the ion which also increases with energy (atleast in the energy regime of this experiment). There was a check done to see if the iSE yield (calculated from IONiSE) which is directly proportional to the stopping power correlated with vacancy creation (Calculated from SRIM), but however there seemed to be no apparent correlation as can be seen from Figure 5.33. Volkert et.al [78] pointed out that SRIM vacancy creation are overestimates since defect interactions and diffusion is not considered in the program, so it can not be ascertained if there is any direct relationship between the iSE yield and radiation damage.

5.5 Conclusion

The combination of the 'semi empirical' model for secondary electron production and the TRIM model for ion stopping power, scattering, and transport, results in a Monte Carlo simulation which can quantitatively interpret helium induced kinetic iSE yield data. This procedure requires that the parameters of the semi-empirical model be determined by fitting to experimental yield data so the validity of the result depends completely on the quality of the experimental data used, but has the merit that, unlike more fundamental models, it can be applied with to both pure elements and complex compounds. The success of the IONiSE model confirms that eSE and iSE generation phenomena are closely related when compared on the basis of incident velocity rather than incident energy and, because the same model can also readily be extended to accommodate protons and ions other than helium, it should allow for a more comprehensive approach to the modeling of charged particle imaging.

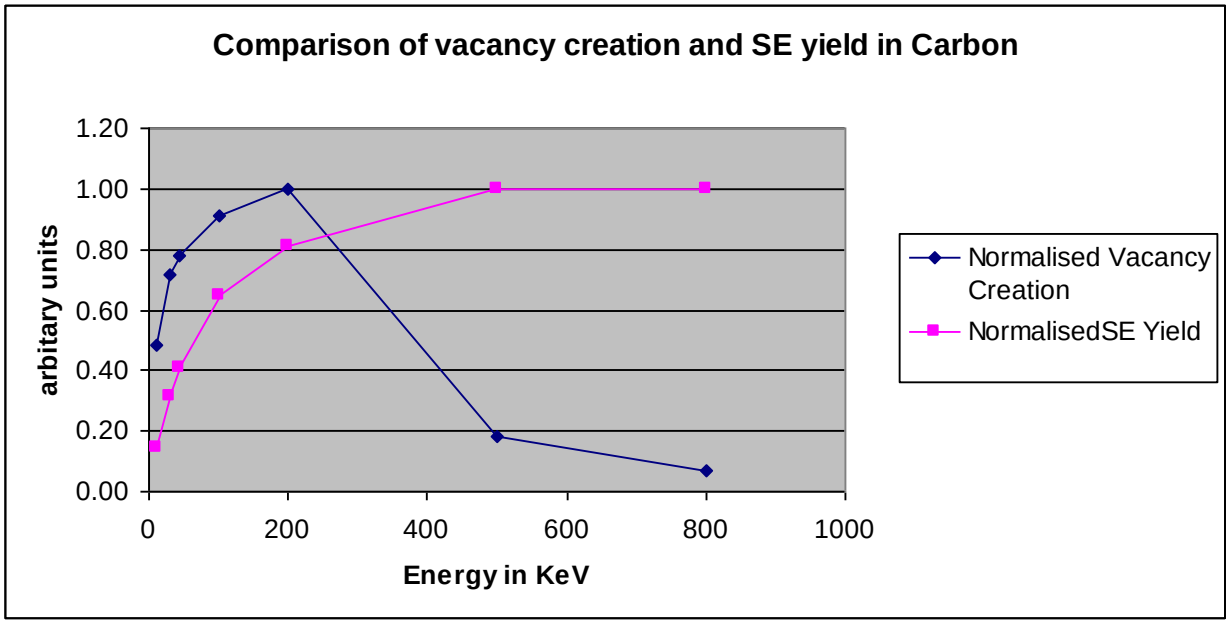

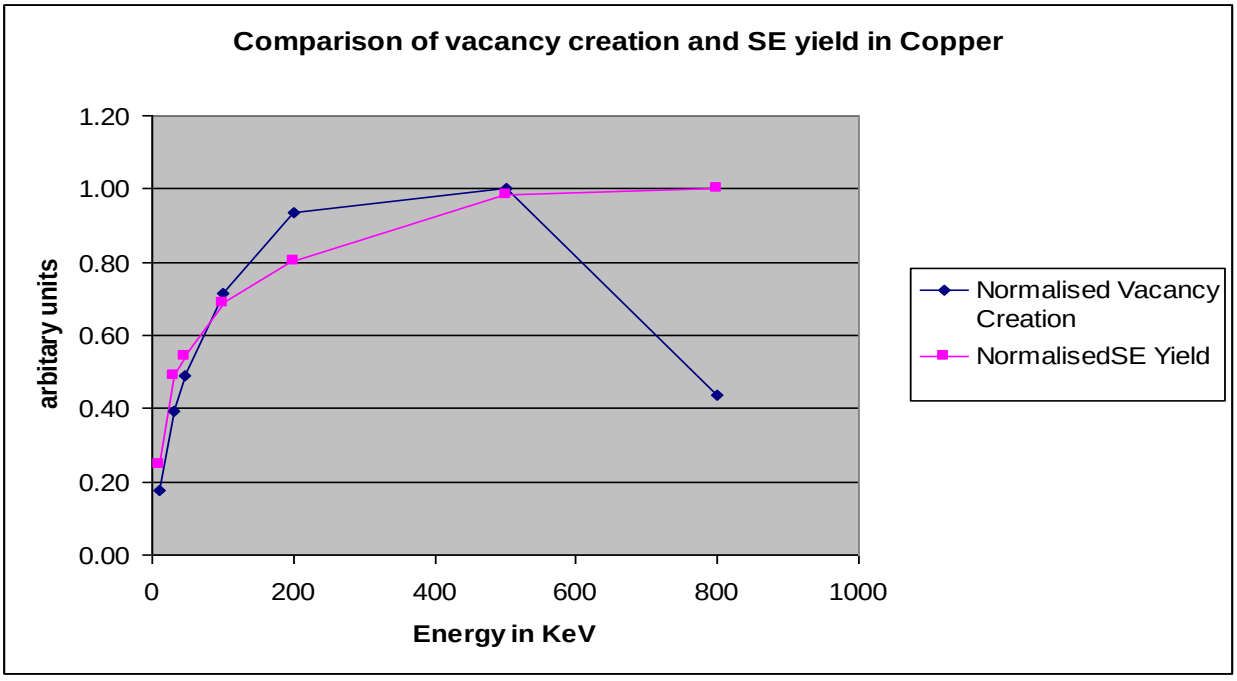

Figure 5.33 Comparing the iSE and Vacancy yields for He^+ ions. Data from IONiSE and SRIM [3]

6. Future Work

6.1 Extending the program for other ions:-

The heavy ion stopping power from SRIM [3] can now be incorporated into IONiSE. Work is underway to extend the existing program to include protons and Gallium ions. The range of protons is comparable to that of the helium ions, but the range of gallium ions is significantly lesser as shown in Figure 6.01. The iSE yields in case of protons like helium ions will be mainly due to the incident ion but however in case of gallium ions there will be significant contribution from sputtered atoms to the total iSE yields. The limitation in using the model for heavier ions like Ar^+ and Ga^+ is that these ions constantly remove material from the target surface and hence the experimental iSE yields that are measured are for surface that have been continuously modified, which makes it a little less reliable.

6.2 Back Scattered ion signal

The helium ion BSI image shows a strong material contrast as shown in Figure 1.12, with the absence of X-ray emission from HIM working at energies below 100 KeV, it would be significantly used as a microanalysis tool. It is therefore necessary to quantify and characterize the BSI signal details like coefficient of BSI, energy spectra of the emitted BSI, angular distribution of BSI, sampling depth and lateral distribution of BSI. The program IONiSE can now be used to get valuable information of all these details. This would also give a estimate of

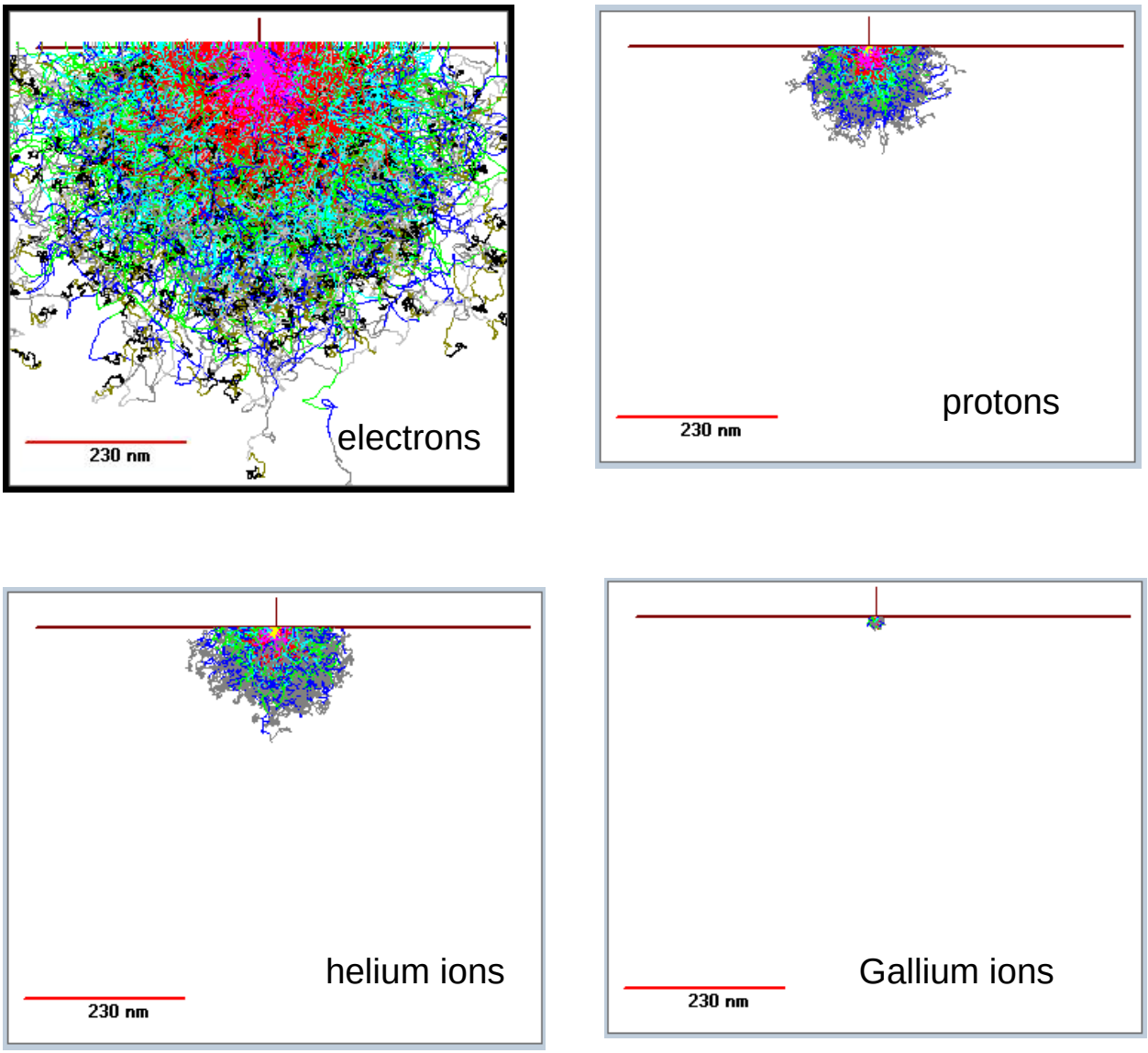

Figure 6.01 Comparing the interaction volume of 20 KeV electrons, protons, helium and gallium ions on copper. Pictures from Banyan and IONiSE.

number of SE3 (SE's due to BSI hitting the polepiece's and inner walls of the specimen chamber) which in a SEM generally contributes to about 50-60 %, incase of HIM it should be significantly higher.

6.2 Transmission of ions

The first Field Ion Microscope (FIM) that was designed by Levi-Setti et.al used protons for imaging, and it was run in a transmission mode. There is both interest and skepticism if helium ion microscope can indeed be run in the transmission mode to get images of materials because the interaction volume of helium ions is very small. The Zeiss ORION group is beginning to get some images in the transmission mode. The preliminary data from IONiSE shows that the 50% transmission range for helium ions is a reasonable thickness of about 600 nm at 200 KeV as shown in Figure 6.02. There will also be engineering that needs to be done to maintain an ion beam at 200 KeV with out significant vibrations, which seems to be one of the main concerns even in the present version of ORION affecting even the current performance of beam being run at 30-50 KeV. If the transmission helium ion microscope is built that it will be a great tool in studying the grain structure of materials because ions have tendency to preferentially channel in certain crystallographic planes and will provide exceptional channeling contrast.

6.3 Energy deposition profiles

The Figure 6.03 shows the energy deposition profile on carbon (chemically close to PMMA) for 50 KeV helium ions and electrons. In case of helium ions the entire energy of the beam is

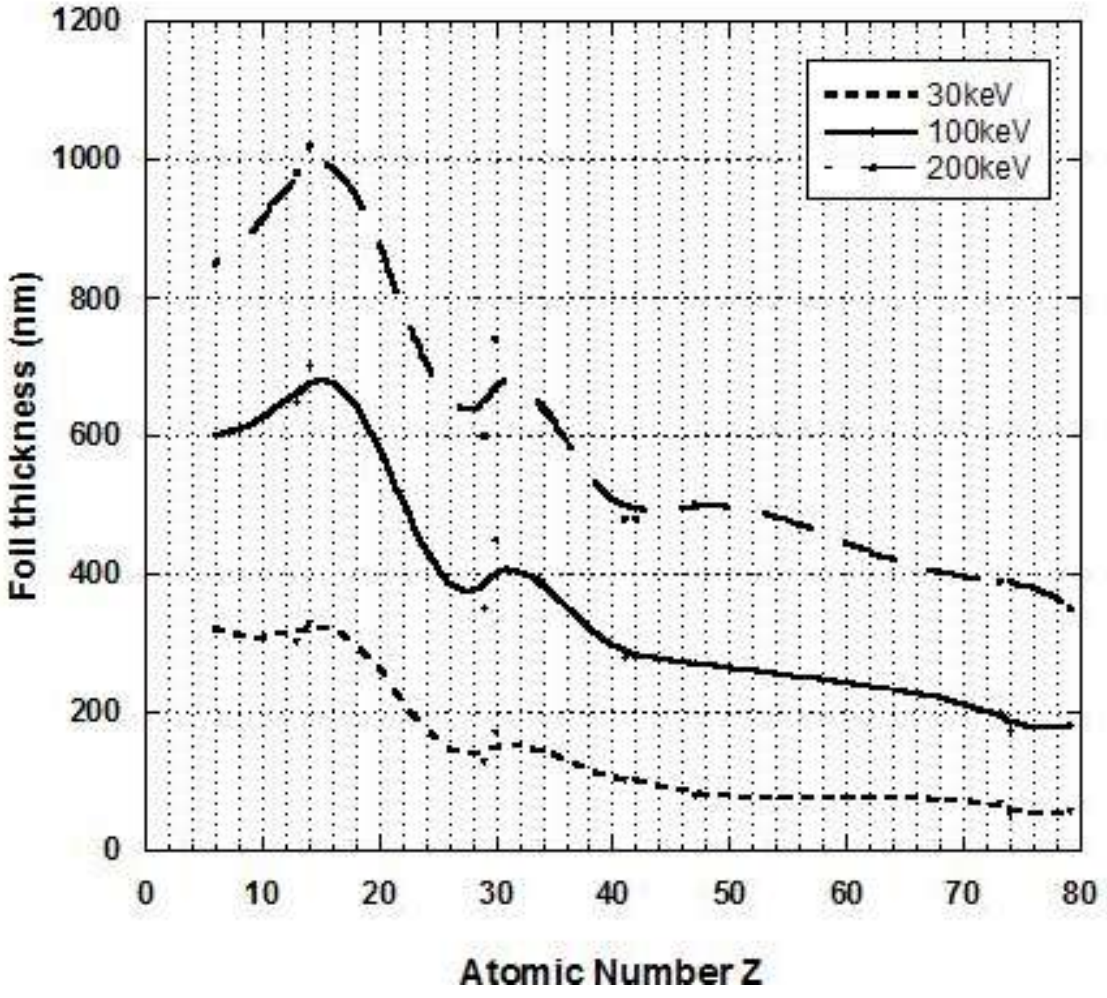

Figure 6.02 The 50% transmission range for helium ions. Data from IONiSE.

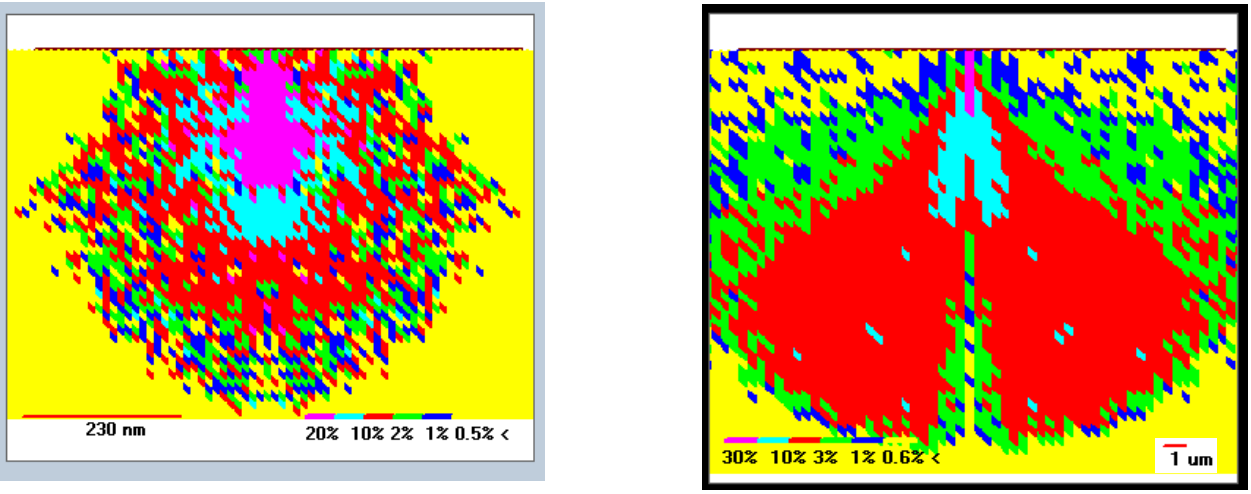

Figure 6.03 Comparing the energy deposition profile for helium ion (left picture) and electrons. Pictures from Banyan and IONiSE.

deposited with in a depth of about 0.5 um while in the 20 um, also in case of helium ions the maximum energy is deposited at the regions near the beam entrance unlike the case of electrons where the deposition is more spread. The energy profile for helium ions is however an underestimate of the actual lithographic development profile that may be expected from helium ions, because in this case there is going to be a significant effect of the recoiling target atoms in the bottom of the interaction volume, hence some undercutting is to be expected with helium ions. Also as explained in chapter 1 the patterns may have high line width roughness due to statistical fluctuations. There is also need for further experimental evidence that the Greeneich et.al [81] limits of PMMA solubility for electrons is also valid for ions.

6.4 Line profiles

The algorithms to measure critical dimension in a CD-SEM should be tailored for the helium ions in case SHIM is going to be used as a metrology tool because both the SE yield and its topographic contrast is going to be significantly different. Figure 6.04 shows the initial model underway to calculate the line profiles.

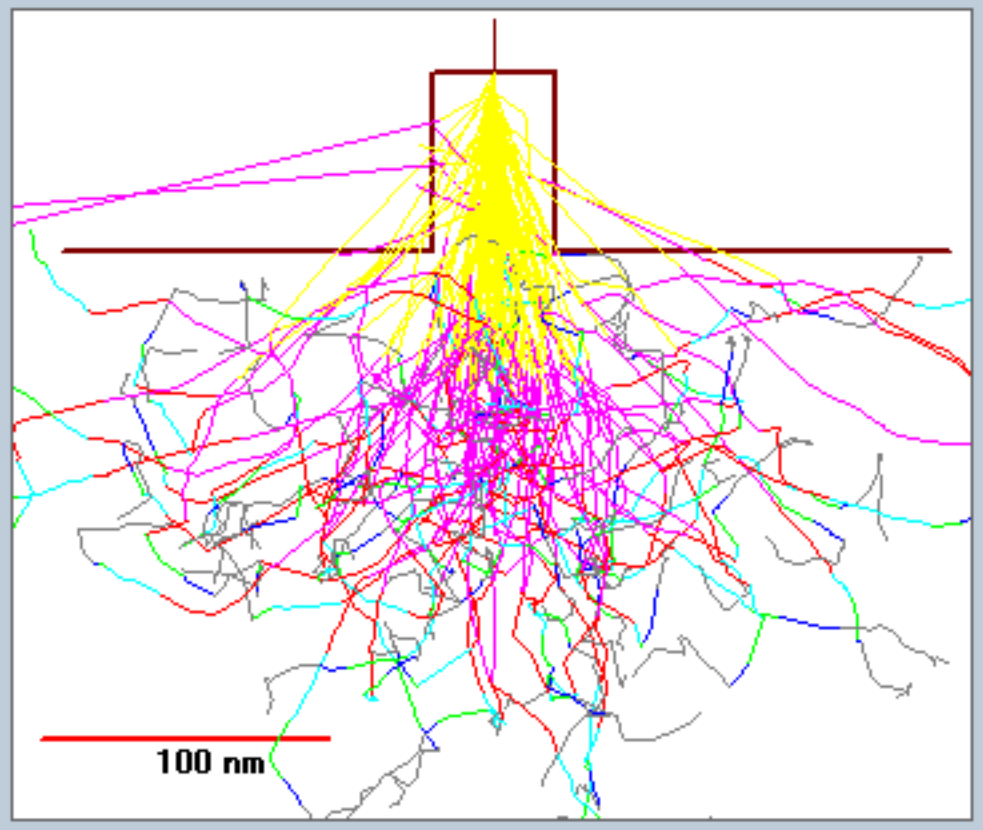

Figure 6.04 showing trajectories for line edge measurements.

References

1. Goldstein J, Newbury D E, Joy D C, Lyman C, Echlin P E, Lifshin E, Sawyer L, and Michael J, “Scanning Electron Microscopy and X-ray Microanalysis”, 3rd Edition 2nd reprint, Kluwer Academic/ Plenum Publishers (2005), 689pp
2. Ward B M, Notte J, and Economou N P, (2006), “Helium ion microscopy”, J.Vac.Sci. Technol. B24, 2871-2874. The “ORION” Helium ion microscope is from Zeiss SMT (Peabody:MA); www.smt.zeiss.com
3. Ziegler J F, Biersack J P, Littmark U, (1985), ‘The stopping and range of ions in solids’, volume 1, (Pergamon Press:NY); www.SRIM.org
4 Joy D C, Luo S, Gauvin R, Hovington P, and Evans N, "Experimental measurements of electron stopping power at low energies", Scanning Microscopy 10, 653-666 (1996)
5 Thomson J J, “Ionization by moving particles”, Phil. Mag. 28, 449-457 (1912)
6. Joy D C, “Monte Carlo Modeling for Electron Microscopy and Microanalysis”, Oxford, University Press: New York, pp 216, (1995)
7. Biersack J P, Haggmark L G, “ A Monte Carlo computer program for the transport of energetic ions in amorphous layers’, Nucl. Instr. and Methods, 174, 257-269 (1980)
8. Lindhard J, Nielsen V, and Scharff M, (in Danish), Mat. Fys. Medd. Dan. Vid. Selsk: 36, No.10 (1968)
9. K.B. Winterbon, P.Sigmund and J.B.Sanders, (in Danish) Mat. Fys. Medd. Dan. Vid.Selsk, 37:No.14 (1970)
10. G P. Mueller, “Total cross-section corresponding to the differential cross-section of Linhard, Nielsen and Scharff’, Radiation Effects 21, 253-258 (1974)
11. Bruining H, ‘Physics and application of secondary electron emission’, (Pergamon

Press:London) (1954)

12. Lai SY, Briggs D, Brown A, and Vickerman J C, 'Relationship between Electron and ion induced SE imaging', Surf. And Interface Analysis 8, 93-111 (1986)
13. Levi-Setti R,'Ion Microscopy' in 'Scanning Electron Microscopy' (IITRI:Chicago), ed O.Johari, 1,1-15, (1983)
14. Schou J, "SE emission from solids by electron and proton bombardment', Scanning Microscopy 2, 607-632 (1988)
15. Nikawa J, "Application of FIB techniques to failure analysis", . (1991), J Vac Sci Technol., B9, 2566.
16. Sakai Y, Yamada T, Suzuki T, Sata T, Ito H, and Ichinokawa T, (1998), 'Contrast mechanisms in SIM imaging of metals', Appl. Phys. Lett. 73, 611-613
17. Baragiola R A, Alonson E V, Ferron J and Oliva-Florio A, (1979), 'Ion induced Electron emission from clean metals', Surface Science 90, 240-255.
18. Sternglass EJ, 'Theory of SE emission by high speed ions', Phys.Rev.108, 1-12 (1957)
19. Benazeth N, 'Review of kinetic iSE from solid metal targets', Nucl. Inst. Meth. 194, 405-413 (1982)
20. Dubus A, Devooght J, Dehase J C, "Theoretical evaluation of ion induced SE" Nucl. Instrum. Meth., B13, 623-626 (1986)
21. Ishitani T, Shimase A, Hosaka S, 'MC simulation of energetic ion behavior in amorphous targets', Jap. J.of Applied Physics, 22, 329-334 (1983)
22. Inai K, Ohya K, and Ishitani T, "Simulation study on image contrast and spatial

Resolution in helium ion microscope", J. Electron Microscopy, 5, 163-169 (2008)

23. Salow H. "Sekundarelektronen-emission", Phys.Zeit. 41, 434-6, (1940)

24. Dekker A J, "Secondary Electron Emission", Solid State Phys., 6, 251-315, (1958)

25. Seiler H, "SE emission in the SEM', J.Appl.Phys.,54, R1-18 (1984)

26. Bethe H A, 'On the theory of Secondary Emission', Phys.Rev.59, 940-1 (1941),

27. Scheinfein M R, Drucker J, and Weiss J K, "SE production pathways determined by electron coincidence spectroscopy", Phys. Rev., 47, 4068-4071, (1993)

28. Lin Y, and Joy D C, "A new study of SE emission data" Surface and Interface Analysis, 35, 895-905, (2005)

29. Clouvas A, Potiriadis C, Rothard H, Hofmann D, Wunsch R, Groeneveld KO, Katsonos A and Xenoulis AC, 'Role of projectile electrons in SE emission from solid surfaces under fast ion bombardment', Phys.Rev.B55, 12086-12098 (1997)

30. Joy D C, 'A model for calculating secondary and backscattered electron yields", J. of Microscopy, 147, 51-64, (1987)

31. Baragiola R A, Alonso E V, Oliva-Florio A, 'Electron emission from clean metal surfaces induced by low-energy light ions', Phys.Rev B19, 121-129 (1979)

32. Evdokimov I N, Mashkova E S, Molchanov VA, Odintsov D D, 'Dependence of the ion-electron emission coefficient on the angle of incidence", Phys.Stat.Sol. 19 ,407-415, (1967)

33. Ferron J, Alonso E V, Baragiola R A, and Oliva-Florio A, 'Dependence of ion-Electron emission from clean metals on the incidence angle of the projectile", Phys.Rev. B24, 4412 - 4419, (1981)

34. Hasselkamp D, Hippler S, Scharmann A, and Schmehl T, "Electron Emission from

Clean Solid Surfaces by Fast Ions", Ann.Physik 47, 555-567, (1990)

35. Dionne G F, 'Origin of SE Emission yield curve parameters', J.Appl.Phys., 46, 3347-3, (1975)

36. En W, and Cheung N W, 'A new method for determining SE yield dependence on Ion energy', IEEE Trans. Plasma Science 24, 1181-1187 (1996)

37. Szapiro B, Rocca J J, Prabhuram T, 'Electron yield of glow discharge materials Under helium ion bombardment', Appl.Phys.Lett., 53, 358-360, (1988)

38. Griffin BJ, Joy DC "Variation of Rutherford Backscattered Ion and Ion induced Secondary Electron Yield with atomic number in the "ORION" Scanning Helium Ion Microscope" , Microscopy and Microanalysis 2008 meeting

39. Morgan J, Notte J, Hill R, Ward B ,"An Introduction to the Helium Ion Microscope" Microscopy Today, Vol 14, July 2006

40. Arshak.K, Mihov.M, Arshak.A, D.McDonagh and D.Sutton, " Focused Ion Beam Lithography – Overview and New approaches", Proc 24th international conference on Microelectronics

41. Melngallis J, " Critical Review Focused ion beam technology and applications", J.Vac.Sci.Technol. B 5(2), Mar/Apr 1987

42. Ian M.Torrens "Interatomic Potentials" Academic Press (1972)

43. Michael Nastasi, James W.Mayer, James K.Hirvonen," Ion-solid interactions: Fundamentals and Applications", Cambridge University Press (1996)

44. French A.P," Newtonian Mechanics", W.W.Norton & Co.(1971)

45. Austin L and Starke H, Ann.Physik,9,271 (1902)

46. M.P.Villard, J.Phys.Theor.Appl. ,8,5(1899)
47. Alonso.E.V, Baragoila.A, J.Ferron,M.M.Jakas and Oliva-Florio, “Z1 dependence of ion-induced electron emission from aluminum”, Phys.Rev B,22,1980
48. Petrov .N.N “New Studies of Electronic Emission from solids under Ion bombardment”, Proceedings 7th Yugoslav symposium and summer school on physics of ionized gases,1974
49. Toglhofer .K, Aumayr.F, Winter HP “ Ion-induced electron emission from metal surfaces – insights from emission statistics” Surf.Sci,281,1993
50. Mulapadi Satya Prasad "Fundamental studies of X-ray and Secondary Electron Spectroscopy”, PhD Thesis, University of Tennessee, 2004
51. David Joy “ Electron Solid Interaction Database”, http://web.utk.edu/~srcutk/htm/interact.htm
52. Kishinevskii L.M, Radiation effects 19 (1973)
53. Parilis E.S, Kishinevskii L.M , “The theory of ion-electron emission”, Soviet Physics – Solid State, 3, 1960
54. Ohya K, Ishitani T “Target material dependence of secondary electron images induced by focused ion beams”, Surface and Coating Technology,158-159,2002
55. Ohya K “Comparative study of target atomic number dependence of ion induced and electron induced secondary electron emission”, Nuclear Inst. And Methods B 206, 2003
56. Ghosh. S.N and Khare. S.P “Secondary Electron Emissions from Metal Surface by High-Energy Ion and Nuetral Atom Bombardments” Physics Review, 125, 1962

57. Baragoila R.A, Alonso.E.V and Oliva Florio.A “Electron emission from clean metal surfaces induced by low energy light ions” Phys.Rev,19,1979
58. Winter H P, Eder H, Aumayr F “Kinetic electron emission in the near-threshold region studied for different projectile charges”, Int. Journal of Mass Spectrometry, 192,1999
59. Ruano G and Ferron J “Ion induced high energy electron emission from copper”,Nucl.Instr. and Meth.in Phys.Res B(2008)
60. Baragoila R.A, Alonso E.V, Ferron J and Oliva-Florio “Ion-induced electron emission from clean metals” , Surf.Sci,90,1979
61. Hagstrum H.D “Inelastic Ion-Surface collisions”, Eds N.H.Tolk et al in Academic Press, New York, 1977.
62. Yuyu Wang, Yongtao Zhao, Qayyum A, Guoqing Xiao “Separation of potential and Kinetic electron emission from Si and W induced by multiply charged neon and argon ions”, Nucl. Intsr and Methods in Physics Research, B 265,2007
63. Nishimura K, Ohya K “Monte carlo simulation of slow-electron cascade in potential electron emission”, Nucl. Instr and Methods in Physics Research B 153,1999
64. Beuhler R.J, Friedman L “A model of secondary electron yields from atomic and polyatomic ion impacts on copper and tungsten surfaces based upon stopping-power calculations”, J.App.Phys,48,1977
65. Lucille Gianuzzi, Fred Stevie “Theory and Applications of focused ion beams”, Springer Series 2005

66. Ranjan Ramachandra, Brendan Griffin and David Joy “A model of secondary electron imaging in the helium ion scanning microscope” Ultramicroscopy (2009)
67. Kasap S.O “Principles of Electronic Materials and Devices” McGraw-Hill 2002
68. Riccardo Levi-Setti “Proton Scanning Microscopy: Feasibility and Promise”, Scanning Electron Microscopy (IITRI Chicago), 1974
69. Scott Wight, Doug Meier, Andras Vladar, Bin Ming, Mike Postek, John Small and Dale Newbury “A comparison of Imaging Modes: Primary electron and He Ion induced”, Proceedings of Microscopy and Microanalysis 2008
70. The Carl Zeiss SMT company website “http://www.smt.zeiss.com/”
71. Broers A N “Resolution limit of PMMA resist for exposure with 50 keV electrons” ,J.Electrochem.Soc.,128,1981
72. L.N. Large and W.S. Whitlock, Proc.Phys.Soc –London, 148, 1962
73. R.D.Brown, P.Rao and P.S.Ho “ Observation of damage in helium ion irradiated gold films using transmission electron microscopy” , Radiation effects, 18, 1973
74. S.K. Erents and G.M. McCracken “ Blistering of molybdenum under helium ion bombardment” , Radiation effects, 18, 1973
75. M.R. Ruhle “Radiation induced voids in metals” U.S.A.E.C office of information services
76. David Cohen-Tanugi and Nan yao “Superior imaging resolution in scanning helium-ion microscopy: A look at beam-sample interactions”, J.Appl.Phys, 104,2008

77. Bradley Thiel and Milos Toth “Secondary electron contrast in low-vacuum/environmental scanning electron microscopy of dielectrics”, J.Appl.Phys,97,2005
78. C.A. Volkert and A.M. Minor “Focused Ion beam Microscopy and Micromachining”, MRS bulletin, 32, 2007
79. Warren J. MoberlynChan, David P.Adams, Michael J.Aziz, Gerhard Hobler and Thomas Schenkel “ Fundamentals of Focused Ion Beam Nanostructural Processing: Below, At, and Above the Surface”, MRS bulletin, 32, 2007
80. Joy D.C and Griffin B.J “Imaging and microanalysis with helium ion beams”, Proc.AMAS-IV Symposium, 2007
81. Greeneich J.S, Van Duzer T, Everhart T.E “Model for exposure of Electron-Resist“, Scanning electron microscopy, 1973

Vita

Ranjan Ramachandra was born in Chennai, India on December 17, 1978. He earned his Bachelor's degree in Mechanical Engineering in the year 2000 from P.E.S. college of engineering affiliated to the University of Mysore, India. His graduating project was Three dimensional graphical simulation of an Robot and he passed with a first class with distinction. From Nov 2000 to June 2004 he worked as a software engineer in Tata Consultancy Services. Here he got to work on different software languages and databases. He also managed a small team and his duties included service level agreement compliance and quality compliance of his project team. He also undertook a Six Sigma green belt project to improve the process of the customer GE Commercial Finance, he was also awarded certificate of appreciation from the customer. He started his graduate studies in Materials Science and Engineering at the University of Tennessee in the fall of 2004. He got his Non Thesis masters in the summer of 2006 under the guidance of Dr. Larry Wadsworth. He started his doctoral studies under the guidance of Dr. David Joy in the fall 2006, his research mainly focused on electron beam interactions, ion beam interaction with solids and nanofabrication techniques. He got his PhD degree in the summer of 2009. He is a member of Microscopy Society of America (MSA), Semiconductor Research Consortium (SRC) and Society of Photonioc Instrumentation Engineers (SPIE).